

Springer Series in Materials Science 287

Kazuaki Sakoda *Editor*

# Electromagnetic Metamaterials

Modern Insights into Macroscopic  
Electromagnetic Fields

 Springer

# Springer Series in Materials Science

Volume 287

## Series Editors

Robert Hull, Center for Materials, Devices, and Integrated Systems,  
Rensselaer Polytechnic Institute, Troy, NY, USA

Chennupati Jagadish, Research School of Physical, Australian National University,  
Canberra, ACT, Australia

Yoshiyuki Kawazoe, Center for Computational Materials, Tohoku University,  
Sendai, Japan

Richard M. Osgood, Department of Electrical Engineering, Columbia University,  
New York, USA

Jürgen Parisi, Universität Oldenburg, Oldenburg, Germany

Udo W. Pohl, Institute of Solid State Physics, Technical University of Berlin,  
Berlin, Germany

Tae-Yeon Seong, Department of Materials Science & Engineering,  
Korea University, Seoul, Korea (Republic of)

Shin-ichi Uchida, Electronics and Manufacturing, National Institute of Advanced  
Industrial Science and Technology, Tsukuba, Ibaraki, Japan

Zhiming M. Wang, Institute of Fundamental and Frontier Sciences - Electronic,  
University of Electronic Science and Technology of China, Chengdu, China

Jamie Kruzic, School of Mechanical & Manufacturing Engineering, UNSW  
Sydney, Sydney, NSW, Australia

The Springer Series in Materials Science covers the complete spectrum of materials research and technology, including fundamental principles, physical properties, materials theory and design. Recognizing the increasing importance of materials science in future device technologies, the book titles in this series reflect the state-of-the-art in understanding and controlling the structure and properties of all important classes of materials.

More information about this series at <http://www.springer.com/series/856>

Kazuaki Sakoda  
Editor

# Electromagnetic Metamaterials

Modern Insights into Macroscopic  
Electromagnetic Fields

 Springer



*Editor*  
Kazuaki Sakoda  
National Institute for Materials Science  
Tsukuba, Ibaraki, Japan

ISSN 0933-033X                      ISSN 2196-2812 (electronic)  
Springer Series in Materials Science  
ISBN 978-981-13-8648-0              ISBN 978-981-13-8649-7 (eBook)  
<https://doi.org/10.1007/978-981-13-8649-7>

© Springer Nature Singapore Pte Ltd. 2019

This work is subject to copyright. All rights are reserved by the Publisher, whether the whole or part of the material is concerned, specifically the rights of translation, reprinting, reuse of illustrations, recitation, broadcasting, reproduction on microfilms or in any other physical way, and transmission or information storage and retrieval, electronic adaptation, computer software, or by similar or dissimilar methodology now known or hereafter developed.

The use of general descriptive names, registered names, trademarks, service marks, etc. in this publication does not imply, even in the absence of a specific statement, that such names are exempt from the relevant protective laws and regulations and therefore free for general use.

The publisher, the authors and the editors are safe to assume that the advice and information in this book are believed to be true and accurate at the date of publication. Neither the publisher nor the authors or the editors give a warranty, expressed or implied, with respect to the material contained herein or for any errors or omissions that may have been made. The publisher remains neutral with regard to jurisdictional claims in published maps and institutional affiliations.

This Springer imprint is published by the registered company Springer Nature Singapore Pte Ltd. The registered company address is: 152 Beach Road, #21-01/04 Gateway East, Singapore 189721, Singapore

*To the memory of Prof. Masanori Hangyo*

# Preface

“Metamaterial” is the generic name to call structured materials whose sizes are smaller than the wavelengths of our interest. So, they are approximately smaller than  $1\ \mu\text{m}$  for optical frequencies and smaller than  $1\ \text{cm}$  for microwaves. In the early stage of the metamaterials research, people were mainly interested in materializing the negative refractive index, for which many new and fascinating electromagnetic phenomena were expected. Later, more diverse applications were found by using these structured materials. So, they are called metamaterials even when their effective refractive index is not negative.

This book describes the novel and fundamental aspects of metamaterials that were developed in the last several years. It is organized as follows. In Chap. 1, the basic idea of metamaterials, that is, the designing of the refractive index, is described. Chapters 2–5 are devoted to metamaterials in optical frequencies. Both top-down (lithography) and bottom-up (self-assembly) techniques are explained in detail, since the precise fabrication of the specimens is a big task in these frequencies. Their particular features like selective thermal emission and its application to  $\text{CO}_2$  gas sensing are shown. Chapters 6–8 deal with terahertz metamaterials, for which the specimen fabrication is relatively easy compared with optical metamaterials, so very precise design and production of various components for terahertz spectroscopy have been achieved. The active control of the terahertz metamaterials made of semiconductors is also described. Chapters 9–11 are devoted to microwave metamaterials, where three unique achievements are presented: Metamaterials with the negative refractive index, dynamic metamaterials based on the discharge plasma, and the meta-atoms emulating quantum phenomena like electromagnetically induced transparency. Chapters 12–15 deal with chiral and non-reciprocal metamaterials. After two chapters that give the framework for the theoretical treatment of the general chiral media and their surface waves, two particular classes of non-reciprocal specimens and their performance are presented: Single chiral metamolecules under a magnetic field and magnetized microstrip lines. Finally, another new feature of periodic metamaterials, that is, the Dirac cone formation in the dispersion relation, is described in Chap. 16.

Many topics described in this book are based on the achievements of the research project *Electromagnetic Metamaterials* organized by MEXT (Ministry of Education, Culture, Sports, Science and Technology), Japan, in which more than 50 professors of universities and researchers of national institutes participated. Prof. Masanori Hangyo of Osaka University was Head Investigator of the project, who also organized the annual Japan–Korea Metamaterials Forum from 2011, which was extended to the A3 (Japan, Korea, and China) Metamaterials Forum later. These project and forums contributed much to the development of metamaterials research. It was our grief that he passed away in October 2014. We deeply thank Prof. Hangyo for his leadership and great efforts in the promotion of the metamaterials and terahertz science.

Tsukuba, Japan

Kazuaki Sakoda

# Contents

<b>1</b>	<b>Modern Insights into Macroscopic Electromagnetic Fields</b> . . . . .	<b>1</b>
	Kazuaki Sakoda	
<b>Part I Metamaterials in Optical Frequencies</b>		
<b>2</b>	<b>Fabrication Techniques for Three-Dimensional Optical Metamaterials</b> . . . . .	<b>7</b>
	Takuo Tanaka	
<b>3</b>	<b>Blackbody Metamaterial Composite Film of Nanoparticle and Polymer</b> . . . . .	<b>43</b>
	Kotaro Kajikawa and Hisashi Karube	
<b>4</b>	<b>Bottom-up Strategies for Fabricating Meta-atoms via Self-assembly of Polymers and Nanoparticles</b> . . . . .	<b>59</b>
	Hiroshi Yabu	
<b>5</b>	<b>UV-Nanoimprinted Metasurface Thermal Emitters for Infrared CO<sub>2</sub> Sensing</b> . . . . .	<b>71</b>
	Hideki T. Miyazaki	
<b>Part II Metamaterials in THz Frequencies</b>		
<b>6</b>	<b>Birefringent Metamaterials for THz Optics</b> . . . . .	<b>89</b>
	Masaya Nagai	
<b>7</b>	<b>Development and Applications of Metasurfaces for Terahertz Waves</b> . . . . .	<b>99</b>
	Keisuke Takano, Boyong Kang, Yuzuru Tadokoro, Kosaku Kato, Makoto Nakajima and Masanori Hangyo	

<b>8</b>	<b>Efficient Optical Modulation of Terahertz Metamaterials Utilizing Organic/Inorganic Semiconductor Hybrid Systems . . . . .</b>	<b>117</b>
	Tatsunosuke Matsui, Keisuke Takano, Makoto Nakajima and Masanori Hangyo	
<b>Part III Metamaterials in Microwave Frequencies</b>		
<b>9</b>	<b>Negative Refractive Index Materials Composed of Metal Patterns and the Applications . . . . .</b>	<b>131</b>
	Hiroshi Kubo	
<b>10</b>	<b>Functional Composites of Discharge Plasmas and Solid Metamaterials . . . . .</b>	<b>151</b>
	Osamu Sakai and Akinori Iwai	
<b>11</b>	<b>Meta-atoms Emulating Quantum Systems . . . . .</b>	<b>169</b>
	Toshihiro Nakanishi and Masao Kitano	
<b>Part IV Chiral and Non-reciprocal Metamaterials</b>		
<b>12</b>	<b>Dispersion Relation in Chiral Media: Credibility of Drude–Born–Fedorov Equations . . . . .</b>	<b>189</b>
	Kikuo Cho	
<b>13</b>	<b>Surface Waves of Isotropic Chiral Metamaterials . . . . .</b>	<b>201</b>
	Hiroshi Miyazaki and Yoji Jimba	
<b>14</b>	<b>Magneto-chiral Metamolecules for Microwaves . . . . .</b>	<b>219</b>
	Satoshi Tomita, Kei Sawada, Hiroyuki Kurosawa and Tetsuya Ueda	
<b>15</b>	<b>Dispersion Engineering of Nonreciprocal Metamaterials . . . . .</b>	<b>235</b>
	Tetsuya Ueda and Tatsuo Itoh	
<b>Part V Novel Aspects</b>		
<b>16</b>	<b>Photonic Dirac Cones and Relevant Physics . . . . .</b>	<b>257</b>
	Kazuaki Sakoda	

# Contributors

**Kikuo Cho** Institute of Laser Engineering, Osaka University, Suita, Osaka, Japan

**Masanori Hangyo** Institute of Laser Engineering, Osaka University, Suita, Osaka, Japan

**Tatsuo Itoh** Electrical Engineering Department, University of California, Los Angeles, Los Angeles, CA, USA

**Akinori Iwai** The University of Shiga Prefecture, Hikone, Japan;  
Kyoto University, Kyoto, Japan

**Yoji Jimba** College of Engineering, Nihon University, Koriyama, Japan

**Kotaro Kajikawa** Interdisciplinary Graduate School of Science and Engineering, Tokyo Institute of Technology, Yokohama, Japan

**Boyong Kang** Institute of Laser Engineering, Osaka University, Suita, Osaka, Japan;  
Center for Advanced Meta-Materials, Yuseong-Gu, Daejeon, Korea

**Hisashi Karube** Interdisciplinary Graduate School of Science and Engineering, Tokyo Institute of Technology, Yokohama, Japan

**Kosaku Kato** Institute of Laser Engineering, Osaka University, Suita, Osaka, Japan

**Masao Kitano** Department of Electronic Science and Engineering, Kyoto University, Kyoto, Japan

**Hiroshi Kubo** Yamaguchi University, Yamaguchi, Japan

**Hiroyuki Kurosawa** National Institute of Information and Communications Technology, Kobe, Hyogo, Japan

**Tatsunosuke Matsui** Department of Electrical and Electronic Engineering, Graduate School of Engineering, Mie University, Tsu, Mie, Japan



**Hideki T. Miyazaki** National Institute for Materials Science, Tsukuba, Ibaraki, Japan

**Hiroshi Miyazaki** Department of Applied Physics, Tohoku University, Sendai, Japan

**Masaya Nagai** Graduate School of Engineering Science, Osaka University, Toyonaka, Japan

**Makoto Nakajima** Institute of Laser Engineering, Osaka University, Suita, Osaka, Japan

**Toshihiro Nakanishi** Department of Electronic Science and Engineering, Kyoto University, Kyoto, Japan

**Osamu Sakai** The University of Shiga Prefecture, Hikone, Japan

**Kazuaki Sakoda** National Institute for Materials Science, Tsukuba, Japan

**Kei Sawada** RIKEN SPring-8 Center, Sayo, Hyogo, Japan

**Yuzuru Tadokoro** Institute of Laser Engineering, Osaka University, Suita, Osaka, Japan

**Keisuke Takano** Institute of Laser Engineering, Osaka University, Suita, Osaka, Japan;  
Center for Energy and Environmental Science, Shinshu University, Nagano, Japan

**Takuo Tanaka** Metamaterials Laboratory, RIKEN Cluster for Pioneering Research and Innovative Photon Manipulation Research Team, RIKEN Center for Advanced Photonics, RIKEN, Saitama, Japan

**Satoshi Tomita** Nara Institute of Science and Technology, Ikoma, Nara, Japan

**Tetsuya Ueda** Electrical Engineering and Electronics, Kyoto Institute of Technology, Sakyo, Kyoto, Japan

**Hiroshi Yabu** WPI-Advanced Institute for Materials Research (AIMR), Tohoku University, Sendai, Japan

# Chapter 1

## Modern Insights into Macroscopic Electromagnetic Fields



Kazuaki Sakoda

**Abstract** A new definition of refractive index is introduced to describe the idea of metamaterials. Their fundamental properties and some of their early investigations are explained. In addition, a basic problem of the macroscopic electromagnetic field is raised regarding the development of metamaterials in optical frequencies.

### 1.1 Introduction

What is *refractive index*? This question may sound strange, since it is well known that the refractive index ( $n$ ) is a material constant, which describes the refraction of light according to Snell's law. It is given by

$$n = \sqrt{(\text{relative permittivity}) \times (\text{relative permeability})}, \quad (1.1)$$

which is also well known. However, many researchers have been involved in answering this question for over fifteen years. The reason is that *metamaterials*, which will be described in the following chapters, have considerably changed the idea of the refractive index. They have raised a modern problem of macroscopic electromagnetic fields as well and materialized strange optical phenomena that people had never imagined.

### 1.2 Microscopic and Macroscopic Electromagnetic Fields

We denote the permittivity and permeability of free space by  $\varepsilon_0$  and  $\mu_0$ , respectively. Then the relative permittivity ( $\varepsilon$ ) and relative permeability ( $\mu$ ) relate the electric field ( $\mathbf{E}$ ) to the electric displacement ( $\mathbf{D}$ ), and the magnetic field ( $\mathbf{H}$ ) to the magnetic flux density ( $\mathbf{B}$ ):

---

K. Sakoda (✉)  
National Institute for Materials Science, Tsukuba, Japan  
e-mail: [sakoda.kazuaki@nims.go.jp](mailto:sakoda.kazuaki@nims.go.jp)

$$\mathbf{D} = \varepsilon\varepsilon_0\mathbf{E}, \quad (1.2)$$

$$\mathbf{B} = \mu\mu_0\mathbf{H}. \quad (1.3)$$

These four vector quantities are electromagnetic fields averaged over a scale that is smaller than the wavelength of our interest and larger than atoms and molecules, which are called macroscopic electromagnetic fields. On the other hand, the electric field in the vicinity of an atomic nuclei, for example, can be very large. However, the microscopic electromagnetic field of this kind is not an object that is dealt with by the permittivity, permeability, or refractive index. These material constants, which can be obtained by measurements, accurately describe the electromagnetic wave propagation in matter.

We learn their definition and properties in this way and believe that the problem of the macroscopic electromagnetic field is settled. However, modern technologies can fabricate artificial structures whose sizes are smaller than the optical wavelengths although they are larger than atoms and molecules. In the case of microwaves whose wavelengths are from millimeters to centimeters, the fabrication of artificial structures smaller than the wavelengths is easy. Then, how much is the refractive index that describes the macroscopic field in this case? Can we define the permittivity and permeability appropriately? These considerations lead us to the idea that the refractive index, which has been regarded as a genuine material constant, may be a quantity that we can design.

### 1.3 Metamaterials

Nowadays, *metamaterial* denotes in a wide sense a structure or an assembly of structures that are larger than atoms and molecules but smaller than the wavelengths of electromagnetic waves of our interest. In a narrow sense, it denotes a structure or an assembly of structures that materialize extraordinary optical phenomena such as negative refraction and cloaking and that are larger than atoms and molecules but smaller than the wavelengths of electromagnetic waves of our interest. Because we usually utilize electromagnetic resonance states to materialize these extraordinary optical phenomena, metamaterials in a narrow sense are fabricated by metallic materials in most cases.

In the early stage of the investigation of metamaterials, it attracted a considerable attention to materialize negative refractive indices with split-ring resonators and metallic wires [1]. When both the permittivity and permeability are negative, the refractive index is also negative. If we regard the permittivity and permeability as real negative numbers in (1.1), the refractive index may look positive, since the inside of the square root is positive as a product of two negative quantities. However, the permittivity and permeability always have an imaginary part to some extent due to energy loss. If we carefully trace the argument of the refractive index in the complex plane, we can find that the real part of the refractive index is negative.

When we compare with the ordinary refraction ( $n > 0$ , Fig. 1.1a), the propagation direction of the refracted wave for negative  $n$  (Fig. 1.1b) is on the opposite side of the normal line of the interface of two media. In this case, we may wonder whether the wave vector ( $\mathbf{k}$ ) component parallel to the interface is conserved. Actually, the wave vector and Poynting's vector ( $\mathbf{E} \times \mathbf{H}$ ) are directed oppositely for  $n < 0$ , so the parallel component of the wave vector is conserved. In ordinary positive  $n$  materials,  $\mathbf{E}$ ,  $\mathbf{H}$ , and  $\mathbf{k}$  compose a right-hand system, whereas they compose a left-hand system in negative  $n$  materials. For this reason, metamaterials with negative  $n$  are often called left-handed materials.

The negative refraction was demonstrated with split-ring resonators ( $\mu < 0$ ) and metallic wires ( $\varepsilon < 0$ ) in the microwave frequencies [2]. When the negative refractive index is obtained, we can materialize flat board lenses as Fig. 1.1c shows. By designing the spatial variation of the refractive index, it was demonstrated that the incident wave can propagate while avoiding an obstacle (Fig. 1.1d) [3]. If we observe from the backside of the obstacle, the incident wave looks as if it came straight through. This strange phenomenon is called cloaking.

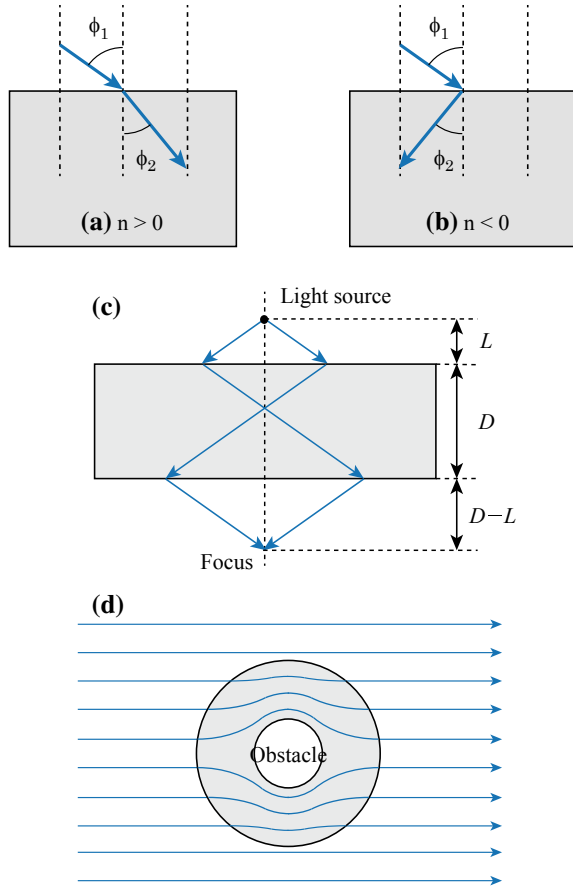
In the case of periodic metamaterials, if we make two dispersion curves degenerate in the center ( $\Gamma$  point) of the Brillouin zone by adjusting their structures, we can materialize an isotropic linear dispersion relation, which is called a Dirac cone. The vertex of the Dirac cone is called the Dirac point, where the refractive index is equal to zero. This phenomenon was discovered by the transmission line theory for microwaves [4]. Later, a general proof was given by the  $\mathbf{k} \cdot \mathbf{p}$  perturbation and group theory [5, 6].

## 1.4 Modern Problems of Macroscopic Fields

Let us go back to our first question, "What is the refractive index?". In the case of microwaves, the size of metamaterials is of the order of  $100 \mu\text{m}$  to  $1 \text{mm}$ , which is different from the sizes of atoms and molecules by several orders of magnitude. So, we can define the refractive index in the usual sense and can calculate the electromagnetic wave propagation by using its spatial variation. On the other hand, we may regard metamaterials as artificial atoms and introduce another refractive index by averaging the electromagnetic field over the scale of  $100 \mu\text{m}$  to  $1 \text{mm}$ . This definition of the refractive index was useful to predict the above-mentioned new phenomena.

In the case of metamaterials in the optical frequencies, however, our question is more serious. The size of the metamaterials is of the order of  $100 \text{nm}$  to  $1 \mu\text{m}$ , and it is becoming smaller as nanotechnologies become more advanced. So, it will become difficult to draw a clear line between the sizes of atoms and metamaterials. Then, many basic questions will arise: What *refractive index* should we use? Can we define the *refractive index* appropriately? Are *permittivity* and *permeability* mutually independent? Metamaterials not only have big potential to materialize novel optical phenomena and fascinating applications but also raise these fundamental questions in optical physics.

**Fig. 1.1** Refraction for **a** a positive refractive index and **b** a negative refractive index. **c** Flat board lens by a metamaterial with  $n = -1$ . **d** Cloaking. The incident wave propagates while avoiding an obstacle



## References

1. D.R. Smith, W.J. Padilla, D.C. Vier, S.C. Nemat-Nasser, S. Schultz, Composite medium with simultaneously negative permeability and permittivity. *Phys. Rev. Lett.* **84**, 4184–4187 (2000)
2. R.A. Shelby, D.R. Smith, S. Schultz, Experimental verification of a negative index of refraction. *Science* **292**, 77–79 (2001)
3. D. Schurig, J.J. Mock, B.J. Justice, S.A. Cummer, J.B. Pendry, A.F. Starr, D.R. Smith, Metamaterial electromagnetic cloak at microwave frequencies. *Science* **314**, 977–980 (2006)
4. A. Sanada, C. Caloz, T. Itoh, Characteristics of the composite right/left-handed transmission lines. *IEEE Microw. Wirel. Compon. Lett.* **14**, 68–70 (2004)
5. J. Mei, Y. Wu, C.T. Chan, Z.-Q. Zhang, First-principles study of Dirac and Dirac-like cones in phononic and photonic crystals. *Phys. Rev. B* **86**, 035141 (2012)
6. K. Sakoda, Proof of the universality of mode symmetries in creating photonic Dirac cones. *Opt. Express* **20**, 25181–25194 (2012)

**Part I**  
**Metamaterials in Optical Frequencies**

# Chapter 2

## Fabrication Techniques for Three-Dimensional Optical Metamaterials



Takuo Tanaka

**Abstract** Metamaterials have attracted much attention because they can provide unexemplified and favorable functionalities and applications in optics and related fields such as negative refractive index, perfect lenses, cloaking, perfect light absorbers, and so on. Because optical metamaterials are artificial sub-wavelength structures, their advancement strongly depends on the development of micro- and nanofabrication techniques. In particular, in spite of the recent progress of these fabrication technologies, the realization of three-dimensional (3D) metamaterials is still one of the big challenges. In this chapter, the recent progress in the fabrication technologies of 3D optical metamaterials is reviewed and discussed.

### 2.1 Introduction

The beginning of this century was the cusp of “metamaterials” [1]. Metamaterials are man-made materials composed of array of tiny metal or dielectric resonant elements, which are sometimes referred to as “meta-atom.” Since meta-atoms are usually designed to be sub-wavelength structure, metamaterials work as quasi-materials and this is why they are called meta-“materials” not meta-“structures.” The most important purpose of engineering metamaterials is to gain emancipated control of light waves using the unexemplified optical properties, phenomena, and functionalities that arise from their structures. Figure 2.1 shows a typical structure of metamaterial that consists of split-ring resonator array integrated into a host material.

A perfect lensing effect realized by negative-index materials is one of such unprecedented functionalities, and metamaterials have attracted increasing interest as promising candidates for controlling the value of the index of refraction to be negative [2]. It is well known that the refractive index of a material is described by the product of the square root of the relative permittivity and the square root of the relative permeability. Because almost all natural substances lose their magnetic responses to

---

T. Tanaka (✉)

Metamaterials Laboratory, RIKEN Cluster for Pioneering Research and Innovative Photon Manipulation Research Team, RIKEN Center for Advanced Photonics, RIKEN, Saitama, Japan  
e-mail: [t-tanaka@riken.jp](mailto:t-tanaka@riken.jp)

© Springer Nature Singapore Pte Ltd. 2019

K. Sakoda (ed.), *Electromagnetic Metamaterials*, Springer Series  
in Materials Science 287, [https://doi.org/10.1007/978-981-13-8649-7\\_2](https://doi.org/10.1007/978-981-13-8649-7_2)



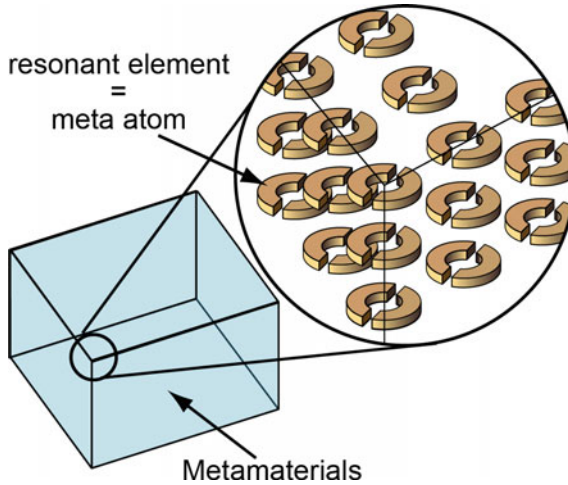


**Fig. 2.1** Schematic of optical metamaterials

the magnetic components of the light and their permeability becomes unity in the optical frequency region, negative-index materials are never found in nature. Recent progress in the creation of optical magnetism by metamaterials realizes novel optical components and phenomena that were previously believed to be unrealizable [3]. In addition to negative-index metamaterials, a wide variety of potential applications have been predicted and demonstrated in the past decade, such as optical cloaking, perfect light absorption, dispersion control, and so on [4].

One of the trends in this research fields is increasing the working frequency of metamaterials, which began in the microwave frequency region around 2.4 GHz, to the visible light regions [5]. Since many efforts have been made by researchers in theoretical studies for realizing optical metamaterials, we have already known what kinds of materials and resonant structures are appropriate for realizing optical metamaterials. Moreover, the recent development of micro- and nanofabrication technologies has brought such ideas to reality, having a huge impact in a wide range of optics and photonics fields [6–8]. However, the realization of true three-dimensional (3D) optical metamaterials is still a challenge, because the current fabrication technologies, such as photolithography and electron beam (EB) lithography, are no more than two-dimensional (2D) patterning techniques and they cannot be applied for fabrication of 3D micro-/nanostructures [9]. In this chapter, we will start to discuss the fundamentals of the 3D metamaterials for modifying the permeability in the optical frequency region clarifying the appropriate material and shape of their structures. After that, we will focus on recent progress of the fabrication techniques for 3D optical metamaterials [10]. Some of the fabrication techniques have been summarized and reviewed in our previous review article [11], but we added several self-organized

and self-assembled techniques as possible candidates for future mass production of metamaterials.

## 2.2 Structure of Optical Metamaterials

In this section, we will discuss the metamaterial structure for modifying magnetic permeability of the materials in the visible light region and clarify the suitable materials and structures for permeability-controlled optical metamaterials [6–8].

### 2.2.1 Dispersion Properties of Gold, Silver, and Copper

In the microwave frequency region (300 M–300 GHz), almost all rare metals such as gold, silver, copper, and so on can be treated as a perfect conductor. This makes it rather easy to discuss their electromagnetic/optical properties. However, in the optical frequency region (about 1–1000 THz), they are not perfect conductor and we need to take care of the dispersion properties of these to use them as materials for metamaterials. So, we would like to start to describe the dispersion properties of metals from THz to ultraviolet (UV) covering the entire visible light region. To do it, we introduced the internal impedance for a unit length and a unit width of the plane conductor ( $Z_s(\omega)$ ) that is described as

$$Z_s(\omega) = \frac{1}{\sigma(\omega) \int_0^T \frac{\exp[ik(\omega)z] + \exp[ik(\omega)(T-z)]}{1 + \exp[ik(\omega)T]} dz} = R_s(\omega) + iX_s(\omega), \quad (2.1)$$

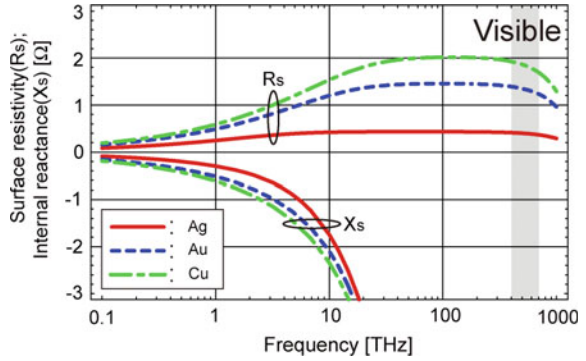
$$k(\omega) = \omega \sqrt{\varepsilon_0 \mu_0 \left[ 1 + i \frac{\sigma(\omega)}{\omega \varepsilon_0} \right]}, \quad (2.2)$$

$$\sigma(\omega) = \frac{\omega_p^2 \varepsilon_0}{\gamma - i\omega}, \quad (2.3)$$

where  $\sigma(\omega)$  is conductivity of metal,  $\sigma(\omega)/(\varepsilon_0\omega)$  in (2.2), and it represents the conduction characteristics of metal, and the real and imaginary parts of  $Z_s(\omega)$  are the surface resistivity  $R_s$  and the internal reactance  $X_s$ , respectively. The integration in the dominator of (2.1) indicates the total current flow through the cross section of the conductor.

Figure 2.2 shows the calculation results of  $Z_s(\omega)$  for gold, silver, and copper.

**Fig. 2.2** Dispersion properties of the internal impedances for a unit length and a unit width of the plate of gold (Au), silver (Ag), and copper (Cu)



### 2.2.2 Dispersion Properties of Split-Ring Resonators

Figure 2.3 shows the calculation model of metamaterial using split-ring resonators (SRRs), which is proposed by Pendry [12]. In Fig. 2.3,  $r$  is the radius of the ring,  $w$  is the width of the ring,  $g$  is the gap distance between two rings of SRR,  $a$  is the unit cell dimension in the  $x$ - $y$  plane, and  $l$  is the distance between adjacent planes of the SRRs along the  $z$ -axis.

Based on the dispersive properties of metals described by (2.1), the frequency dependence of the magnetic responses of the metallic SRRs in the optical frequency region was calculated, and the effective permeability ( $\mu_{eff}$ ) of the SRRs was derived as

$$\mu_{eff} = \mu_{eff} + i\mu_{eff} = 1 - \frac{F\omega^2}{\omega^2 - \frac{1}{CL} + i\frac{Z(\omega)\omega}{L}}, \tag{2.4}$$

where  $C$  and  $L$  are the geometrical capacitance and inductance, and  $F$  and  $Z(\omega)$  are the filling factor and the ring metal impedance defined by

$$F = \frac{\pi r^2}{a^2}, \tag{2.5}$$

**Fig. 2.3** Calculation model of optical metamaterials using split-ring resonators (SRRs)

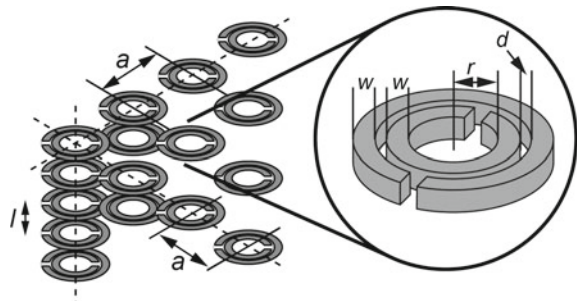
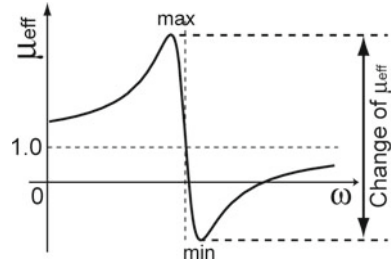


**Fig. 2.4** Dispersion of  $\mu_{\text{eff}}$  by the resonant interaction between SRR and magnetic component of the light



$$C = \frac{2\pi r}{3} \varepsilon_0 \varepsilon_r \frac{K\left[(1-t^2)^{1/2}\right]}{K(t)}, \quad (2.6)$$

$$t = \frac{g}{2w + g}, \quad (2.7)$$

$$L = \frac{\mu_0 \pi r^2}{l}, \quad (2.8)$$

$$Z(\omega) = \frac{2\pi r Z_s(\omega)}{w}, \quad (2.9)$$

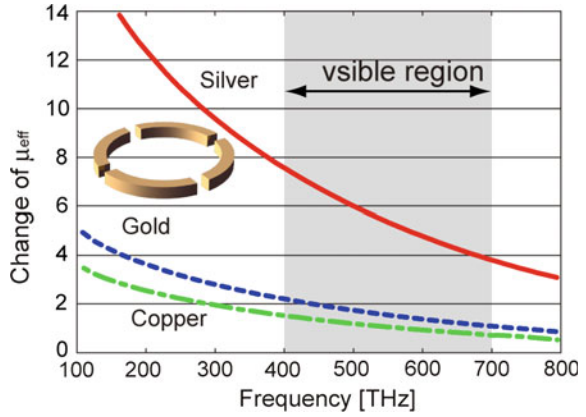
respectively.  $K[\ ]$  of (2.6) is the complete elliptic integral of the first kind. For calculating the geometrical capacitance, Gupta's formula was used to estimate the capacitance coming from the distance between two rings per unit length [13].

By using (2.1) and (2.4) and the empirical values of the plasma frequency ( $\omega_p$ ) and the damping constants ( $\gamma$  of silver, gold, and copper ( $\omega_p = 14.0 \times 10^{15} \text{ s}^{-1}$  and  $\gamma = 32.3 \times 10^{12} \text{ s}^{-1}$  for silver,  $\omega_p = 13.8 \times 10^{15} \text{ s}^{-1}$  and  $\gamma = 107.5 \times 10^{12} \text{ s}^{-1}$  for gold, and  $\omega_p = 13.4 \times 10^{15} \text{ s}^{-1}$  and  $\gamma = 144.9 \times 10^{12} \text{ s}^{-1}$  for copper)), the frequency dispersions of  $\mu_{\text{eff}}$  from 100 THz to 800 THz were calculated [14].



At the resonant frequency of the SRR,  $\mu_{\text{eff}}$  swings positively and negatively as shown in Fig. 2.4. We defined the change of  $\mu_{\text{eff}}$  as the difference between max  $\mu_{\text{eff}}$  and min  $\mu_{\text{eff}}$ . We calculated the dispersion properties  $\mu_{\text{eff}}$  of single ring SRR with four cuts consisting of Au, Ag, or Cu, and plotted the calculation results in Fig. 2.5. From these results, it was found that a three-dimensional SRRs array made of silver gives a strong magnetic response in the visible light frequency region. As also shown in Fig. 2.5, silver SRRs exhibit  $\mu_{\text{eff}}$  changes exceeding 2.0 in the entire visible range, which means  $\mu_{\text{eff}}$  can become a negative value, while the responses of gold and copper SRRs are less than 2.0 in the visible frequency region.

Table 2.1 shows the design strategy of the optical metamaterials that can reveal the magnetic response. In the frequency region less than 100 THz, to realize a relatively low resonant frequency and a low resistance of the metallic structure, the structure should have both a large geometrical capacitance and a wide width of the ring, and the original shape of SRR, which is concentric double rings with gaps, is appropriate. On the other hand, when the frequency becomes higher than 100 THz, the effect of

**Fig. 2.5** Calculated results of the dispersion of  $\mu_{\text{eff}}$  for gold, silver, and copper SRR arrays



**Table 2.1** Design guideline of metamaterial structure

Frequency	<100 THz	100 THz <
Requirement	Large C and small R	Small C and large L
Resonator structure		
Reason for the limitation of magnetic response	Increase of surface resistance	Decrease of L by scaling of SRR

the reactance ( $X_s(\omega)$ ) in the ring becomes more dominant than that of the resistance in the SRR ring. To increase the resonant frequency to such a higher frequency region, the resonant structure should have a small geometrical capacitance, and in order to keep the high Q-value and sufficient magnetic responses, SRR should have a large geometrical inductance. To satisfy these requirements, we proposed that the single ring with a number of cuts is more suitable than the original double-ring SRR, because this is advantageous to prevent the effect of  $X_s(\omega)$ .

### 2.3 Three-Dimensional Metamaterials Versus Bulk Metamaterials

The term “three-dimensional metamaterials” has two different meanings. One is that the shape of metamaterial is three-dimensional and not planate. The other meaning is the functionality of the metamaterial has three degrees of freedom. In this section,

the difference between the dimension of the structure and that of functionality will be discussed.

As already described, one of the most typical unit elements of metamaterial is SRR [12]. An SRR consists of metal rings with several gaps. The metal rings are designed to work as magnetic antenna and inductors, and the gaps work as capacitors. Since the SRR itself works as an LC resonant circuit and there is no antenna whose radiation property is isotropic, metamaterials made with SRRs arrays also inevitably become anisotropic.

When SRRs are placed on  $x$ - $y$  plane as shown in Fig. 2.6a, the structure can be defined as 2D structure. On the other hand, this SRRs array can interact with a magnetic component of light wave that oscillates in the  $z$ -direction and it never interacts with magnetic fields that oscillate in the  $x$ - $y$  plane. Therefore, in terms of the degree of freedom of the magnetic interactions, this structure is categorized as a one-dimensional (1D) metamaterial. Even if such 2D structures are stacked in the  $z$ -direction and they form a bulk (3D) structure, its functionality consistently still remains 1D.

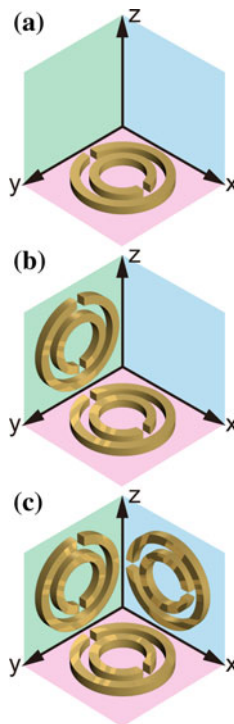


**Fig. 2.6** Three-dimensional structure versus three-dimensional functional metamaterials. **a** Two-dimensional structure but 1D functionality, **b** 3D structure and 2D functionality, and **c** both structure and functionality are 3D

In this sense, we found that the dimension of the structure and that of functionality are completely different. If we want to increase the degree of freedom of metamaterial functions, we need to add different orientated structures as shown in Fig. 2.6b, c. When we add another SRR in the  $x$ - $z$  plane, the metamaterial exhibits 2D optical functions. Moreover, adding an SRR in the  $y$ - $z$  plane makes the structure complete 3D functional metamaterials. In the following part of this chapter, we define the term “bulk metamaterials” as metamaterials whose structure is distributed in  $x$ - $y$ - $z$  3D space irrespective of the dimension of its functionality, and we use the term “3D metamaterials” only for those that have complete 3D functionality.

## 2.4 Fabrication of Three-Dimensional Metamaterials

### 2.4.1 Stacking of Planar Structures to 3D

The easiest way to fabricate a bulk structure might be to stack 2D planar layers. Owing to recent progress in micro- and nanofabrication technologies like photolithography, EB lithography, dry etching techniques, and so on, we can fabricate 2D nanopatterns.

Liu et al. reported an optical metamaterial in which four SRR array structures are stacked by the use of a layer-by-layer technique [15]. In their experiment, 430 nm by 380 nm square SRRs array with an 80 nm linewidth are fabricated using EB lithography, and then four these layers are stacked one-by-one with 70 nm-thick polymer spacing layers as shown in Fig. 2.7. Figure 2.7a shows an oblique incidence view taken by a scanning electron microscope (SEM). In 2009, the same technique was applied to make stereo-SRR dimer metamaterials with various twist angles as shown in Fig. 2.8 [16]. Layer-by-layer technique was also applied by the same team to create a plasmonic-induced transparency (PIT) phenomenon in a multilayer metamaterial in which gold nanorods are stacked on an underlying gold nanowire pair [17]. Because dipole–quadrupole coupling occurred in the PIT structure, they observed a plasmon-induced transmission band in the absorption dips of the upper Au nanorod structure (Fig. 2.9). Multiple stacking of SRRs layers also provides large optical activity [18]. Figure 2.10 shows scanning electron microscope image of the fabricated stacked SRRs. This structure was applied for plasmonic rulers to determine the nanoscale structures of molecules such as proteins, DNA molecules, and so on [19].

In 2012, Kante et al. proposed a two-layer nanosquare ring structure fabricated by the multiple EB lithography methods [20]. In this technique, two layers of gold nanosquare rings were fabricated on a quartz substrate separated by a spacing layer of SU-8. An SEM image of the fabricated two-layer nanoring structure and its schematic image are shown in Fig. 2.11. Two rings are aligned precisely by the EB lithography technique. When one of the rings is fully shifted with respect to the other ring, absorption bands of symmetric and asymmetric modes were overlapped and Fano interference was occurred resulting in appearance of a negative-index band at 1.9  $\mu\text{m}$  in wavelength.



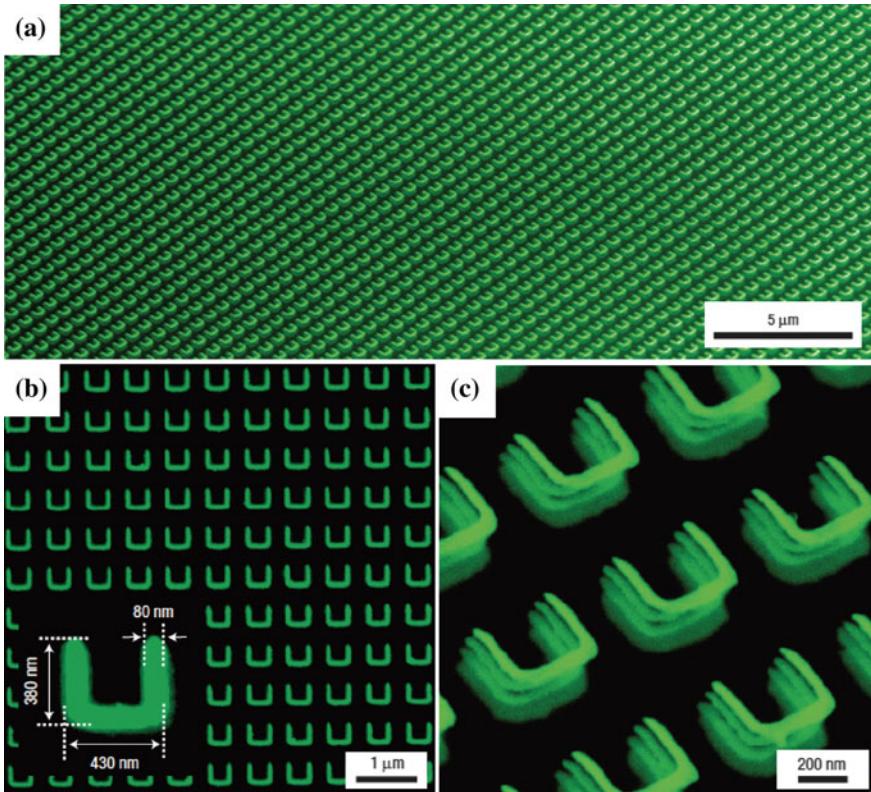
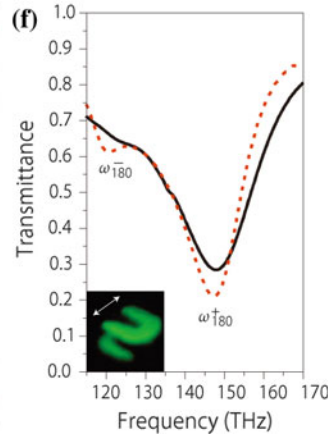
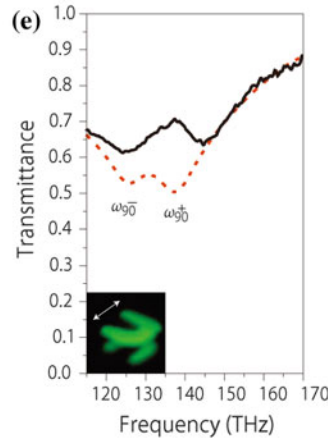
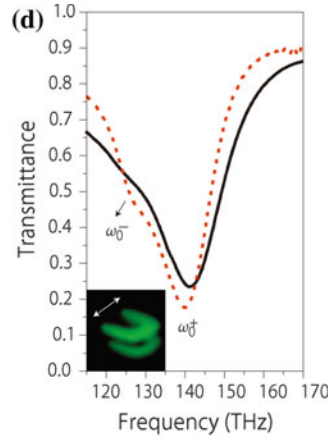
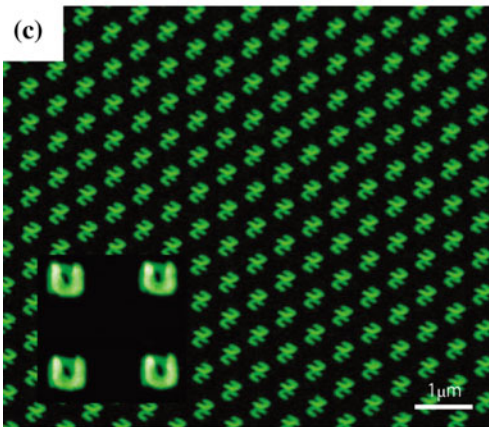
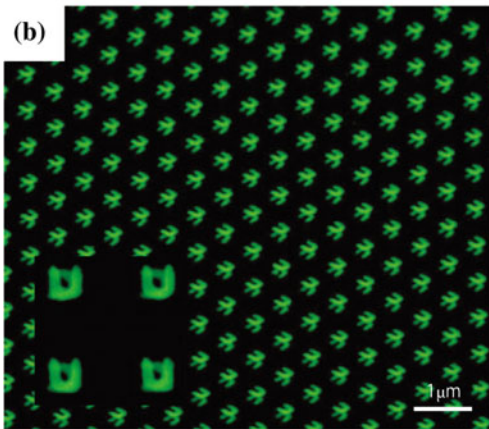
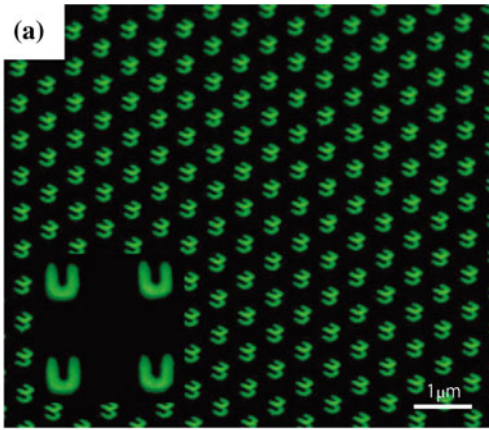


**Fig. 2.7** Scanning electron microscope images of the four-layer SRR structure. **a** Oblique incidence overview and **b** normal view. Inset: magnified view, and **c** enlarged oblique view. Reprinted by permission from Nature Publishing Group: [15], copyright 2008

To realize negative-index metamaterials, Garcia-Meca et al. fabricated a multi-layered fishnet metamaterial by depositing silver and hydrogen silsesquioxane-based resist layers alternatively and then patterned by a focused ion beam milling technique. The result is shown in Fig. 2.12 [21]. In 2008, negative refraction of near-infrared light (1200–1700 nm in wavelength) was experimentally demonstrated by Valentine et al. [22]. Figure 2.13 shows a 21-layer fishnet metamaterial consisting of alternating layers of 30-nm silver and 50-nm magnesium fluoride ( $\text{MgF}_2$ ) patterned by focused ion beam (FIB) milling technique. Additional FIB milling was used by the fishnet metamaterial to form a prism shape. The effective refractive index was experimentally estimated by measuring the absolute angle of refraction. Xu et al. used a multilayer structure of Ag and  $\text{TiO}_2$  to fabricate a negative-index metamaterial in the ultraviolet frequency region and demonstrated flat lens effect as shown in Fig. 2.14 [23]. Zero-index metamaterial in the near-infrared region ( $\lambda = 1.4 \mu\text{m}$ ) was demonstrated using silicon rods separated by a silicon dioxide layer by Moitra et al. in 2013 [24].



◀**Fig. 2.8** Scanning electron microscope images and experimental measurement. **a–c** are oblique views of the **a**  $0^\circ$ , **b**  $90^\circ$ , and **c**  $180^\circ$  twisted gold SRR dimer metamaterials. Insets: normal views. **d–f** are experimental transmittance spectra for the **d**  $0^\circ$ , **e**  $90^\circ$ , and **f**  $180^\circ$  twisted SRR dimer metamaterials. The black and red curves represent the experimental and simulated results, respectively. For the  $90^\circ$  twisted SRR dimer structure, an analyzer is applied behind the sample, which is rotated by  $75^\circ$  with respect to the polarization of the incident light. Reprinted by permission from Nature Publishing Group: [16], copyright 2009

Decker et al. made left-handed and right-handed twisted double-layer cross-structures. Figure 2.15a shows SEM images of the fabricated structures. Experimental results of the polarization dependences on left- and right-handed circularly polarized (LCP and RCP) light are shown in Fig. 2.15b [25].

A flexible 3D negative-index metamaterial fabricated by a nanotransfer printing technique was reported by Chanda et al. Nanotransfer printing technique is a kind of nanoimprinting techniques. The fabrication process is shown in Fig. 2.16a. A multilayer fishnet structure was made on a soft imprinting mold by using EB evaporation, and this multilayer fishnet structure was transferred to the target substrate by contacting the mold against the substrate. They used a polydimethylsiloxane (PDMS) film for the substrate. Using this soft substrate, they demonstrated flexible bulk metamaterials with a negative index of refraction in the near-infrared regime [26].

Chen et al. applied double-exposure EB lithography to fabricate an upright U-shaped 3D metamaterial [27]. A U-shaped upright SRR resonantly interacts with the magnetic component of incident light as shown in Fig. 2.17a. Field enhancement factors were estimated 16 times and 4 times at the center and two prongs of the SRR, respectively. Multilayer photolithography and electroplating techniques were also utilized to fabricate 3D self-standing SRR arrays on a silicon substrate by Fan et al. [28]. While the structure of the fabricated SRR arrays is three-dimensional, it has only one degree of freedom of the magnetic interaction because SRRs are aligned in only one plane. Zhang et al. used the multilayer photolithography and liftoff methods to make a THz metamaterial that consists of 3D unit elements. In 2009, they applied the same technique to fabricate a chiral negative-index metamaterial for 1 THz wave [29]. In 2012, they also applied the same technique to demonstrate chiral switchable metamaterials whose property can be modified by photoexcitation with a femtosecond laser, as shown in Fig. 2.18c [30].

### 2.4.2 Two-Photon Absorption Techniques for Bulk Structures

Photolithography and electron beam lithography have already been widely used as basic technique for fabricating 2D metamaterials, and these techniques are extended to the fabrication of bulk metamaterials by stacking 2D patterns. While these techniques demonstrate good productivity in 2D fabrication, they cannot be applied for the fabrication of 3D structures. Recently, micro-stereolithography [31, 32] and

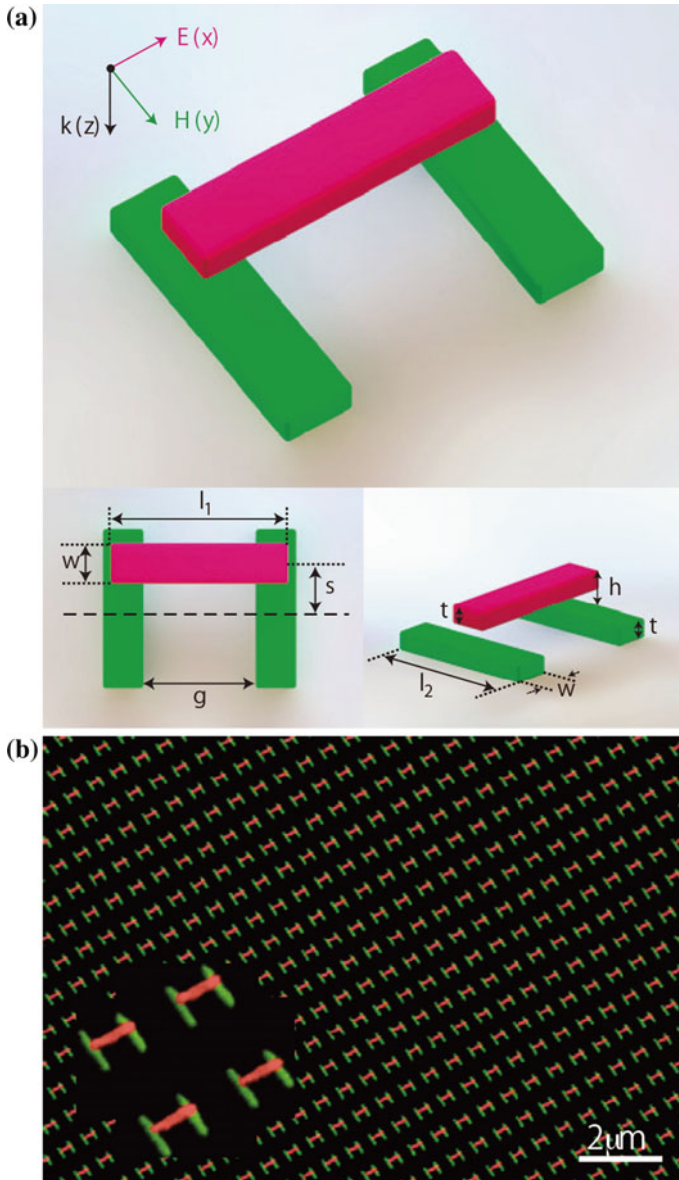


**Fig. 2.9** Structural geometry and scanning electron microscope images. **a** Schematic diagram of the stacked plasmonic EIT structure with definitions of the geometrical parameters:  $l_1 = 355$  nm,  $l_2 = 315$  nm,  $w = 80$  nm,  $g = 220$  nm,  $t = 40$  nm, and  $h = 70$  nm. The periods in both the x- and y-directions are 700 nm. Red color represents the gold bar in the top layer, and green color represents the gold wire pair in the bottom layer. **b** Oblique view of the sample with lateral displacement  $s = 10$  nm. Inset: enlarged view. Reprinted by permission from Nature Publishing Group: [17], copyright 2009



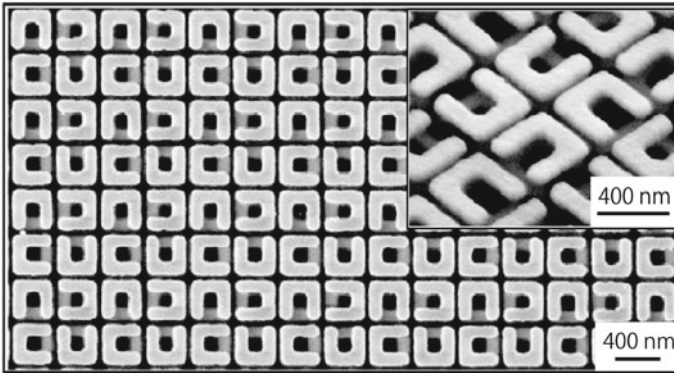


**Fig. 2.10** Electron microscope images of a typical fabricated chiral metamaterial. The normal incidence image illustrates the high alignment accuracy of the two stacked layers. Inset: oblique view onto the sample. Reprinted by permission from [18]. Copyright 2010 by The Optical Society

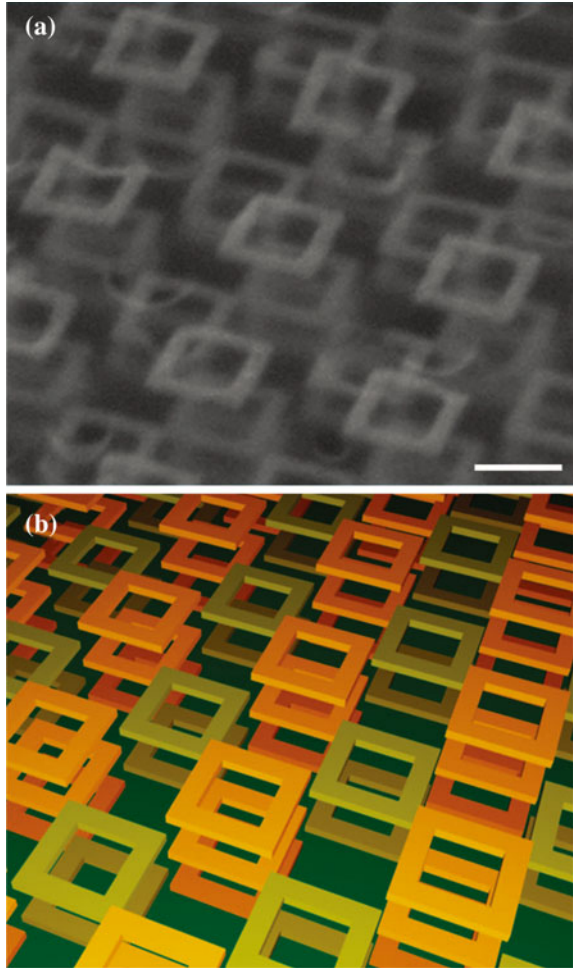
FIB chemical vapor deposition (FIB-CVD) [33] enable us to create 3D structures. However, these techniques are still based on layer-by-layer fabrication and do not inherently have 3D spatial resolution. Therefore, it is still big challenge to make arbitral 3D micro-/nanostructures.

Two-photon absorption (TPA) technique is one of the key technologies to solve the above-mentioned problem. The TPA process was first proposed by Goppert-Mayer in 1931 [34]. Different from the one-photon absorption (OPA), the absorption probability in TPA is proportional to the square of the light intensity, and thus, light absorption is localized only at the focal point of the light. At the same time, successive chemical or physical reactions are confined only in a small volume with three-dimensional spatial resolution. As a result, unlike other fabrication techniques, the TPA process inherently has 3D spatial resolution, with potential applications in fluorescence microscopy [35], optical data storages [36], and lithographic fabrications [37, 38]. In this section, several 3D fabrication techniques for bulk metamaterials based on TPA are reviewed.

#### 2.4.2.1 Two-Photon Fabrication Techniques for 3D Polymer Structures

In 1997, Maruo et al. demonstrated a fabrication technique based on a combination of micro-stereolithography and TPA. This technique offers great potential for the production of 3D polymeric micro-/nanostructures [39]. A near-infrared mode-locked Ti:sapphire laser, whose pulse duration is around 100 fs, is tightly focused on a photopolymerizable resin with a high numerical aperture (NA) objective lens. By scanning the laser beam spot three-dimensionally inside the resin, 3D polymer structures with arbitrary shapes can be fabricated with sub-micrometer spatial resolution. Since the TPA phenomenon occurs only in the region where the photon density is sufficiently high and successive reactions triggered by the light absorption are also

**Fig. 2.11** Three-dimensional chess metamaterial structure. **a** Tilted-view electron microscope image of the 3D structure (ten layers) of stacked broken symmetry nanorings fabricated by stacked electron beam lithography. The structure consists of layers of nanorings separated by an insulator (SU-8). Each layer of nanorings is shifted with respect to the adjacent layer. The dimensions of the rings are: period = 600 nm,  $L = 300$  nm,  $w = 60$  nm,  $t = 30$  nm,  $s = 50$  nm. **b** Sketch of the corresponding metamaterial. Reprinted by permission from Nature Publishing Group: [20], copyright 2012



based on a nonlinear process, the TPA process offers both 3D spatial resolution and the ability to achieve subdiffraction-limit fabrication, as shown in Fig. 2.19 [40].

With such a 3D laser fabrication capability, the so-called direct laser writing (DLW), a wide variety of 3D optical functional devices were made. Photonic crystals, which consist of periodic dielectric structures with dimensions on the wavelength scale, are one of the most important applications for optical communications, but the realization of full 3D photonic bandgap crystals is still a challenge, even when employing cutting-edge semiconductor device fabrication processes [41]. By using DLW, Deubel et al. demonstrated the first fabrication of a large-scale face-centered cubic (fcc) photonic crystal in 2004 [42]. They used a commercially available photoresist, SU-8, in the DLW process and fabricated a complete 3D photonic crystal that exhibits photonic bandgaps at near-infrared wavelengths from 1.3 to 1.7  $\mu\text{m}$ .

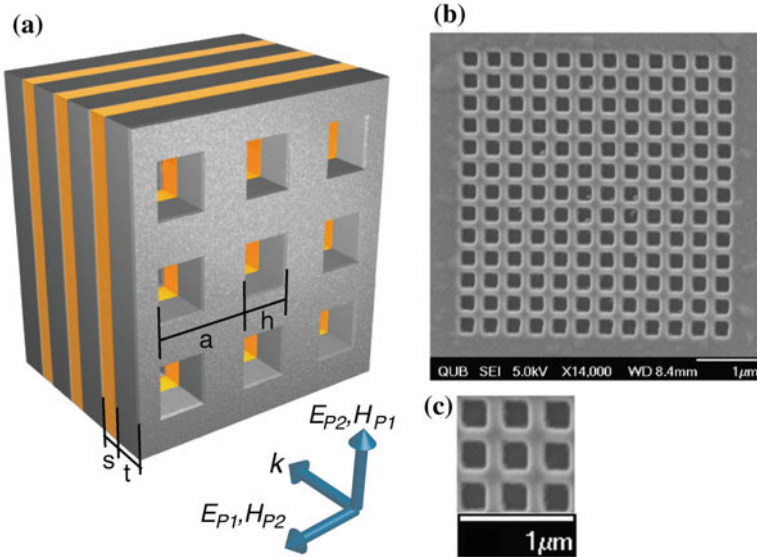


**Fig. 2.12** **a** Schematic of a fishnet metamaterial made up of three unit cells in the propagation direction. The overall number of layers is 7 (4 metal layers and 3 dielectric layers). **b** Top-view SEM image of the fabricated 3-unit cell fishnet structure. **c** Detail of image in (b). Reprinted with permission from [21]. Copyright 2008 by American Physical Society

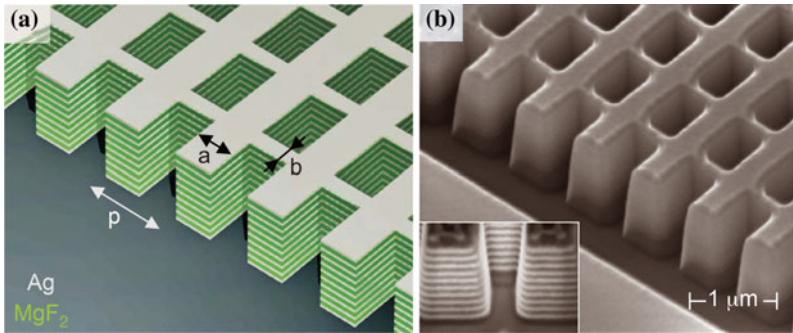
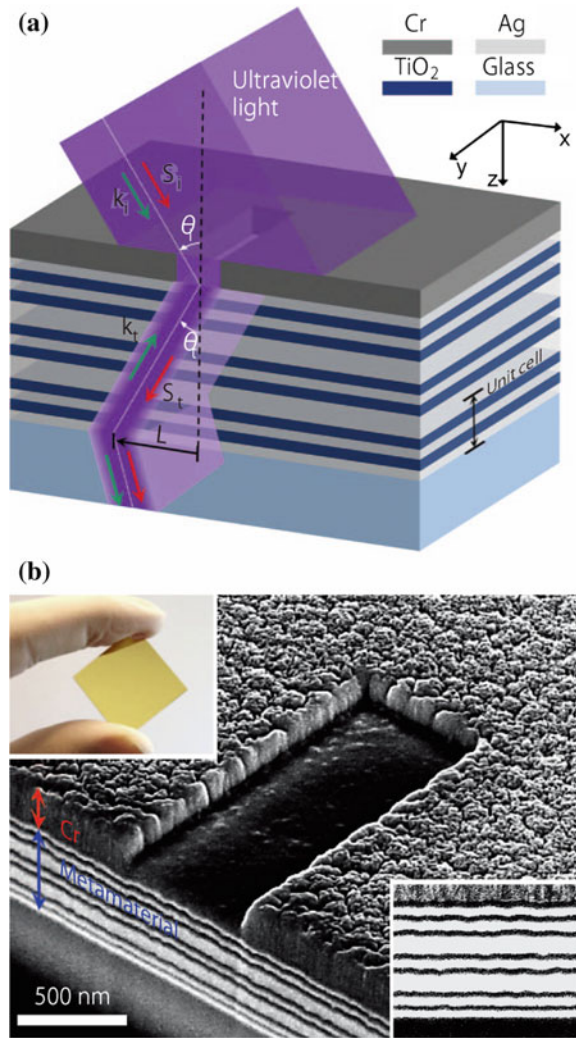


**Fig. 2.13** Diagram and SEM image of fabricated fishnet structure. **a** Diagram of the 21-layer fishnet structure with a unit cell of  $p = 860$  nm,  $a = 565$  nm, and  $b = 265$  nm. **b** SEM image of the 21-layer fishnet structure with the side etched, showing the cross section. The structure consists of alternating layers of 30-nm silver (Ag) and 50-nm magnesium fluoride ( $MgF_2$ ), and the dimensions of the structure correspond to the diagram in (a). The inset shows a cross section of the pattern taken at a  $45^\circ$  angle. The sidewall angle is  $4.3^\circ$  and was found to have a minor effect on the transmittance curve according to simulation. Reprinted by permission from Nature Publishing Group: [22], copyright 2008



**Fig. 2.14** Ultraviolet bulk metamaterial. **a** Schematic of negative refraction of ultraviolet light from air into a coupled plasmonic waveguide metamaterial formed by three vertically stacked MDMDM (M: metal and D: dielectric) unit cells and coated with a beamdefining mask consisting of a rectangular aperture in an opaque Cr film.  $S_i$  and  $S_t$ , incident and transmitted time-averaged Poynting vectors, respectively;  $k_i$  and  $k_t$ , incident and transmitted wavevectors, respectively. **b** Scanning electron microscope image of the fabricated ultraviolet bulk metamaterial, showing the beamdefining aperture, and sectioned by focused ion beam (FIB) milling to reveal the internal metamaterial structure. Left inset: glass slide uniformly coated with 450-nm-thick metamaterial; right inset: magnified cross section of the metamaterial layers. Reprinted by permission from Nature Publishing Group: [23], copyright 2013



The DLW technique allows even complex 3D photonic structures that cannot be fabricated in a layer-by-layer built-up manner. In 2005, Seet et al. demonstrated the fabrication of 3D spiral architecture photonic crystals using SU-8 and observed photonic bandgaps at infrared regime [43]. Based on 3D photonic crystals fabricated by the DLW technique, Ergin et al. recently realized a 3D optical metamaterial that exhibits the so-called invisibility cloaking for unpolarized infrared light [44]. They designed and fabricated a 3D fcc woodpile photonic crystal with a tailored filling fraction on a gold mirror surface and demonstrated carpet cloaking, which is proposed by Li in 2008, at near-infrared wavelengths [45].

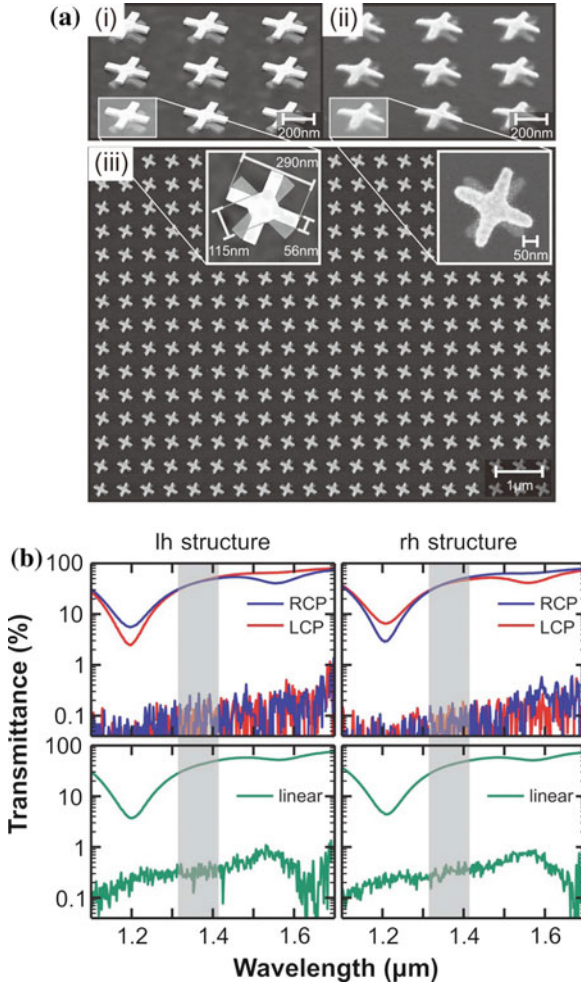


**Fig. 2.15** Left-handed (LH) and right-handed (RH) twisted double-layer cross-structures and their experimental results. **a** Schematic and scanning electron microscope images of chiral metamaterial. (i) Scheme of the chiral metamaterial structure composed of right-handed twisted gold crosses. (ii) Oblique view electron microscope image of a fabricated sample and (iii) normal-view large-area electron microscope image of a right-handed structure. The insets show close-ups. **b** Measured normal incidence transmittance and conversion spectra (logarithmic scale) of the twisted cross-structure. The left column is for an LH structure, and the right column for an RH structure. Transmittance for LCP and RCP is plotted in gray (red online) and black (blue online), respectively. The conversion into the other circular polarization is extremely small and, hence, shown by the same color. In contrast, we find significant conversion of linear polarization (second row) in between the two resonances, where the intensity transmittances for the two incident circular polarizations are closely similar. This regime highlighted in gray delivers pure and large optical activity. Reprinted by permission from [25]. Copyright 2009 by The Optical Society

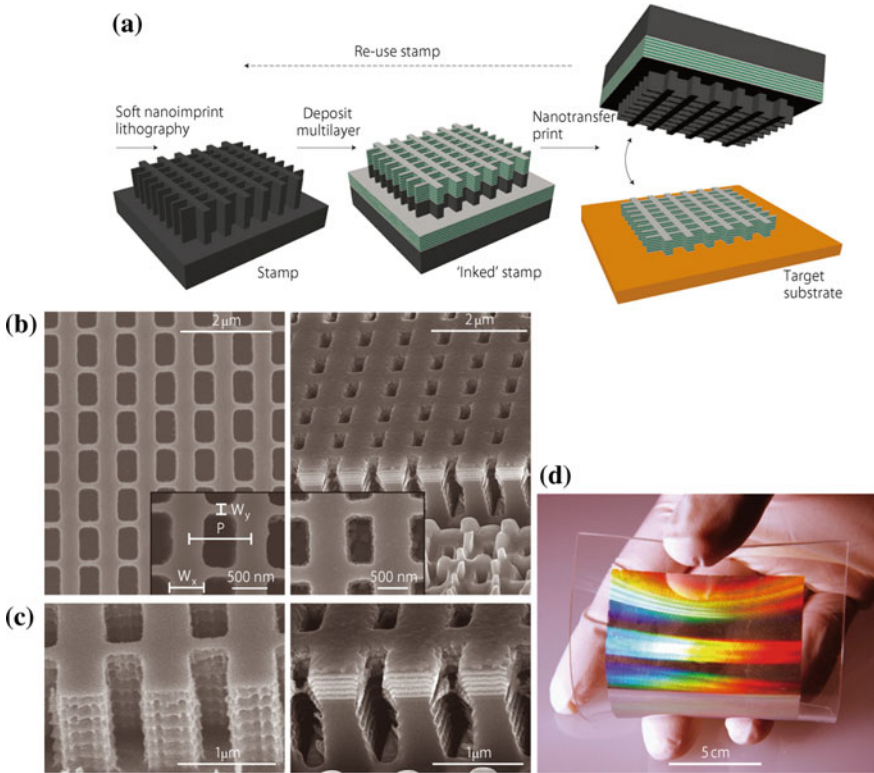


**Fig. 2.16** Fabricating 3D NIMs by transfer printing. **a** Schematic of steps for printing. **b** Top-view SEM image of a silicon stamp (left; inset: magnified view), tilted-view ( $52^\circ$ ) SEM image of a stack of alternating layers of Ag and  $\text{MgF}_2$  on a silicon stamp (middle; inset: magnified top view), cross-sectioned by FIB. **c** Corresponding SEM images of a tilted silicon stamp (left), an eleven-layer Ag/ $\text{MgF}_2$  stack (right). Period  $P$  of the structure is 850 nm, and the depth-averaged widths of the ribs in the fishnet along the  $x$ - and  $y$ -directions are 635 nm ( $W_x$ ) and 225 nm ( $W_y$ ), respectively. The thicknesses of the Ag and  $\text{MgF}_2$  layers are 30 and 50 nm, respectively. **d** Three-dimensional NIM printed with a stamp onto a flexible substrate. Reprinted by permission from Nature Publishing Group: [26], copyright 2011

The spatial resolution of the DLW technique is intrinsically limited by the non-linear characteristics of the TPA process, and it is typically as low as 120 nm for an excitation wavelength of 780 nm [40]. Recently, these limitations were improved by introducing a novel microscopy technique based on stimulated emission depletion (STED) technique [46, 47]. Fischer et al. recently demonstrated STED-DLW by using a specially manufactured photoresist, and its spatial resolution was improved down to 65 nm, while the wavelengths of the excitation and the depletion laser were 810 nm and 532 nm, respectively [48, 49].

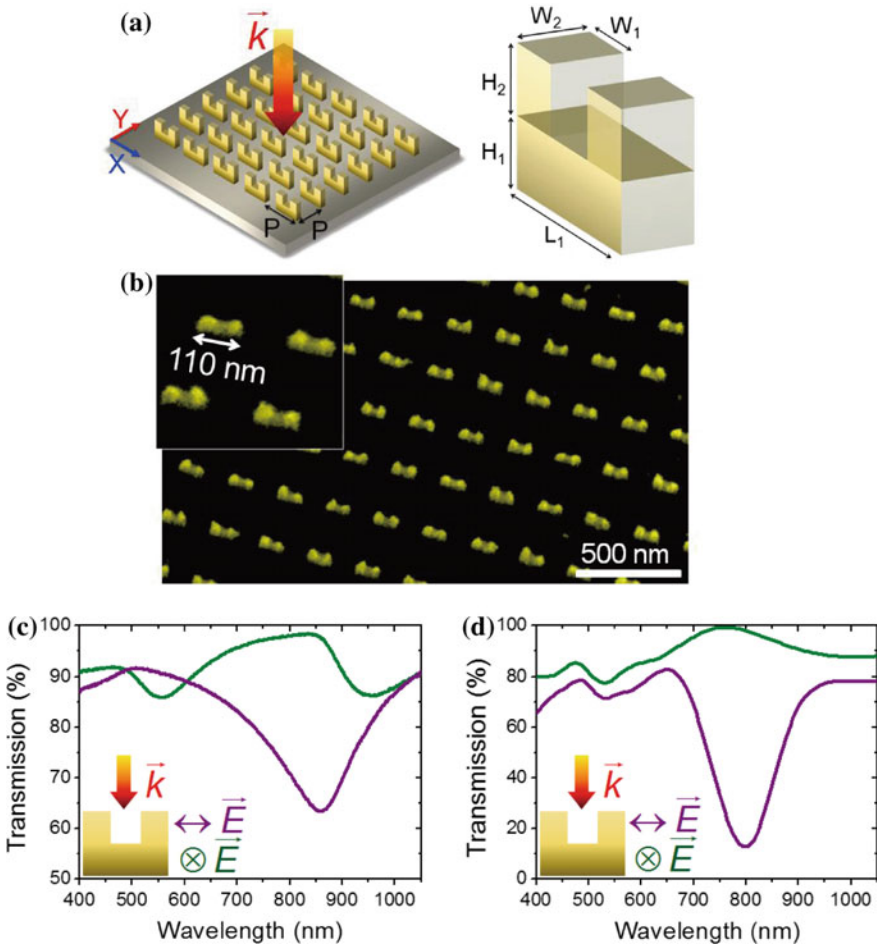
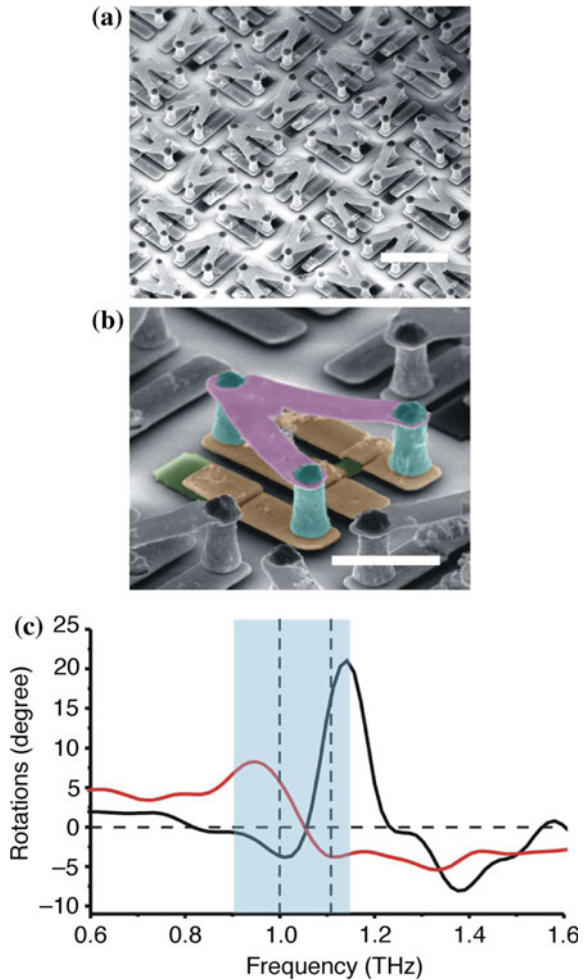


**Fig. 2.17** **a** Schematic diagram showing the feature size of erected U-shaped three-dimensional resonance ring,  $L_1 = 110$  nm,  $H_1 = 30$  nm,  $H_2 = 30$  nm,  $W_2 = 40$  nm,  $W_1 = 40$  nm,  $P = 200$  nm, respectively. The optical properties of the fabricated sample are studied in the case of x-polarized illumination as well as y-polarized illumination. In the case of x-polarized illumination, the electric field of incident light oscillates parallel to the resonant ring. In the case of y-polarized illumination, the electric field of incident light passes through the resonant ring. **b** SEM image of a small region from the fabricated sample. The inset shows a magnified view of four erected U-shaped three-dimensional resonance rings with bottom length  $L_1 = 110$  nm. **c** Experimental transmission spectra for x-polarized illumination (the purple curve) and y-polarized illumination (the green curve). **d** Finite element simulation transmission spectra for x-polarized illumination (the purple curve) and y-polarized illumination (the green curve). The inset in both frames (c) and (d) shows the propagating direction of incident light as well as the polarization direction of incident light related to the resonance ring. Reprinted by permission from [27]. Copyright 2011 by The Optical Society

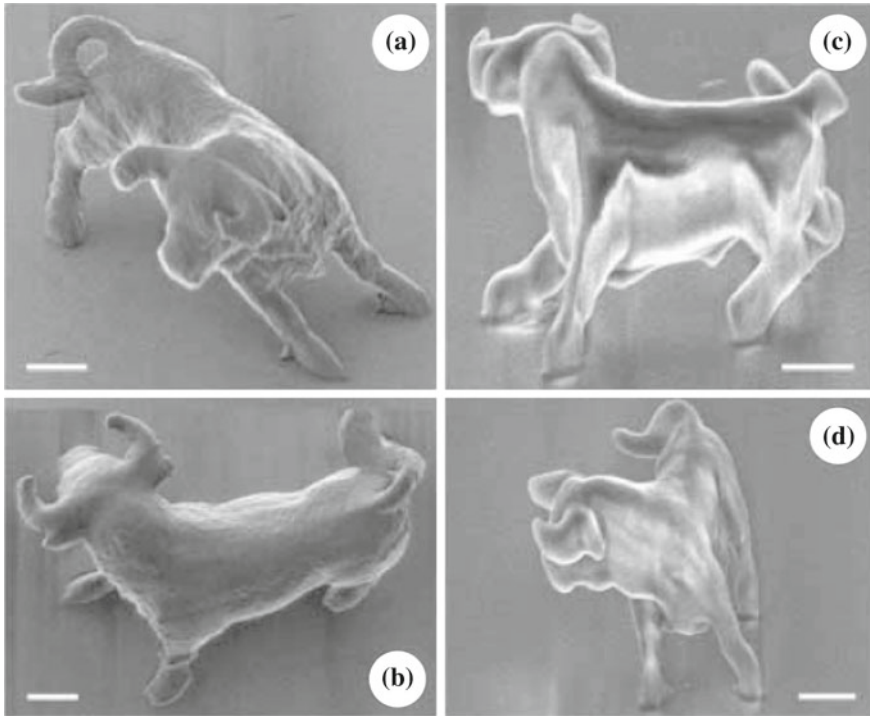
**Fig. 2.18** Experimental demonstration of chiral switching metamaterials. **a** and **b** Scanning electron microscope images of the fabricated metamaterial. The period of the metamaterial is  $50\ \mu\text{m}$ , which is far less than the wavelength of the terahertz waves. Scale bar in **(a)**,  $25\ \mu\text{m}$ . In **b**, the purple, blue, and yellow colors represent the gold structures at different layers and the two silicon pads are shown in green. Scale bar,  $10\ \mu\text{m}$ . **c** The ORD derived from the measured transmission amplitude and phase spectra, without (black) and with (red) photoexcitation. In the shaded area, both the signs of CD and ORD are flipped, indicating the switching of handedness of the metamolecules. Reprinted by permission from Nature Publishing Group: [30], copyright 2012



#### 2.4.2.2 Two-Photon Techniques for 3D Metallic or Metallodielectric Structures

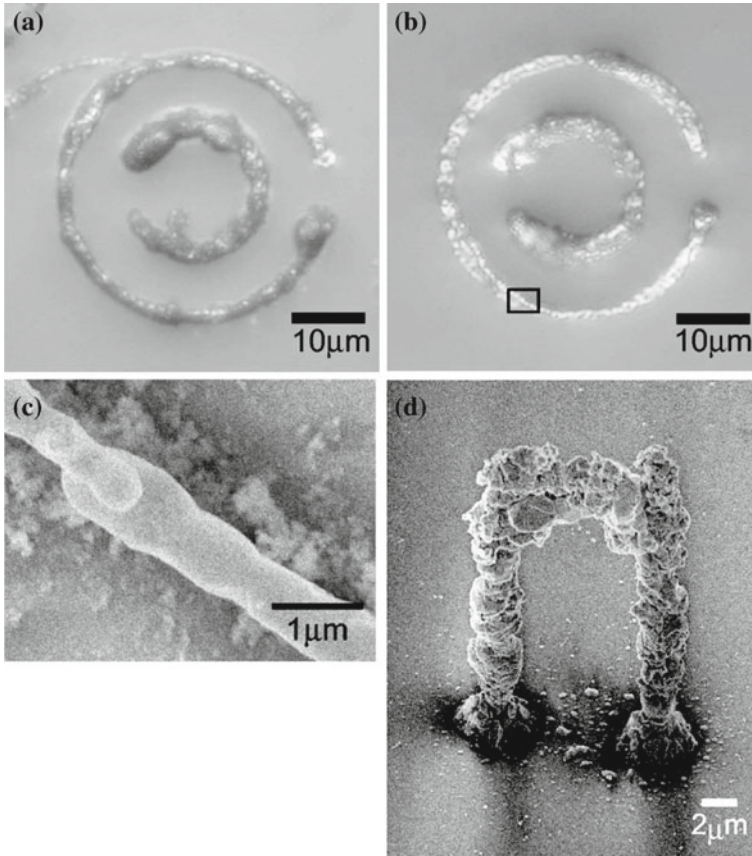
Although two-photon-induced photopolymerization offers wide versatility in the fabrication of 3D complex micro- and nanostructures, only dielectric photonic structures have been developed so far. To gain more functionality in photonic and plasmonic applications, the development of 3D metallic or metallodielectric structures is important and highly demanded. Several reports on the fabrication of 3D metallodielectric structures based on the TPA process have already been published. They can be categorized into two techniques: (i) electroless plating of a polymer template [50] and (ii) photoreduction of metal ions in a polymer matrix/solution [38, 51]. Figure 2.20 shows metal microstructure fabricated by photoreduction of metal ions.





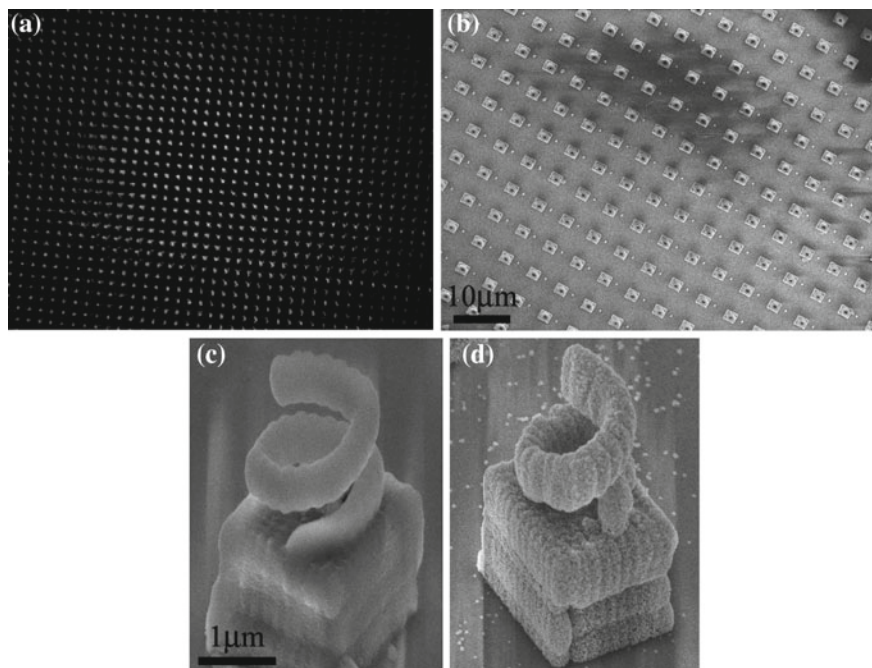
**Fig. 2.19** Microfabrication and nanofabrication at subdiffraction-limit resolution. A titanium–sapphire laser operating in mode-lock at 76 MHz and 780 nm with a 150-fs pulse width was used as an exposure source. The laser was focused by an objective lens of high numerical aperture ( $\sim 1.4$ ). **a** and **b** Bull sculpture produced by raster scanning; the process took 180 min. **c** and **d** The surface of the bull was defined by two-photon absorption (TPA; that is, surface profile scanning) and was then solidified internally by illumination under a mercury lamp, reducing the TPA-scanning time to 13 min. Reprinted by permission from Nature Publishing Group: [40], copyright 2001

Electroless plating on the surface of 3D polymer structures was firstly reported by Farrer et al., and they demonstrated gold/copper coating of selectively functionalized acrylic/methacrylic structures [50]. In 2006, Formanek et al. demonstrated selective silver coating of 3D polymer structures by chemical modification on the polymer surface with stannous chloride ( $\text{SnCl}_2$ ). They also employed a microlens array to realize parallel fabrication and demonstrated mass production of 3D metallodielectric microstructures over a large sample area [52, 53]. Figure 2.21a shows the multiple laser beam spots created by the microlens array, and Fig. 2.21b–d shows the SEM images of the fabricated structures. Takeyasu et al. demonstrated a similar selective coating technique by directly mixing methacrylamide in a resin to selectively activate/deactivate the polymer surface as shown in Fig. 2.22 [54]. Rill et al. fabricated 3D metallodielectric microstructures by combining the DLW process and atomic layer deposition (ALD) as shown in Fig. 2.23. In the process, an SU-8 template of a 3D structure was first coated with  $\text{SiO}_2$  using ALD and then CVD process



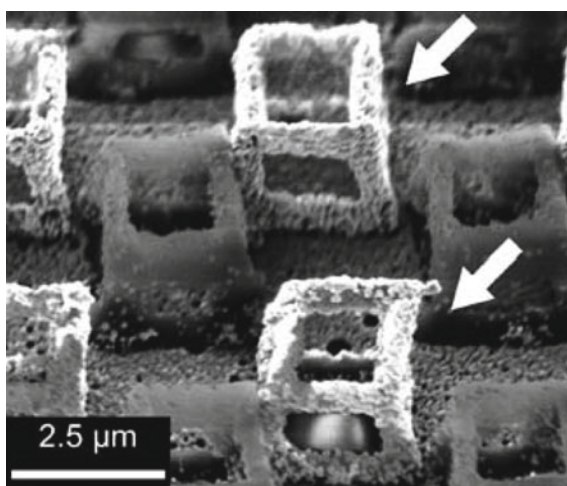
**Fig. 2.20** Micrometal structures fabricated by two-photon-induced metal ion reduction. **a** Optical microscope image of a silver double-ring pattern made by the reduction of an  $\text{AgNO}_3$  aqueous solution. **b** A gold pattern made by reduction of an  $\text{HAuCl}_4$  solution. **c** Scanning electron microscope image of the gold ring. **d** Scanning electron microscope image of micro-sized 3D silver gate structure standing on a glass substrate without any support. The width, height, and linewidth were 12, 16, and 2  $\mu\text{m}$ , respectively. Reprinted with permission from [51]. Copyright 2006 by American Institute of Physics

was applied to realize 3D deposition of silver onto the polymer surface [55]. In contrast to such surface coating techniques, Gansel et al. fabricated 3D metallodielectric microstructures by employing the electrochemical deposition of gold onto an exposed positive-tone photoresist. After removing the polymer template by dry etching, they obtained an array of gold-helix structures. This gold-helix array works as a broadband polarizer for circularly polarized light [56]. These techniques have been extensively improved recently and applied to the development of a wide variety of functional optical/mechanical 3D devices [57–60].



**Fig. 2.21** Two-photon polymerization with microlens array and metal deposition. **a** Intensity profile of the expanded beam measured before the microlens array along the horizontal direction. **b**  $78 \times 58 \mu\text{m}^2$  SEM image of a 3D periodic silver-coated structure fabricated on a hydrophobic-coated glass surface. **c** Tilted magnified view of an individual uncoated polymer structure composed of a cube ( $2 \mu\text{m}$  in size) holding up a spring (height  $2.2 \mu\text{m}$  and inner diameter  $1 \mu\text{m}$ ). **d** SEM image of an individual silver-coated structure after electroless plating. Reprinted by permission from [53]. Copyright 2006 by The Optical Society

**Fig. 2.22** SEM image of silver/polymer 3D microstructures. The size of the structures is  $2 \mu\text{m} \times 2 \mu\text{m} \times 2 \mu\text{m}$ . Reproduced from [54] by permission of Springer, copyright 2008





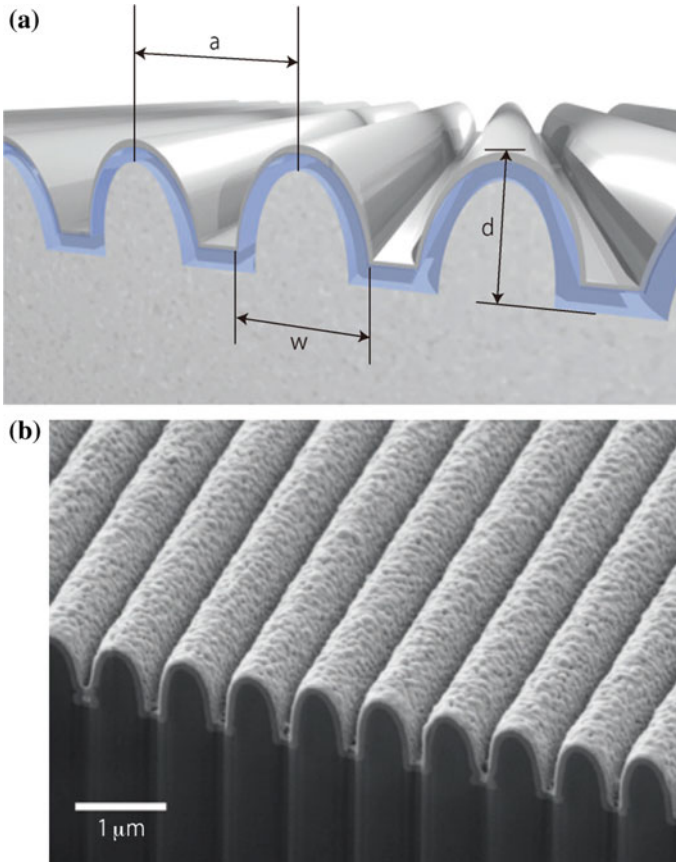


**Fig. 2.23** Metamaterial structure with elongated SRRs. **a** A planar lattice of elongated SRRs. This structure shall serve as a reasonably simple test bed for the novel fabrication approach. Polymer (light gray), silica (blue), and silver (dark gray, reflective). **b** Electron microscope images of fabricated structure. The oblique views show structures that have been cut by a focused ion beam after fabrication to reveal the interior. Reprinted by permission from Nature Publishing Group: [55], copyright 2008

In 2000, Wu et al. reported the photoreduction of metal ions in polymer matrix. They demonstrated the fabrication of silver microstructures inside a  $\text{SiO}_2$  solgel matrix using image formation and developing processes [38]. Similar method was also reported by Duan et al. using titanium ions for the fabrication of functional composite materials [61, 62]. In 2002, Stellacci et al. improved the reduction properties of organic-solvent-soluble silver salt ( $\text{AgBF}_4$ ) in a polymer matrix with ligand-coated silver nanoparticles [63]. They realized electrically conductive silver and gold 3D structures in a polymer matrix, but the resistivity of the metal structures is still low compared with that of bulk metal, implying that the fabricated structures were not fully connected. To make fully connected and electrically conductive 3D metal-

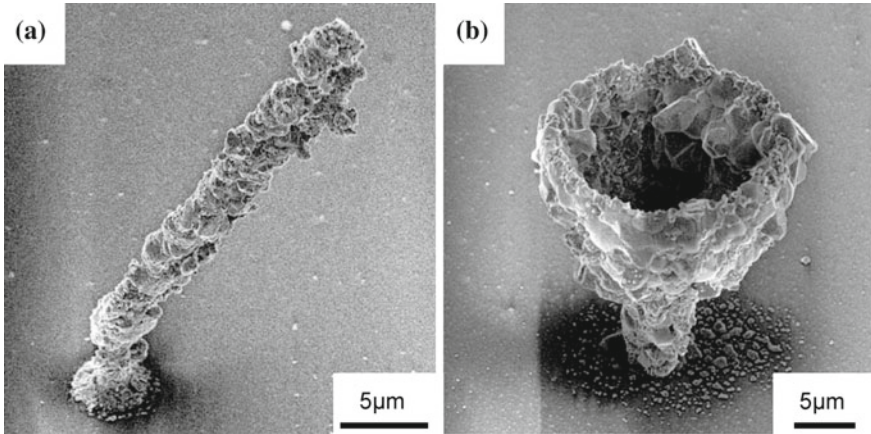


**Fig. 2.24** SEM images of a freestanding **a** silver-tilted rod and **b** silver cup on a substrate. The length of the rod and the angle relative to the substrate were  $34.64\ \mu\text{m}$  and  $60^\circ$ , respectively. The height and the top and bottom diameters of the cup were 26, 20, and  $5\ \mu\text{m}$ , respectively. Reprinted with permission from [64]. Copyright 2006 by American Institute of Physics

lic structures, Tanaka et al. proposed the two-photon-induced reduction of metal complex ions in aqueous solution and demonstrated 3D metallic structures made of silver or gold with superior electrical conductivity [51]. The reduction property and spatial resolution were improved further by introducing a two-photon sensitive dye (coumarin 440) for high-efficiency photoreduction as shown in Fig. 2.24 [64] and surfactant molecules to avoid unwanted crystal growth as shown in Fig. 2.25 [65]. These photoreduction techniques have recently been applied to the fabrication of magnetic metamaterials at infrared frequencies [66].

#### 2.4.2.3 Other Fabrication Techniques for 3D Metallodielectric Structures

Grayscale photolithography method has been widely applied to fabricate 3D polymer structures, and the recent development of digital light processing devices (spatial light modulator) has enhanced its capability for even complex 3D fabrication [67, 68]. However, the fabricated structures are still limited only to surface profiles on photoresist. To extend the 2D capability of conventional photolithography to three dimensions, Burckel et al. developed membrane projection lithography as shown in Figs. 2.26 and 2.27 [69, 70]. Although this technique is based on the conventional lithography process, we can create out-of-plane metallic structures, enabling the fabrication of bulk metamaterials.

A 2D metamaterial has been proposed as a simple yet powerful concept to mold the flow of light in a desired manner [71, 72]. This is termed “metasurface.” Although most of the metasurfaces demonstrated so far are based on 2D planar structures,

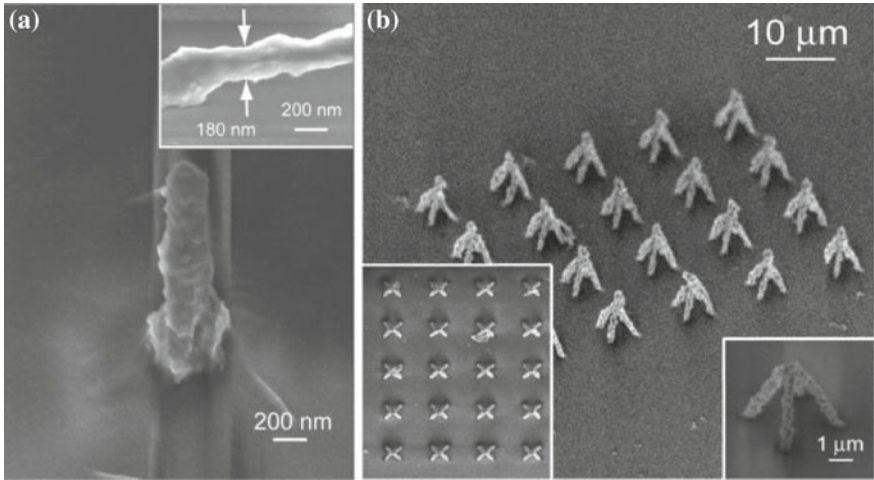


**Fig. 2.25** Three-dimensional silver structures fabricated by surfactant-assisted multiphoton photoreduction. **a** SEM image of the freestanding silver pillar on the coverslip, made by using a laser power of 1.14 mW and a linear scanning speed of 3 mm/s, taken at an observation angle of 45°. The inset is a close-up view of the silver pillar parallel to the substrate, which demonstrates the linewidth of the smallest portion of the silver pillar as 180 nm. **b** SEM image of silver pyramids, fabricated with a laser power of 1.3 mW and scanning speed of 2.5 mm/s, taken at an observation angle of 45°. The inset on the left is a top view of the silver pyramid array. The inset on the right is a close-up view of the silver pyramid. Reproduced from [65] by permission of John Wiley & Sons Ltd.

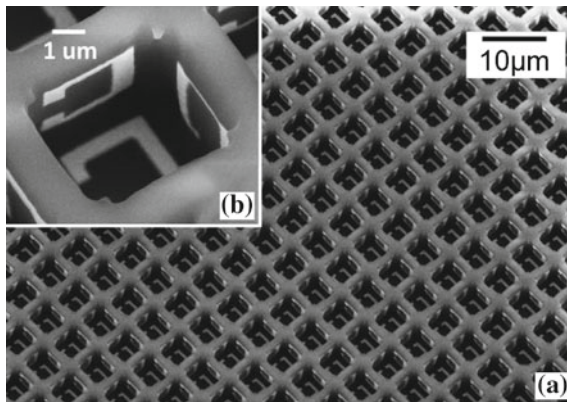
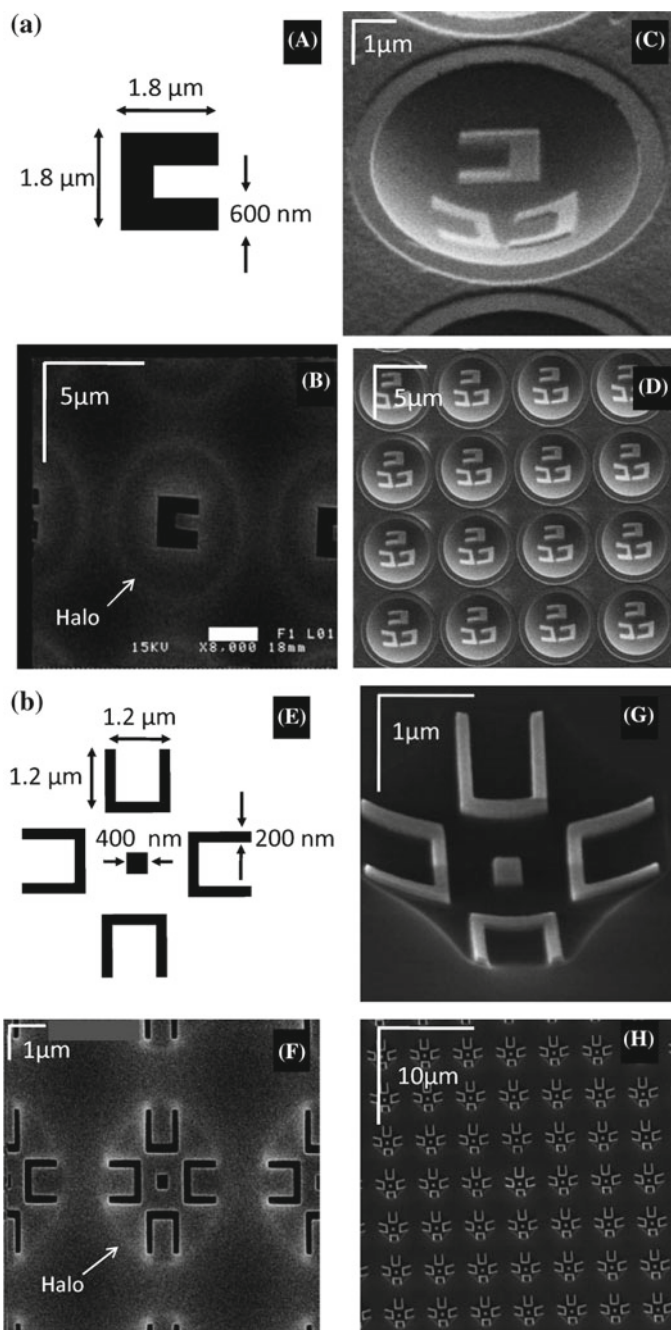


**Fig. 2.26** SEM images of an array of fully 3D metamaterial elements consisting of SRRs on each side of an open cubic cavity arranged in a rectangular lattice. There are five SRRs per unit cell, with dimensions and composition identical to the preceding designs. **a** Low-resolution SEM image. **b** The high magnification inset SEM image shows 3 of the 5 unit cell SRRs. Reproduced from [69] by permission of John Wiley & Sons Ltd.



◀**Fig. 2.27** Three-dimensional metamaterials fabricated by self-aligned membrane projection lithography method. **a** (A) As-drawn pattern. (B) SEM image of membrane suspended over cavity. The halo shows the extent of the cavity. (C) High-resolution SEM image of spheroidal cavity decorated with three instances of the resonator pattern. (D) Lower-resolution SEM image demonstrating uniformity. Samples were uniform to this extent over the entire  $5\text{ mm} \times 5\text{ mm}$  area. **b** (E) Pattern specifications. (F) SEM image of patterned membrane suspended over the cavity. Halo indicates the extent of the cavity. (G) Angled SEM image demonstrating the curved cavity with obviously out-of-plane resonators. (H) Low-resolution SEM image indicating degree of sample uniformity. Reproduced from [70] by permission of John Wiley & Sons Ltd.

extending the technique into the third dimension is the next step to gain more functionality for versatile optical/photonic applications [73–75]. Recently, Ni et al. demonstrated a metasurface on a 3D arbitrarily shaped object to realize carpet cloaking at visible wavelengths [76]. The height profile of the 3D object was firstly obtained by the use of an atomic force microscope (AFM), and then metasurfaces were patterned at each local position by using a standard EB lithography technique with precise focus alignment.

### 2.4.3 *Self-organization and Templating Techniques for Large-Area Metamaterials*

The fabrication technologies that are referred to as top-down techniques, such as photolithography, EB lithography, DLW, and so on, have the strong advantage that they can fabricate diverse patterns with precise controllability of the pattern alignment. However, these techniques are intrinsically time- and energy-consuming, and it is still challenging to fabricate a large amount of micro- and nanostructures because of the low throughput. On the other hand, bottom-up approaches based on self-organized or self-assembling fine structures of metamaterial templates are effectual tools for the mass production of metamaterials.

Yao et al. used a nanoporous alumina that is produced by electrochemical anodization to make a silver nanowire array [77]. Silver nanowire arrays of 60 nm in diameter, 110 nm center-to-center distance, and 4.5  $\mu\text{m}$  or 11  $\mu\text{m}$  in length were fabricated by electrochemical deposition of silver into the pores. Negative refraction was experimentally demonstrated at wavelengths of both 660 nm and 780 nm.

According to theoretical investigations of optical metamaterial structures, metal ring structures with gaps of several nanometers work as the resonant unit of metamaterials (meta-atoms/metamolecules) [78]. To form such structures, a DNA-templating method was proposed by Watanabe et al. [79, 80]. A chemically synthesized gold nanoparticle was bound to an artificially designed and synthesized single strand of DNA with thiol moiety. When three DNA strands with Au nanoparticles are hybridized with each other, a triangular DNA template structure is automatically formed, then three DNA templates are assembled into a trimer ring structure, and



Au nanoparticles formed triangle structure with nanometer-scale gaps. The fabrication process, scanning transmission electron microscope (STEM) images, and AFM images of gold trimer ring structures are shown in Fig. 2.28.

Self-organization of colloidal particles on a substrate can be used for nanofabrication templates. Fredriksson et al. used the hole-mask colloidal lithography technique to make large-scale 2D arrays of nanosized structures [81]. In the first step, randomly dispersed particles are used as a mask for metal deposition to make a metal hole-mask pattern. Using the metal hole-mask and plasma etching, a polymethyl methacrylate (PMMA) sacrificial film was patterned; then, materials were evaporated on the surface of the substrate through the PMMA pattern, and various patterns such as nanodisks, oriented elliptical nanostructures, nanocone arrays, nanodisk pairs, and so on were obtained. Lodewijks et al. also used self-assembled nanospheres as a mask to make large-area double fishnet metamaterial structures [82]. A schematic and SEM images of the fabricated hexagonal double fishnet structures are shown in Fig. 2.29.

Aoki et al. demonstrated a magnetic self-assembly technique to form resonant unit cells of metamaterials [83]. Randomly dispersed gold core-shell microparticles dispersed in water are attracted to the equator plane of the center polystyrene bead and automatically formed a necklace shape structure only applying an external static magnetic field. Figure 2.30 shows optical microscope images of Au microparticle necklace structures assembled by the developed technique.

In 2005, Nastaushev et al. proposed the self-organized formation of micro- and nanotubes from strained metal bifilms [84]. The schematic diagram of the proposed process and the experimental results are shown in Fig. 2.31. They examined the combination of materials and found that the Au/Ti bifilm has the best properties for the tube formation. This structure works as a so-called Swiss roll resonant unit. Mei et al. used the same technique to form an integrated microtube array, and they examined the photoluminescence spectrum of SiO/SiO<sub>2</sub> microtubes [85].

Chen et al. have developed a metal stress-driven self-folding method for self-standing three-dimensional split-ring resonators using residual stress in thin metal films [86]. They demonstrated a 3D SRR array made of Al as shown in Fig. 2.32. In 2015, they applied the technique to fabricate three-dimensional isotropic metamaterials [87]. The fabrication process of the metal stress-driven self-folding method is shown in Fig. 2.33a. The materials for SRR were changed from Al to Au/Ni bifilms. The fabrication process and a scanning electron microscope image of the 3D SRR array are shown in Fig. 2.33b. By using the fabricated bulk metamaterials, they demonstrated isotropic optical responses at the 30 THz, and an extremely low refractive index of 0.35, which is lower than that of vacuum, was demonstrated.

## 2.5 Conclusion and Outlook

The study of metamaterials began in the last decade in the microwave regime and has now been extended to the visible or UV light region. Together with theoretical inves-

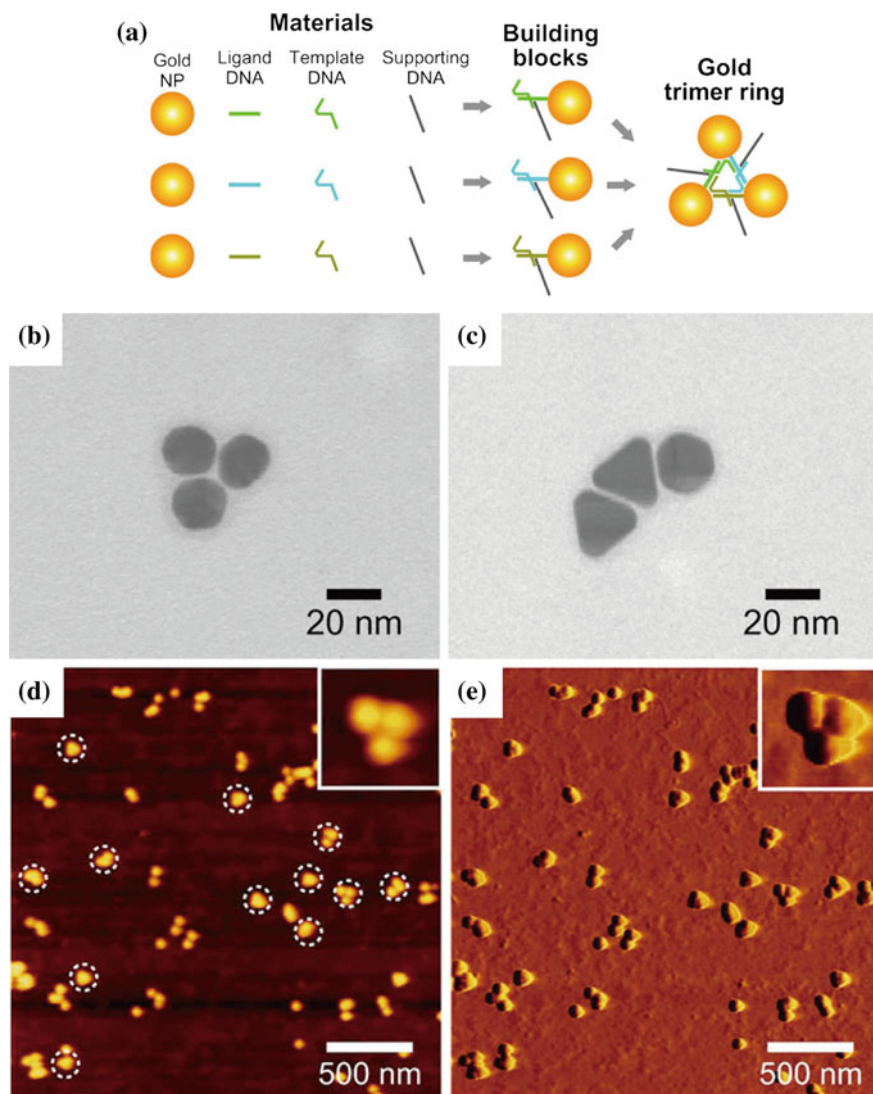


**Fig. 2.28** DNA-templating process for gold trimer rings. **a** Schematic outline of the DNA-templating process for mass production of gold trimer ring. Ligand DNA covalently binds with gold NP and then hybridizes with template DNA and supporting DNA to form building blocks. They finally assemble into a trimer ring structure through hybridization. STEM images of **b** gold ring and **c** linear trimer obtained after AEG separation. AFM **d** height and **e** phase images of gold trimers on quartz substrates. The insets are the enlarged images. The trimers are indicated by the dashed white circles in **(d)**. The height range is 25 nm. Reprinted with the permission from [80]. Copyright 2012 American Chemical Society

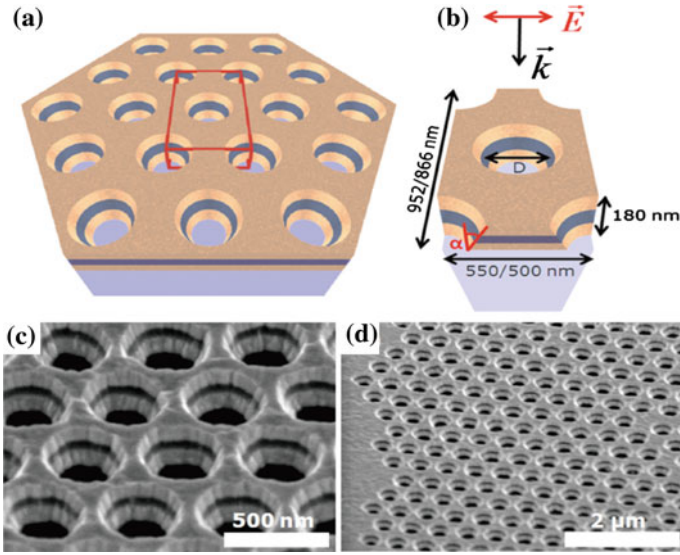


**Fig. 2.29** Self-assembled hexagonal double fishnet structures. **a** Schematic sample structure. **b** Unit cell for simulation dimensions;  $D$  is the diameter, and  $\alpha$  is the  $20^\circ$  sidewall angle of the holes. **c** Detailed scanning electron microscope picture of the nanosphere lithography (NSL) sample and **d** a perfectly ordered domain with some defects. Reprinted with permission from [82]. Copyright 2011 by American Institute of Physics

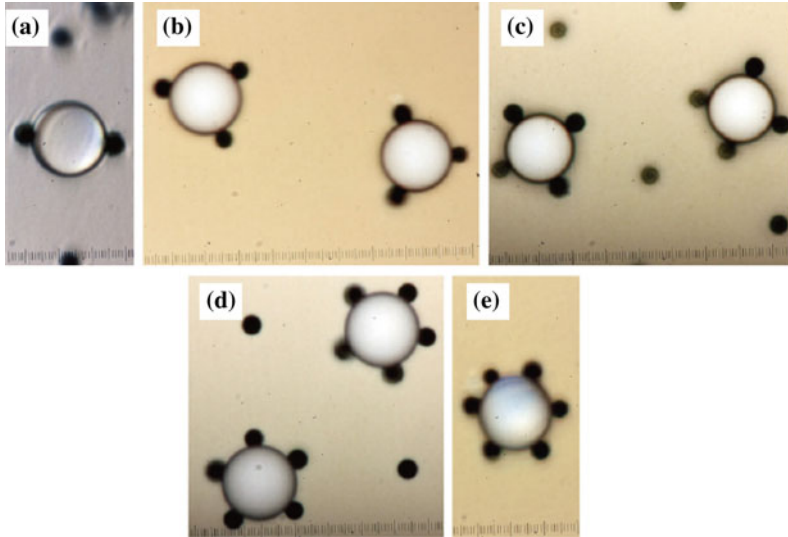


**Fig. 2.30** Magnetic field-induced assembly of necklace structures: **a–e** Necklace structures composed of  $\phi = 2.5 \mu\text{m}$  gold core–shell paramagnetic spheres around  $\phi = 10 \mu\text{m}$  polystyrene center spheres. Ferrofluid concentrations were increased gradually from **(a)** to **(e)**. Reprinted with permission from [83]. Copyright 2012 by American Institute of Physics



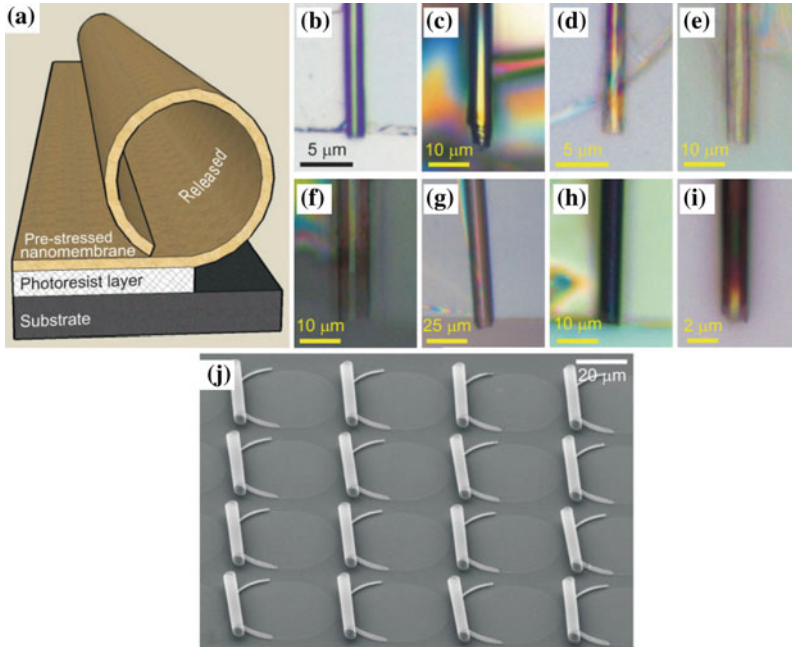


**Fig. 2.31** Roll-up process of a nanomembrane into a tube on photoresist. **a** Schematic diagram illustration. **b–i** Optical images of rolled-up nanomembranes made out of **b** Pt, **c** Pd/Fe/Pd, **d** TiO<sub>2</sub>, **e** ZnO, **f** Al<sub>2</sub>O<sub>3</sub>, **g** Si<sub>3</sub>N<sub>4</sub>, **h** Si<sub>3</sub>N<sub>4</sub>/Ag, and **i** DLC; **j** SEM image of an array of rolled-up SiO/SiO<sub>2</sub> nanomembranes. Reproduced from [85] by permission of John Wiley & Sons Ltd.

tigations, the most important progress that has supported the development of optical metamaterials is the rapid advancement of micro- and nanofabrication technologies. As a result, optical metamaterials are no longer mere conceptual ideas but have already become a practical reality with unexampled and fascinating optical phenomena and applications, such as perfect lenses, optical cloaking, perfect absorbers, and so on. These application ideas are really fascinating, and they stimulate our scientific interests and motivate us to develop new technologies. However, as practical applications, it is worth remembering that a discussion of “killer applications” will be important for demonstrating the real intrinsic potential of metamaterials.

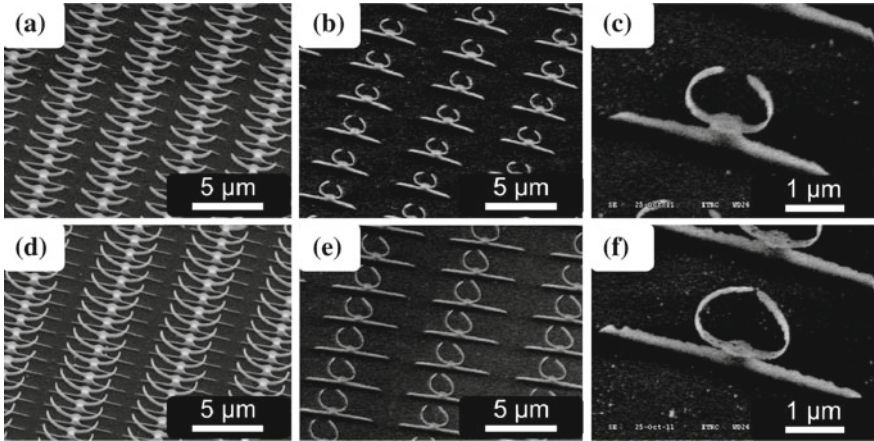


**Fig. 2.32** Oblique view of SEM images with tilting angle of  $40^\circ$  for the three-dimensional split-ring resonators. **a–c** show SRRs with the same arm length of  $2\ \mu\text{m}$  but with different Al film thickness, respectively. The metal thickness (a) = (d) =  $8\ \text{nm}$ , (b) = (e) =  $5\ \text{nm}$ , and (c) = (f) =  $4\ \text{nm}$ , respectively. Figures **d–f** are the SRRs with arm length of  $3\ \mu\text{m}$ . Notice that the bar shapes on the substrate represent the residual fused silica material underneath the metal film, resulting from the shadow effect of etching process. Reprinted by permission from [86]. Copyright 2012 by The Optical Society

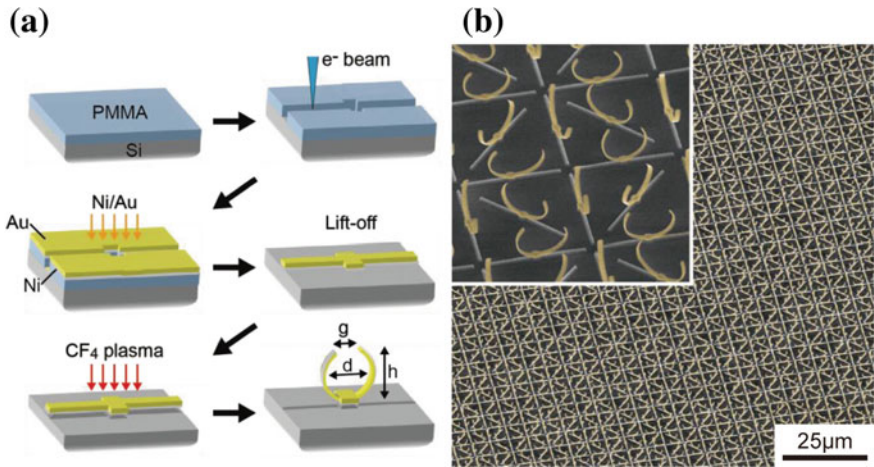


**Fig. 2.33** Three-dimensional split-ring resonators fabricated by metal stress-driven self-folding method. **a** The fabrication process of a 3D SRR; spin-coating resist, electron beam lithography, Ni/Au ( $10/60\ \text{nm}$ ) deposition, liftoff,  $\text{CF}_4$  plasma dry etching, and self-folding (in sequence). The SRR diameter,  $d$ , height,  $h$ , and gap size,  $g$ , were  $2.2\ \mu\text{m}$ ,  $1.8\ \mu\text{m}$ , and  $1.5\ \mu\text{m}$ , respectively. Note that a shadow effect of the arms in the dry etching process produces protruding Si portions under the arms in the last two steps. **b** SEM image of the fabricated isotropic metamaterial consisting of fourfold symmetric 3D SRRs. The inset shows a magnified image, and the total sample area was  $4 \times 4\ \text{mm}^2$ . Reproduced from [87] by permission of John Wiley & Sons Ltd.

## References

1. D.R. Smith, J.B. Pendry, M.C.K. Wiltshire, *Science* **305**, 788 (2004)
2. J.B. Pendry, *Phys. Rev. Lett.* **85**, 3966 (2000)
3. V.M. Shalaev, *Nat. Photon.* **1**, 41 (2007)
4. N.I. Zheludev, *Science* **328**, 582 (2010)
5. C.M. Soukoulis, S. Linden, M. Wegener, *Science* **315**, 47 (2007)
6. A. Ishikawa, T. Tanaka, S. Kawata, *Phys. Rev. Lett.* **95**, 237401 (2005)
7. A. Ishikawa, T. Tanaka, *Opt. Commun.* **258**, 300–305 (2006)
8. A. Ishikawa, T. Tanaka, S. Kawata, *J. Opt. Soc. Am. B* **24**, 510–515 (2007)
9. C.M. Soukoulis, M. Wegener, *Nat. Photon.* **5**, 523 (2011)
10. T. Tanaka, A. Ishikawa, *Nano Converg.* **4**, 34 (2017)
11. A. Ishikawa, T. Tanaka, I.E.E.E.J. Select. Topics. *Quantum Electron.* **19**, 4700110 (2013)
12. J.B. Pendry, A.J. Holden, D.J. Robbins, W.J. Stewart, I.E.E.E. *Trans. Microwave Theory Tech.* **47**, 2075–2084 (1999)
13. K.C. Gupta, R. Garg, I. Bahl, P. Bhartia, *Microstrip Lines and Slotlines*, 2nd edn. (Artech House, 1996), pp. 375–456
14. P.B. Johnson, R.W. Christy, *Phys. Rev. B* **6**, 4370–4379 (1972)
15. N. Liu, H. Guo, L. Fu, S. Kaiser, H. Schweizer, H. Giessen, *Nat. Mater.* **7**, 31 (2008)
16. N. Liu, H. Liu, S. Zhu, H. Giessen, *Nat. Photon.* **3**, 157 (2009)
17. N. Liu, L. Langguth, T. Weiss, J. Kästel, M. Fleischhauer, T. Pfau, H. Giessen, *Nat. Mater.* **8**, 758 (2009)
18. M. Decker, R. Zhao, C.M. Soukoulis, S. Linden, M. Wegener, *Opt. Lett.* **35**, 1593 (2010)
19. N. Liu, M. Hentschel, T. Weiss, A.P. Alivisatos, H. Giessen, *Science* **332**, 1407 (2011)
20. B. Kante, Y.-S. Park, K. O'Brien, D. Shuldman, N.D. Lanzillotti-Kimura, Z.J. Wong, X. Yin, X. Zhang, *Nat. Commun.* **3**, 1180 (2012)
21. C. García-Meca, J. Hurtado, J. Martí, A. Martínez, *Phys. Rev. Lett.* **106**, 067402 (2011)
22. J. Valentine, S. Zhang, T. Zentgraf, E. Ulin-Avila, D.A. Genov, G. Bartal, X. Zhang, *Nature* **455**, 376 (2008)
23. T. Xu, A. Agrawal, M. Abashin, K.J. Chau, H.J. Lezec, *Nature* **497**, 470 (2013)
24. P. Moitra, Y. Yang, Z. Anderson, I.I. Kravchenko, D.P. Briggs, J. Valentine, *Nat. Photon.* **7**, 791 (2013)
25. M. Decker, M. Ruther, C.E. Krieglger, J. Zhou, C.M. Soukoulis, S. Linden, M. Wegener, *Opt. Lett.* **34**, 2501 (2009)
26. D. Chanda, K. Shigeta, S. Gupta, T. Cain, A. Carlson, A. Mihi, A.J. Baca, G.R. Bogart, P. Braun, J.A. Rogers, *Nat. Nanotech.* **6**, 402 (2011)
27. W.T. Chen, C.J. Chen, P.C. Wu, S. Sun, L. Zhou, G.-Y. Guo, C.T. Hsiao, K.-Y. Yang, N.I. Zheludev, D.P. Tsai, *Opt. Express* **19**, 12837 (2011)
28. K. Fan, A.C. Strikwerda, H. Tao, X. Zhang, R.D. Averitt, *Opt. Express* **19**, 12619 (2011)
29. S. Zhang, Y.-S. Park, J. Li, X. Lu, W. Zhang, X. Zhang, *Phys. Rev. Lett.* **102**, 023901 (2009)
30. S. Zhang, J. Zhou, Y.-S. Park, J. Rho, R. Singh, S. Nam, A.K. Azad, H.-T. Chen, X. Yin, A.J. Taylor, X. Zhang, *Nat. Commun.* **3**, 942 (2012)
31. X. Zhang, X.N. Jiang, C. Sun, *Sens. Actuators* **77**, 149 (1999)
32. F. Zhou, Y. Bao, W. Cao, C.T. Stuart, J. Gu, W. Zhang, C. Sun, *Sci. Rep.* **1**, 78 (2011)
33. S. Matsui, T. Kaito, J. Fujita, M. Komuro, K. Kanda, Y. Haruyama, *J. Vac. Sci. Technol. B* **18**, 3181 (2000)
34. M. Goppert-Mayer, *Ann. Phys.* **9**, 273 (1931)
35. W. Denk, J.H. Strickler, W.W. Webb, *Science* **248**, 73 (1990)
36. D.A. Parthenopoulos, P.M. Rentzepis, *Science* **245**, 843 (1989)
37. W. Zhou, S.M. Kuebler, K.L. Braun, T. Yu, J.K. Cammack, C.K. Ober, J.W. Perry, S.R. Marder, *Science* **296**, 1106 (2002)
38. P.-W. Wu, W. Cheng, I.B. Martini, B. Dunn, B.J. Schwartz, E. Yablonovitch, *Adv. Mater.* **12**, 1438 (2000)

39. S. Maruo, O. Nakamura, S. Kawata, *Opt. Lett.* **22**, 132 (1997)
40. S. Kawata, H.-B. Sun, T. Tanaka, K. Takada, *Nature* **412**, 697 (2001)
41. S. Noda, K. Tomoda, N. Yamamoto, A. Chutinan, *Science* **289**, 604 (2000)
42. M. Deubel, G.V. Freymann, M. Wegener, S. Pereira, K. Busch, C.M. Soukoulis, *Nat. Mater.* **3**, 444 (2004)
43. K.K. Seet, V. Mizeikis, S. Matsuo, S. Juodkazis, H. Misawa, *Adv. Mater.* **17**, 541 (2005)
44. T. Ergin, N. Stenger, P. Brenner, J.B. Pendry, M. Wegener, *Science* **328**, 337 (2010)
45. J. Li, J.B. Pendry, *Phys. Rev. Lett.* **101**, 203901 (2008)
46. S.W. Hell, J. Wichmann, *Opt. Lett.* **19**, 780 (1994)
47. S.W. Hell, *Science* **316**, 1153 (2007)
48. J. Fischer, G. von Freymann, M. Wegener, *Adv. Mater.* **22**, 3578 (2010)
49. J. Fischer, M. Wegener, *Adv. Opt. Express* **1**, 614 (2011)
50. R.A. Farrer, C.N. LaFratta, L. Li, J. Praino, M.J. Naughton, B.E.A. Saleh, M.C. Teich, J.T. Fourkas, *J. Am. Chem. Soc.* **128**, 1796 (2006)
51. T. Tanaka, A. Ishikawa, S. Kawata, *Appl. Phys. Lett.* **88**, 081107 (2006)
52. F. Formanek, N. Takeyasu, T. Tanaka, K. Chiyoda, A. Ishikawa, S. Kawata, *Appl. Phys. Lett.* **88**, 083110 (2006)
53. F. Formanek, N. Takeyasu, T. Tanaka, K. Chiyoda, A. Ishikawa, S. Kawata, *Opt. Express* **14**, 800 (2006)
54. N. Takeyasu, T. Tanaka, S. Kawata, *Appl. Phys. A* **90**, 205 (2008)
55. M.S. Rill, C. Plet, M. Thiel, I. Staude, G. von Freymann, S. Linden, M. Wegener, *Nat. Mater.* **7**, 543 (2008)
56. J.K. Gansel, M. Thiel, M.S. Rill, M. Decker, K. Bade, V. Saile, G. von Freymann, S. Linden, M. Wegener, *Science* **325**, 1513 (2009)
57. A. Radke, T. Gissibl, T. Klotzbücher, P.V. Braun, H. Giessen, *Adv. Mater.* **23**, 3018 (2011)
58. T.A. Schaedler, A.J. Jacobsen, A. Torrents, A.E. Sorensen, J. Lian, J.R. Greer, L. Valdevit, W.B. Carter, *Science* **334**, 962 (2011)
59. X. Zheng, H. Lee, T.H. Weisgraber, M. Shusteff, J. DeOtte, E.B. Duoss, J.D. Kuntz, M.M. Biener, Q. Ge, J.A. Jackson, S.O. Kucheyev, N.X. Fang, C.M. Spadaccini, *Science* **344**, 1373 (2014)
60. L.R. Meza, S. Das, J.R. Greer, *Science* **345**, 1322 (2014)
61. X.-M. Duan, H.-B. Sun, K. Kaneko, S. Kawata, *Thin Solid Films* **453–454**, 518 (2004)
62. M. Fukushima, H. Yanagi, S. Hayashi, H.-B. Sun, S. Kawata, *Phys. E* **21**, 456 (2004)
63. F. Stellacci, C.A. Bauer, T. Mayer-Friedrichsen, W. Wenseleers, V. Alain, S.M. Kuebler, S.J.K. Pond, Y. Zhang, S.R. Marder, J.W. Perry, *Adv. Mater.* **14**, 194 (2002)
64. A. Ishikawa, T. Tanaka, S. Kawata, *Appl. Phys. Lett.* **89**, 113102 (2006)
65. Y.-Y. Cao, N. Takeyasu, T. Tanaka, X.-M. Duan, S. Kawata, *Small* **5**, 1144 (2009)
66. A. Ishikawa, T. Tanaka, S. Kawata, *Appl. Phys. Lett.* **91**, 113118 (2007)
67. K. Totsu, M. Esashi, *J. Vac. Sci. Technol. B* **23**, 1487 (2005)
68. A. Rammohan, P.K. Dwivedi, R. Martinez-Duarte, H. Katepalli, M.J. Madou, A. Sharma, *Sens. Actuators B Chem.* **153**, 125 (2011)
69. D.B. Burckel, J.R. Wendt, G.A.T. Eyck, J.C. Ginn, A.R. Ellis, I. Brener, M.B. Sinclair, *Adv. Mater.* **22**, 5053 (2010)
70. D.B. Burckel, J.R. Wendt, G.A.T. Eyck, A.R. Ellis, I. Brener, M.B. Sinclair, *Adv. Mater.* **22**, 3171 (2010)
71. N. Yu, P. Genevet, M.A. Kats, F. Aieta, J.-P. Tetienne, F. Capasso, Z. Gaburro, *Science* **334**, 333 (2011)
72. N. Yu, F. Capasso, *Nat. Mater.* **13**, 139 (2014)
73. X. Ni, A.V. Kildishev, V.M. Shalaev, *Nat. Commun.* **4**, 2807 (2013)
74. L. Huang, X. Chen, H. Mühlenbernd, H. Zhang, S. Chen, B. Bai, Q. Tan, G. Jin, K.-W. Cheah, C.-W. Qiu, J. Li, T. Zentgraf, S. Zhang, *Nat. Commun.* **4**, 2808 (2013)
75. X. Yin, Z. Ye, J. Rho, Y. Wang, X. Zhang, *Science* **339**, 1405 (2013)
76. X. Ni, Z.J. Wong, M. Mrejen, Y. Wang, X. Zhang, *Science* **349**, 1310 (2015)

77. J. Yao, Z. Liu, Y. Liu, Y. Wang, C. Sun, G. Bartal, A.M. Stacy, X. Zhang, *Science* **321**, 930 (2008)
78. A. Ishikawa, T. Tanaka, S. Kawata, *J. Opt. Soc. B* **24**, 510 (2007)
79. T. Ohshiro, T. Zako, R. Watanabe-Tamaki, T. Tanaka, M. Maeda, *Chem. Commun.* **46**, 6132 (2010)
80. R. Watanabe-Tamaki, A. Ishikawa, T. Tanaka, T. Zako, M. Maeda, *J. Phys. Chem. C* **116**, 15028 (2012)
81. H. Fredriksson, Y. Alaverdyan, A. Dmitriev, C. Langhammer, D.S. Sutherland, M. Zach, B. Kasemo, *Adv. Mater.* **19**, 4297 (2007)
82. K. Lodewijks, N. Verellen, W.V. Roy, V. Moshchalkov, G. Borghs, P.V. Dorpe, *Appl. Phys. Lett.* **98**, 091101 (2011)
83. K. Aoki, K. Furusawa, T. Tanaka, *Appl. Phys. Lett.* **100**, 181106 (2012)
84. Y.V. Nastaushev, V.Y. Prinz, S.N. Svitashva, *Nanotechnology* **16**, 908 (2005)
85. Y. Mei, G. Huang, A.A. Solovev, E.B. Urena, I. Monch, F. Ding, T. Reindl, R.K.Y. Fu, P.K. Chu, O.G. Schmidt, *Adv. Mater.* **20**, 4085 (2008)
86. C.C. Chen, C.T. Hsiao, S. Sun, K.-Y. Yang, P.C. Wu, W.T. Chen, Y.H. Tang, Y.-F. Chau, E. Plum, G.-Y. Guo, N.I. Zheludev, D.P. Tsai, *Opt. Express* **20**, 9415 (2012)
87. C.C. Chen, A. Ishikawa, Y.-H. Tang, M.-H. Shiao, D.P. Tsai, T. Tanaka, *Adv. Opt. Mater.* **3**, 44 (2015)

# Chapter 3

## Blackbody Metamaterial Composite Film of Nanoparticle and Polymer



Kotaro Kajikawa and Hisashi Karube

**Abstract** Blackbody metamaterial composite films of nanoparticles and polymer are presented both theoretically and experimentally. Reflectance, transmittance and absorption of the film are calculated on the basis of the Mie theory and Clausius–Mossotti relation, which is equivalent to the Maxwell Garnett theory, at various conditions. We also fabricated the composite metamaterials in which gold nanospherical particles are dispersed in a polyvinylpyrrolidone film. Although the experimental results are in agreement with the calculated spectra in the composite of binary gold nanoparticles with different sizes, the results are somewhat deviated from the calculated spectra of the composite of single-element gold nanoparticles. This may be due to aggregation of the gold nanoparticles at high volume fraction.

### 3.1 Introduction

Light absorbers are important media that can be applied to light-harvesting technology and light emitters. Since metamaterials allow us to form very thin light absorbers, many studies have been carried out [1–4]. This is because we can design the metamaterials to optimize the optical properties, as required. Here, we describe our studies on blackbody metamaterial composite films of nanoparticles and polymer. The broadband absorption stems from the interaction between the nanoparticles, whereas isolated nanoparticles have rather narrow absorption bands at peak wavelengths. The composite film is formed by a simple fabrication procedure and has a high absorption over the visible wavelengths.

---

K. Kajikawa (✉) · H. Karube  
Interdisciplinary Graduate School of Science and Engineering,  
Tokyo Institute of Technology, Nagatsuta, Yokohama 226-8502, Japan  
e-mail: [kajikawa@ep.titech.ac.jp](mailto:kajikawa@ep.titech.ac.jp)

© Springer Nature Singapore Pte Ltd. 2019  
K. Sakoda (ed.), *Electromagnetic Metamaterials*, Springer Series  
in Materials Science 287, [https://doi.org/10.1007/978-981-13-8649-7\\_3](https://doi.org/10.1007/978-981-13-8649-7_3)

## 3.2 Theory

### 3.2.1 Optical Absorption

When light is incident to a layered structure such as a film, as shown in Fig. 3.1a, reflectance, transmittance, scattering and reflection occur. Transmittance  $T$ , reflectance  $R$ , scattering efficiency  $S$  and absorption efficiency  $A$  are in the following relation.

$$R + T + A + S = 1 \quad (3.1)$$

If three parameters  $T$ ,  $R$  and  $S$  are known, absorption efficiency  $A$  is evaluated. When the layered structure is flat,  $S = 0$ , resulting in the relation

$$A = 1 - R - T. \quad (3.2)$$

The transfer matrix method can be used to obtain  $R$  and  $T$ .

### 3.2.2 Layered Structure

The layered structure for the blackbody considered in this study is depicted in Fig. 3.1a. Light is incident from the medium 1 whose refractive index is  $n_1$ . The layer structure is composed of medium 2 with a refractive index  $n_2$  and thickness  $d_2$ . The light is transmitted to medium 3 with a refractive index  $n_3$ . To obtain the condition that the layer is good light absorber, we calculated the absorption  $A$ , as a function of  $n_{Re}$  and  $n_{Im}$ , where  $n_{Re}$  and  $n_{Im}$  are the real and imaginary parts of  $n_2$  [2]. The thicknesses  $d_2 = 50, 100, 150, 200, 300$  and  $500$  nm were examined. The results at a wavelength of  $400$  nm are shown in Fig. 3.2, in which the absorption  $A$  is

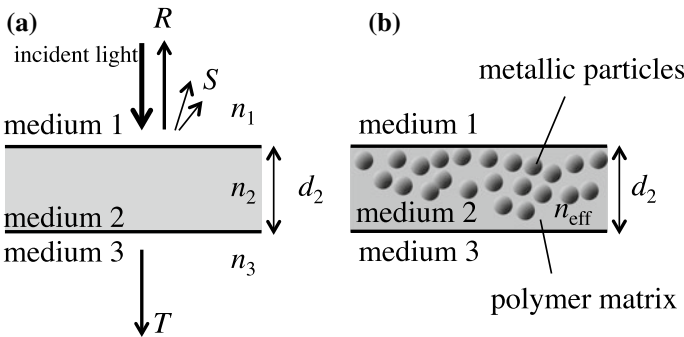


**Fig. 3.1** **a** Three-layer structure considered. **b** The blackbody metamaterial composite film

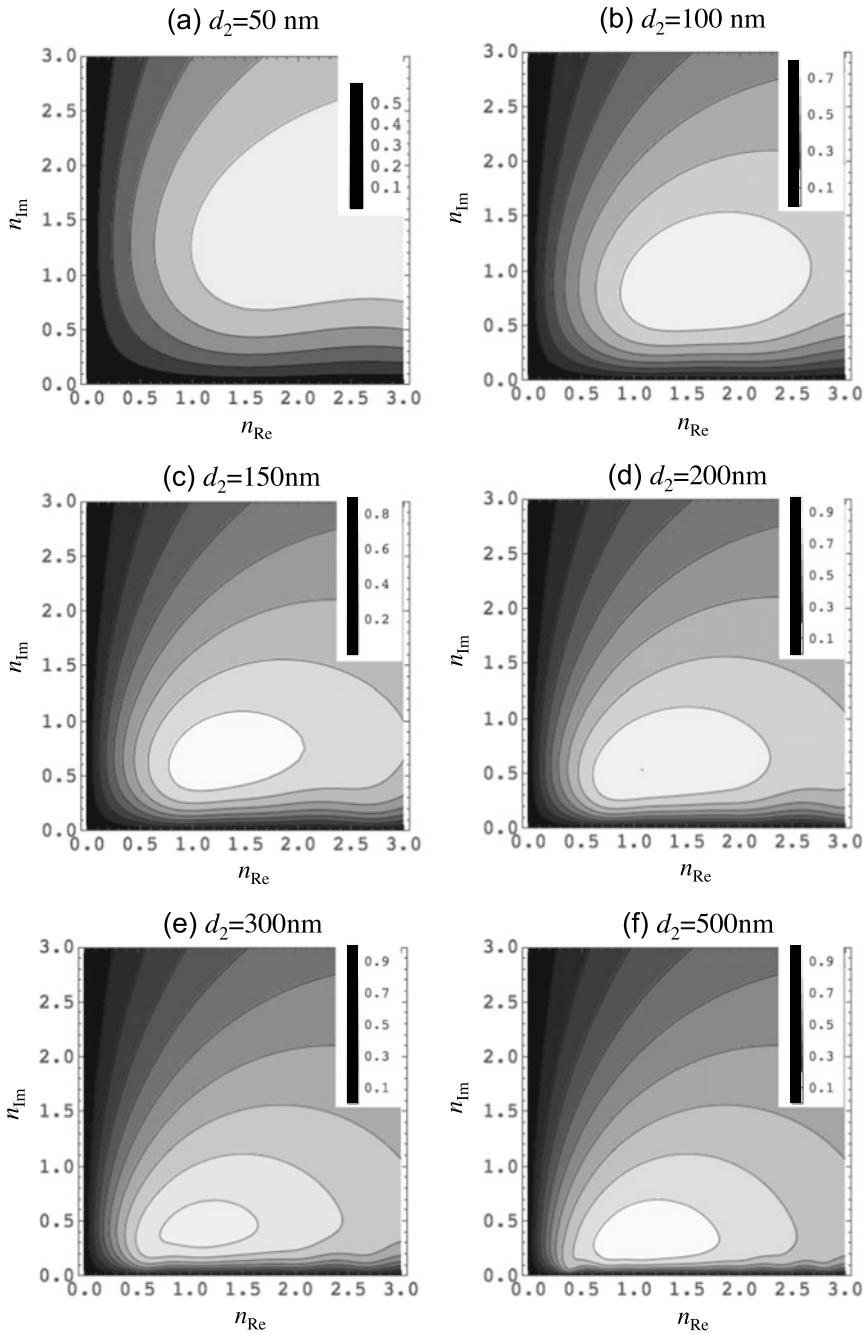
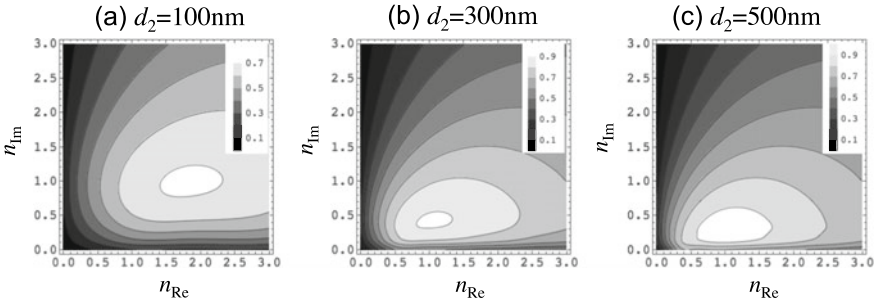


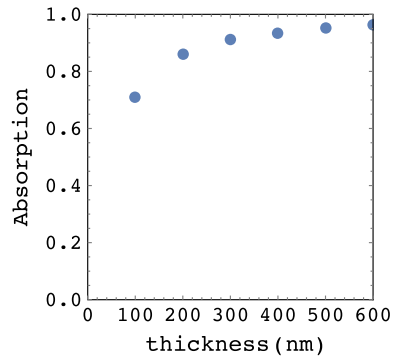
Fig. 3.2 Calculated absorption  $A$  at 400 nm for different  $d_2$





**Fig. 3.3** Calculated mean absorption  $\bar{A}$  over the visible spectral range (400–800 nm) at different  $d_2$

**Fig. 3.4** Calculated maximum mean absorption  $\bar{A}_{\max}$  as a function of  $d_2$



represented in gray scale. When  $d_2 \leq 100$  nm, the absorption is much less than unity whereas there is condition that gives  $A \sim 1$  at  $d \geq 150$  nm. When  $d_2$  is larger, the  $n_{\text{Re}}$  approaches to 1, while it is around 1.5 at  $d_2 = 200$  nm. It is difficult to match the refractive index to be unity because the refractive index of polymers is usually  $\sim 1.5$ .

Figure 3.3 shows mean absorption  $\bar{A}$  over the visible spectral range (400–800 nm). The  $\bar{A} \sim 0.8$  at  $d_2 = 100$  nm, and it is nearly 0.9 at  $d_2 \geq 300$  nm. At these conditions, however, the real part of the refractive index  $n_{\text{Re}}$  should be close to unity for low reflectivity. Figure 3.4 plots the maximum mean absorption  $\bar{A}$  as a function of  $d_2$ . With increasing  $d_2$ ,  $\bar{A}$  increases to unity. When  $d_2 \geq 300$  nm,  $\bar{A} > 0.9$  with the appropriate  $n_2$ . According to these calculations, the conditions for the thin-film blackbody are as  $n_{\text{Re}} = 1 - 1.5$  and  $n_{\text{Im}} \sim 0.3$ , at the thickness of 200–300 nm.

### 3.2.3 Effective Refractive Index

To satisfy the condition for the thin-film blackbody, we consider a composite film of metallic nanoparticles and polymer, as shown in Fig. 3.1b. The effective refractive index  $n_{\text{eff}}$  of the composite is given by the Clausius–Mossotti relation, which is

equivalent to the Maxwell Garnett theory. Suppose that the composite is composed of  $N$  different particle elements with different radii  $r_j$  and a refractive index  $n_j$ . The squared effective refractive index  $n_{\text{eff}}^2$  is written as [1, 5]

$$n_{\text{eff}}^2 = \frac{2 \sum_i^N \frac{f_j}{r_j^3} \alpha_j + 1}{1 - \sum_j^N \frac{f_j}{r_j^3} \alpha_j} n_{\text{mat}}^2. \quad (3.3)$$

Here,  $r_j$  and  $f_j$  are the radius and the volume fraction of the element  $j$ , respectively, and  $n_{\text{mat}}$  is the refractive index of the polymer matrix. The dipole polarizability  $\alpha_j$  of the element  $j$  is

$$\alpha_j = \frac{3r_j^3}{2x_j^3} a_1^j i. \quad (3.4)$$

$x_j$  is the size parameter of the element  $j$ , which is given by

$$x_j = \frac{2\pi}{\lambda_0} r_j n_{\text{mat}}, \quad (3.5)$$

where  $\lambda_0$  is the vacuum wavelength of light. The Mie coefficient  $a_n^j$  of  $n$ th order of the element  $j$  is written as

$$a_n^j = \frac{m_j \psi_n(m_j x_j) \psi_n'(x_j) - \psi_n(x_j) \psi_n'(m_j x_j)}{m_j \psi_n(m_j x_j) \xi_n'(x_j) - \xi_n(x_j) \psi_n'(m_j x_j)}. \quad (3.6)$$

Here, Riccati–Bessel functions  $\psi_n(\rho) = \rho j_n(\rho)$  and  $\xi_n(\rho) = \rho h_n^{(1)}(\rho)$  are used, in which  $j_n(\rho)$  and  $h_n^{(1)}(\rho)$  are the spherical Bessel functions of the first order and the third order, respectively. The prime indicates differentiation with respect to the argument in parentheses.  $m_i$  is the relative refractive index with respect to the refractive index of the polymer matrix:  $m_j = n_j/n_{\text{mat}}$ .

Figure 3.5 shows the real and imaginary parts of the effective refractive index of the composite of gold nanoparticles and polymer, at different particle fractions  $f$  and radii of the particles  $r$ . The refractive index of the polymer is set to be 1.5. When the size of the gold particles is small ( $r = 50$  nm), an absorption band is observed, indicating that the wavelength dispersion is significant. When  $r = 100$  nm, the absorption disappears and gradual increase in the refractive index is observed with the longer wavelength region. When  $r = 200$  nm, the effect of the particle to the optical response is almost absent.

Figure 3.6 shows the real and imaginary parts of the effective refractive index of the composite of gold nanoparticles and polymer, at different  $f$  and  $r$ . The composite of small silver particles shows an absorption band blue-shifted from that from the

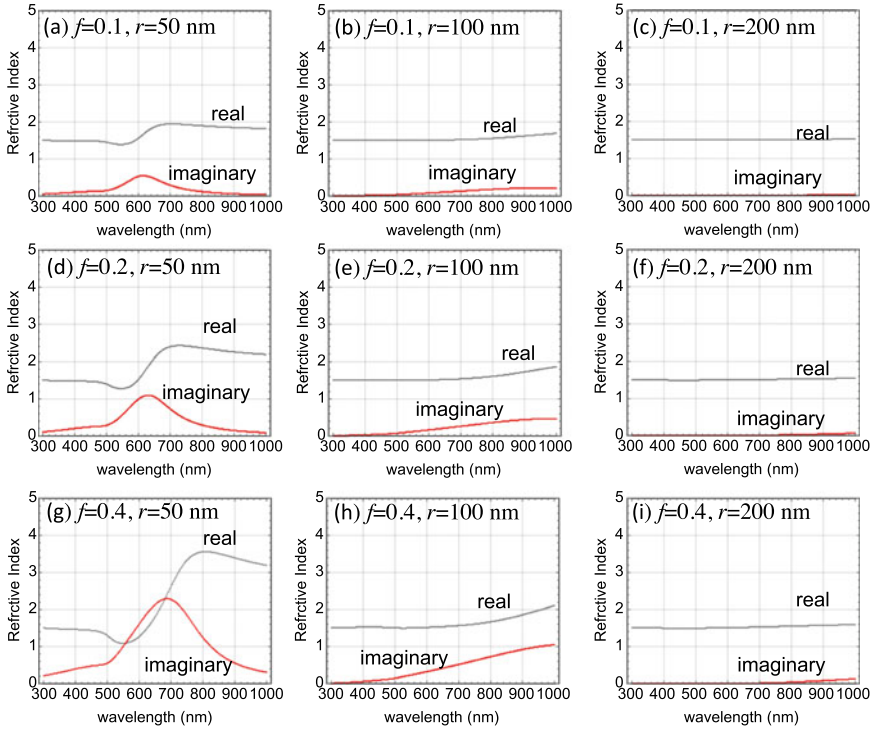


**Fig. 3.5** Calculated real and imaginary parts of the effective refractive index of the composite medium of gold nanoparticles in a polymer thin-film matrix, at a different particle fraction  $f$  and the radius of the particles  $r$

gold composite at  $r = 50$  nm. The composite of larger particles ( $r = 100$  or  $200$  nm) has a refractive index similar to the composite of gold.

The calculated reflectivity  $R$ , transmittance  $T$  and absorption  $A$  of the composite film of gold nanoparticles and polymer, at different  $f$  and  $r$ , are shown in Fig. 3.7. The refractive index of medium 1 and 3 is set to be  $n_1 = n_3 = 1$ , and the refractive index of the polymer to be  $n_{\text{mat}} = 1.5$ . The thickness of the composite film (medium 2) is set to be  $d_2 = 500$  nm. The hatched region is high absorbance ( $A \geq 0.8$ ) at visible wavelengths (400–800 nm). The composite ( $f = 0.2, r = 50$  nm) satisfies the condition ( $A \geq 0.8$ ) over the visible wavelengths, as shown in (d).

The calculated results of  $R, T$  and  $A$  of the composite film of silver nanoparticles and polymer, at different  $f$  and  $r$ , are shown in Fig. 3.8. Parameters  $n_1 = n_3 = 1, n_{\text{mat}} = 1.5$  and  $d_2 = 500$  nm are used. The composites ( $f = 0.2, r = 50$  nm) and ( $f = 0.2, r = 75$  nm) satisfy the condition ( $A \geq 0.8$ ) over the visible wavelengths, as shown in (d) and (e). In both cases, reflectivity is suppressed, as low as  $R \leq 0.2$ , and the transmittance is negligibly small, at the visible wavelengths.

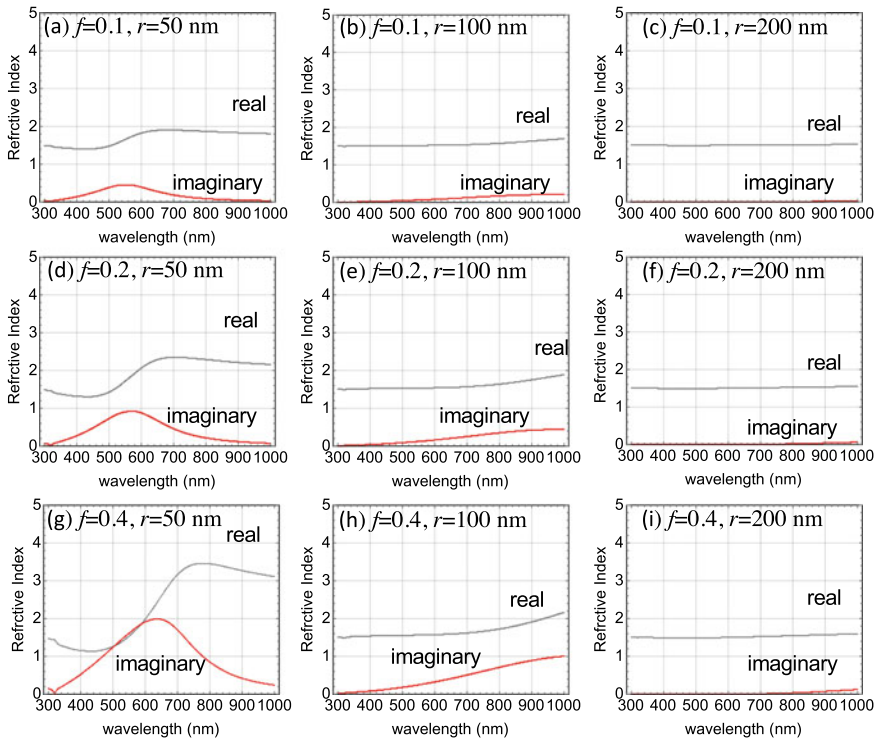


**Fig. 3.6** Calculated real and imaginary parts of the effective refractive index of the composite of silver nanoparticles in a polymer thin-film matrix, at a different particle fraction  $f$  and the radius of the particles  $r$

To find the optimized particle size, the mean absorption  $\bar{A}$  of the composite film of gold nanoparticles and polymer was calculated over the visible wavelengths, at different  $f$  and  $r$ . The results are shown in Fig. 3.9. The greatest mean absorption  $\bar{A} \sim 0.9$  is found in the two conditions ( $f = 0.2, r = 50$  nm) and ( $f = 0.4, r = 75$  nm). The spectra are shown in Fig. 3.7d, h, respectively. Although good  $\bar{A}$  value is given at the condition ( $f = 0.4, r = 75$  nm), the absorbance is less than 0.8 at the long wavelength range (700–800 nm). This is not good condition for blackbody in the visible wavelength range.

The mean absorption  $\bar{A}$  of the composite film of silver nanoparticles and polymer is shown in Fig. 3.10. The greatest mean absorption  $\bar{A} \sim 0.9$  is found in the three conditions ( $f = 0.2, r = 50 - 75$  nm), ( $f = 0.3, r = 75$  nm) and ( $f = 0.4, r = 100$  nm); corresponding spectra are shown in Fig. 3.8d, e and i.<sup>1</sup> Although good  $\bar{A}$  value is given at the condition ( $f = 0.4, r = 75$  nm), the absorbance is less than 0.8 at the short wavelength range (400–450 nm).

<sup>1</sup>The spectra at the condition ( $f = 0.3, r = 75$  nm) is not shown.

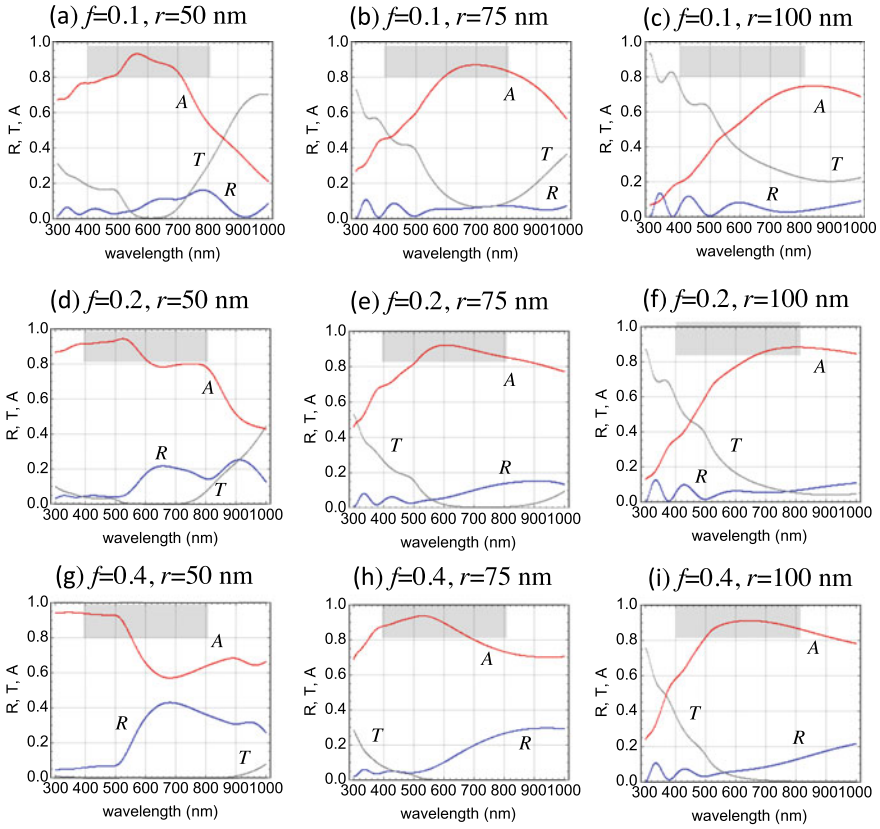


**Fig. 3.7** Calculated reflectivity  $R$ , transmittance  $T$  and absorption  $A$  of the composite film of gold nanoparticles and polymer, at a different particle fraction  $f$  and the radius of the particles  $r$

To have greater absorption, we calculated the mean absorption  $\bar{A}$  of the composite film of binary gold particles and polymer. The fractions and the radii are  $f_1$ ,  $f_2$ ,  $r_1$  and  $r_2$ , respectively. The results of the composite of gold nanoparticles and polymer are shown in the contour plot in Fig. 3.11, at different fractions  $f_1$  and  $f_2$ , as a function of radii  $r_1$  and  $r_2$ . The refractive indexes of the media are set to be  $n_1 = n_3 = 1$  and  $n_{\text{mat}} = 1.5$ . The high absorption ( $A \geq 0.8$ ) is satisfied under a wide range of  $r_1$  and  $r_2$ . The results for the composite of binary silver particles and polymer are shown in Fig. 3.12. The conditions to have high mean absorption  $\bar{A}$  are also broad, similar to the gold composite.

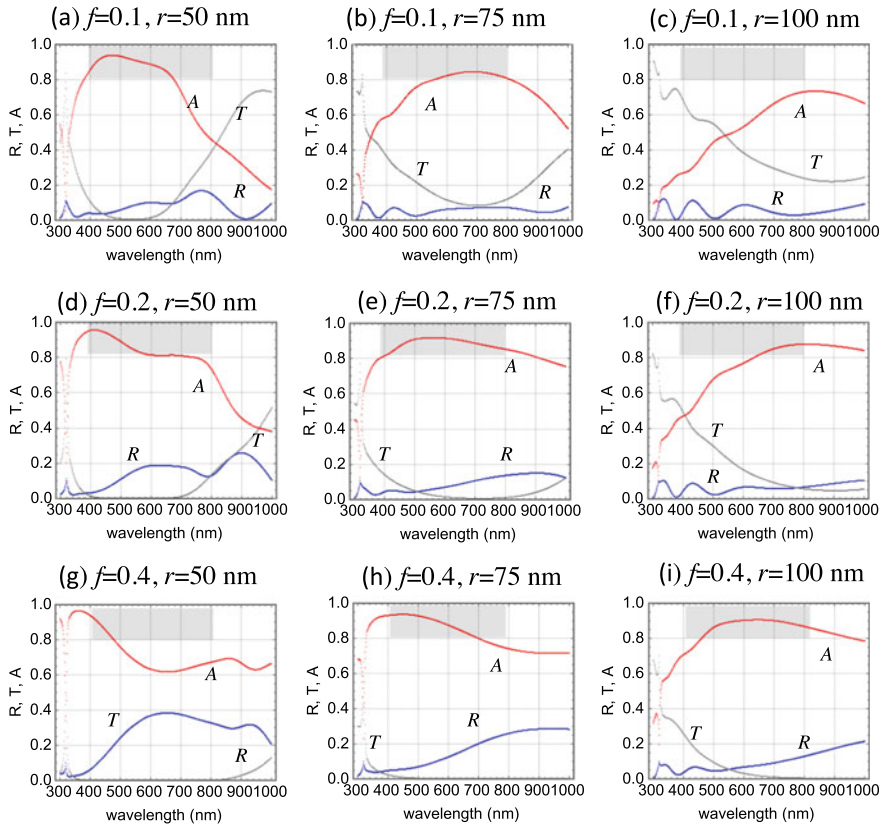


**Fig. 3.8** Calculated reflectivity  $R$ , transmittance  $T$  and absorption  $A$  of the composite of silver nanoparticles and polymer, at a different particle volume fraction  $f$  and the radius of the particles  $r$

### 3.3 Experiment

We show experimental results of reflectance, transmittance and absorption spectra of composite films. The gold nanoparticles were made by the following procedure. Sodium chloroaurate ( $\text{NaAuCl}_4$ ) 79.6 mg (0.2 mmol) was dissolved in pure water (100 mL). Aqueous solution of citric acid at a concentration of 1.5 wt%, used for reduction of  $\text{NaAuCl}_4$ , was added to the sodium chloroaurate solution at  $80^\circ\text{C}$  with stirring for 10 min. It was radiationally cooled to the room temperature. An ethanol solution of polyvinylpyrrolidone (PVP) at 4 wt% was added to the solution to prevent aggregation of the particles. The amount of the PVP solution was 100 mL. The size of the gold nanoparticles was controlled by the amount of the aqueous solution of citric acid. Addition of 2 mL and 4 mL of the citric acid solution affords us the gold particles of radii of 50 nm and 37.5 nm, respectively. The size of the particles was evaluated by scanning electron microscopy.

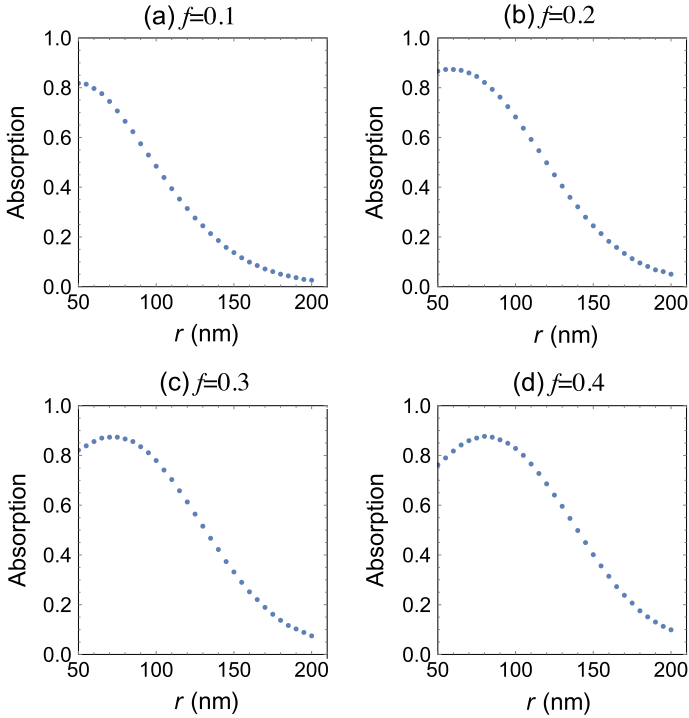


**Fig. 3.9** Calculated maximum mean absorption  $\bar{A}$  of the composite film of gold nanoparticles and polymer, at a different particle fraction  $f$  and the radius of the particles  $r$

For the gold particles larger than of a radius of 50 nm, a mixture of ascorbic acid (8.1 wt%) and citric acid (1.5 wt%) was used for reduction. Sodium chloroaurate ( $\text{NaAuCl}_4$ ) 82.4 mg (0.2 mmol) was dissolved in pure water (100 mL). After heating the sodium chloroaurate solution at  $80^\circ\text{C}$ , 2 mL of the mixture solution of ascorbic acid and citric acid was added. After stirring for 1 min, an ethanol solution of PVP at 4wt% was added to prevent aggregation.

Since the gold particle solutions were low density to form a film, they were concentrated by centrifugation. The composite film was fabricated on a glass substrate by the spin-coating method. The thickness of the film was evaluated with a Dektak Stylus Profiler.

Experimental results of  $R$ ,  $T$  and  $A$  of the 750-nm-thick composite film of gold nanoparticles and polymer are shown in Fig. 3.13a. The radius of the nanoparticles was  $r = 100$  nm, and the volume fraction was  $f = 0.4$ . The absorption of the composite film is over 0.9 in visible spectrum range with negligible transmittance and low reflection below 0.1. The absorbance is gradually decreased with the wavelength. The refractive index of the composite film calculated with the parameters  $r = 100$  nm and  $f = 0.4$  is shown in Fig. 3.13b. The  $R$ ,  $T$  and  $A$  calculated are shown in Fig. 3.13c. While the results of experimental and theoretical results were in



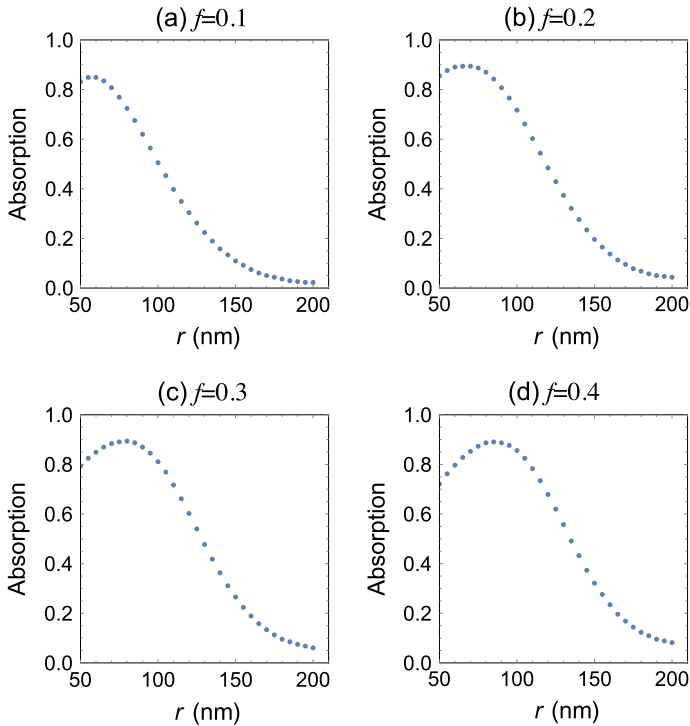


**Fig. 3.10** Calculated maximum mean absorption  $\bar{A}$  of the composite film of silver nanoparticles and polymer, at a different particle fraction  $f$  and the radius of the particles  $r$

good agreement with wavelengths 400–500 nm, they are not in good agreement with the wavelengths longer than 500 nm. A possible reason is that aggregation occurs owing to the high concentration  $f = 0.4$  and the optical absorption is changed from that of the nanoparticles isolated and dispersed in the polymer matrix.

Experimental results of  $R$ ,  $T$  and  $A$  of the 260-nm-thick composite film of binary gold particles and polymer are shown in Fig. 3.14a. The particles were  $r_1 = 100$  and  $r_2 = 37.5$  nm with volume fractions of  $f_1 = 0.3$  and  $f_2 = 0.1$ , respectively. Small particles were used to elevate the volume fraction. The absorption of the composite film is over 0.8 in visible spectrum range with negligible transmittance and low reflection below 0.1. The refractive index of the composite film calculated with the parameters is shown in Fig. 3.14b, and the calculated  $R$ ,  $T$  and  $A$  are shown in Fig. 3.14c. The results were almost in agreement probably due to no aggregation in the binary mixture.

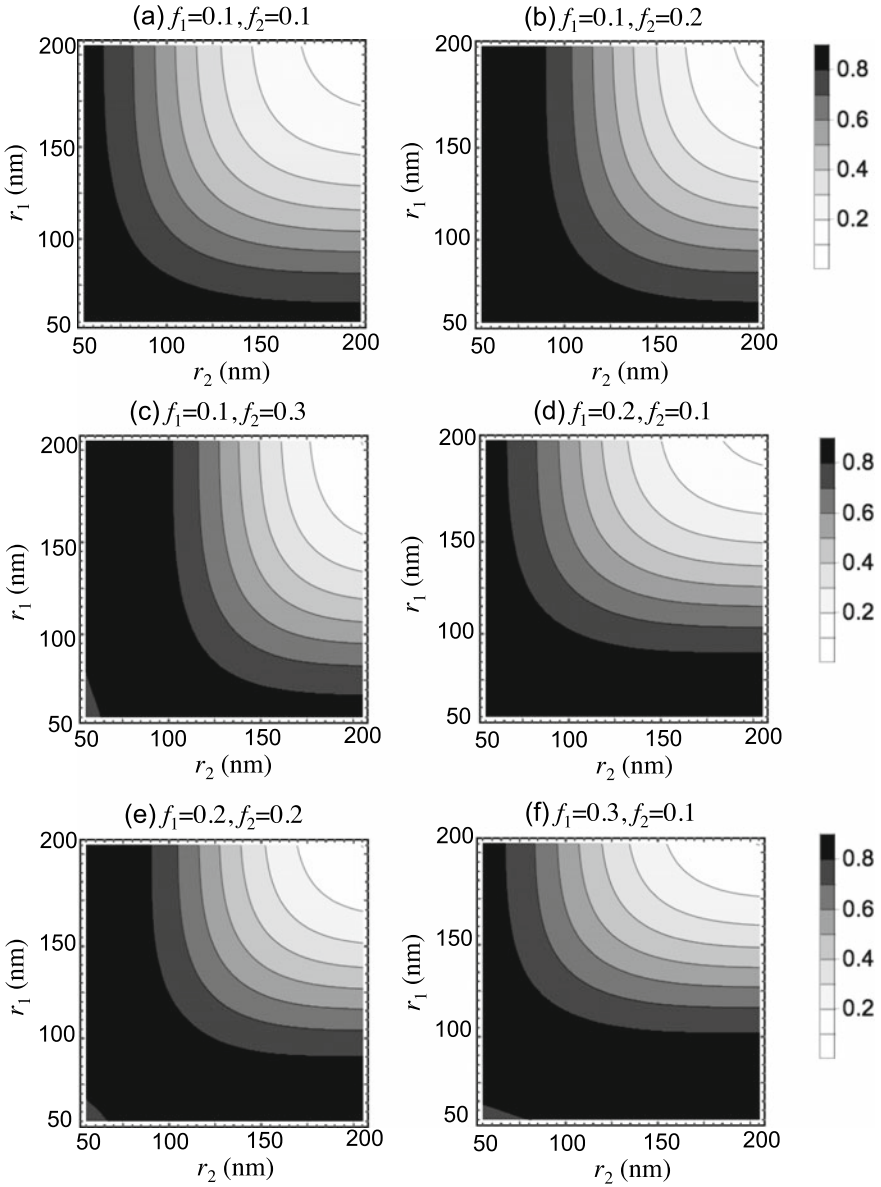


**Fig. 3.11** Calculated mean absorption  $\bar{A}$  of the composite film of binary gold nanoparticles and polymer, at different particle fractions  $f_1, f_2$  and the radii of the particles  $r_1, r_2$

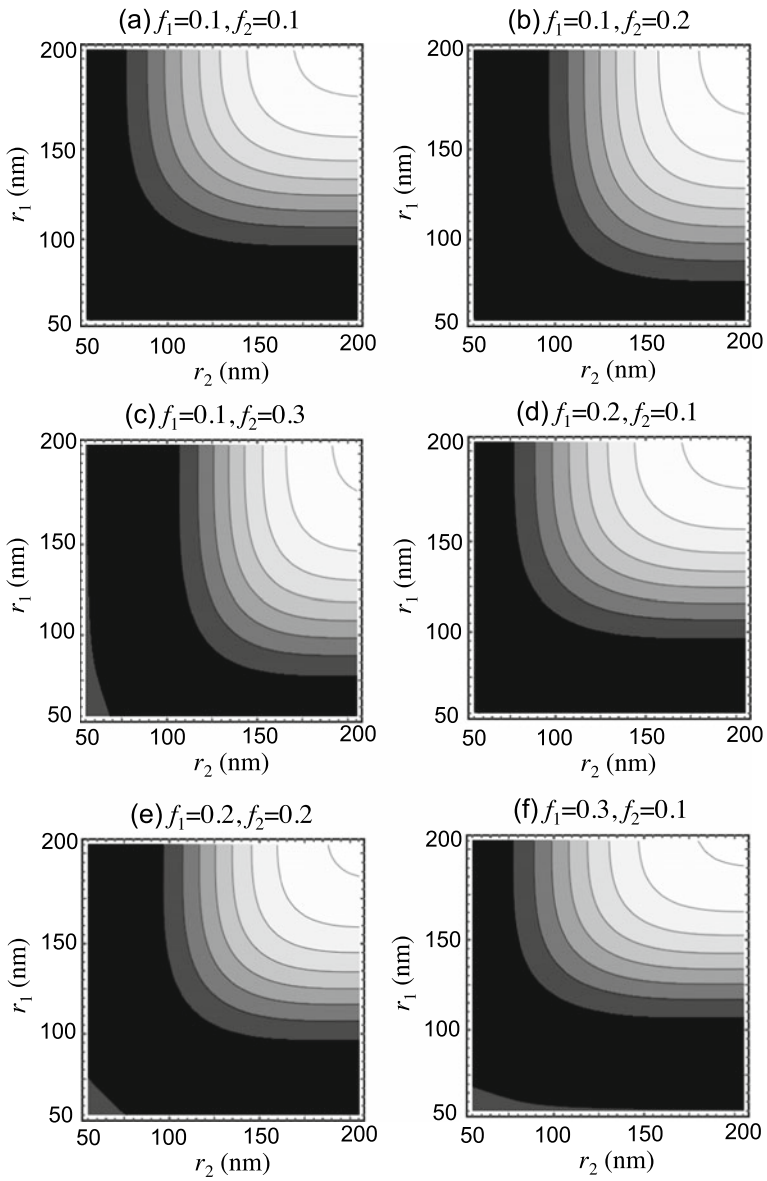


**Fig. 3.12** Calculated mean absorption  $\bar{A}$  of the composite film of binary silver nanoparticles and polymer, at different particle fractions  $f_1, f_2$  and the radii of the particles  $r_1, r_2$

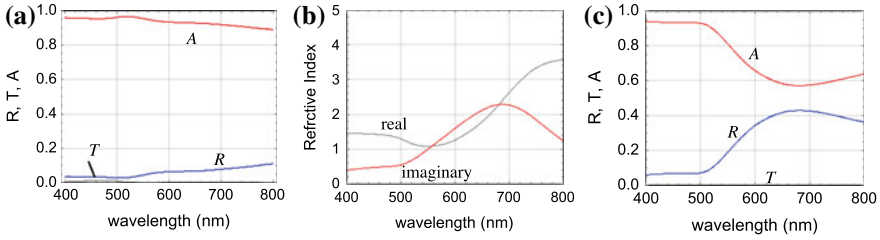


**Fig. 3.13** **a** Experimental results of  $R$ ,  $T$  and  $A$  of the 750-nm-thick composite film of gold nanoparticles and a thin PVP film. The diameter of the nanoparticles was  $r = 100$  nm, and the volume fraction was  $f = 0.4$ . **b** The refractive index of the composite film and **c**  $R$ ,  $T$  and  $A$  calculated with the parameters  $r = 100$  nm and  $f = 0.4$

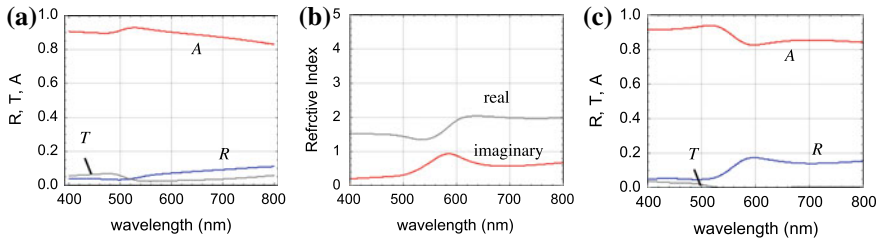


**Fig. 3.14** **a** Experimental results of  $R$ ,  $T$  and  $A$  of the 260-nm-thick composite film of binary gold nanoparticles and a thin PVP film. The nanoparticles were  $r_1 = 100$  and  $r_2 = 37.5$  nm with volume fractions of  $f_1 = 0.3$  and  $f_2 = 0.1$ . **b** The refractive index of the composite film and **c**  $R$ ,  $T$  and  $A$  calculated with the parameters  $r_1 = 100$ ,  $r_2 = 37.5$ ,  $f_1 = 0.3$  nm and  $f_2 = 0.1$

### 3.4 Summary

Theoretical and experimental results of blackbody metamaterial composite film of nanoparticles and polymer have been discussed. Although the experimental results are in agreement with the calculated spectra in the composite of binary gold nanoparticles and polymer, the results are deviated from the calculated spectra in the composite of single-element gold nanoparticles and polymer. This may be due to aggregation of the gold nanoparticles at high volume fraction.

**Acknowledgements** This work was partially supported by a Grant-in-Aid for Scientific Research (No. 25109707, 26600023, 26286058, 16K13696) and Bilateral Program from the Japan Society for the Promotion of Science.

### References

1. V.G. Kravets, S. Neubeck, A.N. Grigorenko, Plasmonic blackbody: strong absorption of light by metal nanoparticles embedded in a dielectric matrix. *Phys. Rev. B* **81**, 165401 (2010)

2. V.G. Kravets, F. Schedin, A.N. Grigorenko, Plasmonic blackbody: almost complete absorption of light in nanostructured metallic coatings. *Phys. Rev. B* **78**, 205405 (2008)
3. Y. Ebihara, R. Ota, T. Noriki, M. Shimojo, K. Kajikawa, Biometamaterials: black ultrathin gold film fabricated on lotus leaf. *Sci. Rep.* **5**, 15992 (2015)
4. Y. Ebihara, Y. Sugimachi, T. Noriki, M. Shimojo, K. Kajikawa, Biometamaterials: dark ultrathin gold film fabricated on taro leaf. *Opt. Mat. Express* **6**, 1429–1435 (2015)
5. W.T. Doyle, Optical properties of a suspension of metal spheres. *Phys. Rev. B* **39**, 9852–9858 (1989)

# Chapter 4

## Bottom-up Strategies for Fabricating Meta-atoms via Self-assembly of Polymers and Nanoparticles



Hiroshi Yabu

**Abstract** In this chapter, bottom-up strategies for fabricating nanoscale ring structures to produce optical metamaterials are described. Co-assemblies of submicrometer-sized spherical polymer particles and metal nanoparticles spontaneously form three-dimensional (3D) nano-ring arrays among polymer particles through self-assembly of metal nanoparticles at the evaporation meniscus. Colloidal assemblies of submicrometer particles, which form 3D periodic structures, are used as templates to assemble metal nanoparticles and block copolymers. Block copolymers form phase-separated structures tens of nanometers in size; thus, metal nanoparticles can be self-assembled into the phase-separated block copolymers. These bottom-up methodologies are useful for fabricating optical metamaterials.

### 4.1 Introduction

Optical metamaterials, which can modulate the refractive indices of materials from positive to negative in the visible light region, are attractive for their applications ranging from high-resolution optical microscopy beyond the diffraction limit [4] to optical cloaking [5]. Theoretical calculations indicate that metallic nano-resonators smaller than the wavelength of visible light, which have electromagnetic resonance with electromagnetic radiation, are required for realizing optical metamaterials [6]. Current top-down microfabrication technologies have been used to prepare two-dimensional (2D) arrays of these meta-atoms on solid substrates, and their optical properties have been investigated [7]. However, the angular dependences of the opti-

---

This chapter is based on the following three articles: [1] Hiroshi Yabu, Tatsuya Jinno, Kazutaka Koike, Takeshi Higuchi and Masatsugu Shimomura, *Macromolecules* 44(15), 5868–5873 (2011), Copyright © 2011 American Chemical Society; [2] Hiroshi Yabu, Tatsuya Jinno, Kazutaka Koike, Takeshi Higuchi, Masatsugu Shimomura, *J. Polym. Sci. Pt. B-Polym. Phys.* 49(24), 1717–1722 (2011), Copyright © 2011 Wiley Periodicals, Inc. [3] Hiroshi Yabu, *Langmuir* 29(4), 1005–1009 (2013), Copyright © 2013 American Chemical Society.

---

H. Yabu (✉)

WPI-Advanced Institute for Materials Research (AIMR), Tohoku University, Sendai, Japan  
e-mail: [hiroshi.yabu.d5@tohoku.ac.jp](mailto:hiroshi.yabu.d5@tohoku.ac.jp)

cal properties must be measured owing to the 2D nature of the arrays, and the arrays require expensive, elaborate multistep fabrications. Therefore, a simple process to fabricate three-dimensional (3D) metallic nano-resonators is desirable.

Bottom-up strategies, including self-assembly and chemical synthesis of nano-structures, provide alternative ways to create arrays of 3D metallic nano-resonators. An essential technique for bottom-up fabrication is arranging metallic nanoparticles (NPs) which have plasmonic properties and interact with visible light [8]. In this chapter, we describe bottom-up approaches based on colloidal self-assembly and polymer phase separation for creating 3D arrays of NPs.

## 4.2 Formation of Metallic Shells on the Surface of Microspheres

Thin metallic shells formed on the surface of microspheres smaller than the light wavelength provide ideal conditions for interacting with visible light. The small noble metal shells have plasmonic resonances with visible and ultraviolet light and absorb visible light, and their spherical shape means that the optical properties do not depend on angle.

There are two approaches to forming metallic shells: chemically plating microsphere surfaces with metals and heterocoagulation of metal NPs. Plating is the simple chemical reduction of metal ions on the surface of silica or polymer particles. Halas et al. reported the formation of silver nano-shells on silica NPs and measured their optical properties (Fig. 4.1a) [9]. However, because silver has self-catalytic properties, controlling the surface roughness is difficult, which may affect the plasmonic properties of the nano-shell structures.

Heterocoagulation of metallic NPs on microsphere surfaces is another technique for forming metallic NP arrays on the surface of microspheres [10]. The plasmonic resonance of metal NPs is enhanced by plasmonic coupling among NPs, resulting in strong electromagnetic resonance. Furthermore, the resonance wavelength can be controlled by tuning the size and plasmonic coupling of metal NPs to red-shift the absorption wavelength.

Kanahara et al. also reported the formation of nano-shell structures composed of Au NPs on polymer blended particles of amino-terminated poly(butadiene) (PB-NH<sub>2</sub>) and poly(styrene) (PS) [11]. PB-NH<sub>2</sub> and PS were dissolved in tetrahydrofuran (THF), and then water was mixed into the solution. After complete evaporation of THF, core-shell polymer blended particles with PB-NH<sub>2</sub> shells, were formed (Fig. 4.1b). Owing to the cationic amine groups, the surface charge of the blended particles was positive. Negatively charged Au NPs stabilized with citrate molecules adhered to the surface of the blended particles and formed Au NP shells. Furthermore, Au NPs diffused into the shell, and then multilayered NP assemblies were formed on the shell layer owing to the low glass transition temperature of PB. The plasmonic resonance of these core-shell composite particles was red-shifted from



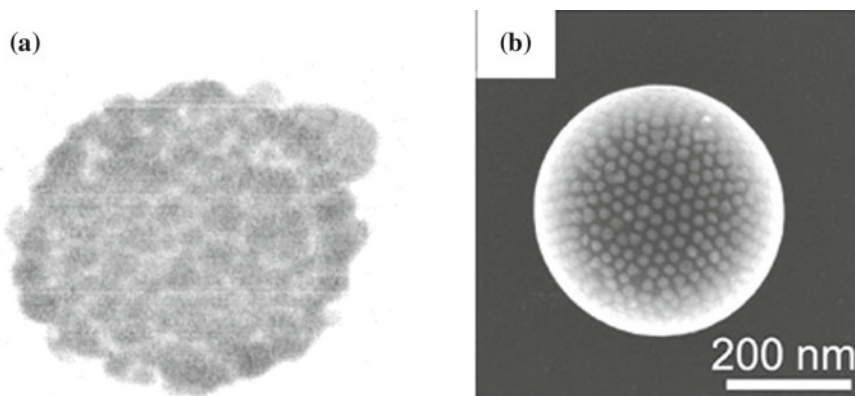


**Fig. 4.1** **a** TEM image of silver-plated silica NPs [9] and **b** SEM image of Au NPs and polymer composite particles [11]. (a, b) are reprinted with permission from J. B. Jackson, N. J. Halas, *J. Phys. Chem. B* 2001, 105(14), 2743, Copyright (2001) American Chemical Society and M. Kanahara, H. Sato, T. Higuchi, A. Takahara, H. Jinnai, K. Harano, S. Okada, E. Nakamura, Y. Matsuo, H. Yabu, *Part. Part. Syst. Char.* 2014, 32(4), 441, Copyright (2014) by John Wiley Sons, Inc. Reprinted by permission of John Wiley & Sons, Inc., respectively

500 to 780 nm, and the top peak wavelength was controlled by changing the number of assembled Au NPs, allowing arbitrary control of the resonance wavelength. Based on the high electromagnetic resonance with visible and near-infrared wavelength light, surface-enhanced Raman scattering signals from absorbed molecules were obtained from these composite particles.

The morphology of the microphase-separated structure in composite particles consisting of metal NPs and the block copolymer is controlled by many factors, including the molecular weight, the copolymerization ratio of block copolymers, the NP concentration, and the NP size. Yabu et al. reported the effects of the size and concentration of Au NPs on the microphase-separated structure in composite particles consisting of Au NPs and a block copolymer (Fig. 4.2) [2].

PS-*b*-P2VP-stabilized Au NPs [12] and PS-SH-stabilized Au NPs have been synthesized [13]. The inner structure of block copolymer particles depends on the copolymerization ratio of each polymer segment. PS-*b*-PI forms lamellar structures in the bulk state, and unidirectionally stacked lamellar structures or onion-like structures in particles were used. Figure 4.3a–c shows transmission electron microscopy (TEM) images of the composite particles. Each particle was spherical with a diameter of ~300 nm and had onion-like microphase-separated structures, which were the same as in the block copolymer.

Cross-sectional TEM images showed that the position of the Au NPs depended on their size (Fig. 4.3d–f). Au NPs were present in each of the PS layers in the onion-like block copolymer particles. In contrast, Au NPs were only located on the surface of the onion-like block copolymer particles and were not present in the inner layers in larger Au NPs. Because the Au NPs were smaller than the thickness of the PS layers in composite particles, the Au NPs simultaneously precipitated with the

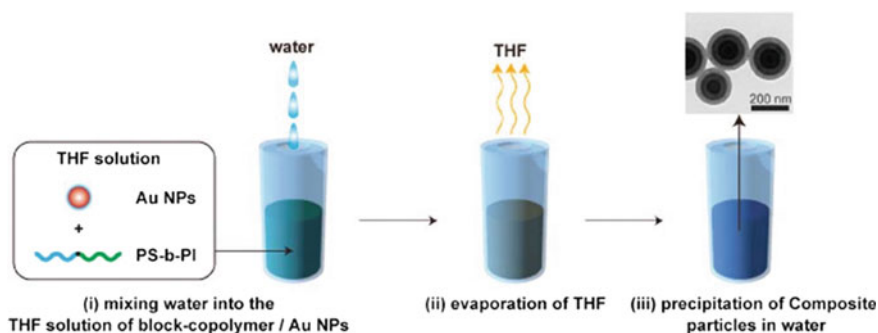


**Fig. 4.2** Schematic illustration of the preparation of composite particles. The figure is reprinted from [2] H. Yabu, K. Koike, T. Higuchi, M. Shimomura, *J. Polym. Sci. Polym. Phys.* 2011, 49(24), 1717, Copyright (2011), by John Wiley Sons, Inc. Reprinted by permission of John Wiley & Sons, Inc.

block copolymers and were included in the layers. However, when the thickness of the layer of Au NPs was greater than the thickness of PS layer, the Au NPs remained on the outer layer of the composite particles, even though the Au NPs simultaneously precipitated with the block copolymers.

Figure 4.3g–i show close-up TEM images and models of the single PS layers of the composite particles. The Au NPs in the composite particles were randomly dispersed in the PS layer (Fig. 4.3g). However, the Au NPs in composite particles were located in the center of the PS layer and were aligned parallel to the layers (Fig. 4.3i). Because the polymer-stabilizing Au NP was a low-molecular-weight polymer, the Au NPs were incorporated into the polymer chains of the PS moieties (model images, insets of Figs. 4.3g–i). The polymer-stabilizing Au NP is a higher-molecular-weight polymer and was aligned in the center of the PS phase, which is the lowest density area of the polymer chains, although the Au NPs are small enough to be incorporated into the PS phase.

When the number of PS moieties in PS-b-PI was decreased, a large number of Au NPs were introduced into the composite particles with an onion-like microphase-separated structure. To increase the number of Au NPs in the composite particles, the mixing ratio of Au NPs in the solution of PS-b-PI and Au NPs was increased. However, the morphologies of the composite particles changed from lamellar to cylindrical and spherical phases as the amount of Au NPs increased owing to the increase in the fraction of PS and PS-stabilized Au NPs phases (Fig. 4.4). The number of PS moieties in PS-b-PI was decreased to maintain the lamellar morphology as the amount of Au NPs increased.

The control of microphase-separated structures in composite particles consisting of Au NPs and a block copolymer was achieved by changing the Au NP size, the mix ratio, and the copolymerization ratio of the block copolymers. The Au NP size controlled where the NPs were introduced in the composite particle. These results reveal a set of guiding principles for creating metal–polymer composite particles.

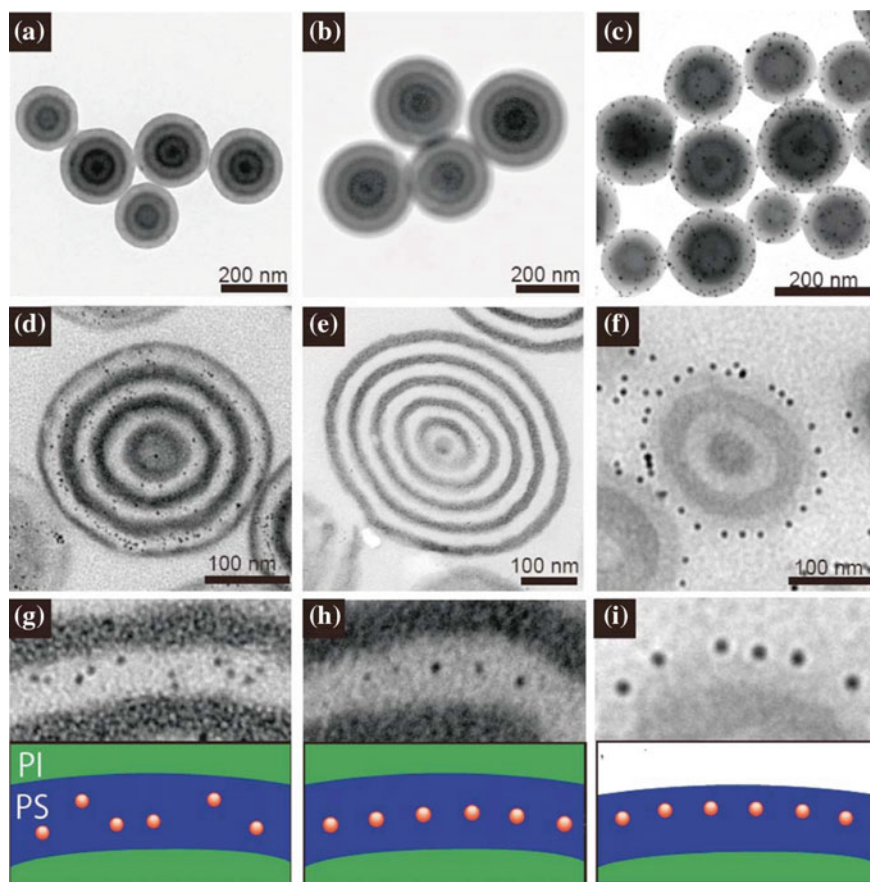


**Fig. 4.3** TEM images of composite particles composed of PS-*b*-PI ( $M_{n(PS)} = 45.0$  kg/mol,  $M_{n(PI)} = 31.0$  kg/mol) and Au NPs stabilized with PS-SH ( $M_{n(PS)} = 1.0$  kg/mol) (a), PS-*b*-PI ( $M_{n(PS)} = 45.0$  kg/mol,  $M_{n(PI)} = 31.0$  kg/mol) and Au NPs stabilized with PS-SH ( $M_{n(PS)} = 11.5$  kg/mol) (b), and PS-*b*-PI ( $M_{n(PS)} = 143$  kg/mol,  $M_{n(PI)} = 81.0$  kg/mol) and Au NPs stabilized with PS-*b*-P2VP ( $M_{n(PS)} = 25.5$  kg/mol,  $M_{n(P2VP)} = 23.5$  kg/mol) (c). Cross-sectional TEM images of composite particles in a, b, and c are shown in d, e, and f, and close-up images of the cross-sectional TEM images are shown in g, h, and i, respectively. The images are reproduced from [2] H. Yabu, K. Koike, T. Higuchi, M. Shimomura, *J. Polym. Sci. Polym. Phys.* 2011, 49(24), 1717, Copyright (2011), by John Wiley Sons, Inc. Reprinted by permission of John Wiley & Sons, Inc.

### 4.3 Colloidal Self-assembly of Metallic NPs

Binary colloidal systems of submicrometer-sized PS particles and Au NPs produce ring arrays of Au NPs. Colloidal particles have been used as templates in a bottom-up approach to creating nano-ring structures. Chemical vapor deposition and physical vapor deposition of metals and metal oxides in colloidal assemblies of particles have been used to form 2D ring arrays. Xia and co-workers developed a simple method for

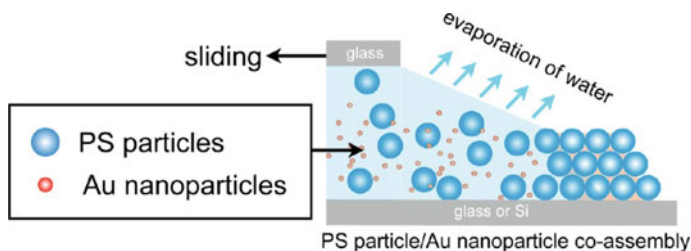


**Fig. 4.4** Schematic illustration of the co-assembly process [3]. Hiroshi Yabu, *Langmuir* 29(4), 1005–1009 (2013), Copyright © 2013 American Chemical Society

fabricating 2D metal nano-ring arrays by edge-spreading lithography using colloidal particles and an etching process [14]. Goedel and colleagues reported submicrometer gold rings, which were fabricated by imprinting colloidal particles in polymer films and filling the interior of the imprinted surfaces with the metal ions. Cremer and co-workers prepared double-ring structures by using water stain templates for nanolithography [15]. Yang and co-workers fabricated ring arrays by embossing spherical particle assemblies on polymer films [16].

Additionally, patterned inorganic NP assemblies have been fabricated on solid substrates through the capillary condensation of NP suspensions. Yabu and Shimomura found that various micropatterns, including a dot pattern and a line-and-space pattern, can be simply fabricated by sandwiching a polymer and Au NP suspension between two parallel substrates [17]. The Au NPs were concentrated at the three-phase contact line of the suspension at the edge of the upper substrate and were deposited at the meniscus of the solution when the solution concentration at the edge exceeded the NP solubility. After the suspension receded, the concentration gradually increased again, and deposition of materials occurred intermittently, forming periodic micropatterns. Because the Au NPs precipitated at the three-phase line of the suspension supplied from the edge of the substrate, the prepared dots and lines were well aligned along the meniscus edge. By exploiting this capillary condensation mechanism, Lin et al. [18] used spherical templates to fabricate various concentric ring patterns from functional materials on the micrometer scale.

Recently, Savinova and co-workers formed 2D gold nano-ring arrays by a colloidal templating technique that involved the reduction of gold ions patterned beneath polymer particles [19]. Chen et al. fabricated nano-ring arrays of CdSe NPs on a solid substrate [15] by co-assembly of PS colloidal particles and CdSe NPs during simple evaporation of solvent and removing PS colloidal particles with adhesive tape. These reports demonstrate the fabrication of 2D nano-ring structures on solid substrates; however, there are few reports of 3D nano-ring assemblies.

Yabu also reported a bottom-up approach to creating 3D assemblies of Au nano-rings [3]. Hexagonally assembled colloidal crystals were formed by drying aqueous dispersions of PS colloidal particles and Au NPs, and nano-rings composed of Au NPs and PS colloidal particles were also formed. Figure 4.4 shows the formation of the co-assembly of PS colloidal particles and Au NPs. First, two solid substrates were

placed parallel separated by a gap of about 500  $\mu\text{m}$ , and an aqueous dispersion of PS particles and Au NPs was injected into the gap between the two glass substrates. The upper glass substrate was slid across the bottom at a velocity of 1  $\mu\text{m/s}$  to create a co-assembly of PS colloidal particles and Au NPs. After complete evaporation of the water, the surface and cross-sectional structures of co-assemblies were observed by scanning electron microscopy (SEM). The field emission (FE)-SEM image (Fig. 4.5) shows hexagonally arranged PS colloidal particles. The darker contrast regions at the connection sites among the PS colloidal particles correspond to high electron densities and indicate the formation of Au NPs assemblies.

The size of the nano-rings could be controlled from tens to hundreds of nanometers. After sintering, the Au NPs formed Au nano-rings. This simple approach provides a potentially useful path to new plasmonic materials and unique metamaterials for the visible light region.

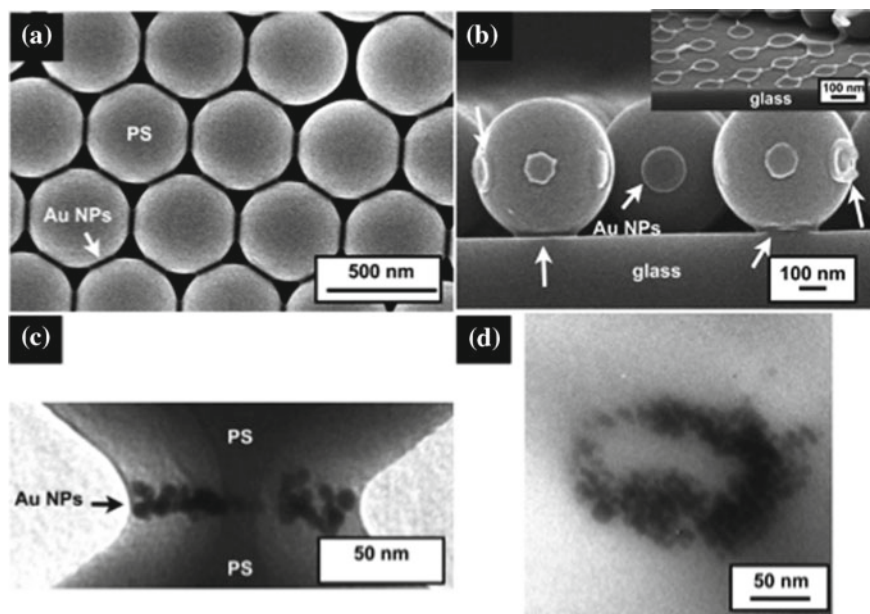


**Fig. 4.5** SEM image (a), cross-sectional SEM image (b), TEM image (c), and cross-sectional TEM image (d) of a co-assembly of 500 nm PS spheres and 5 nm Au NPs. Images are reprinted with permission from H. Yabu, *Langmuir* 2013, 29(4), 1005 [3]. Copyright (2001) American Chemical Society

#### 4.4 Preparing NP Arrays by Combining Colloidal and Block Copolymer Self-assembly

Block copolymer microphase separation structures are suitable candidates for the bottom-up approach to arranging metal NPs. Recent developments in living polymerization have allowed the preparation of a wide variety of block copolymers that have a high affinity for metal NPs and form unique microphase separation structures. Many studies have been published detailing the assembly of metal NPs in 2D and 3D microphase separation structures in bulk or thin-film block copolymers [18]. The microphase separation of block copolymers can create periodic nanoscale structures, in which metal NP assemblies are arranged along the microphase separation structure. However, the orientation of the microphase separation structure's nano-domain, which contains the metal NPs, cannot be controlled, and the domain sizes of the microphase separation structures are too small for optical and electrical applications. Mesoscale templates avoid these problems by arranging the nano-domains of the microphase separation structures.

The microphase separation structures were arranged along the interface between the template and the block copolymer; the structure depended on the boundary conditions and size of the confined space in the template. Thin-film (one-dimensional) confinement [20], 2D confinement systems [21], and 3D confinement [22] have been reported. Inverse opals are suitable templates for 3D confinement systems because their pore size is comparable to the characteristic length of the microphase separation in block copolymers [23]. Dispersions of submicrometer- or micrometer-sized colloidal particles can be assembled into fine crystals by evaporating the solvent, spin-coating, or compression. Inverse opals can be prepared by molding colloidal crystals with another material and removing the template colloid. By using colloidal crystals and inverse opals as confinement spaces, frustrated block copolymer microphases can be created.

Yabu et al. constructed 3D Au NP assemblies embedded in the microphase separation structures of confined block copolymers in the pores of inverse opals [1]. They synthesized polymer-stabilized Au NPs, and submicrometer PS colloidal crystals were prepared by a simple coating method. After molding a PS colloidal crystal with poly(vinyl alcohol) (PVA), block copolymers and Au NPs were introduced into the PVA inverse opal from solution (Fig. 4.6).

Figure 4.7a shows an FE-SEM image of an Au NPs/PS-*b*-PI composite array. The spherical submicrometer structure reflects the structure of the inverse opal template prepared from 248 nm PS colloidal particles. The cross-sectional image of the Au NPs/PS-*b*-PI composite array also shows that spherical domains were formed in the film (Fig. 4.7b). The close-up image of the single spherical domain shows onion-like microphase separation structures, consisting of gray PI phases and bright PS phases (Fig. 4.7c). In the more closed inner structure, black dots are visible in the PS phases, which were identified as Au NPs (Fig. 4.7d). In the cross-sectional images of an Au NPs/PS-*b*-PI composite array prepared from 498 nm PS particles (Figs. 4.7e, f), the multilayered structures of the spherical domains are clear, and the periodicity of each



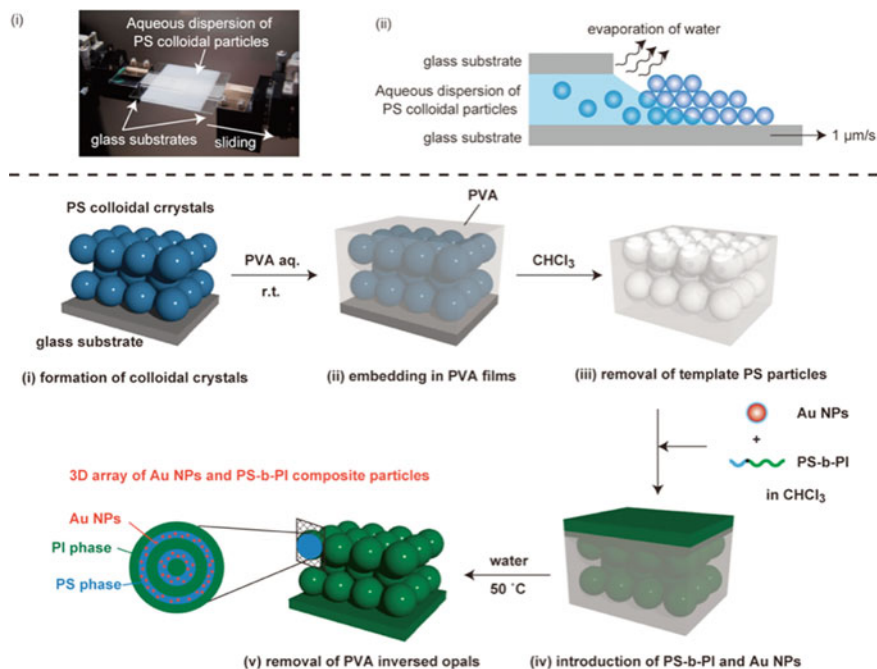


**Fig. 4.6** Photograph of coating apparatus (i) and the schematic illustration of colloidal crystal preparation (ii). Schematic illustration of the preparation of inverse opals and Au NPs and block copolymer composites (b). Images are reprinted with permission from H. Yabu, T. Jinno, K. Koike, T. Higuchi, M. Shimomura, *Macromolecules* 2011, 44(15), 5868 [1]. Copyright (2011) American Chemical Society

microphase-separated structure is same as for the 248 nm PS particles. The array of Au NPs is visible in the PS phase (Fig. 4.7f).

An onion-like microphase separation structure was formed, even though the volume fraction of PI ( $f_{PI}$ ) value for PS-b-PI was 0.74. The thermodynamically stable microphase separation structure of this block copolymer is PS cylinders dispersed in a PI matrix. The morphologies of the inner-phase separation structures of block copolymer particles can be controlled by the amount of metal NPs. Based on thermogravimetric analysis, the Au NPs contained free PS-SH molecules. Because the PS-SH-stabilized Au NPs and free PS-SH molecules were incorporated into the PS phase, the volume fraction of the PS phase increased, and a lamellar microphase separation structure was formed. The microphase separation structures of block copolymers in 3D confinement spaces were affected by the size of the confinement spaces and the affinity of the polymer segments for the template materials. Experimental analysis of 3D confinement systems in block copolymer particles indicated that when the ratio between the periodicity of a microphase separation structure ( $L_0$ ) and the diameter of the confinement space ( $D$ ) ( $D/L_0$ ) was smaller than 2.0, frustrated phases appeared. These phases are different from the microphase separation



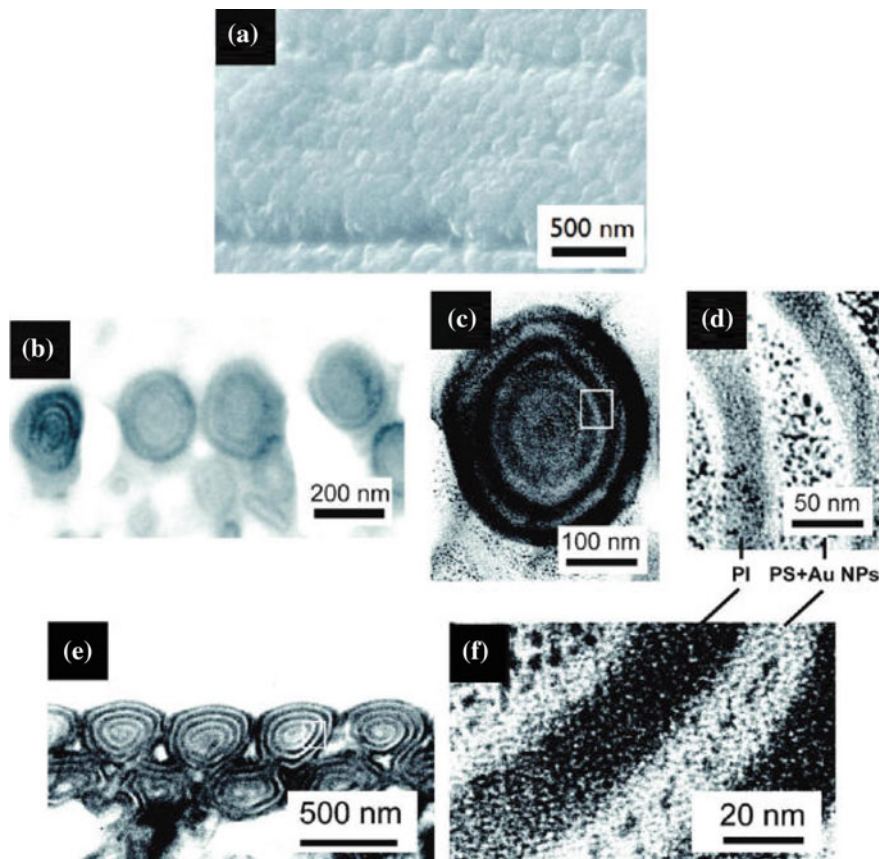


**Fig. 4.7** FE-SEM image of the Au NPs and block copolymer composite in an inverse opal prepared from 248 nm PS colloidal crystals (a), cross-sectional (b) and close-up cross-sectional (c) TEM images of Au NPs, cross-sectional TEM image of block copolymer composite (d), and cross-sectional TEM images of Au NPs (e) and block copolymer composites (f) in an inverse opal prepared from 498 nm PS colloidal crystals. Images are reprinted with permission from H. Yabu, T. Jinno, K. Koike, T. Higuchi, M. Shimomura, *Macromolecules* 2011, 44(15), 5868 [1]. Copyright (2011) American Chemical Society

structures observed in the bulk system. When the affinity ( $R$ ) of one of the polymer segments in the block copolymer used for the confinement space material was higher than that of the other segments, the microphase separation structure was arranged along the interface between the domain of the block copolymer and the confinement space. In this case, the  $D$  value (249 nm) was sufficiently larger than  $L_0$  to prevent the frustrated phase from appearing.

## 4.5 Summary

Combining colloidal self-assembly and phase separation of block copolymers is a promising method for fabricating nanoscale metal nano-rings that respond to visible light without angular dependency. Because colloidal particles smaller than 1  $\mu\text{m}$  can be assembled into submicrometer-scale periodic structures, they can be used as templates for assembling metal NPs [24] and block copolymers arranged into structures tens of nanometers in size. 3D structures on this size scale are difficult to access by using top-down microfabrication technologies; therefore, the bottom-up methodologies we have described are useful for fabricating optical metamaterials.

## References

1. H. Yabu, T. Jinno, K. Koike, T. Higuchi, M. Shimomura, *Macromolecules* **44**(15), 5868 (2011)
2. H. Yabu, K. Koike, T. Higuchi, M. Shimomura, *J. Polym. Sci. Polym. Phys.* **49**(24), 1717 (2011)
3. H. Yabu, *Langmuir* **29**(4), 1005 (2013)
4. W.J. Padilla, D.N. Basov, D.R. Smith, *Mater. Today* **9**(7), 28 (2006)
5. P.-Y. Chen, J. Soric, A. Alú, *Adv. Mater.* **24**(44), 281 (2012)
6. C.M. Soukoulis, S. Linden, M. Wegener, *Science* **315**, 47 (2007)
7. N. Liu, H. Guo, L. Fu et al., *Nat. Mater.* **1**, 31 (2007)
8. B. Gong, X. Zhao, Z. Pan, S. Li, X. Wang, Y. Zhao, C. Juo, *Sci. Rep.* **4**, 4 (2015)
9. J.B. Jackson, N.J. Halas, *J. Phys. Chem. B* **105**(14), 2743 (2001)
10. M. Kanahara, M. Shimomura, H. Yabu, *Soft Matter* **10**, 275 (2014)
11. M. Kanahara, H. Sato, T. Higuchi, A. Takahara, H. Jinnai, K. Harano, S. Okada, E. Nakamura, Y. Matsuo, H. Yabu, *Part. Part. Syst. Char.* **32**(4), 441 (2014)
12. J.P. Spatz, S. Mössmer, C. Harmann, M. Möller, *Langmuir* **16**, 407 (2000)
13. M. Brust, J. Fink, D. Bethell, D.J. Schiffrin, C.J. Kiely, *Chem. Soc. Chem. Commun.* 1655 (1995)
14. J.M. McLellan, M. Geissler, Y. Xia, *J. Am. Chem. Soc.* **126**, 10830 (2004)
15. J. Chen, W.S. Liao, X. Chen, T. Yang, S.E. Wark, D.H. Son, J.D. Batteas, P.S. Cremer, *ACS Nano* **3**, 173 (2009)
16. X. Chen, Z. Chen, N. Fu, G. Lu, B. Yang, *Adv. Mater.* **15**, 1413 (2003)
17. H. Yabu, M. Shimomura, *Adv. Funct. Mater.* **15**(4), 575 (2005)
18. T. Lin, C.L. Li, R.M. Ho, J.C. Ho, *Macromolecules* **43**(7), 3383 (2010)
19. M. Bayati, P. Patoka, M. Giersig, E.R. Savinova, *Langmuir* **26**, 3549 (2010)
20. N. Koneripalli, N. Singh, R. Levicky, F.S. Bates, P.D. Gallagher, S.K. Satija, *Macromolecules* **28**(8), 2897 (1995)
21. H.Q. Xiang, K. Shin, T. Kim, S.I. Moon, T.J. McCarthy, T.P. Russell, *Macromolecules* **37**(15), 5660 (2004)
22. A.C. Arsenault, D.A. Rider, N. Tereault, J.I.L. Chen, N. Coombs, G.A. Ozin, I. Manners, *J. Am. Chem. Soc.* **127**(28), 9954 (2005)
23. P. Jiang, M.J. McFarland, *J. Am. Chem. Soc.* **126**, 13778 (2004)
24. X. Yu, H. Zhang, J.K. Oliverio, P.V. Braun, *Nano Lett.* **9**, 4424 (2009)

# Chapter 5

## UV-Nanoimprinted Metasurface Thermal Emitters for Infrared CO<sub>2</sub> Sensing



Hideki T. Miyazaki

**Abstract** A polarization- and angle-independent dual-band metasurface thermal emitter for CO<sub>2</sub> sensing was developed. The metasurface was based on a stacked Au/Al<sub>2</sub>O<sub>3</sub>/Au structure in which orthogonal rectangular Au patches were alternately arrayed, generating nearly perfect blackbody radiation with emittance as high as 0.98 at 4.26 and 3.95  $\mu\text{m}$ . The metasurface was integrated on a Joule heater fabricated on a SiN membrane so that infrared light is radiated by applying voltage. Subwavelength-sized metasurfaces were manufactured by mass-producible, cost-effective ultraviolet nanoimprint lithography, and the emitter chip was mounted on a standard package compatible with conventional optoelectronic devices. A simple single-layer lift-off process was enabled by employing an organic-solvent-soluble UV resist. The metasurface emitter was applied to a CO<sub>2</sub> sensor and was demonstrated to reduce required electric power by 31% as compared with a conventional blackbody emitter, due to the suppressed unnecessary radiation. Results demonstrate that commercialization of metasurface infrared thermal emitters is becoming a reality.

### 5.1 Introduction

#### 5.1.1 Gas Sensing Based on Infrared Emitters

Concentrations of CO<sub>2</sub>, one of the most important greenhouse gases, are most commonly measured using an optical method called the non-dispersive infrared (NDIR) technique [1]. NDIR sensors determine the concentration of a specific gas from the transmission ratio at two wavelengths, one of which is selected so that only the target molecule is absorbing and the matrix is non-absorbing, while the other (reference wavelength) is selected so that both are non-absorbing. Compared with non-optical gas sensors, NDIR sensors offer outstanding gas selectivity and accuracy but exhibit remarkable power consumption and have a short battery life.

---

H. T. Miyazaki (✉)

National Institute for Materials Science, 1-2-1 Sengen, Tsukuba, Ibaraki 305-0047, Japan  
e-mail: [MIYAZAKI.Hideki@nims.go.jp](mailto:MIYAZAKI.Hideki@nims.go.jp)

Conventional NDIR sensors employ blackbody thermal emitters such as microbulbs. Nonlinear optics, which are widely used for obtaining mid-infrared radiation in laboratories, require large-scale systems. Light-emitting diodes for mid-infrared wavelengths can generate low output. There has recently been remarkable progress related to quantum cascade lasers, but these are still expensive and not yet widely used. For these reasons, thermal emitters are currently the only choice as light sources for NDIR sensors. However, only a very small portion of the radiation selected from the broadband output by two narrow-band filters is utilized; most radiation is discarded. Thus, the NDIR technique is fundamentally energy inefficient when conventional thermal emitters are used.

### ***5.1.2 Thermal Emission Engineering***

Thermal emission has been recognized in the past few decades as engineerable by using nanostructured surfaces made of plasmonic or phononic materials [2–8]. Interest in controlled thermal emission in the context of metamaterials has further increased since the first demonstration of a perfect metamaterial absorber [9]. Recent plasmonic thermal emitters are mostly based on stacked metal/insulator/metal (MIM) cavities. At first, stacked MIM structures on a plane were utilized as magnetic atoms that constitute metamaterials [10, 11]. These were later recognized as manufacturable cavities that exhibit controlled and strong interactions with vertically incident light [12]. There are also reports of thermal emission from metal patches [13] and stripes [14] on insulator/metal substrates. The emission properties of these structures are dominated by subwavelength-sized MIM cavities or antennas arrayed with a period shorter than the wavelength. They can therefore be called metamaterial surfaces or metasurfaces.

### ***5.1.3 Toward Engineered Thermal Emitters for CO<sub>2</sub> Sensing***

The development of emitters for NDIR sensing of a specific gas is quite limited [15]. For practical applications, perfect blackbody radiation that peaks at two exact wavelengths and insensitivity to polarization and angle are crucial. Some of these properties have been demonstrated in the past several years, during which dual-band metasurfaces based on rectangular patches [16], patchworks of different cavities [17–19], or stacked cavities [20] have been realized. Polarization independence has been achieved by combining orthogonal elements [21–23]. Although most of these works showed only engineered absorption, some actually demonstrated multi-wavelength thermal emission [16, 17].

Another problem is fabrication. Conventional metasurface thermal emitters are fabricated by electron-beam lithography, which has low throughput and is imprac-

tical for industrial mass production. In addition, the emitter is incompatible with conventional optoelectronic devices.

In this section, we introduce metasurface thermal emitters that generate polarization- and angle-independent nearly perfect blackbody emission at two wavelengths necessary for CO<sub>2</sub> sensing through alternate arrangement of orthogonal rectangular patches [24, 25]. The metasurface is integrated on a membrane heater, and the infrared waves are produced by applying voltage. The thermal emitters are manufactured by a cost-effective, mass-producible ultraviolet (UV) nanoimprint lithography (NIL) technique. The use of an organic-solvent-soluble UV resist enables simple fabrication by a single-layer lift-off process. Moreover, the emitter chips mounted in standard packages are completed and used for CO<sub>2</sub> concentration measurement. These results demonstrate that commercialization of metasurface infrared thermal emitters is now becoming a reality.

## 5.2 Design

### 5.2.1 Metasurface

The target wavelengths are 4.26 and 3.95 μm (referred to as  $\lambda_1$  and  $\lambda_2$ , respectively) according to the standard dual-band detectors for CO<sub>2</sub> sensors [1]. The 4.26 μm wavelength is absorbed by CO<sub>2</sub> molecules, while 3.95 μm is not absorbed and can therefore be used as a reference signal. By arraying rectangular metal patches with a size of  $L_1 \times L_2$  while alternating the direction with period  $P$  on a dielectric film with thickness  $T$  and refractive index  $n$  (Fig. 5.1a), we attempted to find an optimum design that provides perfect blackbody emission (perfect absorption [26]) without polarization and angle dependence. We use Au as the metal, and for the dielectric we use Al<sub>2</sub>O<sub>3</sub>, which exhibits low loss around 4 μm and can be deposited with a high thickness precision by atomic layer deposition (ALD).

The resonance wavelengths are mainly determined by  $n$ ,  $T$ ,  $L_1$ , and  $L_2$ .  $P$  affects the height of the emittance peaks. The effective refractive index of a MIM waveguide is given as  $n_{eff} \approx n(1 + 2\delta/T)^{1/2}$  [13, 27, 28], where  $\delta$  is the skin depth of Au. Therefore, the length of the cavity for the resonant wavelength of  $\lambda_0$  is determined as  $L \approx \lambda_0/(2n_{eff}) \approx \lambda_0/\{2n(1 + 2\delta/T)^{1/2}\}$ . For small  $T$  values,  $L_1$ ,  $L_2$ , and optimal  $P$  are short, thereby resulting in a deep subwavelength, angle-independent structure. However, the quality factor  $Q$  is low, because the fields mainly stay in lossy Au clads [29], producing excessive unnecessary radiation. By contrast, a higher  $Q$  is achievable for larger  $T$  values, but the optimum  $P$  has a close value as  $\lambda_1$  and  $\lambda_2$ , and angle dependence due to diffraction emerges.

The thicknesses of the top Au patches and Al<sub>2</sub>O<sub>3</sub> film ( $T$ ) were set at 100 nm and 50 nm, respectively. As a result of maximizing emittance (absorptance) at  $\lambda_1$  and  $\lambda_2$  while minimizing emittance at other wavelengths, we found a set of values ( $T = 50$  nm,  $L_1 = 930$  nm,  $L_2 = 850$  nm, and  $P = 1.5$  μm) that exhibit a maximum

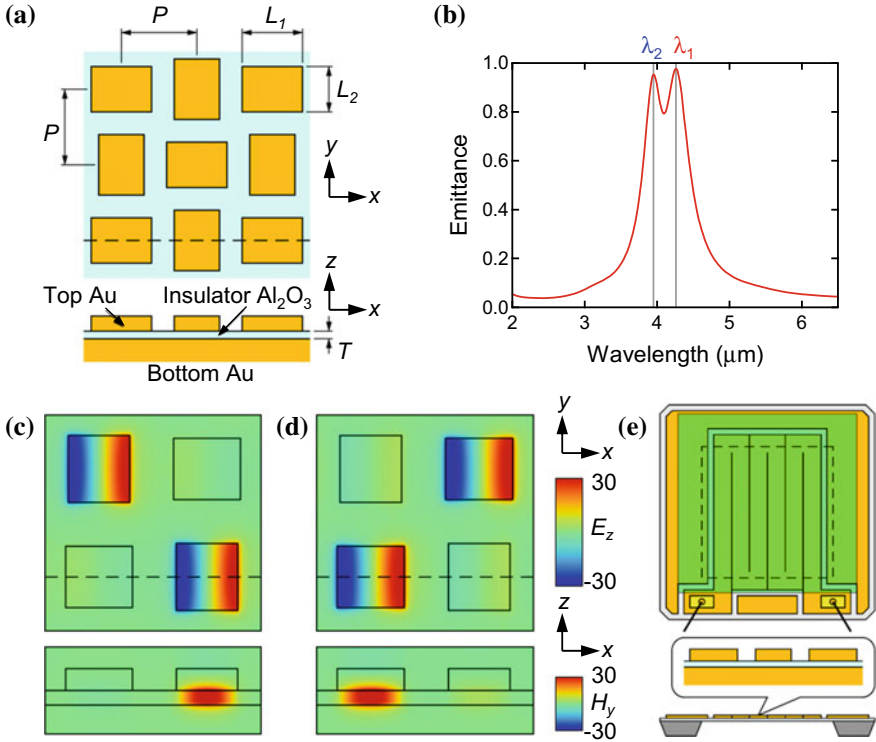


**Fig. 5.1** **a** Top view of the dual-band metasurface thermal emitter (upper) and the cross section along the dashed line (lower). **b** Emittance spectrum ( $x$  polarization,  $z$  direction) calculated for the optimum design, which is identical for  $y$  polarization. **c**, **d** Electromagnetic fields at  $\lambda_2$  and  $\lambda_1$ , respectively ( $x$  polarization,  $z$  direction). Upper:  $E_z$ ; lower:  $H_y$  after  $90^\circ$  phase rotation along the dashed lines. Although these fields are calculated for vertical incidence, the same fields are thermally excited and  $x$ -polarized emission is generated when the metasurface is heated. **e** Upper: top view of the emitter chip. The metasurface pattern shown in **(a)** is fabricated in the green area. Dashed lines show the border of the thin membrane. Lower: a cross section

emittance of 0.98, as shown in Fig. 5.1b. The resonant modes for  $\lambda_1$  and  $\lambda_2$  are displayed in Fig. 5.1c, d, respectively. At each wavelength, a standing wave of the first-order guided mode of the MIM structure is formed along the corresponding side. The field is localized mainly in the lossless  $\text{Al}_2\text{O}_3$ , thereby obtaining a relatively sharp resonance ( $Q \sim 11$ ). This system is invariant to  $90^\circ$  rotations around the  $z$ -axis, making the proposed emitter polarization independent.

The spectra and electromagnetic fields in this study are calculated by rigorous coupled-wave analysis and finite difference time-domain methods, respectively (Synopsys, RSoft CAD). Reported values are used for the dielectric constant of Au [30]. The refractive index of  $\text{Al}_2\text{O}_3$  is set at 1.52 [24, 25, 31].

## 5.2.2 *Integrated Emitter*

To heat only the emission area while keeping the substrate near room temperature, the metasurface is fabricated on a meander Joule heater made of Au supported on a thin membrane. Figure 5.1e shows the overall structure. This Joule heater also serves as the bottom Au layer of the metasurface. The emitter chip is a 3.4 mm square, which is suitable for standard packages. The central 2.1 mm square area of the substrate is made of a 500-nm-thick amorphous SiN membrane to achieve thermal isolation and minimize thermal mass. The blank space outside the heater is also covered with Au. This is necessary for precise NIL patterning (discussed later in 5.4.4). The metasurface shown in Fig. 5.1a is formed in the central 2.0 mm square area.

## 5.3 Nanoimprint Lithography

### 5.3.1 *Fundamentals*

Metamaterials in optical frequencies consist of elements that are smaller than the optical wavelength. Photolithography-based fabrication is thus impractical, possible only through use of a state-of-the-art, large-scale stepper for memory chips. Conventionally, optical metamaterials were demonstrated using electron-beam lithography or focused ion-beam techniques. However, their low throughput and high cost make them impractical for mass production. Thus, NIL is considered an ideal solution for creating optical metamaterials. The NIL technique produces resist patterns based on mechanical transfer from a nanostructured mold. Instant patterning over a large area without the restriction of optical wavelengths is possible [32].

Figure 5.2 shows the basic flow of NIL techniques, which are roughly classified into two types: thermal NIL and UV-NIL. In the thermal NIL process (Fig. 5.2a), a mold is pressed against a thermoplastic polymer film coated on a substrate under heat, transferring the pattern. The system is then cooled, and the mold is released [33]. In the UV-NIL process (Fig. 5.2b), a UV-transparent mold, usually made of quartz, is pressed against a UV-curable polymer film on a substrate, irradiated by UV light, and then released [34]. In both cases, a residual resist film is present on the bottom, and the substrate is not exposed. This residual layer is removed by dry etching until the substrate is exposed. In this way, nanostructured resist patterns equivalent to those by electron-beam exposure and subsequent development are formed. The following processes are the same as in conventional electron-beam lithography. Thermal NIL requires time to raise and lower the temperature of the mold and specimen. By contrast, UV-NIL is a room-temperature process with higher throughput.

There are two options for lithography-based metal patterning: dry etching or a lift-off process (Fig. 5.3). In dry etching (Fig. 5.3a), a metal film is deposited on the substrate, on which the resist mask pattern forms. Directional dry etching is then



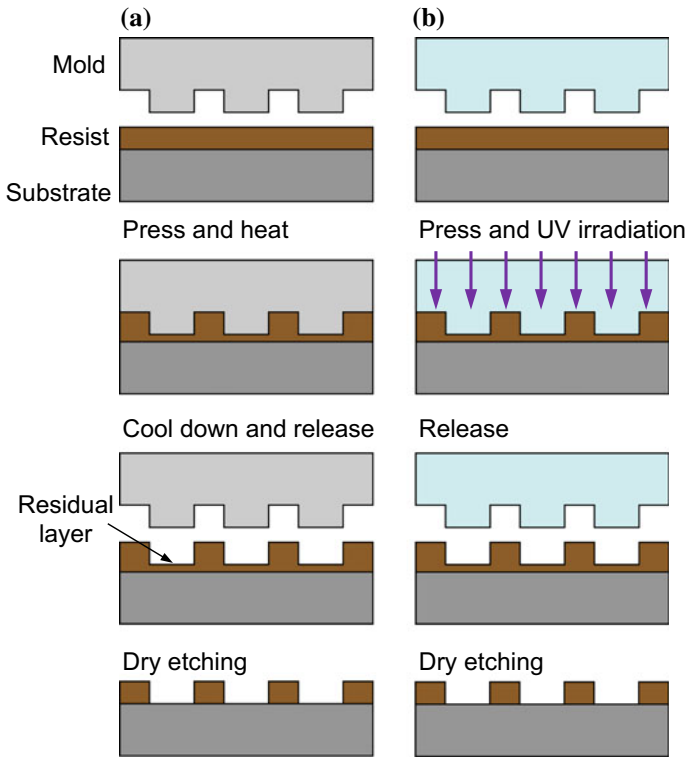


**Fig. 5.2** Schematic of the NIL process. **a** Thermal and **b** UV-NIL techniques

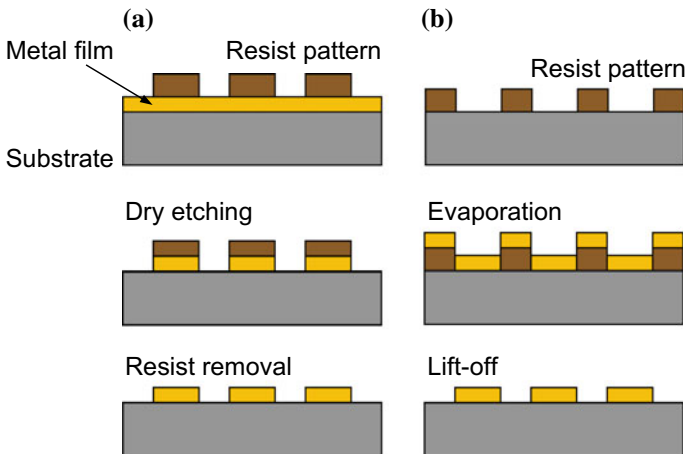


**Fig. 5.3** Lithography-based fabrication of metallic patterns. **a** Dry etching and **b** lift-off processes

applied until metal film on the unmasked region is perfectly removed. Metal patterns are completed by removing the resist. In the lift-off process (Fig. 5.3b), a resist pattern is first formed on the substrate, onto which a metal film is evaporated. Finally, the metal on the resist is removed by dissolving in an organic solvent. The dry etching process requires accurate control of the etched depth, care in re-deposition of the etched materials, and degradation of the mask. The lift-off process is therefore much simpler and more reliable, thereby making it suitable for mass production.

### 5.3.2 *UV-NIL Followed by Lift-off*

However, UV-NIL has been incompatible with lift-off processes. Resist materials for thermal NIL can be used for both dry etching and lift-off. The first NIL was accomplished by a combination of thermal NIL and lift-off, demonstrating the excellent applicability of the NIL [33]. Nonetheless, UV resins for UV-NIL generally do not dissolve in organic solvents after photocuring, because of crosslinks initiated by the UV irradiation, meaning that lift-off is not applicable.

Lift-off processes for UV-NIL were conventionally realized by a bilayer resist technique, which uses a soluble underlayer and two-step dry etching [35]. However, this complicated process diminishes the advantages of lift-off techniques. Here, we employ a recently developed organic-solvent-soluble UV resist [36]. Lift-off with a single-layer resist is enabled by this new UV resist, retaining the advantage of a simple lift-off process.

## 5.4 Fabrication

### 5.4.1 *Preparation of Heater Substrate*

Figure 5.4 shows the fabrication process of the metasurface thermal emitter. Both sides of a Si substrate with size of 30 mm square and thickness 0.38 mm are coated with a 500-nm-thick amorphous SiN film. The SiN is Si-rich to provide suitable tensile stress. Thirty-six emitter chips with size 3.4 mm square are arranged in a  $6 \times 6$  matrix on this substrate. First, SiN windows for the membranes and cutting slots are formed on the back of the substrate (Fig. 5.4a). After depositing the first 50-nm-thick  $\text{Al}_2\text{O}_3$  film with ALD, meander Joule heater patterns made of Ti (50 nm), Pt (50 nm), and Au (100 nm) are patterned. The  $\text{Al}_2\text{O}_3$  and Pt are barrier layers for preventing the diffusion of Si atoms into Au [37], and the Ti layer is the adhesion layer of Pt and  $\text{Al}_2\text{O}_3$ . The second  $\text{Al}_2\text{O}_3$  layer is then deposited for the metasurface insulator layer (Fig. 5.4b).

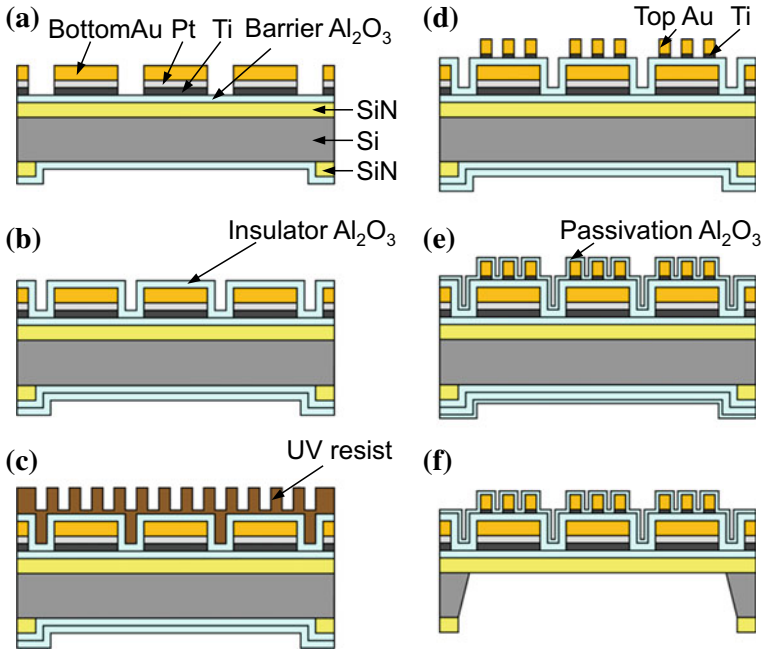


**Fig. 5.4** Fabrication process for the metasurface thermal emitter. **a** SiN windows are formed on the back, the  $\text{Al}_2\text{O}_3$  layer for the diffusion barrier is deposited, and the Joule heater made of Ti, Pt, and Au films is patterned. **b** The second  $\text{Al}_2\text{O}_3$  layer for the insulator of the MIM structure with thickness  $T$  is deposited. **c** The organic-solvent-soluble UV resist is coated and then UV-NIL is processed. **d** The residual resist is dry-etched, and the adhesion Ti and top Au layers are evaporated and lifted off. **e** The third  $\text{Al}_2\text{O}_3$  layer with a precise thickness is deposited for passivation and peak wavelength control. **f** Anisotropic etching with KOH is applied to the Si substrate from the back, and the membrane and cutting slots are formed. Reprinted from [25]. Copyright 2015, National Institute for Materials Science

#### 5.4.2 Metasurface Patterning by UV-NIL

We used a micropattern imprinting machine (ST50, Toshiba Machine) for UV-NIL [38, 39]. A quartz mold (30 mm square, 1 mm thick) with 250-nm-high rectangular mesas corresponding to the Au patches was prepared using electron-beam lithography and dry etching. After cleaning with piranha solution and vacuum UV light [40], the mold is coated with a release agent (SAMLAY-A, Nippon Soda). An organic-solvent-soluble UV resist (NIAC705, Daicel) is coated and prebaked on the heater side of the substrate. The resist thickness is approximately 250 nm. The mold and the substrate are manually positioned with a precision of approximately  $\pm 250 \mu\text{m}$ . The mold is pressed against the substrate at a pressure of 1.8 MPa for 5 min, irradiated with UV light (365 nm) with a power density of  $37 \text{ mW}/\text{cm}^2$  for 10 s and  $33 \text{ mW}/\text{cm}^2$  for 60 s, and post-baked (Fig. 5.4c). Afterward, a residual resist layer with thickness 10–20 nm at the bottom is removed by reactive ion etching with  $\text{O}_2$  and  $\text{N}_2$  gases

until the insulator  $\text{Al}_2\text{O}_3$  layer on the heater is exposed. Then, adhesion Ti and top Au layers with thicknesses of 3 nm and 100 nm, respectively, are evaporated and lifted off with N-methyl-2-pyrrolidone (Fig. 5.4d).

### 5.4.3 Post-processing

The third  $\text{Al}_2\text{O}_3$  layer is deposited by ALD for surface passivation (Fig. 5.4e). The back is then etched with KOH (Fig. 5.4f). The substrate is attached to a special holder for one-sided etching, and the membrane and cutting slots are fabricated by anisotropic etching of Si with KOH (8 mol/L, 82–88 °C) [41]. Finally, the chips are separated, mounted on a stem, wire bonded with 25- $\mu\text{m}$ -thick Al wires, and encapsulated with a cap.

### 5.4.4 Precise Wavelength Tuning

In NIL, fabricated patterns cannot be modified after the mold is prepared. The top rectangular Au patches actually fabricated using the mold prepared for realizing the designed dimensions in Fig. 5.1a are larger than expected. However, the optical properties of the MIM structures can be tuned by other parameters. First, through variations in the thickness of the metasurface insulator layer  $T$ , the resonance wavelength can be varied by changing the wavelength of the surface plasmon mode [42], with thicker layers leading to shorter wavelengths. The resonance wavelength is also affected by the thickness of the passivation layer, with thicker layers leading to longer wavelengths [43]. Shorter wavelengths are first realized through a thicker insulator layer, then adjusted through thickness of the passivation layer with a precision of 0.1 nm.

Uniformity of pattern dimensions is crucial. Stacking of multiple patterns is indispensable in most realistic devices, like our heater-integrated metasurface emitters. However, there have been few reports describing NIL on pre-patterned substrates [44]. At first, the resonance wavelengths of the metasurface were not uniform across the heater due to deformation of the substrate during the NIL [33] resulting from the height difference between the heater pattern and the blank area. We therefore adjusted the surface levels by coating the blank area outside the heater pattern with Ti, Pt, and Au layers (Fig. 5.1e). Optical uniformity drastically improved as a result [25].

We set the thickness of the insulator  $\text{Al}_2\text{O}_3$  layer as  $T = 81$  nm to obtain slightly shorter wavelengths than the target values. We then measured the absorption spectrum and precisely determined the passivation  $\text{Al}_2\text{O}_3$  layer thickness [25].

### 5.4.5 Fabrication Results

Figure 5.5 shows a chip during the process and the completed emitters. Figure 5.5b shows scanning electron micrographs of the metasurface. After the KOH etching (Fig. 5.5d), the bridges at the four corners are broken to separate the chips. The chip is mounted on a TO-5<sup>1</sup> stem, wire bonded, and encapsulated with a cap (Fig. 5.5e). The window is a 0.25-mm-thick sapphire plate with a high transparency up to a

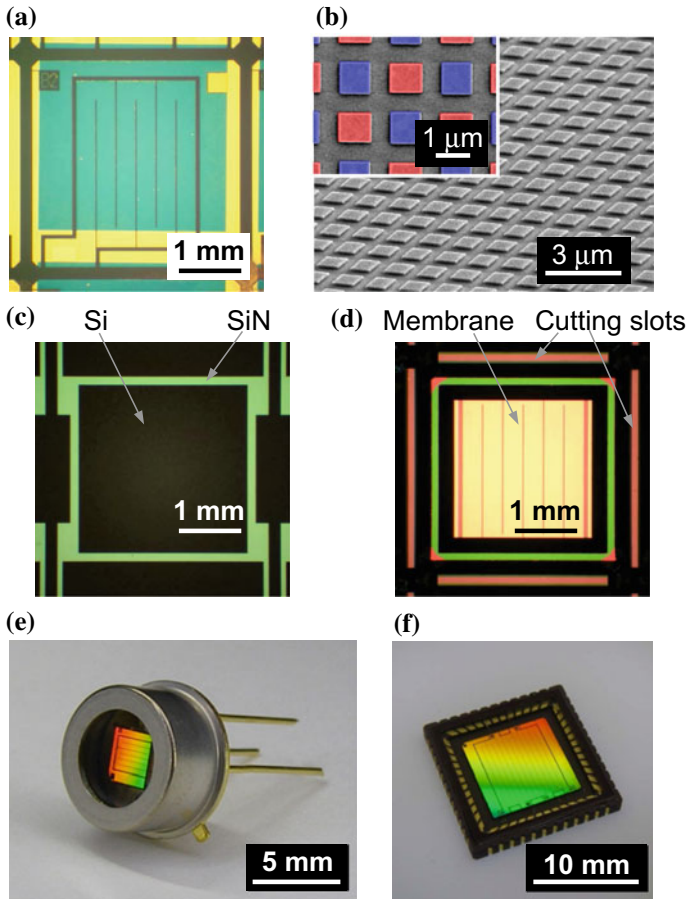


**Fig. 5.5** Emitters during the process. **a** After patterning of the top Au layer. **b** Scanning electron micrograph of the metasurface, seen from an oblique direction. Inset: vertical view. Horizontally (red) and vertically (blue) long rectangles. **c** Backside of the Si substrate before and **d** after the KOH anisotropic etching. The back of the Joule heater pattern can be seen at the center square area of **(d)**. Cutting slots are formed along the four sides of the frame, and the four bridges at the corners support the chip. **e** Completed metasurface emitter in a TO-5 package, and **f** a C-QFN (LCC) package

<sup>1</sup>TO: Transistor Outline.

wavelength of 6  $\mu\text{m}$ . The Joule heater resistance is 18  $\Omega$  at room temperature. The NIL technique is advantageous to producing a large device with high throughput. In this study, we also prepared a mold for 10 mm square areas and demonstrated large emitters with a C-QFN (LCC)<sup>2</sup> package with a 0.30-mm-thick sapphire window (Fig. 5.5f). According to Planck's law, thermally emitted power is proportional to the area. A large emitter is therefore necessary for generating large optical power.

## 5.5 Optical Properties

### 5.5.1 Emission Spectra at Various Temperatures

Figure 5.6 shows properties of the TO-5 metasurface emitter in Fig. 5.5e. Figure 5.6a displays the emission spectra at various voltages observed with a Fourier transform infrared spectrometer (JASCO, FT/IR-6200). At the maximum voltage of 1.30 V, the temperature is 305 °C. Figure 5.6a also shows the emission power of a blackbody emitter at the same temperature. This emitter is equivalent to the metasurface emitter, in which a blackbody paint (TASCO, THI-1B, emittance: 0.94, thickness: 2–5  $\mu\text{m}$ ) is coated on the Joule heater instead of the metasurface (similarly assembled in a TO-5 package). These emitters are placed in a vacuum (0.2 Pa) to remove thermal loss due to air convection. The temperatures of the emitter surfaces at each voltage were determined by comparison of their emission spectra with equivalent emitters mounted on a temperature-controlled substrate. Figure 5.6a shows that the metasurface emitter generates the same radiation intensity at the two wavelengths as a conventional blackbody emitter at a lower voltage (lower power) while drastically suppressing unnecessary emissions. The reference blackbody required 1.53 V to reach the same temperature.

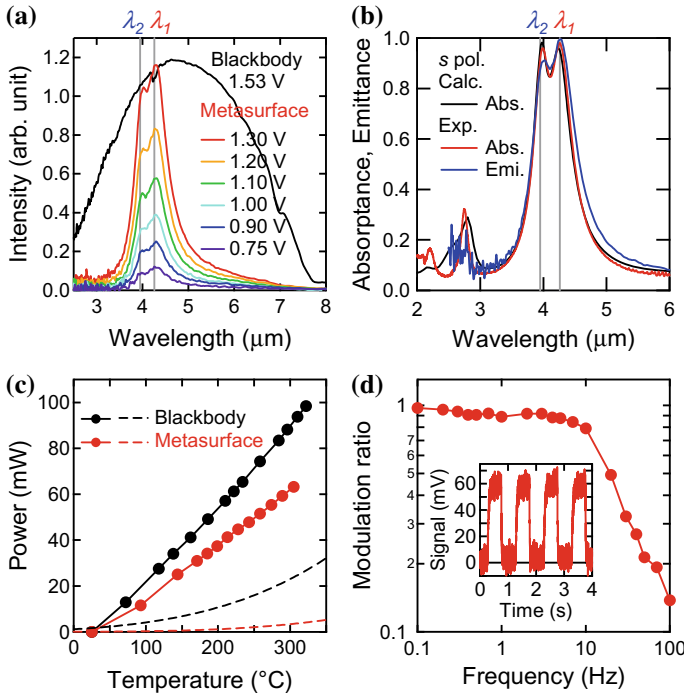
### 5.5.2 Absorptance Versus Emittance

Figure 5.6b shows the absorptance of the metasurface as determined by reflection measurements and the corresponding calculation results. Excellent agreement between the experiment and the calculation, and the equivalence of emittance and absorptance are demonstrated. The maximum emittance is as high as 0.98, close to the perfect blackbody limit. The emittance spectra at different temperatures are almost identical.

We also measured the emission spectra in various directions for both polarizations and found that our emitter has negligible angle and polarization dependence. The results also agreed well with calculations [24]. Therefore, the areal integration of the

---

<sup>2</sup>C-QFN: Ceramic Quad Flat No Lead Package. LCC: Ceramic Leadless Chip Carrier.



**Fig. 5.6** **a** Emission spectra of the metasurface thermal emitter at various voltages (color) and those for an equivalent blackbody (black, the same  $305^{\circ}\text{C}$  temperature as the metasurface at 1.30 V). **b** Experimental absorbance (red) and emittance spectra (blue) of the metasurface thermal emitter. Calculated absorbance for the actual dimensions (black;  $T = 81$  nm,  $L_1 = 1006$  nm,  $L_2 = 915$  nm, and  $P = 1.50$   $\mu\text{m}$ ) is also displayed. **c** Relationship between electrical power and temperature for the metasurface (red) and blackbody emitters (black). Dashed lines show the estimated emission powers. **d** Relationship between the modulation ratio at  $\lambda_1$  and the frequency. In this measurement, the maximum temperature is  $300^{\circ}\text{C}$  at  $f = 1.0$  Hz (duty ratio: 50%). The inset shows the raw signal at  $f = 1.0$  Hz

spectra in Fig. 5.6a straightforwardly indicates the total emission power for both the metasurface and blackbody emitters.

### 5.5.3 Power Reduction

Figure 5.6c shows the relationship between the electrical power and the temperature of the emitters. To achieve the same temperature, the blackbody requires higher power compared with the metasurface emitter; using a metasurface emitter reduces the required power by 31%. Figure 5.6c also displays as dashed lines the emission power calculated from Planck's law. The reduced input power is consistent with the estimated decrease in emission power. We estimate the emission power from the



metasurface at 300 °C to be 3.4 mW, so most of the electrical power (59 mW) is not used for radiation, but instead dissipated by conduction from the membrane to the frame. In this study, the membrane is designed to be excessively rigid due to fears of fracture. In previous studies by other researchers, conduction loss reductions as low as 15 mW [45] or even below 1 mW have been reported [46]. Similar optimization of membrane design should drastically reduce conduction loss, remarkably improving power saving factors against the blackbody emitter.

### 5.5.4 Frequency Response

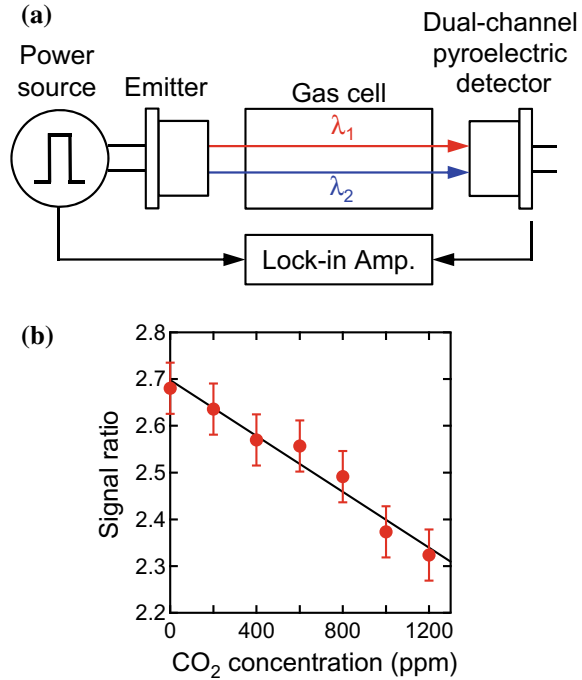
In CO<sub>2</sub> sensors, the transmitted infrared power is detected with high sensitivity by modulating the emitter power. Figure 5.6d presents the relationship between the modulation frequency  $f$  and the modulation ratio at  $\lambda_1$  of the metasurface emitter. The signal is recorded with a HgCdTe infrared photodetector (VIGO, PVI-2TE-10.6; cut-off frequency: 300 kHz) combined with a bandpass filter (center: 4.26  $\mu\text{m}$ ; width: 0.18  $\mu\text{m}$ ). The modulation ratio is defined as  $(I_{max} - I_{min})/(I_{max} + I_{min})$ , where  $I_{max}$  and  $I_{min}$  are the maximum and minimum signal of the photodetector, respectively. The inset shows the raw signal at  $f = 1$  Hz. The cut-off frequency at  $-3$  dB is  $f = 20$  Hz. This modulation speed is sufficient for CO<sub>2</sub> sensors.

However, this result simultaneously suggests a serious limitation of thermal emitters: Minimizing conduction loss restricts the heat escape channel, diminishing the modulation speed. Consequently, there is a trade-off between power efficiency and frequency response. To overcome this limit, we must incorporate a modulation mechanism other than direct temperature control. Recently, high-frequency electrical modulation of thermal emission has been demonstrated in a photonic crystal thermal emitter based on inter-subband transitions [47]. Dynamic control of emittance has also been shown in metasurface thermal emitters [48].

### 5.5.5 Application to CO<sub>2</sub> Sensing

We constructed a CO<sub>2</sub> NDIR sensor employing the developed TO-5-packaged metasurface emitter (Fig. 5.7a). This sensor features a dual-channel pyroelectric detector (InfraTec, LIM-222-DH) for CO<sub>2</sub> sensors, in which two filters centered at 4.26 and 3.95  $\mu\text{m}$  with bandwidths of 0.18 and 0.09  $\mu\text{m}$ , respectively, are attached in front. A gas cell is sandwiched between the emitter and the detector. The path length is 61 mm, which is a typical value for CO<sub>2</sub> sensors. The gas cell is first filled with N<sub>2</sub> gas at 1 atm, and we change the CO<sub>2</sub> concentration by adding CO<sub>2</sub> gas. For optical chopping, the input voltage is directly modulated with the waveform in the inset of Fig. 5.6d. The poor signal-to-noise ratio shown by the error bars is due to the absence of optics to enhance efficiency. The signal ratio of  $\lambda_1$  to  $\lambda_2$  linearly decreases as CO<sub>2</sub> gas is added (Fig. 5.7b). The signal change is  $-4.4\%$  at 400 ppm (typical atmospheric air).

**Fig. 5.7** **a** Configuration of the CO<sub>2</sub> NDIR sensor. **b** Relationship between the signal ratio of  $\lambda_1$  to  $\lambda_2$  and the CO<sub>2</sub> concentration. The error bars show standard deviations



This result clearly reveals that our mass-producible dual-band metasurface emitter is readily applied to CO<sub>2</sub> sensing.

## 5.6 Summary

In summary, we demonstrated metasurface infrared thermal emitters that are mass-producible and nearly ready for commercialization. We manufactured dual-band, polarization- and angle-independent metasurface thermal emitters integrated with a membrane Joule heater tailored for CO<sub>2</sub> sensors by a UV-NIL combined with a single-layer lift-off process. The use of an organic-solvent-soluble UV resist was key to developing a simple, practical fabrication process. Furthermore, we realized hermetically encapsulated emitters in a package form compatible with conventional optoelectronic devices and used these for monitoring CO<sub>2</sub> concentrations. Although thermal loss must be further reduced by improving the membrane design, our metasurface infrared thermal emitters are close to commercialization. The emitter can be easily applied to a different gas by changing the cavity lengths. In particular, using this emitter in CO sensors, which presently depend on non-optical methods with low reliability, would realize a battery-powered, highly selective sensor for preventing fatal CO poisoning accidents.

## References

1. J. Hodgkinson, R.P. Tatam, *Meas. Sci. Technol.* **24**, 012004 (2013)
2. P.J. Hesketh, J.N. Zemel, B. Gebhart, *Nature* **324**, 549 (1986)
3. S. Maruyama, T. Kashiwa, H. Yugami, M. Esashi, *Appl. Phys. Lett.* **79**, 1393 (2001)
4. J.-J. Greffet, R. Carminati, K. Joulain, J.-P. Mulet, S. Mainguy, Y. Chen, *Nature* **416**, 61 (2002)
5. F. Kusunoki, J. Takahara, T. Kobayashi, *Electron. Lett.* **39**, 23 (2003)
6. S.Y. Lin, J. Moreno, J.G. Fleming, *Appl. Phys. Lett.* **83**, 380 (2003)
7. M.-W. Tsai, T.-H. Chuang, C.-Y. Meng, Y.-T. Chang, S.-C. Lee, *Appl. Phys. Lett.* **89**, 173116 (2006)
8. K. Ikeda, H.T. Miyazaki, T. Kasaya, K. Yamamoto, Y. Inoue, K. Fujimura, T. Kanakugi, M. Okada, K. Hatada, S. Kitagawa, *Appl. Phys. Lett.* **92**, 021117 (2008)
9. N.I. Landy, S. Sajuyigbe, J.J. Mock, D.R. Smith, W.J. Padilla, *Phys. Rev. Lett.* **100**, 207402 (2008)
10. G. Dolling, C. Enkrich, M. Wegener, J.F. Zhou, C.M. Soukoulis, S. Linden, *Opt. Lett.* **30**, 3198 (2005)
11. V.M. Shalaev, W. Cai, U.K. Chettiar, H.-K. Yuan, A.K. Sarychev, V.P. Drachev, A.V. Kildishev, *Opt. Lett.* **30**, 3356 (2005)
12. G. Leveque, O.J.F. Martin, *Opt. Lett.* **31**, 2750 (2006)
13. I. Puscasu, W.L. Schaich, *Appl. Phys. Lett.* **92**, 233102 (2008)
14. Y.-H. Ye, Y.-W. Jiang, M.-W. Tsai, Y.-T. Chang, C.-Y. Chen, D.-C. Tzuang, Y.-T. Wu, S.-C. Lee, *Appl. Phys. Lett.* **93**, 033113 (2008)
15. K. Masuno, T. Sawada, S. Kumagai, M. Sasaki, *IEEE Photon. Technol. Lett.* **23**, 1661 (2011)
16. P.E. Chang, Y.W. Jiang, H.H. Chen, Y.T. Chang, Y.T. Wu, L.D.C. Tzuang, Y.H. Ye, S.C. Lee, *Appl. Phys. Lett.* **98**, 073111 (2011)
17. X. Liu, T. Tyler, T. Starr, A.F. Starr, N.M. Jokerst, W.J. Padilla, *Phys. Rev. Lett.* **107**, 045901 (2011)
18. J. Hendrickson, J. Guo, B. Zhang, W. Buchwald, R. Soref, *Opt. Lett.* **37**, 371 (2012)
19. P. Bouchon, C. Koechlin, F. Pardo, R. Haidar, J.-L. Pelouard, *Opt. Lett.* **37**, 1038 (2012)
20. J. Wang, C. Fan, P. Ding, J. He, Y. Cheng, W. Hu, G. Cai, E. Liang, Q. Xue, *Opt. Express* **20**, 14871 (2012)
21. Z.H. Jiang, S. Yun, F. Toor, D.H. Werner, T.S. Mayer, *ACS Nano* **5**, 4641 (2011)
22. K.B. Alici, A.B. Turhan, C.M. Soukoulis, E. Ozbay, *Opt. Express* **19**, 14260 (2011)
23. K. Aydin, V.E. Ferry, R.M. Briggs, H.A. Atwater, *Nature Commun.* **2**, 517 (2011)
24. H.T. Miyazaki, T. Kasaya, M. Iwanaga, B. Choi, Y. Sugimoto, K. Sakoda, *Appl. Phys. Lett.* **105**, 121107 (2014)
25. H.T. Miyazaki, T. Kasaya, H. Oosato, Y. Sugimoto, B. Choi, M. Iwanaga, K. Sakoda, *Sci. Technol. Adv. Mater.* **16**, 035005 (2015)
26. J.-J. Greffet, M. Nieto-Vesperinas, *J. Opt. Soc. Am. A* **15**, 2735 (1998)
27. S. Collin, F. Pardo, J.-L. Pelouard, *Opt. Express* **15**, 4310 (2007)
28. J. Le Perchec, Y. Desieres, R. Espiau de Lamaestre, *Appl. Phys. Lett.* **94**, 181104 (2009)
29. Y. Kurokawa, H.T. Miyazaki, *Phys. Rev. B* **75**, 035411 (2007)
30. A.D. Rakic, A.B. Djurisic, J.M. Elazar, M.L. Majewski, *Appl. Opt.* **37**, 5271 (1998)
31. X. Liu, T. Starr, A.F. Starr, W.J. Padilla, *Phys. Rev. Lett.* **104**, 207403 (2010)
32. J. Taniguchi, H. Ito, J. Mizuno, T. Saito (eds.), *Nanoimprint Technology: Nanotransfer for Thermoplastic and Photocurable Polymers* (Wiley, Chichester, 2013)
33. S.Y. Chou, P.R. Krauss, P.J. Renstrom, *Appl. Phys. Lett.* **67**, 3114 (1995)
34. J. Haisma, M. Verheijen, K. van den Heuvel, J. van den Berg, *J. Vac. Sci. Technol. B* **14**, 4124 (1996)
35. M.D. Austin, H. Ge, W. Wu, M. Li, Z. Yu, D. Wasserman, S.A. Lyon, S.Y. Chou, *Appl. Phys. Lett.* **84**, 5299 (2004)
36. T. Nishino, N. Fujii, H. Miyake, T. Yukawa, J. Sakamoto, R. Suzuki, H. Kawata, Y. Hirai, *J. Photopolym. Sci. Technol.* **23**, 87 (2010)

37. A. Hiraki, E. Lugujo, J.W. Mayer, *J. Appl. Phys.* **43**, 3643 (1972)
38. B. Choi, M. Iwanaga, H.T. Miyazaki, K. Sakoda, Y. Sugimoto, *J. Micro/Nanolith. MEMS MOEMS* **13**, 023007 (2014)
39. B. Choi, M. Iwanaga, H.T. Miyazaki, K. Sakoda, Y. Sugimoto, *Appl. Phys. Lett.* **105**, 201106 (2014)
40. M. Nakao, M. Yamaguchi, S. Yabu, *J. Nonlinear Opt. Phys. Mater.* **19**, 773 (2010)
41. M. Elwenspoek, H.V. Jansen, *Silicon Micromachining* (Cambridge University Press, Cambridge, 1998)
42. H.T. Miyazaki, Y. Kurokawa, *Phys. Rev. Lett.* **96**, 097401 (2006)
43. A.V. Whitney, J.W. Elam, S. Zou, A.V. Zinovev, P.C. Stair, G.C. Schatz, R.P. Van Duyne, *J. Phys. Chem. B* **109**, 20522 (2005)
44. S. Kataza, K. Ishibashi, M. Kokubo, H. Goto, J. Mizuno, S. Shoji, *Jpn. J. Appl. Phys.* **48**, 06FH21 (2009)
45. N. Moelders, M.U. Pralle, M.P. McNeal, I. Puscasu, L. Last, W. Ho, A.C. Greenwald, J.T. Daly, E.A. Johnson, T. George, *Mat. Res. Soc. Symp. Proc.* **729**, U5.2 (2002)
46. M. De Zoysa, T. Asano, K. Mochizuki, A. Oskooi, T. Inoue, S. Noda, *Nat. Photon.* **6**, 535 (2012)
47. T. Inoue, M. De Zoysa, T. Asano, S. Noda, *Nat. Mater.* **13**, 928 (2014)
48. X. Liu, W.J. Padilla, *Adv. Opt. Mater.* **1**, 559 (2013)

**Part II**  
**Metamaterials in THz Frequencies**

# Chapter 6

## Birefringent Metamaterials for THz Optics



Masaya Nagai

**Abstract** Terahertz (THz) region is typically referred to as the frequencies from 100 GHz to 30 THz, which lies between the infrared and microwaves. Since the typical wavelength of the THz wave is hundreds micrometer, we can easily fabricate the metallic structure with the size comparable with its wavelength, and the bulky three-dimensional metamaterial is not huge. Recent development of the ultrafast-pulsed laser technique allowed the generation and detection of the THz electromagnetic pulse, which has led to easy characterization of the medium with the time-domain spectroscopy. Therefore, there are many reports on the metamaterials in the THz frequency region. Metamaterials have been used as the practical optics in the THz region. Many materials are not transparent in this frequency region, so the artificial media based on the periodic structures of the metal such as the metal slit array and metal hole array have been developed. In this chapter, we review the recent advances of the metamaterials in the THz frequency region.

### 6.1 THz Optics Based on the Parallel Metal Plate Waveguides

Metamaterials are the artificial media with the controllable refractive index and are attractive for the present optics in the THz frequency region. It is because many materials are not transparent in this frequency region, and we can easily fabricate the metal structures with the size comparable with the wavelength of several hundred micrometers. There are many two-dimensional metasurface, which are used as the THz optics such as the polarizer and band-pass filter.

Recently, a simple THz optics composed of stacked parallel metal plates with a gap distance has been demonstrated. It is a parallel metal plate waveguide (PPWG) ensemble, which is categorized as the simple three-dimensional metamaterial. The PPWG is one of the simplest waveguides, and there are many explanations in the textbook of microwave technologies [1] because its operation is similar to that of

---

M. Nagai (✉)

Graduate School of Engineering Science, Osaka University, Toyonaka 560-8531, Japan  
e-mail: [mnagai@mp.es.osaka-u.ac.jp](mailto:mnagai@mp.es.osaka-u.ac.jp)

© Springer Nature Singapore Pte Ltd. 2019

K. Sakoda (ed.), *Electromagnetic Metamaterials*, Springer Series  
in Materials Science 287, [https://doi.org/10.1007/978-981-13-8649-7\\_6](https://doi.org/10.1007/978-981-13-8649-7_6)

many other waveguides. The electromagnetic wave propagates in the PPWG as the transverse electric (TE) and the transverse magnetic (TM) modes with the different phase velocities. Thus, a PPWGs ensemble is a birefringent medium, and the frequency-dependent behavior of the PPWG brings in the unique phase optics in wide THz frequency region. It has been applied in various practical THz optics, such as polarizer, novel filter, prisms, and lenses.

In this section, the propagation properties in the waveguide and the application of phase shifter are introduced.

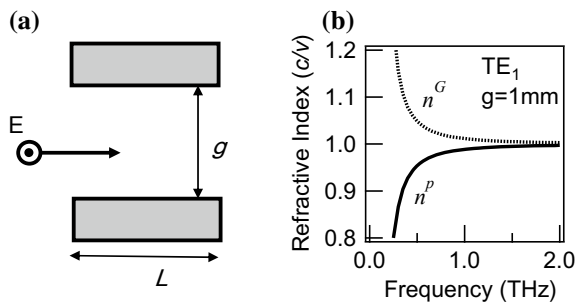
## 6.2 Transverse Electric Waveguide Mode in Parallel Plate Waveguides

In order to understand the PPWG mode, we assume the simple waveguide composed of two flat conducting plates with a gap distance  $g$ , as shown in Fig. 6.1a. When the electromagnetic waves are incident with a polarization parallel to the metal plates, the light propagates as a TE waveguide mode. Above the cut-off frequency  $\nu_c = c/2g$ , its phase velocity is higher than the speed of light in vacuum. According to waveguide theory [1], the phase velocity of the lowest TE<sub>1</sub> mode is faster than the light velocity in the vacuum as

$$v_{TE} = \frac{c}{\sqrt{1 - (\nu_c/\nu)^2}}. \tag{6.1}$$

Solid curve in Fig. 6.1b shows the phase index  $n = c/v_{TE}$  of the TE waveguide mode in the PPWGs with  $g = 1$  mm. The assembly of the waveguides can be considered as the homogeneous medium with the refractive index of  $0 < n < 1$ . While many of the materials in nature have a high refractive index in the THz region, this artificial medium has a refractive index smaller than one. This dispersion is similar to plasma dispersion, where the plasma frequency corresponds to the cut-off frequency  $\nu_c$ . Thus, the dispersion can be easily tuned by adjusting the gap distance  $g$ . In the microwave region, this waveguide concept is useful to demonstrate funda-

**Fig. 6.1** **a** Scheme of TE waveguide mode in PPWGs. **b** Phase index  $n$  and group index  $n^G$  in the PPWGs





mental electromagnetic phenomena in the artificial medium, but they were relatively bulky because of long wavelengths.

In the THz frequency region, its wavelength of this frequency is sub-millimeter, so the accuracy required for compact waveguide is not so high. While the surface impedance increases with the frequency, energy loss of THz waveguide with the several centimeter lengths is negligible. Therefore, various optics based on PPWGs have been demonstrated [2]. A pair of PPWGs allows universal filter that provides low-pass, high-pass, band-pass, and stop band or notch filtering in the THz frequency regime [3]. Prism-shaped PPWGs with constant gap distance allow us to demonstrate the fundamental optical phenomena of internal reflection and Brewster's effect [4]. A concave PPWG-lens exhibit a focus, which is both strongly frequency dependent due to the dispersion [4–6]. Furthermore, effective refractive index is almost zero just above the cut-off frequency, which is attractive in viewpoint of novel epsilon-near-zero optics [5].

The waveguide with varying the plate separation behaves as the medium with gradient index at the given frequency, and the THz wave propagating inside an inhomogeneous dielectric medium will bend toward the high-index region [7]. This concept allows novel fisheye lens in the THz frequency region [8].

### 6.3 Carrier Envelope Phase Control with the Parallel Metal Plate Waveguides

The dispersion of TE waveguide mode causes the following group velocity  $v_g$  in the PPWGs,

$$v_{TE}^g = c\sqrt{1 - (v_c/v)^2}, \quad (6.2)$$

which is slower than the light velocity in vacuum and phase velocity  $v_{TE}$ . The corresponding group index  $n^g = c/v_{TE}^g$  is added as the dashed curve in Fig. 6.1b. This difference causes functional propagation properties of a-few-cycle THz pulse in the medium. Here, we assume the constant group velocity in whole frequency region. When a-few-cycle pulse is incident to this media with the phase velocity different from the group velocity, the carrier envelop phase (CEP) of the propagating pulse changes continuously as it moves forward in the medium maintaining the pulse duration. Figure 6.2 shows its scheme. It is critical in the present extreme nonlinear optics such as high harmonic generation in gases, because the phenomena are strongly dependent of the CEP of the a-few-cycle excitation pulse [9, 10]. Recent development of the laser technique brings in the generation of the intense a-few-cycle phase-locked THz pulse, which has strong electric and magnetic fields for the extreme nonlinear optics [11]. CEP is also fundamental to THz pulses and CEP-locked THz pulse can be easily generated via optical rectification process, but

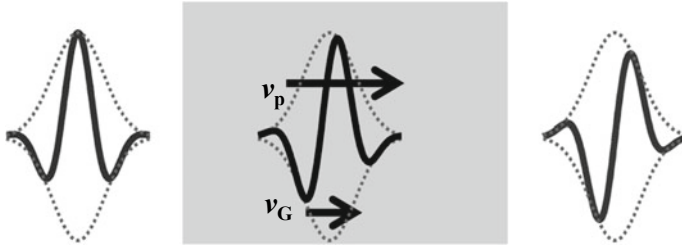


**Fig. 6.2** Scheme of the carrier envelope control in the medium with the dispersion

practical adjusting technique has been missing. Therefore, PPWGs are promising for a simple passive component for controlling the CEP of a-few-cycle THz pulses.

Figure 6.3a shows the temporal electric-field profiles of transmitted THz pulses with the polarization parallel (TE mode; bold) to the metal plates. Tens of  $50 \times 10 \text{ mm}^2$  steel plates were prepared with chemical etching and were aligned with an equal gap distance. This is assumed as the medium with the thickness of  $L = 10 \text{ mm}$ . We define the original electric-field profile with its main peak at the maximum point of the envelope, namely  $E(t) = A(t) \cos(2\pi\nu t)$ , where the envelope function  $A(t)$  also has its maximum at  $t = 0 \text{ ps}$ . The upper in Fig. 6.3b shows the power spectrum of the incident THz pulse with a center frequency of 0.7 THz. The pulse after passing through the medium with  $g = 1 \text{ mm}$  is negatively chirped due to the large group velocity dispersion. This chirp becomes almost negligible for  $g \geq 2 \text{ mm}$ , and the CEP of the pulse slightly shifts to earlier times. Thus, only the CEP of the THz pulse is modulated maintaining other properties. When the gap is  $g = 2 \text{ mm}$ , the pulse profile becomes “sin-like,” which is expressed as  $E(t) = A(t) \sin(2\pi\nu t)$ . The lower in Fig. 6.3b shows the complex transmission coefficients of these media. We add the

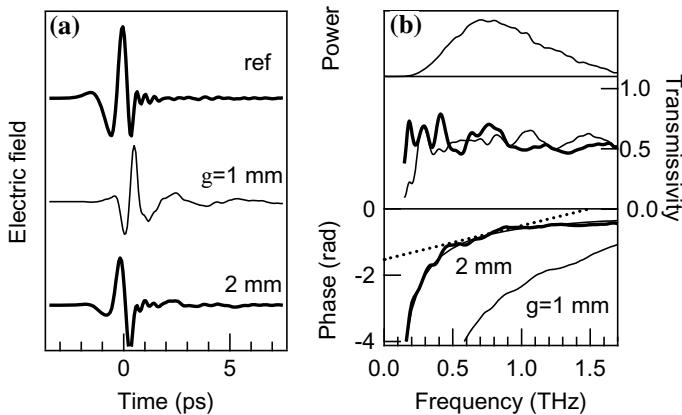


**Fig. 6.3** **a** Temporal electric-field profiles of incident and transmitted THz pulses with the polarization parallel to the metal sheets with  $L = 10 \text{ mm}$ . **b** The upper panel shows the power spectrum of the incident THz pulse. The lower panels show the complex transmission coefficients

theoretical curves of the phase spectra as the following,

$$\phi_{TE} = 2\pi\nu L \left( \frac{1}{v_{TE}} - \frac{1}{c} \right) = \frac{2\pi\nu L}{c} \left( \sqrt{1 - (v_c/\nu)^2} - 1 \right). \quad (6.3)$$

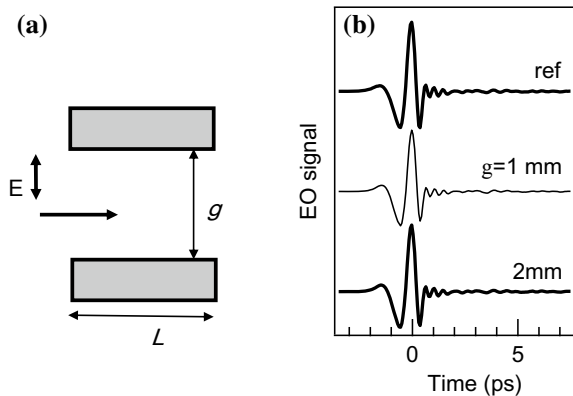
The CEP shift can be denoted as the  $y$ -intersect of the tangent line of the spectral phase at the center frequency of 0.7 THz, and actually is close to  $\pi/2$  for  $g = 2$  mm. The intensity transmission of this optics is 60%. This transmission loss is mainly due to the diffraction.

## 6.4 Transverse Magnetic Waveguide Mode in Parallel Plate Waveguides

Parallel metal plate waveguides are promising as low-loss broadband THz waveguides. When an electromagnetic wave is incident with a polarization perpendicular to the metal plates, light propagates in PPWGs in the TM waveguide mode. Figure 6.4a shows a schematic of this. In the case of plain metal sheet, this is the lowest-order transverse magnetic (TM<sub>0</sub>) mode, which corresponds to the transverse-electromagnetic (TEM) mode in the PPWG. Since the wave of the TEM waveguide mode propagates with the same velocity as the velocity of light in vacuum, we can ignore group velocity dispersion. Figure 6.4b shows the time profiles of incident and transmitted THz pulses with the polarization perpendicular to the metal sheets with  $L = 10$  mm. It indicates the profile of the transmitted THz pulse independent of  $g$ . These waveguides have therefore been developed for applications as low-loss waveguides [12, 13] and are also useful for spectroscopy of small amounts of precious samples in the waveguide [14, 15].

PPWGs are essentially birefringent media owing to the different dispersions of TE and TEM waveguide modes. TEM waves can propagate in PPWGs even below

**Fig. 6.4** **a** Scheme of TM waveguide mode in PPWGs. **b** The temporal electric-field profiles of incident and transmitted THz pulses with the polarization perpendicular to the metal sheets with  $L = 10$  mm



the cut-off frequency of the TE waveguide mode. This structure thus behaves as a polarizer. In the THz frequency region, the wire-grid structure is one of the most common polarizers and is provided by PPWGs. The TE mode transmission power  $T_{TE}$  below the cut-off frequency is given by

$$T_{TE} = \exp\left(-\sqrt{k_c^2 - k^2}L\right), \quad (6.4)$$

where  $k$  is the wavenumber,  $k_c = \pi/d$  is the wavenumber at the cut-off frequency, and  $L$  is the length of the PPWG. In general, the extension ratio of the wire-grid polarizer is very low because  $L$  is small, and so a thicker artificial medium is important for improving the extension ratio. PPWG-based polarizers can be used for cut-through metal slits, and an ideal THz polarizer with a high extinction ratio and transmission power has been demonstrated [16].

## 6.5 Phase Shifter Based on the Parallel Metal Plate Waveguides

An ensemble of PPWGs is an artificial medium with the controllable dispersion above the cut-off frequency of the TE waveguide mode, which can be designed as a phase shifter. Polarization conversion optics is one of the most fundamental optics for the novel application of the electromagnetic wave, and we usually use the quartz phase shifter in the optical frequency region. However, there are few transparent birefringent materials in the THz frequency region, so artificial medium is promising. In the PPWGs, phase difference of the transmitted THz pulse between TE and TM waveguide modes depends on the frequency, so the matching between group velocities of TE and TM waveguide mode is required.

It is well known that the sub-wavelength periodic structures on the metal plate such as the hole array, corrugation, and pillar array modulate TM wave propagation [1, 17]. It brings in the sharp frequency resonance. In the THz frequency region, Bingham et al. fabricated parallel metal plates with a cylindrical hole array and a cylindrical pillar array [18], and clearly showed the existence of a stop band in the TM mode of the parallel metal plate waveguide. Its resonance is determined by the pitch of the structures. Below this resonance frequency  $\nu_0$ , the TM wave propagates slowly [19], and both phase and group velocity of the TM waveguide mode are lower than that in vacuum. It can also be assumed as spoof surface plasmons, which emulate optical frequency surface plasmons on flat metallic surfaces [20, 21].

Assuming that the waveguide ensemble behaves as an effective medium with single Lorentz oscillator with a resonance frequency of  $\nu_0$ , the phase shift for the TM mode is phenomenologically simplified with neglecting the damping as follows:

$$\phi_{TM} = \frac{2\pi \nu L}{c} \left( \sqrt{1 + \frac{A\nu_0^2}{\nu_0^2 - \nu^2}} - 1 \right) \tag{6.5}$$

The dispersion of the TM waveguide mode is shown as the solid curve in Fig. 6.5b with the parameters  $L = 10$  mm,  $\nu_0 = 1.5$  THz, and  $A = 0.0022$ . That of the TE waveguide mode is added as the dashed curve with the cut-off frequency of  $\nu_c = 0.1$  THz. The phase for both TM and TE modes increases with frequency between  $\nu_c$  and  $\nu_0$ . The phase difference between the two modes is added in the lower panel of Fig. 6.5b. There is the minimum of the phase difference at 1.0 THz, and an approximately constant phase shift can be obtained at around 1.0 THz. The periodic structure on the metal plates does not influence the dispersion in the TE waveguide mode because of narrow electric-field distribution at the metal surface. Therefore, it reduces the propagation speed in TM mode without the modulation of the TE waveguide mode.

For the experimental demonstration of PPWG-based phase shifter, three types of the thin steel sheets with the different periodic structures through-hole array [22] or pillar array [23] were rectangularly shaped by the chemical etching, and they were stacked with the same gap distance using commercial metal washers. Figure 6.6 shows the scheme of the PPWGs, and parameters are listed in Table 6.1, where  $p$  and  $a$  are the pitch and the diameters of through-holes/pillars, respectively.  $h$  is the height of the pillars. Since holes or pillars are arranged in a triangular lattice, the resonant frequencies of the structures of PPWGs 1–3 are  $\nu_0 = c/\sqrt{3} p = 3.4, 1.7,$  and  $0.86$  THz. The cut-off frequencies of TE waveguide modes are  $\nu_0 = 0.17, 0.10,$  and

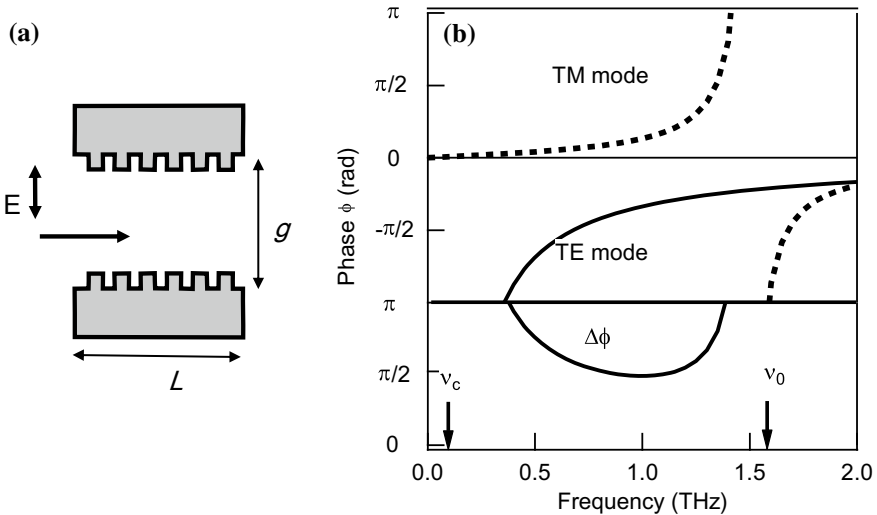


**Fig. 6.5** **a** Scheme of the artificial medium based on the PPWGs with the periodic structures on the metal surface. **b** The dispersion of the TE (solid curves) and TM (dashed curves) waveguide modes in the PPWGs with the periodic structures on the metal surface

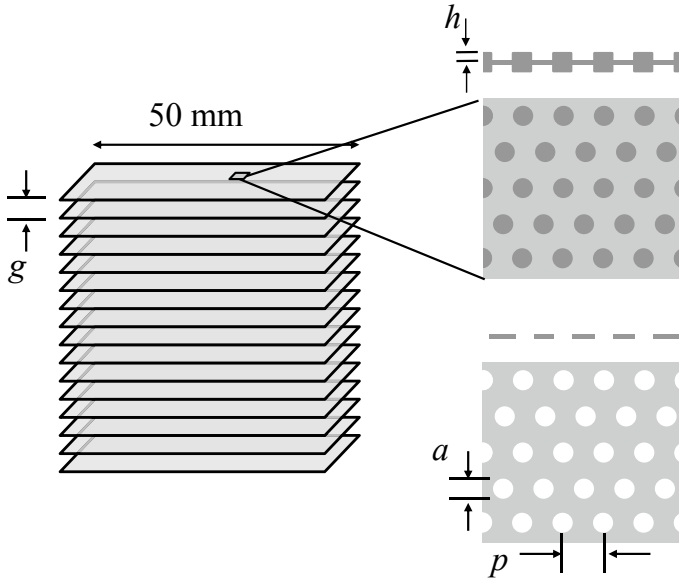


**Fig. 6.6** Scheme of the artificial medium based on the PPWGs

**Table 6.1** Parameters of the PPWGs' assemblies

No.	Size of one sheet (mm)	$g$ (mm)	surface	$p$ ( $\mu\text{m}$ )	$a$ ( $\mu\text{m}$ )	$h$ ( $\mu\text{m}$ )
1	$50 \times 10$	0.9	Pillar	50	20	3.7
2	$50 \times 10$	1.5	Through-hole	100	66	–
3	$50 \times 20$	2.8	Through-hole	200	140	–

0.05 THz, respectively. These frequencies can be tuned by changing the size and pitch of the structures, but PPWGs with pillar array are preferred as a high-frequency phase shifter. It is because thinner metal sheets must be used for maintaining the aspect ratio of the through-hole formed by chemical etching, which causes bending of the metal sheets.

The phase retardation for these PPWGs can also be evaluated with conventional THz time-domain spectroscopy. The transmissivities of these artificial media are around 60%. The upper panel of Fig. 6.7 shows the transmittance of the TM waveguide mode. The resonances appear at  $\nu_0 = 3.4, 1.7,$  and  $0.86$  THz, respectively, below which the velocity of TM waveguide mode becomes slow. The lower panel shows the phase difference  $\Delta\phi$  of the transmitted THz pulses between the polarizations parallel and perpendicular to the metal sheets. For the artificial medium 1–3, the minimums of  $\Delta\phi$  lie at 2.5, 1.0, and 0.5 THz, respectively, and the values of  $\Delta\phi$  were approximately  $\pi/2$  in the vicinity of this frequency. Therefore, these artificial media based

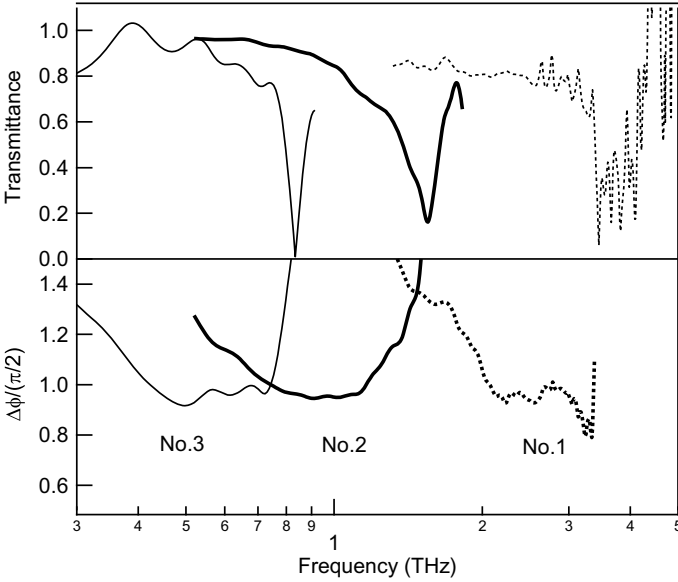


**Fig. 6.7** Upper shows the transmittances of the three PPWG ensembles for the polarization perpendicular to the metal sheets. The lower panel shows the phase difference  $\Delta\phi$  of the transmitted THz pulses between the polarizations parallel and perpendicular to the metal sheets

on the stacked parallel metal plates with structures function as achromatic quarter wave plates over an arbitrary frequency range.

Various polarization conversion optics have been demonstrated, which are based on the metasurface [24, 25]. They have wide available bandwidth, low dephasing, and high conversion. However, PPWG-based phase shifters are essentially birefringent media without the chirality, and they promise the same performance of the polarization conversions from the linear polarization to the circular polarization and vice versa. A circularly polarized THz pulses converted from linearly polarized THz wave with a  $\delta = \pi/2$ -phase shifter are reflected by some reflector. It is converted to linearly polarized THz wave with the same phase shifter, whose polarization direction is perpendicular to that of the incident pulse. This returning wave can be extracted using a polarization beam splitter.

This wave contains information about the reflection coefficients of the reflector for one circularly polarized field. For the low precision of the  $\delta = \pi/2$ -phase shifter, the polarization of the THz wave on the reflector is distorted. However, this distorted component is not extracted with a polarization beam splitter. Consequently, we can evaluate the reflection coefficient for the circularly polarized field, even with a low-precision phase shifter. Experimentally, THz time-domain spectroscopy on a doped InSb wafer under a magnetic field has been demonstrated using these phase shifters and a wire-grid polarizer [26]. The evaluated complex conductivity spectrum in a circularly polarized field was shifted by the cyclotron frequency while maintaining



the Drude-like spectral shape. This technique using a phase shifter paves the way for new simple magneto-optical spectroscopy methods.

## References

1. D. Pozar, *Microwave Engineering* (Wiley, 1998)
2. R. Mendis, D.M. Mittleman, *Opt. Express* **17**, 14839–14850 (2009)
3. R. Mendis, A. Nag, F. Chen, D.M. Mittleman, *Appl. Phys. Lett.* **97**, 131106 (2010)
4. R. Mendis, *IEEE Trans. Microw. Theory Tech.* **58**, 1993–1998 (2010)
5. V. Pacheco-Peña, V. Torres, B. Orazbayev, M. Beruete, M. Navarro-Cía, M. Sorolla, N. Engheta, *Appl. Phys. Lett.* **105**, 243503 (2014)
6. R. Mendis, M. Nagai, Y. Wang, N. Karl, D.M. Mittleman, Terahertz artificial dielectric lens. *Sci. Rep.* **6**, 23023 (2016)
7. R. Mendis, J. Liu, D.M. Mittleman, *Appl. Phys. Lett.* **101**, 111108 (2012)
8. J. Liu, R. Mendis, D.M. Mittleman, *Appl. Phys. Lett.* **103**, 031104 (2013)
9. T. Brabec, F. Krausz, *Rev. Mod. Phys.* **72**, 545–591 (2000)
10. A. Baltuška, Th Udem, M. Uiberacker, M. Hentschel, E. Goulielmakis, Ch. Gohle, R. Holzwarth, V.S. Yakovlev, A. Scrinzi, T.W. Hänsch, F. Krausz, *Nature* **421**, 611–616 (2003)
11. M. Nagai, Y. Kamon, E. Matsubara, Y. Minowa, M. Ashida, *Proceedings of SPIE—The International Society for Optical Engineering*, vol. 9361 (2015)
12. R. Mendis, D. Grischkowsky, Undistorted guided-wave propagation of subpicosecond terahertz pulses. *Opt. Lett.* **26**, 846–848 (2001)
13. R. Mendis, D. Grischkowsky, THz interconnect with low loss and low group velocity dispersion. *IEEE Microw. Wirel Compon. Lett.* **11**, 444–446 (2001)
14. J. Zhang, D. Grischkowsky, *Opt. Lett.* **29**, 1617 (2004)
15. R. Mendis *J. Appl. Phys.* **101**, 083115 (2007)
16. T. Suzuki, M. Nagai, Y. Kishi, *Opt. Lett.* **41**, 325–328 (2016)
17. L. Brillouin, *J. Appl. Phys.* **19**, 1023–1041 (1948)
18. A. Bingham, Y. Zhao, D. Grischkowsky, *Appl. Phys. Lett.* **87**, 051101 (2005)
19. J. Kitagawa, M. Kodama, S. Koya, Y. Nishifuji, D. Armand, Y. Kadoya, *Opt. Express* **20**, 17271–17280 (2012)
20. E.S. Lee, J.-K. So, G.-S. Park, D. Kim, C.-S. Kee, T.-I. Jeon, *Opt. Express* **20**, 6116–6123 (2012)
21. M.A. Kats, D. Woolf, R. Blanchard, N. Yu, F. Capasso, *Opt. Express* **19**, 14860–14870 (2011)
22. M. Nagai, N. Mukai, Y. Minowa, M. Ashida, J. Takayanagi, H. Ohtake, *Opt. Lett.* **39**, 146–149 (2014)
23. M. Nagai, N. Mukai, Y. Minowa, M. Ashida, T. Suzuki, J. Takayanagi, H. Ohtake, *Opt. Express* **23**, 4641–4649 (2015)
24. N.K. Grady, J.E. Heyes, D.R. Chowdhury, Y. Zeng, M.T. Reiten, A.K. Azad, A.J. Taylor, D.A.R. Dalvit, H.-T. Chen, *Science* **340**, 1304 (2013)
25. V. Torres, N. Sánchez, D. Etayo, R. Ortuño, M. Navarro-Cía, *IEEE Photon. Tech. Lett.* **26**, 1679 (2014)
26. T. Morimoto, G. Yamashita, M. Nagai, M. Ashida, *Appl. Phys. Express* **9**, 022402 (2016)

# Chapter 7

## Development and Applications of Metasurfaces for Terahertz Waves



Keisuke Takano, Boyong Kang, Yuzuru Tadokoro, Kosaku Kato,  
Makoto Nakajima and Masanori Hangyo

**Abstract** The development of optical components, in the terahertz frequency range, composed of artificial metallic structures is reviewed, with particular focus on two-dimensional metamaterials (metasurfaces). Various electromagnetic responses and associated fundamental terahertz optical components such as polarizers, wave plates, lenses, and absorbers can be derived even from two-dimensional structures made from common materials. Such terahertz optical components are light and thin, made from readily available materials, and are easy to fabricate owing to the long wavelength of terahertz waves. Both linear and nonlinear optical responses in metamaterials have been developed. The generation of terahertz waves by the nonlinear optical response in silver nanostructures is investigated with a view to designing the nonlinear response of the light and terahertz waves in metamaterials.

### 7.1 Introduction

Terahertz waves are electromagnetic radiation with a frequency typically in the range of 0.1–10 THz. Corresponding wavelengths range from 3 mm to 30  $\mu\text{m}$  and lie between the infrared and millimeter-wave regimes. As a result of this wavelength scale, the size of elements of metamaterials is of the order of microns. It is not difficult to fabricate deep subwavelength structures. The size of the components made of metamaterials can be also of the order of several tens of millimeters, suitably small for easy handling. Another feature of this frequency range is the very large permit-

---

**Masanori Hangyo** Deceased on Oct. 25, 2014.

---

K. Takano (✉) · B. Kang · Y. Tadokoro · K. Kato · M. Nakajima · M. Hangyo  
Institute of Laser Engineering, Osaka University, 2-6 Yamadaoka, Suita, Osaka 565-0871, Japan  
e-mail: [ksk\\_takano@shinshu-u.ac.jp](mailto:ksk_takano@shinshu-u.ac.jp)

K. Takano  
Center for Energy and Environmental Science, Shinshu University, 4-17-1 Wakasato Nagano,  
Nagano 380-8553, Japan

B. Kang  
Center for Advanced Meta-Materials, 156 Gajeongbuk-Ro, Yuseong-Gu, Daejeon 34103, Korea

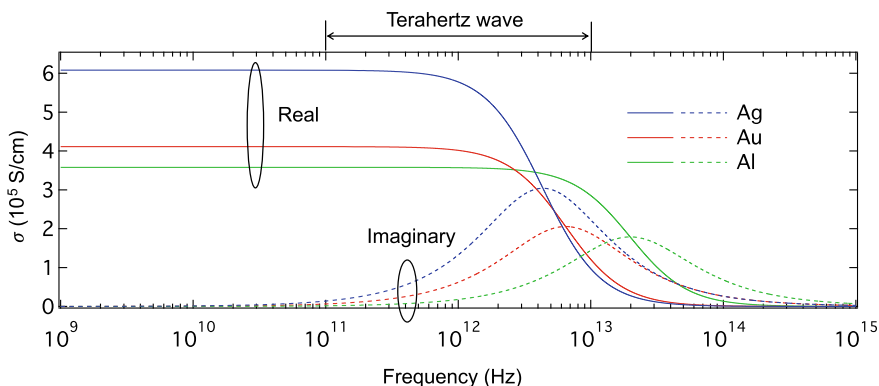


**Fig. 7.1** Dispersion of the complex conductivity in aluminum, gold, and silver calculated within the Drude model

tivity and conductivity of metals. Dispersion in typical metals is described by the Drude model below terahertz frequencies. Figure 7.1 plots the complex conductivities of silver, gold, and aluminum between  $10^9$  and  $10^{15}$  Hz [1]. Metallic conductivity at terahertz frequencies is significantly higher than at optical frequencies and there is low dispersion below 1 THz, the so-called Hagen–Rubens regime [2]. Because of the large conductivity, provided a piece of metal is thicker than the skin depth ( $\sim 100$  nm for Au at 1 THz) and there are no resonances with a high quality factor or a long interaction length, the metal is well approximated by a perfect conductor below terahertz frequencies. Thus, because of their ease of fabrication and the low loss of metals, terahertz components involving two-dimensional artificial metallic structures have typically been used in the terahertz range. Such two-dimensional structures are called frequency-selective surfaces (FSSs) [3]. After the discovery of metamaterials, FSSs have been considered as a constitutive element of metamaterials, two-dimensional metamaterials, or metasurfaces. Advanced features have been added to FSSs operating in the microwave to light regimes.

The last few decades have seen the development of terahertz optical components, efficient sources, and detectors made from artificial structures. Fundamental and practical terahertz components such as polarizers, wave plates, absorbers, and modulators can be made using metasurfaces and artificial structures. This chapter describes the development of terahertz components and demonstrates how the nonlinear response of metal nanoparticles can be exploited to produce a source of coherent terahertz waves.

## 7.2 Terahertz Components

### 7.2.1 Polarizers

Terahertz time-domain spectroscopy (THz-TDS) systems are standard and powerful spectroscopic tools operating in the terahertz region [4]. Femtosecond laser pulses are converted to broadband coherent terahertz pulses by photoconductive antennas, nonlinear optical crystals, etc. Photoconductive antennas and nonlinear optical crystals are also used for detection. By using a part of the femtosecond pulses as a sampling gate, a time-domain waveform of the electric fields can be directly obtained. Fourier transforming the time-domain waveforms yields both amplitude and phase spectra. By comparing the amplitude and phase spectra of the samples with those of a reference, both the real and imaginary parts of the refractive index of the samples are obtained. The polarization states can also be easily determined by using only polarizers [5].

Given the two mutually independent polarization components, the polarization states can be calculated. The complex Fourier amplitudes of the electric fields in the  $x$ - and  $y$ -directions [ $E_x(\omega)$  and  $E_y(\omega)$ ], which propagate in the  $z$ -direction in free space, are expressed as

$$\begin{bmatrix} E_x(\omega) \\ E_y(\omega) \end{bmatrix} = \frac{1}{\sqrt{2}} \begin{pmatrix} 1 & 1 \\ 1 & -1 \end{pmatrix} \begin{bmatrix} E_{+45^\circ}(\omega) \\ E_{-45^\circ}(\omega) \end{bmatrix}. \quad (7.1)$$

Here,  $E_{+45^\circ}(\omega)$  and  $E_{-45^\circ}(\omega)$  are the complex Fourier amplitudes of the electric field in directions  $\pm 45^\circ$  relative to the  $x$ -axis. By converting the basis from linear to circular polarization, the complex Fourier amplitudes of the left- and right-handed circular polarizations are described as

$$\begin{bmatrix} E_L(\omega) \\ E_R(\omega) \end{bmatrix} = \frac{1}{\sqrt{2}} \begin{pmatrix} 1 & -i \\ 1 & i \end{pmatrix} \begin{bmatrix} E_x(\omega) \\ E_y(\omega) \end{bmatrix}. \quad (7.2)$$

The ellipticity  $\chi(\omega)$  and polarization angle  $\phi(\omega)$  of an arbitrary terahertz pulses are given by [6]

$$\tan \chi(\omega) = \frac{|E_L(\omega)| - |E_R(\omega)|}{|E_L(\omega)| + |E_R(\omega)|}, \quad \phi(\omega) = \frac{1}{2} \arg \left[ \frac{E_R(\omega)}{E_L(\omega)} \right]. \quad (7.3)$$

The polarization states can be determined by THz-TDS by using only linear polarizers. Birefringence and optical activity have been measured for applications in materials science and industry. For opaque materials, ellipsometers have also been developed in the terahertz region [7–9].

The accuracy of a polarization measurement depends on the polarizer efficiency. Wire-grid polarizers have been known as the standard polarizers at terahertz frequencies and consist of two-dimensional metal wire arrays as shown in Fig. 7.2.

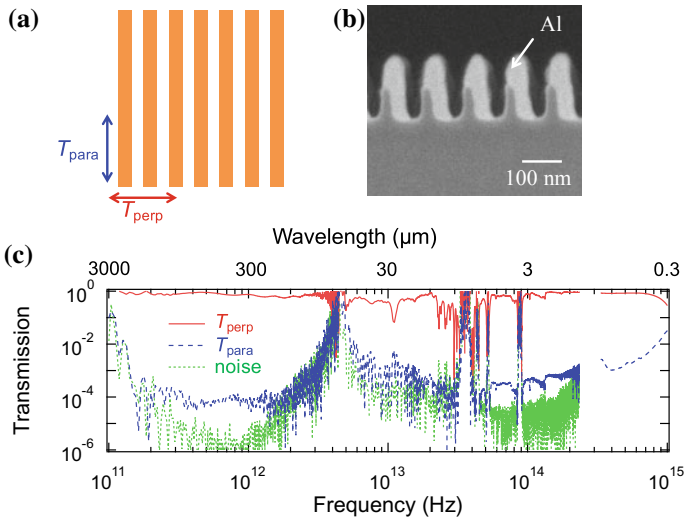


**Fig. 7.2** **a** Schematic of a wire-grid structure. **b** SEM image of the cross section of the wire-grid structure fabricated on cyclo-olefin polymer film by a nanoimprint process. **c** Transmission spectra for the polarizations perpendicular ( $T_{\text{perp}}$ ) and parallel ( $T_{\text{para}}$ ) to the wires. They are compared with the noise spectra of the measurements

This is the same structure as that used for designing a negative permittivity [10]. For the polarization component oriented parallel to the wires, the wire-grid structure behaves effectively like a diluted metal with an effective plasma frequency determined by the period and diameter of wires. For the perpendicular component, the electrons in the thin wire do not reflect the electromagnetic waves of wavelength longer than the wire diameter. The wire-grid structure then behaves like a dielectric [11, 12]. This anisotropy of the wire-grid structures is the basis of polarizers [13, 14].

The bandwidth of wire-grid polarizers depends on the wire period. An ultra-broadband polarizer is achieved with a deep subwavelength structure [15]. Figure 7.2b shows a cross section of the wire-grid structure fabricated by the nanoimprint technique on a cyclo-olefin polymer film. A nickel-grating mold was put on a cured resin layer on the film, and the resin was cured by exposure to ultraviolet light. After peeling off the mold, the aluminum layer was formed by oblique deposition. The period and height of the grating were 100 and 160 nm, respectively. The transmission coefficients for the perpendicular ( $T_{\text{perp}}$ ) and parallel ( $T_{\text{para}}$ ) polarizations were measured between  $10^{11}$  and  $10^{15}$  Hz. Terahertz time-domain spectroscopy, Fourier-transform infrared spectroscopy, and spectral photometry were used in frequency ranges  $0.1\text{--}5 \times 10^{12}$  Hz,  $5\text{--}230 \times 10^{12}$  Hz, and  $0.33\text{--}1.58 \times 10^{15}$  Hz, respectively. Because cyclo-olefin polymer is one of the most transparent materials at terahertz frequencies,  $T_{\text{perp}} > 0.8$  below 4 THz. Although there are opaque frequency ranges above 5 THz owing to absorption by cyclo-olefin polymer,  $T_{\text{para}}$  is smaller than  $10^{-4}$  between  $10^{11}$  and  $10^{14}$  Hz.

A conventional free-standing wire-grid polarizer is made of tungsten wire with a high tensile strength [14]. As the wire diameter and period are limited to several micrometers to maintain mechanical strength, the bandwidth of the free-standing wire grid remains below several terahertz. The fabrication of deep subwavelength structures on optically thin films is possible for terahertz waves. The nanoimprint wire-grid polarizer demonstrated here has a high efficiency and ultra-broadband operation resulting from the deep subwavelength fabrication. Large-area films can also be fabricated with a roll-to-roll process, and arbitrary shapes can be cut out easily using scissors. This nanoimprint polarizer film is one of the most practical polarizers available for making terahertz polarimeters. Such wire-grid polarizer sheets are now commercially available. Metasurfaces on thin films are also a tractable element to form three-dimensional bulk metamaterials. Stacking fabricated films is one way to obtain bulk metamaterials [16].

### 7.2.2 Wave Plates and Asymmetric Transmission

Birefringence is the underlying physical basis of wave plates. At terahertz frequencies, birefringence in quartz crystals has been exploited to fabricate wave plates [17], but birefringence in stacked parallel metal plates can also be used. The phase difference between transverse magnetic (TM) and transverse electric (TE) waves produces birefringence, and achromatic wave plates can be designed [18, 19]. An isolator is another important component realized by exploiting the non-reciprocity of magnetic materials [20].

A different approach to designing wave plates is to use metasurfaces with anisotropic and chiral shapes. Anisotropy in the shape of the metasurfaces produces anisotropic transmission coefficients for linear polarizations [21]. Chirality causes anisotropy for left- and right-handed circular polarizations [22–24]. Optical activity and circular dichroism result from chirality. A chiral structure is a three-dimensional structure whose mirror image does not coincide with the original one by either translation or rotation. In contrast to the non-reciprocity of Faraday rotation in magnetic media, and because of time-reversal symmetry, optical activity and circular dichroism in chiral structures are indifferent to whether the electromagnetic waves impinge on the front or back of the chiral structure. However, the asymmetric transmission coefficients, which depend on the incident direction, can be designed by the metasurfaces while retaining reciprocity [25, 26]. Here, broadband asymmetric transmission for circular polarizations in the terahertz frequency ranges by a symmetry-broken structure.

In general, the vectors of the input and output electric fields ( $\mathbf{E}^i$ ,  $\mathbf{E}^o$ ) are related by the  $2 \times 2$  matrix representing the transmission coefficients as  $\mathbf{E}^o = \mathbf{t}_{lin} \mathbf{E}^i$ , where

$$\mathbf{t}_{lin} = \begin{pmatrix} t_{xx} & t_{xy} \\ t_{yx} & t_{yy} \end{pmatrix} = \begin{pmatrix} A & B \\ C & D \end{pmatrix}. \quad (7.4)$$

Here, the bases  $\mathbf{E}^i$  and  $\mathbf{E}^o$  are linear polarizations and it is assumed there are no electric field components in the  $z$ -direction. A metasurface is considered with  $M_{xy}$  mirror symmetry. When (7.4) is invariant under the  $M_{xy}$  symmetry operation, then  $B = C$ . Additionally, by a basis transformation into circular polarization, (7.4) is transformed into

$$\mathbf{t}_{\text{circ}}^f = \begin{pmatrix} t_{RR} & t_{RL} \\ t_{LR} & t_{LL} \end{pmatrix} = \begin{pmatrix} A + D & (A - D) - 2iB \\ (A - D) + 2iB & A + D \end{pmatrix}, \quad (7.5)$$

where  $R$  and  $L$  denote the right- and left-handed circular polarizations, respectively. All materials forming the metasurface are reciprocal, and therefore, the Lorentz reciprocal theorem is not violated [27]. Applying the Lorentz reciprocal theorem to (7.5), the transmission matrix for back-side incidence on the metasurfaces becomes

$$\mathbf{t}_{\text{circ}}^b = \begin{pmatrix} t_{RR} & -t_{LR} \\ -t_{RL} & t_{LL} \end{pmatrix} = \begin{pmatrix} A + D & -(A - D) - 2iB \\ -(A - D) + 2iB & A + D \end{pmatrix}. \quad (7.6)$$

The difference in the total power transmission coefficients for front- and back-side illuminations is [28, 29]

$$\Delta^f = T_R^f - T_R^b = (|t_{RR}|^2 + |t_{LR}|^2) - (|t_{RR}|^2 + |-t_{RL}|^2) = |t_{LR}|^2 - |t_{RL}|^2. \quad (7.7)$$

The metasurfaces displaying  $M_{xy}$  mirror symmetry can exhibit asymmetric transmission ( $\Delta^f \neq 0$ ).

Figure 7.3 shows an example of a broken-symmetry metasurface with  $M_{xy}$  mirror symmetry, which can achieve asymmetric transmission. Gold film on MgO sub-

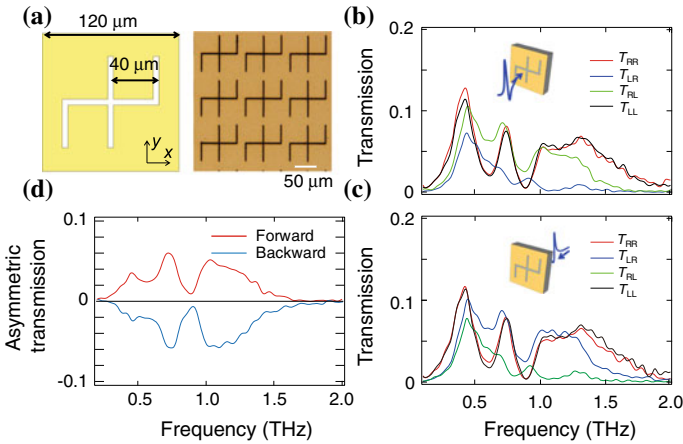


**Fig. 7.3** **a** Schematic of a unit cell of a metasurface and micro-photograph of the sample. Transmission matrix elements for **b** forward and **c** backward irradiations. **d** Asymmetric transmission coefficients for forward and backward irradiations



strates was ablated by femtosecond laser pulses to form the patterns. The gold film and substrate thicknesses were 200 nm and 2 mm, respectively. The transmission coefficients were measured by THz-TDS and normalized with that of the substrate. The  $x$ - and  $y$ -polarized terahertz pulses impinged from the front and back of the sample, and the transmission matrix for the linear polarizations  $t_{\text{lin}}$  was measured using wire-grid polarizers. By performing a basis transformation from (7.4) to (7.5), the transmission matrix for the circular polarizations  $t_{\text{circ}}$  was obtained.

Figure 7.3b and c plots the squared absolute value of each matrix element  $T_{ij} = |t_{ij}|^2$  corresponding to irradiation from the front and back, respectively. The transmission peaks are attributed to the resonances of the shape of the design on the metasurface. As expected from the  $M_{xy}$  mirror symmetry, the asymmetric transmission coefficients  $\Delta^f$  are not zero, as shown in Fig. 7.3d. When the metasurface is irradiated from the front, it is more transparent to right-hand circular polarizations. When irradiated from the back, the sign of  $\Delta^f$  is reversed and the metasurface is more transparent to left-handed circular polarizations. The asymmetric transmission coefficient at the transmission peak at 0.4 THz is 0.04, which is 1/10 of the transmission peak of 0.12. As shown here, polarization- and direction-sensitive asymmetric transmission can be designed using only reciprocal materials and planar structures.

### 7.2.3 Lenses

Designing a lens requires a spatial phase-shift gradient. Because metasurfaces are thin, their resonances produce an almost discontinuous plane of electromagnetic phases. By arranging the subwavelength resonators to design a phase-shift gradient, it is possible to achieve ultra-thin or flat optical components such as a lens, wavefront controller, or arbitrary-angle beam sweeper [30]. There is no definite distinction between these and conventional phased array antennas.

A conventional lens for terahertz waves is composed of a dielectric, such as plastic or highly resistive silicon. The lens can be designed by introducing a structural gradient in a stack of parallel metal plates [31–33]. In contrast to conventional lenses, arbitrary impedances and refractive indices can be designed. Lenses, however, are bulky because of the long wavelength of the terahertz waves. Flat optical components constructed from metasurfaces may be suitable for wireless communication devices [34, 35]. Another approach is to use hyper-lenses to observe near-field images [36].

### 7.2.4 Absorbers

The complex transmission and reflection coefficients from a vacuum to a thin film (Fig. 7.4a) on a substrate are approximately [37, 38]

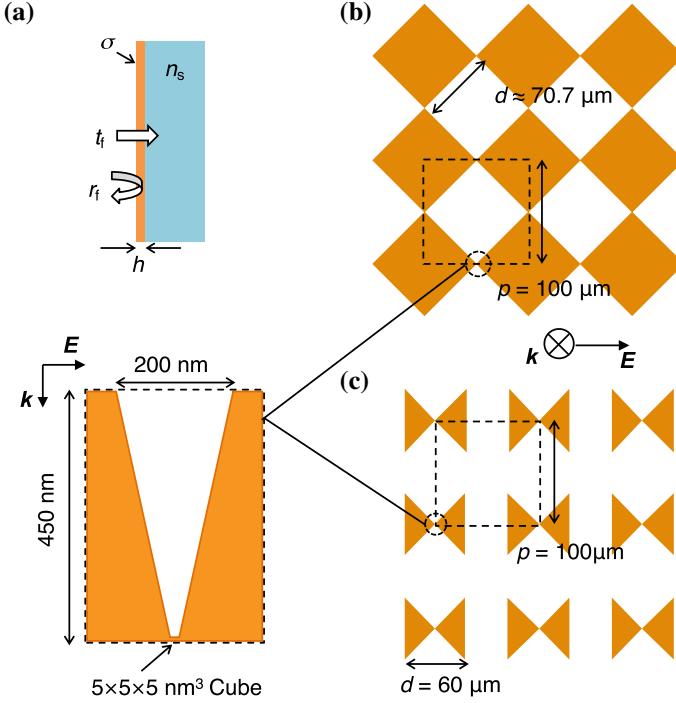


**Fig. 7.4** Schematics of **a** a thin film on a substrate, **b** checkerboard pattern, and **c** bowtie antenna array. In the finite-element method (FEM) simulation, the tops of the squares and triangles are tapered and connected with  $5 \times 5 \times 5 \text{ nm}^3$  chips, as shown in the inset

$$t_f \sim \frac{2}{1 + n_s + z_0 \sigma h}, r_f \sim \frac{1 - n_s - z_0 \sigma h}{1 + n_s + z_0 \sigma h}, \quad (7.8)$$

where  $n_s$ ,  $z_0$ ,  $\sigma$ , and  $h$  are the substrate refractive index, vacuum impedance, film conductivity, and film thickness, respectively. The energy absorption coefficient of the thin film on the substrate is calculated as

$$A_f \sim 1 - |t_f|^2 n_s - |r_f|^2 = \left| \frac{4z_0 \sigma h}{(1 + n_s + z_0 \sigma h)^2} \right|. \quad (7.9)$$

Equation (7.9) specifies a maximum  $A_f = 1/(1 + n_s)$  for a sheet conductivity of  $\sigma h = (1 + n_s)/z_0$ . For a high-resistivity silicon substrate ( $n_s = 3.42$ ), the sheet conductivity for maximal absorption is approximately 0.0117 S. Such a conductivity is achieved in thin and rough metallic films [38, 39]. Aside from absorbers, broadband anti-reflection coating was demonstrated using gold thin films [38].

A self-complementary design [40] of metasurfaces also achieves broadband absorption. Consider two metasurfaces with mutually complementary patterns. For example, a periodic metal hole array and a disk array, where the holes and disks

have the same diameter, form mutually complementary patterns. Babinet's principle [41] implies that the complex amplitude transmission and reflection coefficients of an original and complementary pattern ( $t_O, r_O$ ) and ( $t_C, r_C$ ), satisfy [42]

$$t_O + t_C = 1 \text{ and } r_O + r_C = -1. \quad (7.10)$$

When the original and complementary patterns are identical, the pattern is called self-complementary. A self-complementary pattern satisfies  $t_O = t_C$  and  $r_O = r_C$ . Combining this with (7.10) and (7.9), we then have  $t_O = t_C = t_S = 1/2$  and the maximum energy absorption  $A = A_S = 1/2$ . Frequency-independent absorption can be designed using self-complementary patterns.

The checkerboard pattern in Fig. 7.4b is one of the simplest possible self-complementary patterns. Nakata and Urade et al. theoretically and experimentally demonstrated that checkerboard patterns with an appropriate resistivity can achieve frequency-independent transmission and absorption coefficients [43, 44]. In Fig. 7.5, the real part of the complex amplitude transmission coefficient and the energy absorption coefficient of the checkerboard pattern on a silicon substrate were simulated, and compared with those of the bowtie antenna array (Fig. 7.5a). The checkerboard pattern is composed of gold squares, where the frequency dispersion of the conductivity ( $\sigma_{Au}$ ) is given by the Drude model (Fig. 7.1) [1]. The squares are connected with small metallic chips with volume  $5 \times 5 \times 5 \text{ nm}^3$ . When the conductivity of the chips is made to be  $\sigma_{Au}/10$  to satisfy  $t_S = 1/2$ , a transmission coefficient with little dispersion is obtained. Simultaneously, the broadband energy absorption coefficient shown in Fig. 7.5b is obtained. The energy absorption maximum in the film on the silicon substrate (with  $n_s = 3.42$ ) is  $A \sim 0.226$ . The absorption value near 0.226 is achieved by the checkerboard pattern with an appropriate conductivity. The resonance of the bowtie antenna array also achieves the maximal absorption (Fig. 7.5b). However, the absorption bandwidth is much greater in self-complementary checkerboards. Thin metallic film and the checkerboard pattern differ in terms of where the

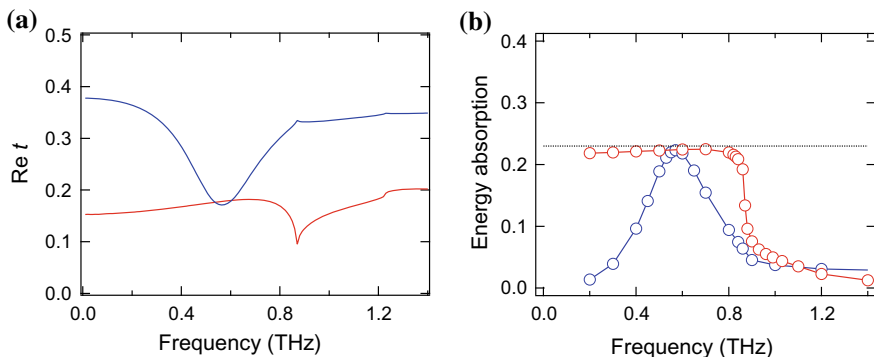


**Fig. 7.5** **a** Real part of complex amplitude transmission coefficients and **b** simulated absorption spectra for the checkerboard (red) and bowtie antenna array (blue) by the FEM method

electromagnetic energy is absorbed. In the latter case, most of the absorption occurs at the small connections between the squares, where the induced currents are concentrated. [45] This property is promising for terahertz sensors, bolometer, and other detectors.

We note that randomness in the connection between the squares results in energy loss similar to that due to absorption for transmission coefficients [45–47]. It is also noted that the absorption coefficient of the thin film is limited to 1/2 by virtue of (7.9). To obtain  $A = 1$ , multilayer or bulk structures are required. Absorbing films composed of double-layered metasurfaces have been demonstrated. When the reflected waves from the first and the second metasurface layers interfere destructively, the electromagnetic waves are trapped and absorbed almost perfectly into the film and resonators [48, 49]. By exploiting the phase discontinuity of the metasurface resonances, it is possible to design an absorber that is much thinner than the wavelength.

Dielectric resonators can be used instead of planar resonator arrays to design an absorber. Figure 7.6a and b shows a schematic and a scanning electron microscope image of a terahertz-wave absorber, composed of  $\text{TiO}_2$  sphere resonators [50]. Since the permittivity of  $\text{TiO}_2$  is approximately  $\varepsilon \sim 100 + i1$  at 1 THz [51], a subwavelength spherical resonator can be obtained [52]. Spheres of 53.3  $\mu\text{m}$  diameter were fabricated using micro-flow channels. The microspheres were arranged in a triangular lattice with period 68.4  $\mu\text{m}$ . A metal mesh with holes forming a triangle lattice was used to arrange the spheres. The metal mesh was placed on a glue-covered surface on aluminum substrate. The spheres were sprinkled onto the metal mesh and fixed with the glue in the holes. The metal mesh was then peeled off by hand, leaving the spheres behind, forming a triangular lattice. The energy absorption coefficient for normal incidence was measured using a reflection-type THz-TDS system, as shown in Fig. 7.6c. The two observed absorption peaks are attributed to the Mie resonances of the spheres. In Fig. 7.6d, the distributions of the magnetic fields on the cross section of the spheres were simulated using a finite-element method (Ansys, HFSS). The distributions displaying features of TE and TM modes of the first Mie resonance were simulated at 0.54 and 0.73 THz, respectively. The destructive interference between the electromagnetic fields scattered from the Mie resonances and reflected from the substrate produces the absorption peaks of 85% at 0.52 THz and 96% at 0.71 THz, experimentally. The manufacturing process for the absorber of terahertz waves demonstrated here is simple, economical, and applicable even to curved surfaces.

Terahertz-wave absorbers can be also be made from highly absorbing materials, such as a carbon nanotube forest [53] and magnetic materials [53]. In the terahertz region, however, magnetic materials are rare and should be sufficiently thick owing to the wavelength of the terahertz waves. By using artificial structures such as metamaterials and photonic crystals [54], thin but efficient absorbers can be achieved with common materials. Terahertz detectors based on the temperature increase in films have been developed [39, 55, 56]. The thinness of the metamaterial absorbers is useful for bolometric detectors.

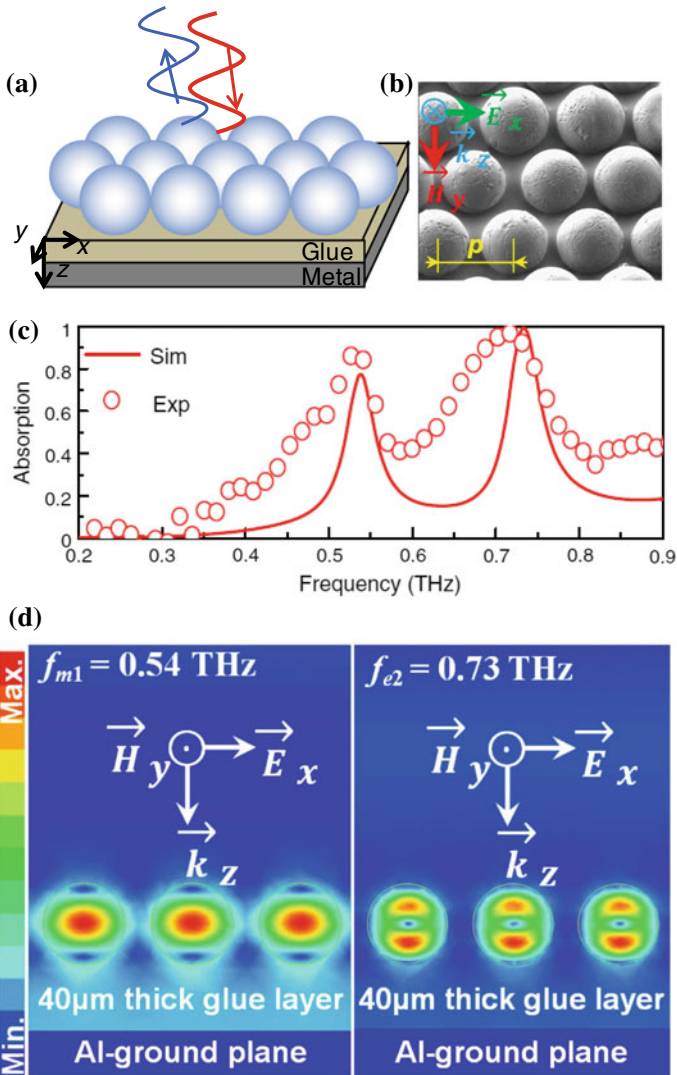


**Fig. 7.6** **a** Schematic and **b** SEM image of a TiO<sub>2</sub> sphere array on a metal substrate. **c** Experimental and simulated absorption spectra. **d** Simulated distribution of magnetic fields on the cross section of the spheres at 0.54 and 0.73 THz. Reproduced with permission from R. Yahiaoui et al., Opt. Lett. **40**, 3197 (2015). Copyright 2015 Optical Society of America

### 7.3 Nonlinear Response of Metamaterials to Terahertz Waves

A metamaterial acts like an ensemble of metallic resonators. Electromagnetic waves are confined and enhanced in the vicinity of the resonators. The nonlinear response of the surrounding material is induced by strong electromagnetic fields. In the terahertz region, the role of the nonlinear effects around metamaterials is twofold: firstly, when a metamaterial resonates with terahertz waves, the enhanced terahertz near-field can induce a nonlinear response. Studies of nonlinearity induced by terahertz waves have been conducted mainly using recently developed table-top terahertz pulse sources. Femtosecond laser pulses are converted to terahertz pulses with peak electric fields greater than several 100 kV/cm by a tilted-pulse-front excitation of the nonlinear optical crystal prism [57, 58]. Furthermore, the electric and magnetic fields of the terahertz pulses are enhanced around the metallic resonators. For example, the insulator–metal transition of vanadium oxide has been induced by the intense terahertz electric fields enhanced by split-ring resonators [59]. Intense terahertz magnetic fields also have been paving the way to manipulate electron spins [60–62]. Furthermore, the intense terahertz fields cause not only microscopic material property change [63] but also irreversible macroscopic structural changes [64–66]. The intense terahertz fields might be a material processing tool such as the microwave oven and laser machining.

Secondly, nonlinear electromagnetic response in optical metamaterials can be used to generate terahertz pulses. Welsh et al. have reported broadband terahertz pulses generated from a metallic grating irradiated by femtosecond near-infrared laser pulses [67, 68]. The terahertz generation was enhanced by the plasmon resonances in the gratings. Subsequently, the mechanism of terahertz generation was also discussed in metallic nanostructures such as metal films in the percolation limit [69], gold nanospheres [70], and nanoparticle arrays [71]. At present, since the incident laser pulse energy density is of the order of 1 GW/cm<sup>2</sup>, electron emission from the nanostructures and electron acceleration by the ponderomotive force are considered to form the generation mechanism [68, 72, 73]. Electron emission is a nonlinear process caused by multi-photon ionization and tunneling ionization induced by intense laser fields. Since the ponderomotive acceleration is also a nonlinear process, the efficiency of terahertz generation displays a complex and high-order nonlinearity with respect to the incident laser power [67, 72]. When the incident laser pulse energy density is of the order of 1 MW/cm<sup>2</sup>, one observes an optical rectification by the nonlinear response due to the modulation of the electron density [69, 70]. The nonlinear process is strongly enhanced by the resonating structures, though the precise mechanism is still debated.

We here demonstrate terahertz pulse generation from silver nano-metal ink [74]. The nano-ink was composed of silver nanoparticles of approximate diameter 5 nm, dispersed in tetradecane solvent. By annealing at 220°C for 1 h in air, the nanoparticles melt, connect, and become metalized. Nano-metal ink is used in printing electronics. Recent progress in printing technology has enabled the fabrication of 1- $\mu$ m-

thin lines by a simple and economical process [75]. The resolution of an advanced ink-jet printer suffices to fabricate terahertz devices and metamaterials [76–78].

The silver nano-ink was spin-coated onto cover glass, and a change in the metallic luster was observed for several baking temperatures, as shown in Fig. 7.7a. Metallic luster was observed between 220 and 235 °C. The film conductivity was evaluated by THz-TDS. Transmission decreased rapidly for annealing temperatures ranging from 205 to 220 °C, as shown in Fig. 7.7c. Here, transmission is defined by  $T = \int |E_{film+glass}(t)|^2 dt / \int |E_{glass}(t)|^2 dt$ , where  $E_{film+glass}(t)$  and  $E_{glass}(t)$  represent the time-domain waveforms transmitted through, respectively, the nano-ink film on glass substrate and cover glass only, in the THz-TDS measurements. As the nanoparticles melt and connect, nanostructures of size 100 ~ 200 nm form, depending on the baking temperature, as observed in the scanning electron microscope (SEM) image (Fig. 7.7b). The nanostructures grow with increasing baking temperature. When the cluster size exceeds the percolation threshold, the conductivity increases rapidly and results in a decrease in the transmission.

The nanostructure morphology is critical for terahertz generation. The terahertz pulses are generated by irradiating the baked nano-ink with regenerative amplified femtosecond laser pulses. As shown in the schematic in Fig. 7.8a, the incident pulse was p-polarized and incident at 45°. The generated terahertz pulses were collected by parabolic mirrors onto a 1-mm-thick ZnTe crystal. The time-domain waveforms of the p-polarized component were measured by electro-optical sampling. The time-domain waveforms generated from the nano-ink at three baking temperatures are shown in Fig. 7.8b. The Fourier-transformed spectra typically cover frequencies up to 3 THz, a limit imposed by the coherence length in the ZnTe crystal (Fig. 7.8c).

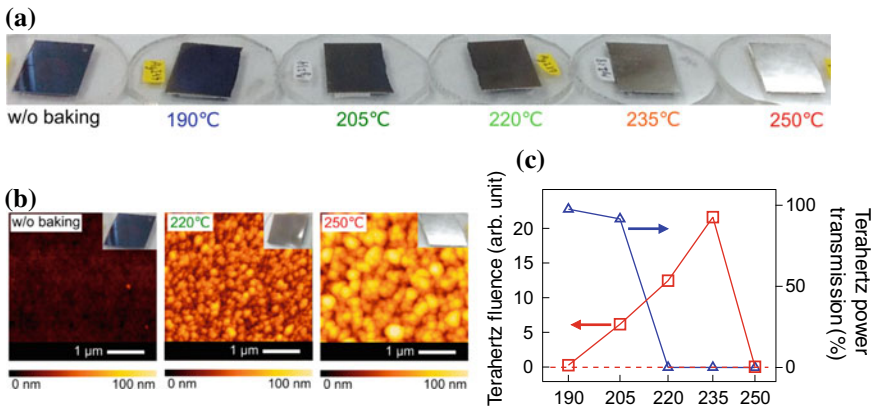


**Fig. 7.7** **a** Photograph of the silver nano-metal ink baked at various temperatures. **b** AFM images of nanoparticle ink without baking, baked at 220 and 250 °C. **c** Squares, left axis: baking temperature dependence of the terahertz-wave fluence between 190 and 250 °C. Triangles, right axis: power transmittance at the average frequency of 0.7 THz, evaluated by the THz-TDS. Reproduced with permission from K. Kato et al., *Opt. Lett.* **41**, 2125 (2016). Copyright 2016 Optical Society of America

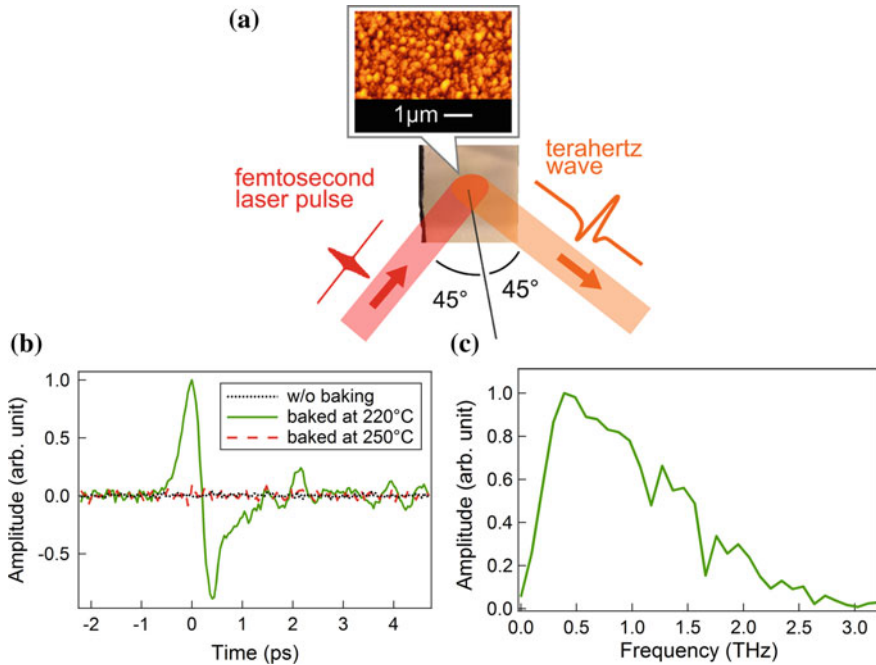


**Fig. 7.8** **a** Experimental configuration. **b** Terahertz waveforms emitted from the silver nanoparticle ink pumped by p-polarized pump pulses at different baking temperatures. **c** Amplitude spectrum obtained by Fourier transforming the waveform for the sample baked at 220 °C. Reproduced with permission from K. Kato et al., *Opt. Lett.* **41**, 2125 (2016). Copyright 2016 Optical Society of America

The generation efficiency strongly depends on the baking temperature. The terahertz pulses are not generated from the nano-ink without baking; with baking, this occurs above 250 °C. The fluences of the generated terahertz waves for the different baking temperatures are plotted in Fig. 7.7c.

The relation between the percolation threshold and the generation of terahertz waves has been discussed in terms of the enhancement of plasmon resonances [67, 69, 72]. Electric fields are enhanced by localized plasmon resonances on the metallic surface near the percolation threshold and enhance the efficiency of terahertz generation. The best conditions for terahertz generation exist clearly around 235 °C, which differs slightly from the 220 °C baking temperature that marks the decrease in transmission, as plotted in Fig. 7.7. This temperature difference presumably arises from the nanostructural difference between the surface and the inside of the film. Electric field enhancement is important for terahertz generation. However, the decrease in transmission measured by THz-TDS reflects the conductivity averaged over the whole film. Once the lower particles are connected, the increase in the conductivity causes a rapid decrease in the transmission, which does not correspond to the electric field enhancement factor.



Despite the low terahertz-wave generation efficiency obtainable from metal nanostructures, there are some advantages. Since metallic nanostructures do not absorb infrared light, broadband generation is expected as well as terahertz generation from air plasma [79]. The operating (resonant) wavelength and symmetry properties can be designed by artificial structures [80, 81]. Luo et al. demonstrated terahertz generation from metasurfaces, which depended on the symmetry of such resonators [80]. Using only common materials, it is possible to make disposable and large-area terahertz sources that are suitable for high-power laser excitation [82, 83]. The challenge of resolving phase mismatch is also being addressed. Phase matching in a four-wave mixing process was demonstrated in epsilon-near-zero metamaterials [84]. The arbitrary electromagnetic phase control is one of the features of the metamaterials. Further improvements to the terahertz generation efficiency are also expected. Here, we reported that silver nano-ink can generate terahertz waves by laser irradiation [74]. A type of terahertz source could thus be designed and fabricated by ink-jet printing.

## 7.4 Summary and Perspective

This chapter described the development of terahertz components using two-dimensional metasurfaces. The devices and properties introduced here involve only a fraction of the terahertz techniques based on the artificial structures like metamaterials. Common advantages of such devices are their thinness, lightness, design versatility, and ease of fabrication, and the rich supply of materials. As long as the resonators are used, despite the limited operating frequency, narrowband metasurfaces are suitable for sensing applications. Alternatively, the operating frequency range can be extended by tuning the material properties and structures using an external stimulus [85, 86]. The nonlinear response of the metasurfaces is another actively controllable property. Thin and light planar elements made from common materials are expected to become constituents of future compact and mobile terahertz devices.

**Acknowledgements** This chapter summarized our work done over five years in the Institute of Laser Engineering, Osaka University, under the direction of Prof. Hangyo, one of the present co-authors, who sadly passed away on October 25, 2014. The authors are deeply grateful for his gentle spirit and brilliant mentorship.

We would also like to thank all the colleagues who were involved in this work, including Prof. Fumiaki Miyamaru, Dr. Yosuke Nakata, Dr. Yoshiro Urade, Dr. Tsubasa Nishida, Dr. Riad Yahiaoui, Prof. Tahsin Akalin, and Dr. Hideaki Kitahara; Mr. Yasuyuki Kawazu, Mr. Hiroshi Yokoyama, and Mr. Yuji Tanaka from Asahi Kasei E-materials Corp.; the graduate students from Osaka University, Yoku Tanaka, Tomohiro Nishikawa, Motoki Asai, and Kenichiro Hanai.

This work was supported by a Grant-in-Aid for Young Scientists (A) (No. 16H06025) from the Japan Society for the Promotion of Science (JSPS) and a Grant-in-Aid for Scientific Research on Innovative Areas “Electromagnetic Metamaterials” (No. 22109003) from The Ministry of Education, Culture, Sports, Science and Technology (MEXT), Japan.

## References

1. M.A. Ordal, R.J. Bell, R.W. Alexander, L.L. Long, M.R. Querry, *Appl. Opt.* **24**, 4493 (1985)
2. M. Dressel, G. Gruner, *Electrodynamics of Solids* (Cambridge University Press, Cambridge, 2002)
3. T.K. Wu, *Frequency Selective Surface and Grid Array* (Wiley, New York, 1995)
4. M. Hangyo, M. Tani, T. Nagashima, *Int. J. Infrared Millim. Waves* **26**, 1661 (2005)
5. T. Nagashima, M. Tani, M. Hangyo, *J. Infrared Millim. Terahertz Waves* **34**, 740 (2013)
6. E.D. Palik, J.K. Furdyna, *Rep. Prog. Phys.* **33**, 307 (1970)
7. T. Nagashima, M. Hangyo, *Appl. Phys. Lett.* **79**, 3917 (2001)
8. N. Matsumoto, T. Fujii, K. Kageyama, H. Takagi, T. Nagashima, M. Hangyo, *Jpn. J. Appl. Phys.* **48**, 09KC11 (2009)
9. K. Yatsugi, N. Matsumoto, T. Nagashima, M. Hangyo, *Appl. Phys. Lett.* **98**, 212108 (2011)
10. J.B. Pendry, *Phys. Rev. Lett.* **47**, 73 (1996)
11. J. Shen, P. Catrysse, S. Fan, *Phys. Rev. Lett.* **94**, 197401 (2005)
12. J. Shin, J.-T. Shen, P.B. Catrysse, S. Fan, *IEEE J. Sel. Top. Quantum Electron.* **12**, 1116 (2006)
13. J. Young, H. Graham, E. Peterson, *Appl. Opt.* **4**, 1023 (1965)
14. C.L. Mok, W.G. Chambers, T.J. Parker, A.E. Costley, *Infrared Phys.* **19**, 437 (1979)
15. K. Takano, H. Yokoyama, A. Ichii, I. Morimoto, M. Hangyo, *Opt. Lett.* **36**, 2665 (2011)
16. F. Miyamaru, S. Kuboda, K. Taima, K. Takano, M. Hangyo, M.W. Takeda, *Appl. Phys. Lett.* **96**, 081105 (2010)
17. J. Masson, G. Gallot, *Opt. Lett.* **31**, 265 (2006)
18. M. Nagai, N. Mukai, Y. Minowa, M. Ashida, J. Takayanagi, H. Ohtake, *Opt. Lett.* **39**, 146 (2014)
19. M. Nagai, N. Mukai, Y. Minowa, M. Ashida, T. Suzuki, J. Takayanagi, H. Ohtake, *Opt. Express* **23**, 4641 (2015)
20. M. Shalaby, M. Peccianti, Y. Ozturk, R. Morandotti, *Nat. Commun.* **4**, 1558 (2013)
21. X.G. Peralta, E.I. Smirnova, A.K. Azad, H.-T. Chen, A.J. Taylor, I. Brener, J.F. O'Hara, *Opt. Express* **17**, 773 (2009)
22. M. Kuwata-Gonokami, N. Saito, Y. Ino, M. Kauranen, K. Jefimovs, T. Vallius, J. Turunen, Y. Svirko, *Phys. Rev. Lett.* **95**, 227401 (2005)
23. T. Kan, A. Isozaki, N. Kanda, N. Nemoto, K. Konishi, H. Takahashi, M. Kuwata-Gonokami, K. Matsumoto, I. Shimoyama, *Nat. Commun.* **6**, 8422 (2015)
24. K. Kamata, Z. Piao, S. Suzuki, T. Fujimori, W. Tajiri, K. Nagai, T. Iyoda, A. Yamada, T. Hayakawa, M. Ishiwara, S. Horaguchi, A. Belay, T. Tanaka, K. Takano, M. Hangyo, *Sci. Rep.* **4**, 4919 (2015)
25. R. Singh, E. Plum, C. Menzel, C. Rockstuhl, A.K. Azad, R.A. Cheville, F. Lederer, W. Zhang, N.I. Zheludev, *Phys. Rev. B* **80**, 153104 (2009)
26. Z. Li, M. Gokkavas, E. Ozbay, *Adv. Opt. Mater.* **1**, 472 (2013)
27. R.J. Potton, *Rep. Prog. Phys.* **67**, 717 (2004)
28. C. Menzel, C. Rockstuhl, F. Lederer, *Phys. Rev. A* **82**, 053811 (2010)
29. C. Menzel, C. Helgert, C. Rockstuhl, E.-B. Kley, A. Tünnermann, T. Pertsch, F. Lederer, *Phys. Rev. Lett.* **104**, 253902 (2010)
30. N. Yu, P. Genevet, M.A. Kats, F. Aieta, J.-P. Tetienne, F. Capasso, Z. Gaburro, *Science* **334**, 333 (2011)
31. W.E. Kock, *Bell Syst. Tech. J.* **27**, 58 (1948)
32. R. Mendis, M. Nagai, Y. Wang, N. Karl, D.M. Mittleman, *Sci. Rep.* **6**, 23023 (2016)
33. T. Konno, T. Suzuki, J.C. Young, M. Saigusa, K. Takano, H. Kitahara, M. Hangyo, T. Suzuki, *Appl. Phys. A Mater. Sci. Process.* **109**, 1103 (2012)
34. J. Neu, B. Krolla, O. Paul, B. Reinhard, *Opt. Express* **18**, 27748 (2010)
35. D. Hu, X. Wang, S. Feng, J. Ye, W. Sun, Q. Kan, P.J. Klar, Y. Zhang, *Adv. Opt. Mater.* **1**, 186 (2013)
36. A. Andryieuski, A.V. Lavrinenko, D.N. Chigrin, *Phys. Rev. B* **86**, 121108 (2012)

37. M. Tinkham, *Phys. Rev.* **104**, 845 (1956)
38. A. Thoman, A. Kern, H. Helm, M. Walther, *Phys. Rev. B* **77**, 195405 (2008)
39. F. Keilmann, K.F. Renk, *Appl. Phys. Lett.* **18**, 452 (1971)
40. Y. Mushiake, *Self-Complementary Antennas* (Springer, London, 1996)
41. J.D. John, *Classical Electrodynamics*, 3rd edn. (Wiley, New York, 1999)
42. R. Ulrich, *Infrared Phys.* **7**, 37 (1967)
43. Y. Nakata, Y. Urade, T. Nakanishi, M. Kitano, *Phys. Rev. B* **88**, 205138 (2013)
44. Y. Urade, Y. Nakata, T. Nakanishi, M. Kitano, *Phys. Rev. Lett.* **114**, 237401 (2015)
45. K. Takano, Y. Tanaka, G. Moreno, A. Chahadih, A. Ghaddar, X.-L. Han, F. Vaurette, Y. Nakata, F. Miyamaru, M. Nakajima, M. Hangyo, T. Akalin, *J. Appl. Phys.* **122**, 063101 (2017)
46. B. Tremain, C.J. Durrant, I.E. Carter, A.P. Hibbins, J.R. Sambles, *Sci. Rep.* **5**, 16608 (2015)
47. K. Takano, F. Miyamaru, K. Akiyama, H. Miyazaki, M.W. Takeda, Y. Abe, Y. Tokuda, H. Ito, M. Hangyo, *Opt. Express* **22**, 24787 (2014)
48. N. Landy, S. Sajuyigbe, J. Mock, D. Smith, W. Padilla, *Phys. Rev. Lett.* **100**, 207402 (2008)
49. C.M. Watts, X. Liu, W.J. Padilla, *Adv. Mater.* **24**, OP98 (2012)
50. R. Yahiaoui, K. Hanai, K. Takano, T. Nishida, F. Miyamaru, M. Nakajima, M. Hangyo, *Opt. Lett.* **40**, 3197 (2015)
51. N. Matsumoto, T. Hosokura, K. Kageyama, H. Takagi, Y. Sakabe, M. Hangyo, *Jpn. J. Appl. Phys.* **47**, 7725 (2008)
52. K. Takano, Y. Yakiyama, K. Shibuya, K. Izumi, H. Miyazaki, Y. Jimba, F. Miyamaru, H. Kitahara, M. Hangyo, *IEEE Trans. Terahertz Sci. Technol.* **3**, 812 (2013)
53. M.J. Paul, N.A. Kuhta, J.L. Tomaino, A.D. Jameson, L.P. Maizy, T. Sharf, N.L. Rupesinghe, K.B.K. Teo, S. Inampudi, V.A. Podolskiy, E.D. Minot, Y.-S. Lee, *Appl. Phys. Lett.* **101**, 111107 (2012)
54. R. Kakimi, M. Fujita, M. Nagai, M. Ashida, T. Nagatsuma, *Nat. Photonics* **8**, 657 (2014)
55. C. Pradere, J.-P. Caumes, D. Balageas, S. Salort, E. Abraham, B. Chassagne, J.-C. Batsale, *Quant. Infrared Thermogr. J.* **7**, 217 (2010)
56. Y. Tadokoro, T. Nishikawa, B. Kang, K. Takano, M. Hangyo, M. Nakajima, *Opt. Lett.* **40**, 4456 (2015)
57. J. Hebling, G. Almasi, I. Kozma, J. Kuhl, *Opt. Express* **10**, 1161 (2002)
58. H. Hirori, A. Doi, F. Blanchard, K. Tanaka, *Appl. Phys. Lett.* **98**, 091106 (2011)
59. M. Liu, H.Y. Hwang, H. Tao, A.C. Strikwerda, K. Fan, G.R. Keiser, A.J. Sternbach, K.G. West, S. Kittiwatanakul, J. Lu, S.A. Wolf, F.G. Omenetto, X. Zhang, K.A. Nelson, R.D. Averitt, *Nature* **487**, 345 (2012)
60. T. Kampfrath, K. Tanaka, K.A. Nelson, *Nat. Photonics* **7**, 680 (2013)
61. T. Kurihara, K. Nakamura, K. Yamaguchi, Y. Sekine, Y. Saito, M. Nakajima, K. Oto, H. Watanabe, T. Suemoto, *Phys. Rev. B* **90**, 144408 (2014)
62. Y. Mukai, H. Hirori, T. Yamamoto, H. Kageyama, K. Tanaka, *Appl. Phys. Lett.* **105**, 3 (2014)
63. H. Hoshina, H. Suzuki, C. Otani, M. Nagai, K. Kawase, A. Irizawa, G. Isoyama, *Sci. Rep.* **6**, 27180 (2016)
64. A.C. Strikwerda, M. Zalkovskij, K. Iwaszczuk, D.L. Lorenzen, P.U. Jepsen, *Opt. Express* **23**, 11586 (2015)
65. M. Seo, J.-H. Kang, H.-S. Kim, J. Hyong Cho, J. Choi, Y. Min Jhon, S. Lee, J. Hun Kim, T. Lee, Q.-H. Park, C. Kim, *Sci. Rep.* **5**, 10280 (2015)
66. K. Takano, H. Harada, M. Yoshimura, M. Nakajima, *Appl. Phys. Lett.* **112**, 163102 (2018)
67. G.H. Welsh, N.T. Hunt, K. Wynne, *Phys. Rev. Lett.* **98**, 026803 (2007)
68. G.H. Welsh, K. Wynne, *Opt. Express* **17**, 2470 (2009)
69. G. Ramakrishnan, P. Planken, *Opt. Lett.* **36**, 2572 (2011)
70. K. Kajikawa, Y. Nagai, Y. Uchiho, *Opt. Lett.* **37**, 4053 (2012)
71. D.K. Polyushkin, E. Hendry, E.K. Stone, W.L. Barnes, *Nano Lett.* **11**, 4718 (2011)
72. D.K. Polyushkin, I. Márton, P. Rácz, P. Dombi, E. Hendry, W.L. Barnes, *Phys. Rev. B* **89**, 125426 (2014)
73. G.K.P. Ramanandan, G. Ramakrishnan, N. Kumar, A.J.L. Adam, P.C.M. Planken, *J. Phys. D Appl. Phys.* **47**, 374003 (2014)

74. K. Kato, K. Takano, Y. Tadokoro, M. Nakajima, *Opt. Lett.* **41**, 2125 (2016)
75. K. Murata, K. Masuda, *E-Print Printable Electron.* **1**, 108 (2011)
76. M. Walther, A. Ortner, H. Meier, U. Löffelmann, P.J. Smith, J.G. Korvink, U. Löffelmann, *Appl. Phys. Lett.* **95**, 251107 (2009)
77. K. Takano, T. Kawabata, C.F. Hsieh, K. Akiyama, F. Miyamaru, Y. Abe, Y. Tokuda, R.P. Pan, C.L. Pan, M. Hangyo, *Appl. Phys. Express* **3**, 016701 (2010)
78. K. Takano, Y. Chiyoda, T. Nishida, F. Miyamaru, T. Kawabata, H. Sasaki, M.W. Takeda, M. Hangyo, *Appl. Phys. Lett.* **99**, 161114 (2011)
79. X. Lu, X.-C. Zhang, *Front. Optoelectron.* **7**, 121 (2014)
80. L. Luo, I. Chatzakis, J. Wang, F.B.P. Niesler, M. Wegener, T. Koschny, C.M. Soukoulis, *Nat. Commun.* **5**, 3055 (2014)
81. T. Matsui, S. Tomita, M. Asai, Y. Tadokoro, K. Takano, M. Nakajima, M. Hangyo, H. Yanagi, *Appl. Phys. A* **122**, 157 (2016)
82. A. Gopal, S. Herzer, A. Schmidt, P. Singh, A. Reinhard, W. Ziegler, D. Brömmel, A. Karmakar, P. Gibbon, U. Dillner, T. May, H.G. Meyer, G.G. Paulus, *Phys. Rev. Lett.* **111**, 1 (2013)
83. S. Tokita, S. Sakabe, T. Nagashima, M. Hashida, S. Inoue, *Sci. Rep.* **5**, 8268 (2015)
84. H. Suchowski, K. O'Brien, Z.J. Wong, A. Salandrino, X. Yin, X. Zhang, *Science* **342**, 1223 (2013)
85. A. Boardman, V.V. Grimalsky, Y.S. Kivshar, S.V. Koshevaya, M. Lapine, N.M. Litchinitser, V.N. Malnev, M. Noginov, Y.G. Rapoport, V.M. Shalaev, *Laser Photon. Rev.* **5**, 287 (2011)
86. H.-T. Chen, J.F. O'Hara, A.K. Azad, A.J. Taylor, *Laser Photon. Rev.* **5**, 513 (2011)

# Chapter 8

## Efficient Optical Modulation of Terahertz Metamaterials Utilizing Organic/Inorganic Semiconductor Hybrid Systems



**Tatsunosuke Matsui, Keisuke Takano, Makoto Nakajima and Masanori Hangyo**

**Abstract** We have utilized highly efficient optical modulation of terahertz (THz) transmission in organic/inorganic semiconductor hybrid system for active control of THz metamaterials. We have investigated highly efficient optical modulation of THz transmission through Si substrate coated with thin layer of organic  $\pi$ -conjugated material, copper phthalocyanine (CuPc) under various continuous-wave (CW) laser light irradiation conditions using THz time-domain spectroscopy. It has been believed that the charge carrier transfer from inorganic semiconductor substrate to  $\pi$ -conjugated material is crucial for efficient optical modulation of THz transmission. We found that the thickness of CuPc layer is a critical parameter to realize high charge carrier density for efficient optical modulation of THz transmission. We also investigated several solution-processable  $\pi$ -conjugated materials instead of CuPc and found that some of them show better modulation efficiency than CuPc. We fabricated a silver split-ring resonator (SRR) array metamaterial on CuPc-coated Si utilizing superfine ink-jet printer and succeeded in obtaining efficient modulation of THz resonant responses of SRR array metamaterials by CW laser light irradiation. Our findings may be utilized to fabricate various types of THz active metamaterials utilizing printing technologies.

---

**Masanori Hangyo** Deceased on Oct. 25, 2014.

This chapter is based on the following articles: T. Matsui et al., *Opt. Lett.* 38, 4632 (2013). Copyright 2013 ©The Optical Society and T. Matsui et al., *Jpn. J. Appl. Phys.* 55, 03DC12 (2016). Copyright 2016 ©The Japan Society of Applied Physics.

---

T. Matsui (✉)

Department of Electrical and Electronic Engineering, Graduate School of Engineering, Mie University, Tsu, Mie 514-8507, Japan  
e-mail: [matsui@elec.mie-u.ac.jp](mailto:matsui@elec.mie-u.ac.jp)

K. Takano · M. Nakajima · M. Hangyo

Institute of Laser Engineering, Osaka University, Suita, Osaka 565-0871, Japan

© Springer Nature Singapore Pte Ltd. 2019

K. Sakoda (ed.), *Electromagnetic Metamaterials*, Springer Series in Materials Science 287, [https://doi.org/10.1007/978-981-13-8649-7\\_8](https://doi.org/10.1007/978-981-13-8649-7_8)

## 8.1 Introduction

Since Pendry et al. put forward a basic concept of obtaining negative magnetic permeability utilizing artificial subwavelength resonant elements such as split-ring resonators (SRRs) in 1999 [1], numerous studies have been carried out to develop novel optical materials and devices in a wide spectrum range, from microwaves and terahertz (THz), to near-infrared and visible light. Such novel optical materials are now called metamaterials, and various optical functionalities cannot be obtained in natural materials have been realized utilizing them, such as negative refraction, superlensing, optical cloaks, and so on [2–6]. The first experimental demonstration of negative refraction was performed in microwave frequency range by Shelby et al. in 2001 [7]. In 2004, Yen et al. first succeeded in obtaining negative permeability based on magnetic resonance using an SRR array in THz frequency range [8] and numerous studies have been conducted in this actively studied spectral range [9–11].

The SRRs play crucial roles as building blocks in metamaterials [1]. The resonant characteristics of the SRRs determine the working frequency of the metamaterials, and such resonant frequencies are typically restricted only in the narrow frequency range. Various attempts have been made to tune the resonant frequency of metamaterials by external stimuli including optical, thermal, and electrical means [9–18]. In 2006, Padilla et al. succeeded in optical modulation of resonant responses of the SRR metamaterials utilizing a GaAs as substrate, in which the amount of free charge carriers could be optically tuned, and thus, their THz responses could also be controlled [12]. Such optical modulation of the THz wave has been studied not only in the field of metamaterials, but also from other viewpoints such as filters, modulators, and imagers [19]. In 2011, Yoo et al. reported that the efficiency of the optical modulation of the THz transmission through a silicon (Si) substrate can be drastically enhanced by depositing a thin layer of organic  $\pi$ -conjugated material, copper phthalocyanine (CuPc) [20]. They have shown that the THz transmission through Si substrate coated with a thin layer of CuPc decreases when irradiated with low-power (tens of mW) continuous-wave (CW) laser light. When the Si substrate was used alone, or when CuPc was deposited on a quartz substrate instead of on Si, no remarkable modulation was observed. It has been perceived that this effect was caused by metallization of the CuPc layer due to a charge transfer from Si to CuPc. There is no way to create free charge carriers in CuPc directly through optical excitation. This is because tightly bound electron–hole pairs (Frenkel-type excitons) are formed and they cannot be dissociated easily due to the strong exciton binding energy typical in organic  $\pi$ -conjugated materials with low dielectric permittivity. Therefore, the organic/inorganic semiconductor interface should play a crucial role in the modulation mechanism. We have utilized highly efficient optical modulation of THz transmission in such organic/inorganic semiconductor hybrid system and succeeded in realizing efficient optical modulation of THz responses of SRR array metamaterials [21].

## 8.2 Sample Fabrication and THz-TDS Measurements

In Fig. 8.1, molecular structure of CuPc and experimental setup for optical modulation of THz transmission are schematically shown. We used a 540- $\mu\text{m}$ -thick, highly resistive Si ( $> 2.0 \times 10^4 \Omega \text{ cm}$ , Optostar Ltd.) that is transparent to THz wave as a substrate. We purchased copper(II) phthalocyanine ( $\beta$ -form powders) from Sigma-Aldrich and used without purification as the organic  $\pi$ -conjugated material. A thin film of CuPc was deposited by thermal evaporation and subsequently annealed at 250  $^\circ\text{C}$  to induce transition to  $\beta$ -phase in which the highest modulation could be achieved, as reported by Yoo et al. [20]. We have also investigated optical modulation characteristics of various solution-processable organic  $\pi$ -conjugated materials instead of CuPc. Here, we show results of two low molecules: a well-known fullerene derivative electron acceptor, [6,6]-phenyl-C61-butyric acid methyl ester (PCBM), and 6,13-bis(triisopropylsilylethynyl) pentacene (TIPS-pentacene), which is extensively studied as an active layer of organic thin-film transistors [22]. These materials were purchased from Sigma-Aldrich and used without purification. To form thin films, a spin-coating was used and toluene was used as solvents. These films were also thermally annealed at 250  $^\circ\text{C}$ .

The optical characteristics in the THz range were investigated using typical THz time-domain spectroscopy (THz-TDS). For the optical modulation experiment, a 532-nm CW laser (Spectra-Physics) was used. At this wavelength, there is no much absorption in CuPc, and therefore, free charge carriers can only be excited in Si [23]. The area of the illuminated spot is larger than the beam waist of the THz wave.

In our study, modulation factor (MF) is employed in order to quantitatively evaluate the degree of optical modulation of THz transmission and MF is defined as the change of the integrated transmitted power of THz radiation due to CW laser light irradiation as follows:

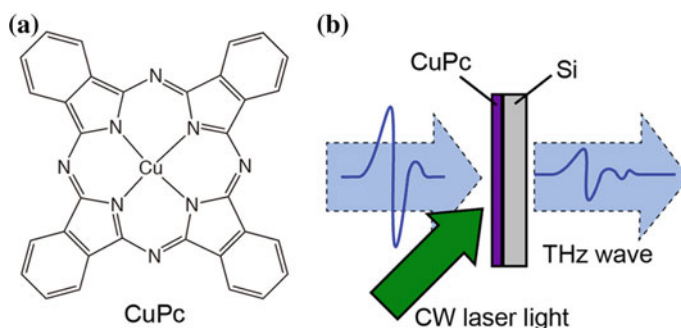


**Fig. 8.1** Schematic representation of **a** molecular structure of copper phthalocyanine (CuPc) and **b** experimental setup for optical modulation of THz transmission in Si substrate coated with thin layer of CuPc. Adapted with permission from [21], ©The Optical Society

$$MF = \frac{\int |E_{OFF}(\omega)|^2 d\omega - \int |E_{ON}(\omega)|^2 d\omega}{\int |E_{OFF}(\omega)|^2 d\omega}, \quad (8.1)$$

where  $E_{OFF}(\omega)$  and  $E_{ON}(\omega)$  are the frequency-domain field amplitudes of the transmitted THz radiation when the laser is off and on, respectively [21, 22]. The integration was performed over the frequency range from 0.2 to 1.5 THz. A higher MF reflects a larger decrease of THz transmission under CW laser light irradiation and thus reflects higher degree of THz transmission modulation.

We have fabricated a silver SRR array on a Si substrate coated with a 200-nm CuPc film, utilizing a superfine ink-jet printer (SIJ printer, SIJTechnology, Inc.) [24–27]. An SRR array with a total area of  $5 \times 5 \text{ mm}^2$  was fabricated. The dimensions of each SRR meta-atom were designed following that of Padilla et al. [12] such that they showed magnetic resonance in the THz region. Therefore, the period ( $\Lambda$ ), side length ( $L$ ), width ( $W$ ), and gap ( $G$ ) were made to be 100, 60, 12, and 6  $\mu\text{m}$ , respectively. The samples were annealed at 240 °C. The photo-induced change of the THz responses was investigated using the same THz-TDS system. However, the electric field of the linearly polarized THz radiation is made to be perpendicular to the SRR gap, so that magnetic resonance can be initiated [12].

### 8.3 Mechanism of Optical Modulation of Terahertz Transmission in Organic/Inorganic Semiconductor Hybrid System

Figure 8.2a shows the THz transmission spectra without CW laser light irradiation for the bare Si substrate and Si coated with thin layer of CuPc of different thicknesses. There is no significant difference between the bare Si and CuPc-coated Si. In Fig. 8.2b, the THz transmission spectra of the same samples under CW laser light irradiation with an intensity of  $2.5 \times 10^3 \text{ mW/cm}^2$  are shown. Upon laser light irradiation, the THz transmission decreases to almost zero, especially in CuPc thinner than 200 nm. However, the transmission modulation becomes smaller when the thickness of CuPc is further increased [21]. In Fig. 8.2c, the MF of the THz transmission is summarized as a function of thickness of the deposited CuPc film. Without the CuPc film, MF is  $\sim 0.54$ ; however, it increases drastically to almost unity by depositing a CuPc film thinner than 200 nm. By increasing thickness of the CuPc layer further, MF decreases again and reaches a value that is almost the same as without the CuPc film. As was discussed so far [20–22], the charge carrier transfer from Si to CuPc seems to play a crucial role in the THz transmission modulation. From the value of the absorption coefficient of Si at 530 nm,  $7850 \text{ cm}^{-1}$  [28], the optical excitation of free charge carriers should occur at the surface (interface) of the Si to a skin depth of micrometers. The mismatch of the band alignment between Si and CuPc and the bended energy band relationship at the interface drives the free charge carriers to move toward the Si/CuPc interface. The band alignment between these two materi-



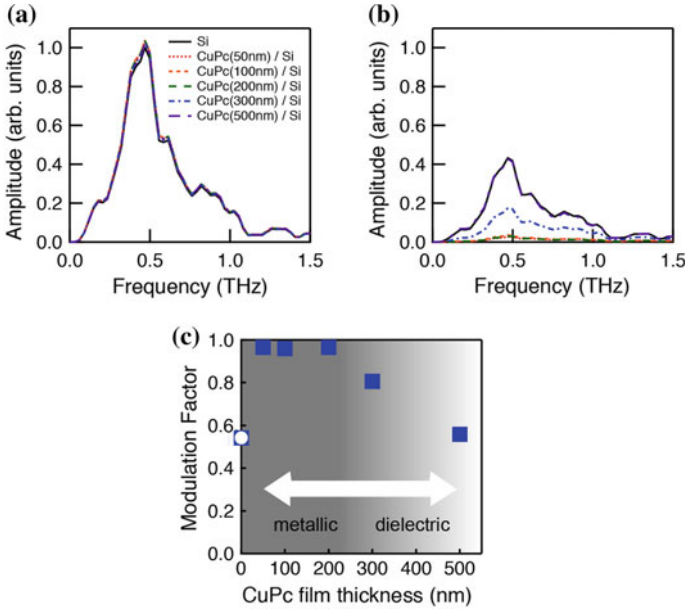


**Fig. 8.2** Summary of optical modulation of THz transmission experiment in Si substrate coated with thin layer of CuPc of different thicknesses. THz transmission spectra through a bare Si substrate and Si coated with thin CuPc films of different thicknesses **a** without and **b** with a CW laser light irradiation of  $2.5 \times 10^3 \text{ mW/cm}^2$ . **c** CuPc film thickness dependence on the MF for THz transmissions. Adapted with permission from [21], ©The Optical Society

als allows charges to transfer into the CuPc layer. Assuming every incident photons ( $n_p$ ,  $\sim 6.7 \times 10^{18} \text{ cm}^{-2}\text{s}^{-1}$ ) under laser light with intensity of  $2.5 \times 10^3 \text{ mW/cm}^2$  at 532 nm creates one charge carrier in the Si, and also assuming the lifetime ( $\tau$ ) of these charge carriers is  $50 \mu\text{s}$ , the following equation of carrier dynamics,

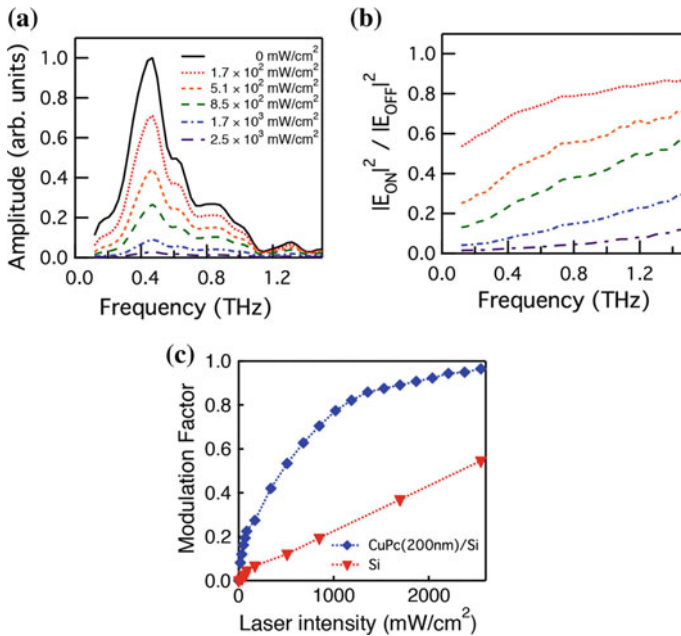
$$\frac{dn}{dt} = n_p - \frac{n}{\tau}, \tag{8.2}$$

gives us charge carrier density in the Si substrate at equilibrium ( $n_e = n_p \tau$ ) of  $\sim 3.3 \times 10^{14} \text{ cm}^{-2}$ . Assuming all of these photo-induced charge carriers in the Si substrate transfers into the 200-nm-thick CuPc, charge carrier density in the CuPc thin layer ( $n_c$ ) should be  $\sim 1.7 \times 10^{19} \text{ cm}^{-3}$ , which gives the plasma frequency of  $\sim 36 \text{ THz}$  assuming the effective mass of charge carriers is the same with electron mass. This simple examination tells us the charge carrier density increases after being transferred to the CuPc layer when the CuPc layer is thin enough and shifts the plasma frequency to show metallic characteristics in the THz spectral range of our interest. The concentration effect of the transferred free charge carriers in the thin CuPc layer might be the major origin in the metallization of CuPc, which agrees well with the CuPc thickness dependence of MF summarized in Fig. 8.2c [21]. The skin depth of

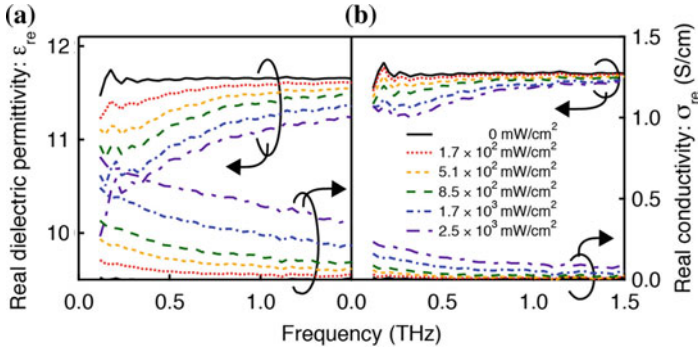
the THz radiation penetrating into the metallic CuPc should be shallow and therefore showing less transmission and higher MF. On the contrary, when the thickness of the CuPc films becomes thicker, the CuPc behaves as a dielectric due to the relatively low charge carrier density and therefore becomes more transparent in THz and the MF decreases.

Figure 8.3a shows the THz transmission spectra through CuPc-coated Si under different laser light irradiances. The thickness of the CuPc film was 200 nm. With increasing laser light intensity, the THz transmission decreases gradually and drops to approximately zero at  $2.5 \times 10^3$  mW/cm<sup>2</sup>. The transmission spectra at each laser light intensity, normalized to those with no laser irradiation, are shown in Fig. 8.3b. The THz transmission modulation is more remarkable at lower frequencies. In Fig. 8.3c, the MF of Si coated with 200-nm CuPc is summarized as a function of laser intensity and that of Si is also shown for comparison. The MF is drastically enhanced by the deposition of a CuPc film. These results clearly indicate that the THz transmission modulation in Si can be enhanced easily by a simple deposition of a thin CuPc film [21].

In order to investigate further the underlying physical mechanism of the enhanced modulation efficiency of the THz transmission, we have analyzed the dielectric prop-



**Fig. 8.3** THz transmission spectra through a 200-nm CuPc film on a Si substrate **a** under different laser light irradiances and **b** those of normalized with THz transmission spectra without laser irradiation. **c** The laser intensity dependence of the MF for THz transmission through a bare Si substrate and Si coated with a 200-nm CuPc film. Adapted with permission from ref [21], ©The Optical Society



**Fig. 8.4** Real dielectric permittivity ( $\epsilon_{re}$ ) and real conductivity ( $\sigma_{re}$ ) spectra under different laser light irradiances of **a** a Si substrate coated with a 200-nm CuPc film analyzed as a composite and **b** a bare Si substrate. Adapted with permission from [21], ©The Optical Society

erties of CuPc-coated Si under different CW laser light irradiation conditions [21]. The complex dielectric permittivity and the complex conductivity were retrieved from Fourier-transformed transmission spectra, which contains both amplitude and phase information. Figure 8.4a shows real dielectric permittivity ( $\epsilon_{re}$ ) and the real conductivity ( $\sigma_{re}$ ) spectra of a 200-nm CuPc film on a Si substrate under different laser light irradiances. In Fig. 8.4b, the corresponding spectra for a bare Si substrate are shown for comparison. We have used CW laser light for the excitation of charge carriers in the Si substrate and performed the THz transmission measurements under some equilibrium conditions. In these situations, it may be more reasonable to assume that bare Si substrate and CuPc-coated Si are in the different equilibrium condition, and thus, their THz response should also be different under CW laser light irradiation. Thus, the THz dielectric characteristics of CuPc/Si two-layer system cannot be analyzed separately. Therefore, we have analyzed CuPc-coated Si as a single-layer composite material. Without CW laser irradiation, the dielectric response shows almost no dispersion and almost the same value with and without the CuPc film. However, with increasing CW laser light intensity, the real dielectric permittivity decreases especially at lower frequencies, which can be attributed to a Drude-like metallic response. This may explain why higher modulation was obtained for lower frequencies as seen in Fig. 8.3b. In our system, the thickness of CuPc is less than 0.5% of that of Si; however, the optically induced change in the dielectric response is remarkable in CuPc-coated Si. This implies that the thin CuPc layer contributes significantly to the dielectric property when analyzed as a composite material and the optically induced change in the dielectric permittivity of the CuPc layer should be much larger than it appeared. It is reasonable to expect that the permittivity drops to negative values, as in a Drude-like response. The optically induced change in real conductivity is also remarkable in CuPc-coated Si, and it should also be much higher than it appeared under CW laser light irradiation.

We also investigated several solution-processable  $\pi$ -conjugated materials instead of CuPc [22], and here, we show results of two low molecules, PCBM and TIPS-

pentacene. PCBM does not show much absorption at 532 nm similar to CuPc; on the contrary, TIPS-pentacene shows strong absorption. Yoo et al. also showed that optical THz modulation could be induced by backward excitation, i.e., excitation from the Si side [29]. This technique is suitable for materials that show strong absorption at the wavelength of exciting CW laser light; thus, we employed this technique for TIPS-pentacene. In Fig. 8.5a and b, such forward and backward excitation configurations are schematically shown. In Fig. 8.5c, MF of PCBM is shown as a function of CW laser light intensity, along with that of CuPc for comparison. The forward excitation was used in this experiment. PCBM showed better MF than CuPc. In Fig. 8.5d, MF of TIPS-pentacene and that of CuPc investigated with backward excitation configuration are summarized as a function of CW laser light intensity. TIPS-pentacene also showed better MF than CuPc. Highly efficient optical modulation of THz transmission in these solution-processable organic  $\pi$ -conjugated materials may be useful for future printed THz electronics and photonics [22].

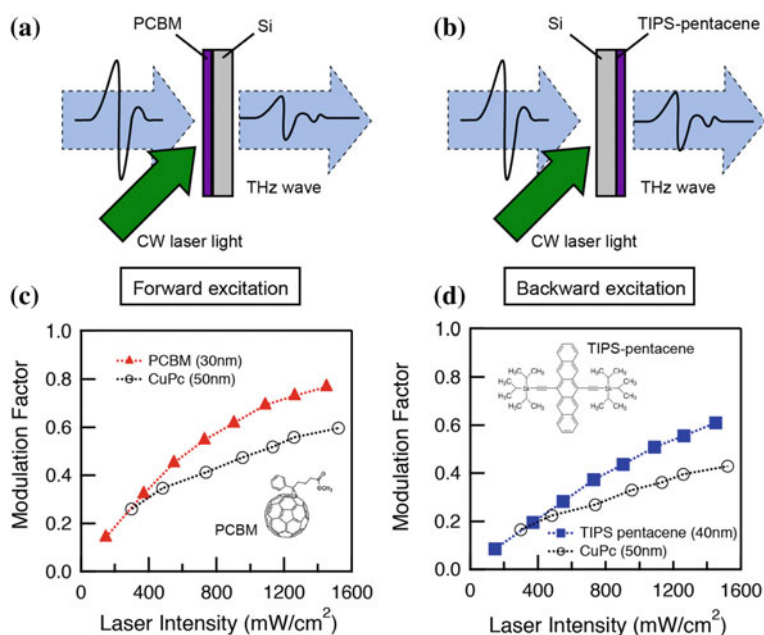


**Fig. 8.5** Schematic representation of optical modulation of THz transmission in **a** forward and **b** backward excitation configurations. Summary of the laser intensity dependence of the MF of THz transmission in the **c** PCBM and CuPc with forward excitation (inset: molecular structure of PCBM) and **d** TIPS-pentacene and CuPc with backward excitation (inset: molecular structure of TIPS-pentacene). Adapted with permission from ref [22], ©The Japan Society of Applied Physics

## 8.4 Efficient Optical Modulation of Terahertz Metamaterials Utilizing Organic/Inorganic Semiconductor Hybrid System as Substrate

We have employed Si coated with thin layer of CuPc as substrates to realize efficient optical modulation of THz metamaterials [21]. A silver SRR array metamaterial was fabricated on CuPc-coated Si by using a superfine ink-jet printer as described above. Figure 8.6a shows a laser microscope image of the fabricated Ag SRR array.

Figure 8.6b shows the normalized THz transmission spectra through the SRR array fabricated on a CuPc-coated Si substrate under different laser light irradiances, and Fig. 8.6c shows that of a bare Si substrate for comparison. In both devices, sharp transmission dips induced by resonant interaction with the SRRs can be recognized. The dip in transmission at the lower ( $\omega_0 \sim 0.32$  THz) and higher ( $\omega_1 \sim 0.85$  THz) frequencies could be attributed to the electric–magnetic coupled resonance and the half-wave resonance, respectively [12, 21]. The depth of each dip is different between SRRs on CuPc-coated Si and on bare Si substrate even without laser light irradiances, which might be attributed to the slight difference in the formed SRR structures due to the different surface conditions even printed under the same operation conditions of the SIJ printer. On the contrary, the frequencies of the dips of these resonances are exactly the same, which implies that there is no influence from the change in the capacitive and/or the inductive resonant characters of SRRs. These results imply that

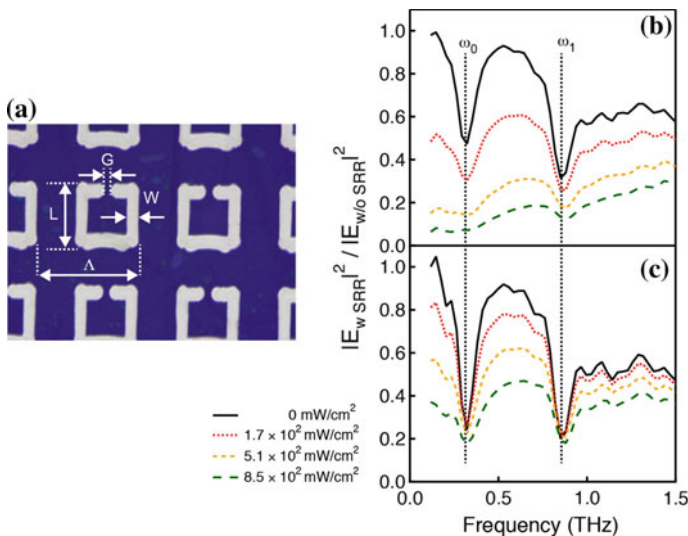


**Fig. 8.6** **a** Laser microscope image of the fabricated Ag SRR array on a 200-nm CuPc film on a Si substrate. Normalized THz transmission spectra under different CW laser light irradiances through the SRR array fabricated on **b** a 200-nm CuPc film on a Si substrate and **c** bare Si substrate. Adapted with permission from [21], ©The Optical Society

there is some difference in the oscillator strength of the resonance, which might be attributed to the slight difference in the thickness of formed SRRs. Upon increasing the laser light intensity, the transmission decreases in all frequencies of interest, but the large difference between the two samples can be well recognized at the two resonances at  $\omega_0$  and  $\omega_1$ . In the SRR array fabricated on the Si substrate, the level of the transmission dip at the two resonances does not change significantly, and the sharp resonant dip remains even at higher CW laser light irradiations (Fig. 8.6c). On the other hand, in the sample fabricated on CuPc-coated Si, the transmission decreases at the two resonances as well, and almost no features can be recognized at higher laser light intensities. These results imply that the optically induced efficient metallization in CuPc-coated Si is highly efficient enough to short the capacitive gap of the SRR and erase its resonant effect. Our results can be better understood by comparing with the pioneering work of photo-induced dynamic modulation of SRR response on semi-insulating GaAs by Padilla et al. introduced above [12]. In their case, the electric–magnetic coupled resonance ( $\omega_0$ ) becomes less and disappears first, then half-wave resonance ( $\omega_1$ ) becomes less pronounced, and background transmission also decreases (Fig. 8.3a of [12]). In our device fabricated on CuPc-coated Si, similar trend can be seen; however, the decrease of background transmission due to the metallization seems to be much stronger. This implies that the efficiency of metallization in CuPc-coated Si is quite high and might also be attributed to the fact that we have used CW laser excitation instead of the laser pulse [12].

## 8.5 Conclusions

In conclusions, we have analyzed the THz transmission characteristics of CuPc-coated Si under various CW laser light irradiation conditions using THz-TDS. The charge carrier transfer from Si to CuPc is crucial for the optically induced metallic behavior of CuPc-coated Si. It was shown that the thickness of the CuPc layer is a critical parameter to realize high charge carrier density for metallization. We also investigated several solution-processable organic  $\pi$ -conjugated materials instead of CuPc and found that PCBM and TIPS-pentacene show better modulation efficiency than CuPc. We have fabricated Ag SRR array metamaterial using superfine ink-jet printer on CuPc-coated Si and demonstrated highly efficient optical modulation of the SRR resonance. Our findings may open the way to fabricate various types of metamaterials utilizing printing technologies, which has strong benefit such as easy and low cost.

**Acknowledgements** This work has been supported in part by a Grant-in-Aid for Scientific Research on Innovative Areas (No. 22109001 and No. 25109709) from the Ministry of Education, Culture, Sports, Science, and Technology (MEXT), Japan and in part by a Grant-in-Aid for Scientific Research, KAKENHI, for Scientific Research (B) (No. 25286063) from the Japan Society for the Promotion of Science (JSPS), Japan, and by the joint research project of the Institute of Laser Engineering, Osaka University (No. 2015B1-17). The authors acknowledge graduate students worked on the project: Ryosuke Takagi, Yuto Inose, Shota Kuromiya, and Hiroki Mori.

## References

1. J.B. Pendry, A.J. Holden, D.J. Robbins, W.J. Stewart, *IEEE Trans. Microw. Theory Tech.* **47**, 2075 (1999)
2. V.M. Shalaev, *Nat. Photonics* **1**, 41 (2007)
3. H. Chen, C.T. Chan, P. Sheng, *Nat. Mater.* **9**, 387 (2010)
4. C.M. Soukoulis, M. Wegener, *Nat. Photonics* **5**, 523 (2011)
5. J.B. Pendry, A. Aubry, D.R. Smith, S.A. Maier, *Science* **337**, 549 (2012)
6. N.I. Zheludev, Y.S. Kivshar, *Nat. Mater.* **11**, 917 (2012)
7. R.A. Shelby, D.R. Smith, S. Schultz, *Science* **292**, 77 (2001)
8. T.J. Yen, W.J. Padilla, N. Fang, D.C. Vier, D.R. Smith, J.B. Pendry, D.N. Basov, X. Zhang, *Science* **303**, 1494 (2004)
9. M. Rahm, J.-S. Li, W.J. Padilla, *J. Infrared Millim. Terahertz Waves* **34**, 1 (2013)
10. A.K. Azad, J.F. O'Hara, R. Singh, H.-T. Chen, A.J. Taylor, *IEEE J. Sel. Top. Quantum Electron.* **19**, 8400416 (2013)
11. M. Hangyo, *Jpn. J. Appl. Phys.* **54**, 120101 (2015)
12. W.J. Padilla, A.J. Taylor, C. Highstrete, M. Lee, R.D. Averitt, *Phys. Rev. Lett.* **96**, 107401 (2006)
13. H.-T. Chen, J.F. O'Hara, A.K. Azad, A.J. Taylor, R.D. Averitt, D.B. Shrekenhamer, W.J. Padilla, *Nat. Photonics* **2**, 295 (2008)
14. H.-T. Chen, W.J. Padilla, J.M.O. Zide, A.C. Gossard, A.J. Taylor, R.D. Averitt, *Nature* **444**, 597 (2006)
15. L. Ju, B. Geng, J. Horng, C. Girit, M. Martin, Z. Hao, H.A. Bechtel, X. Liang, A. Zettl, Y.R. Shen, F. Wang, *Nat. Nanotechnol.* **6**, 630 (2011)
16. S.H. Lee, M. Choi, T.-T. Kim, S. Lee, M. Liu, X. Yin, H.K. Choi, S.S. Lee, C.-G. Choi, S.-Y. Choi, X. Zhang, B. Min, *Nat. Mater.* **11**, 936 (2012)
17. T. Driscoll, H.-T. Kim, B.-G. Chae, B.-J. Kim, Y.-W. Lee, N.M. Jokerst, S. Palit, D.R. Smith, M.D. Ventra, D.N. Basov, *Science* **325**, 1518 (2009)
18. H. Tao, A.C. Strikwerda, K. Fan, W.J. Padilla, X. Zhang, R.D. Averitt, *Phys. Rev. Lett.* **103**, 147401 (2009)
19. Y. Kitoh, M. Yamashita, T. Nagashima, M. Hangyo, *Jpn. J. Appl. Phys.* **40**, L1113 (2001)
20. H.K. Yoo, C. Kang, Y. Yoon, H. Lee, J.W. Lee, K. Lee, C.-S. Kee, *Appl. Phys. Lett.* **99**, 061108 (2011)
21. T. Matsui, R. Takagi, K. Takano, M. Hangyo, *Opt. Lett.* **38**, 4632 (2013)
22. T. Matsui, H. Mori, Y. Inose, S. Kuromiya, K. Takano, M. Nakajima, M. Hangyo, *Jpn. J. Appl. Phys.* **55**, 03DC12 (2016)
23. Y. Nakato, M. Shioji, H. Tsubomura, *J. Phys. Chem.* **85**, 1670 (1981)
24. K. Murata, J. Matumoto, A. Tezuka, Y. Matsuba, H. Yokoyama, *Microsyst. Technol.* **12**, 2 (2005)
25. K. Murata, K. Masuda, *E-Print Printable Electron.* **1**, 108 (2011)
26. K. Takano, T. Kawabata, C.F. Hsieh, K. Akiyama, F. Miyamaru, Y. Abe, Y. Tokuda, R.P. Pan, C.L. Pan, M. Hangyo, *Appl. Phys. Express* **3**, 016701 (2010)
27. K. Takano, Y. Chiyoda, T. Nishida, F. Miyamaru, T. Kawabata, H. Sasaki, M.W. Takeda, M. Hangyo, *Appl. Phys. Lett.* **99**, 161114 (2011)
28. M.A. Green, *Sol. Energy Mater. Sol. Cells* **92**, 1305 (2008)
29. H.K. Yoo, C. Kang, J.W. Lee, Y. Yoon, H. Lee, K. Lee, C.-S. Kee, *Appl. Phys. Express* **5**, 072402 (2012)

**Part III**  
**Metamaterials in Microwave**  
**Frequencies**



# Chapter 9

## Negative Refractive Index Materials Composed of Metal Patterns and the Applications



Hiroshi Kubo

**Abstract** In this chapter, the aim is to highlight some negative refractive index (NRI) materials composed of metal patterns. First, the dielectric and the magnetic properties of opposite metal patterns are discussed. After the operation principle and the effective permittivity and the permeability are described, a NRI material composed of metal patterns on both sides of dielectric substrates is shown. Secondly, a bulk-type NRI material composed of metal patterns on side face of dielectric prisms is shown. The metal patterns constitute a slot line where a wave is guided. To understand how the structure causes the electric and the magnetic properties, the structure is expressed by the equivalent circuit for the guided modes and, using the circuit, the dispersion characteristics are calculated. A NRI slab lens is made of the material to measure the refocus distributions.

### 9.1 Introduction

A variety of metamaterial structures has been studied for basic theoretical researches and applications [1–4]. Metamaterials are composed of many elements smaller than wavelength. Exotic properties of metamaterials are determined by the properties of the elements and their arrangement. Metals are mostly used to design the elements exhibiting negative permittivity and negative permeability. Current flows along the metal surface and electric charges are stored on the surface. Magnetic energy and electric energy concentrate around the metal, so that the metal element has a significant effect on the properties of the metamaterials.

Metal patterns can be formed on a planar substrate comparatively easily by photolithography. In microwave frequencies and millimeter frequencies, this fabrication method is applied to make a planar circuit on a dielectric substrate like a microstrip line and a coplanar line. Recently, metal patterns have also been fabricated by printing technology and can be formed even on the surfaces of a three-dimensional shape by

---

H. Kubo (✉)

Yamaguchi University, 2-16-1 Tokiwadai, Yamaguchi Ube 755-8611, Japan  
e-mail: [kubo@yamaguchi-u.ac.jp](mailto:kubo@yamaguchi-u.ac.jp)

laser processing. In this chapter, we present negative refractive index (NRI) materials composed of metal patterns as follows;

1. One-dimensional (1D) NRI materials composed of metal strips on dielectric substrates
2. Two-dimensional (2D) NRI materials composed of metal patterns on side face of prisms

NRI materials have been composed of two kinds of elements, which are dielectric elements with negative permeability and magnetic elements with negative permeability, directed in proper directions according to an electric field and a magnetic field, respectively. First, we show that an 1D NRI material can be materialized by employing only a kind of metal pattern with a simple rectangular shape on multilayer substrates [5].

The transmission line method has been proposed for creating NRI materials [6–8]. By applying this method to microstrip lines and coplanar lines, planar circuit-type left-handed transmission lines have been formed on planar substrates [9–11]. Second, we construct a bulk-type 2D NRI material by forming planar circuit patterns on the side faces of dielectric prisms arranged in a 2D lattice [12, 13].

## 9.2 NRI Materials Composed of Metal Strips

NRI materials are composed of two kinds of elements, where one is  $\varepsilon$ -negative and the other is  $\mu$ -negative, or  $\mu$ -negative elements put in a guided-wave structure whose effective permittivity becomes negative owing to evanescent fields below the cutoff frequency of the transverse electric-type (TE-type) guided mode. The elements do not necessarily exhibit negative properties of permittivity or permeability for all components of electromagnetic field vectors. Thus, the elements have to be arranged so as to face the appropriate directions according to the left-handed field vectors in the material. Moreover, the direction of the guided field vector in the material should be made the same as the direction of an incident wave field from the outside to decrease reflection. For example, a guided field in the material is excited efficiently by a plane wave from the air when the electric field vector and the magnetic field vector lie in the transverse plane. These conditions are necessary for constituting NRI materials, but they cause problems in the fabrication process of the materials.

The material in Fig. 9.1 is composed of metal strips on both sides of a dielectric substrate. The periodic metal strips on the front side or the back side work as elements with negative permittivity for an external electric field parallel to the longer direction of the strips. A phaser chart of the external electric field  $E_{ext}$  and charges  $q$  is shown in Fig. 9.2a. In the resonant circuit of inductance of a strip and capacitance of a gap between the upper and lower strips, current  $I$  flows in phase delayed by  $90^\circ$  from the external electric field above the resonant frequency. Charges are stored at both ends of the strip in phase delayed by  $90^\circ$  from the current. Thus, positive charges

**Fig. 9.1** Structure composed of metal strips on both sides of dielectric substrates. The metal strips are arranged in the same position on the front and back sides

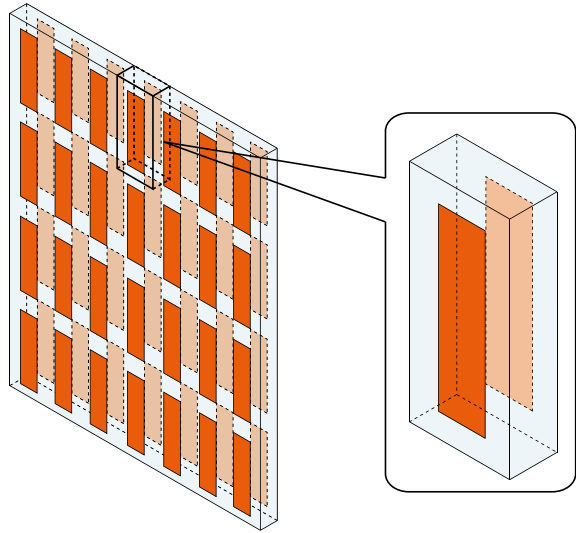
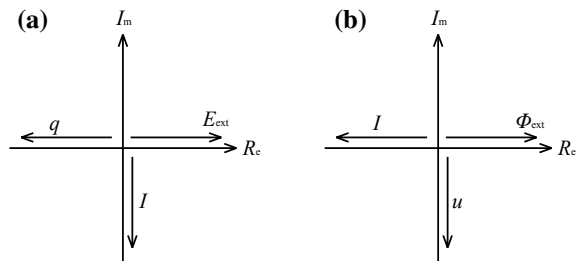


**Fig. 9.2** Phasor chart. **a** External electric field  $E_{ext}$  and charges  $q$  at the top of a metal strip. **b** External magnetic flux  $\Phi_{ext}$  and current  $I$  along a pair of metal strips



are stored at the end opposite to the direction of the electric field. This phenomenon indicates that the element has negative permittivity.

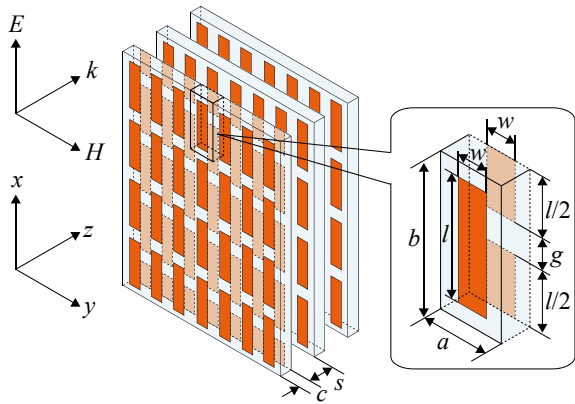
A pair of strips on both sides works as an element with negative permeability for the external magnetic flux  $\Phi_{ext}$  crossing the two strips horizontally as shown in the phasor chart of Fig. 9.2b. Inductance of a pair of strips and capacitance between the two strips constitute a resonant circuit. Electromotive force  $u$  along the closed circuit is in phase delayed by  $90^\circ$  from the external magnetic flux. Current  $I$  flows in phase delayed by  $90^\circ$  from the electromotive force above the resonant frequency. Owing to the current, magnetic field is generated in the opposite phase to the external magnetic field. This phenomenon indicates that the element has negative permeability.

The structure of metal strips exhibits negative permittivity for vertical electric fields and negative permeability for horizontal magnetic fields. Thus, it may act as an NRI material suited to x-polarized wave propagating in the z-direction. However, the former resonant frequency is higher because the capacitance between the gap is small compared with the capacitance between a pair of strips on both sides. It is difficult to obtain negative permittivity in the same frequency region as negative permeability [14].

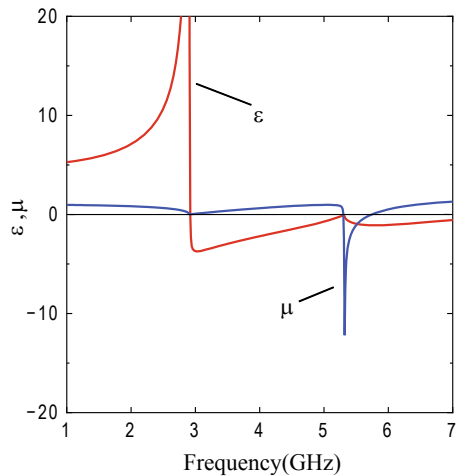
Figure 9.3 shows the structure of a NRI material composed of only rectangular metal strips on dielectric substrates. The strips are arranged alternately on the front side and the back side. The front strips and the back strips are overlapped to make the capacitance between them large. Effective permittivity and permeability of a unit cell for a plane wave are plotted in Fig. 9.4. Both permittivity and permeability are negative from 5.3 to 5.8 GHz.

Figure 9.5a shows schematic electric fields around the strips, where only permittivity is negative. The electric fields between the upper and lower strips indicate that positive charges are stored at the upper ends of the front and back strips and negative charges are stored at the lower ends. The strips work as dielectric elements. The electric fields between the front and back strips indicate that there exists capacitance between them. This capacitance is added to the capacitance of the gap to decrease the former resonant frequency.

**Fig. 9.3** NRI structure composed of metal strips on both sides of dielectric substrates. The metal strips are arranged alternately on the front and the back sides. Reprinted from Kubo, H., Yoshida, T., Sanada, A., and Yamamoto, T., IEICE Trans. Electron., Vol. E95-C, No. 10, p. 1658, 2012. Copyright©2012 IEICE



**Fig. 9.4** Effective permittivity and permeability of a unit cell composed of the strip pair for  $a = 12.8$ ,  $b = 12.8$ ,  $c = 1.6$ ,  $s = 3.2$ ,  $g = 0.8$ ,  $w = 3.0$ ,  $l = 12$  mm,  $\epsilon_r = 10.2$ , and  $\tan \delta = 0.0004$



**Fig. 9.5** Electric field distributions. The black arrows denote the directions of currents. **a** The electric fields of the front and back strips are in phase. **b** The electric fields of the front and back strips are in reverse phase. Reprinted from Kubo, H., Yoshida, T., Sanada, A., and Yamamoto, T., IEICE Trans. Electron., Vol. E95-C, No. 10, p. 1659, 2012. Copyright©2012 IEICE

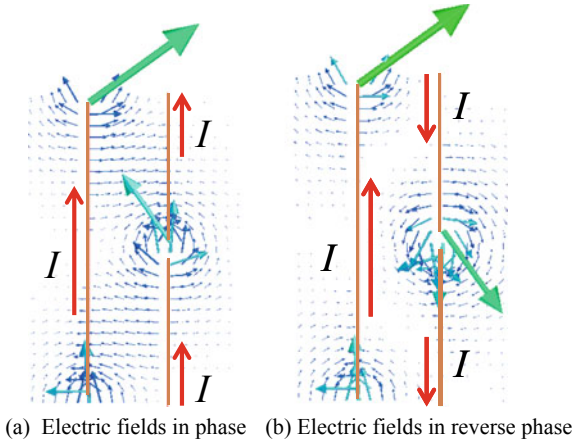


**Fig. 9.6** Dispersion relations of NRI material composed of metal strips arranged alternately on the front side and the back side for  $a = 12.8$ ,  $b = 21.8$ ,  $c = 3.175$ ,  $s = 12$ ,  $w = 3$  mm,  $\epsilon_r = 2.17$ , and  $\tan \delta = 0.00085$ . Reprinted from Kubo, H., Yoshida, T., Sanada, A., and Yamamoto, T., IEICE Trans. Electron., Vol. E95-C, No. 10, p. 1659, 2012. Copyright©2012 IEICE

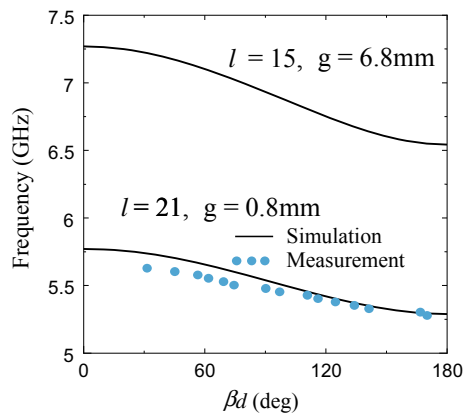
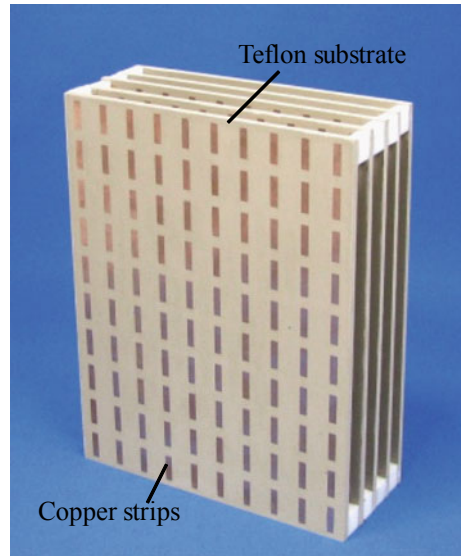


Figure 9.5b shows schematic electric fields in the frequency range where both the permittivity and the permeability are negative. The electric fields circulating in the closed circuit of the front and back strips indicate that the strips act as a magnetic element.

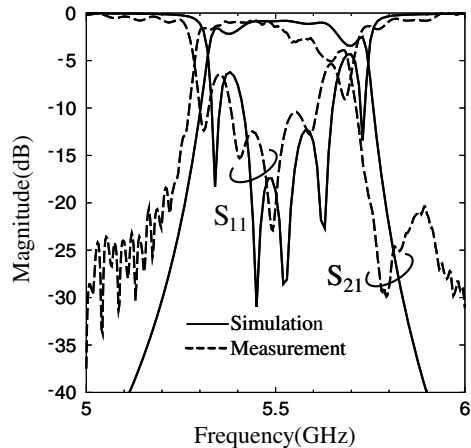
Dispersion relations proper to the mode in NRI materials are found in Fig. 9.6. The dispersion curves move to lower frequency when the gap  $g$  is short. The reason is that the inductance and the capacitance of the elements become large and the two resonant frequencies decrease.

Figure 9.7 is a photograph of a material with five layers of substrates. Incident waves from a horn antenna into the material are used to measure the phase constant. The values are plotted by dark circles in Fig. 9.6. The transmission and reflection characteristics are plotted by the broken lines in Fig. 9.8.  $S_{21}$  is normalized by  $S_{21}$  without the material.  $S_{11}$  is normalized by  $S_{11}$  of a copper sheet used instead of the material.

**Fig. 9.7** Photograph of a fabricated NRI material with five layers of dielectric substrates. Rectangular metal substrates. Rectangular metal strips are arranged on both sides of the dielectric substrates. The strips on the back side are shifted by half in the vertical direction



**Fig. 9.8** Transmission characteristics of the NRI material composed of five layers in Fig. 9.7. The simulation results are calculated by a full-wave electromagnetic simulator. Reprinted from Kubo, H., Yoshida, T., Sanada, A., and Yamamoto, T., IEICE Trans. Electron., Vol. E95-C, No. 10, p. 1660, 2012. Copyright©2012 IEICE



### 9.3 Bulk-Type NRI Materials Composed of Slot Lines

The transmission line theory presents a useful guideline for constituting NRI materials. NRI materials are expressed by a distributed constant circuit with series capacitances and shunt inductances. By applying the theory to planar circuits, microstrip line-type and coplanar line-type left-handed transmission lines have been investigated [9–11]. The theory has also been applied to form metal patterns with the distributed constant circuit on a three-dimensional shape to constitute a 2D bulk-type NRI material [12, 13].

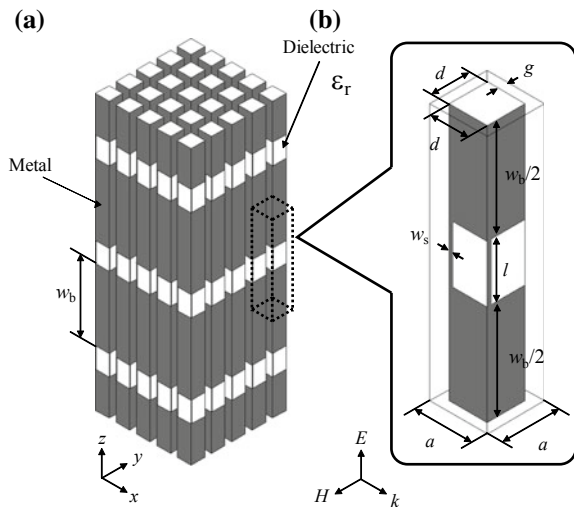
### 9.3.1 Square Lattice Arrangement

Figure 9.9a shows a structure operating as a 2D bulk-type NRI material for the wave incident from the air. As shown in Fig. 9.9b, unit cells are stacked periodically to constitute a rectangular prism of the structure. Prisms are arranged in the form of a square lattice in the  $x$ - $y$  plane. Two wide metal patterns with width  $w_b$  constitute a slot line on dielectric rectangular prisms. A guided mode of the slot line has a  $z$ -polarized electric field between the two patterns and has a magnetic field in the  $x$ - $y$  plane. Thin metal patterns between the two patterns act as shunt inductance. Two wide patterns facing each other between two prisms make up a capacitor in the  $x$ -direction or  $y$ -direction. The two wide patterns act as a stub of the slot line on prisms. When a  $z$ -polarized plane wave is incident, electric fields have the same phase at every slot line on a prism, and the stub works as a short stub with length  $w_b/2$ . Then impedance of the stub is capacitive when  $w_b/2$  is between a quarter wavelength and a half wavelength. By adjusting the geometrical parameters properly, the structure has shunt inductance and series capacitance in a frequency region.

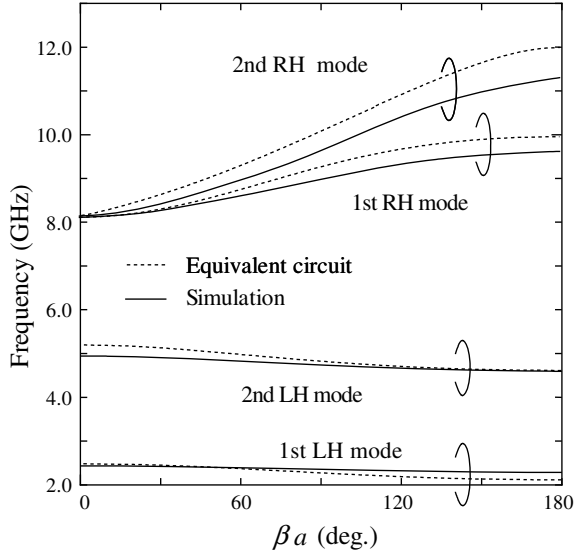
Dispersion relations of  $z$ -polarized waves are plotted in Fig. 9.10. The solid lines are dispersion curves calculated by a full-wave electromagnetic simulator. The first and second right-handed (RH) modes and left-handed (LH) modes are plotted. In the second LH mode, the electric fields have the same phase at every slot line along a prism. In the first LH mode, the same phase and reverse phase are repeated alternately. When a  $z$ -polarized plane wave or cylindrical wave is incident to the material, the second mode is excited more efficiently for a  $z$ -polarized plane wave or cylindrical wave incident from the outer region to the material.

The behavior of the modes propagating along the unit cells arranged in the  $x$ -direction is expressed by an equivalent circuit. The arrangement of unit cells in a

**Fig. 9.9** Structure of a 2D bulk-type NRI material composed of slot lines on dielectric prisms arranged in the form of a rectangular lattice. **a** The overall structure. **b** A unit cell. Reprinted from Kubo, H., Nishibayashi, K., Yamamoto, T., and Sanada, A., IEICE Trans. Electron., Vol. E96-C, No. 10, p. 1274, 2013. Copyright©2013 IEICE



**Fig. 9.10** Dispersion relations of a 2D bulk-type NRI material composed of slot lines for  $a = 12$ ,  $d = 8$ ,  $g = 2$ ,  $l = 12$ ,  $w_b = 42$ ,  $w_s = 0.1$  mm, and  $\epsilon_r = 2.0$ . The solid lines are dispersion relations calculated by an electromagnetic simulator. The broken lines are dispersion relations calculated by the equivalent circuit. Reprinted from Kubo, H., Nishibayashi, K., Yamamoto, T., and Sanada, A., IEICE Trans. Electron., Vol. E96-C, No. 10, p. 1274, 2013. Copyright©2013 IEICE



line has a symmetric plane parallel to the  $x$ - $y$  plane and a symmetric plane parallel to the  $x$ - $z$  plane. The horizontal symmetric plane is replaced with an electric wall, and the vertical symmetric plane is replaced with a magnetic wall. Unit cells are divided by the two walls into four parts with height  $(w_b + l)/2$  and width  $d/2$ . One period of a quarter part of a unit cell arrangement is expressed by the circuit in Fig. 9.11. This circuit is not an elaborate one based on an electromagnetic analysis. However, we can understand the operating principle to clarify the relation between the propagation mode and the structure from the circuit. The parameters are  $a = 12$  mm,  $d = 8$  mm,  $g = 2$  mm,  $l = 12$  mm,  $w_b = 42$  mm,  $w_s = 0.1$  mm, and  $\epsilon_r = 2.0$ . Two wide patterns facing each other in the air gap with width  $2g$  constitute a stub with width  $d/2$  and height  $2g$ . The stub impedance  $Z_s$  is expressed by

$$Z_s = \begin{cases} jZ_{ch} \tan \frac{k_0 w_b}{2} & \text{for electric wall} \\ -jZ_{ch} \cot \frac{k_0 w_b}{2} & \text{for magnetic wall} \end{cases} \quad (9.1)$$

$$Z_{ch} = \sqrt{\frac{\mu_0}{\epsilon_0}} \frac{d}{4g} \quad (9.2)$$

$$k_0 = \omega \sqrt{\epsilon_0 \mu_0} \quad (9.3)$$

where the expression of the electric wall or the expression of the magnetic wall is chosen based on the field of the propagation mode. The magnetic wall is chosen for the first mode, and the electric wall is chosen for the second mode.

The narrow metal pattern with length  $l/2$  acts as an inductor. The inductance value  $L_p$  is given by [15]



$$L_p = 100l \left( \log \frac{l}{2w_s} + 1.19 + 0.22 \frac{2w_s}{l} \right) \tag{9.4}$$

where  $L_p$  is in nanohenries.  $L_p$  is determined to be 6.36 nH. The calculated curves in Fig. 9.9 show that two RH modes have a cutoff frequency at 8.11 GHz. If the cutoff is caused by the resonant frequency of the series component of the equivalent circuit,  $Z_s$  has to be same value for the two modes. However,  $Z_s$  depends on the boundary conditions, and the values of the first and second modes are different. Thus, the cutoff frequency depends on the resonant frequency of the shunt components of  $L_p$  and  $C_p$ . When the parallel circuit of  $L_p$  and  $C_p$  is capacitive, RH modes can be guided. From  $L_p = 6.36$  nH and the cutoff frequency 8.11 GHz,  $C_{sh}$  is determined to be 0.0605 pF.

The dielectric and the two wide metal patterns constitute a slot line as described previously.  $L_s$  is the series inductance of the transmission line composed of the dielectric, the wide pattern, and an electric wall on the symmetric plane. The value of  $L_s$  is half that of the slot line. After analyzing the slot line with an electromagnetic simulator and calculating the line constants of the distributed constants circuit,  $L_s$  is determined to be 7.75 nH.  $L_s/2$  is the series inductance caused by the wide pattern with length  $d/2$  parallel to the  $y$ - $z$  plane.

When the same four-port circuits in Fig. 9.11 are connected infinitely, the phase constant of the guided modes in the distributed constant circuit is given by [16]

$$\cos \beta a = \frac{A + D}{2} \tag{9.5}$$

$A$  and  $D$  are given by

$$A = D = \frac{(j\omega L_s + Z_s)(2Z_{sh} + j\omega L_s) + 2Z_{sh}(Z_{sh} + j\omega L_s)}{2Z_{sh}^2} \tag{9.6}$$

where

$$Z_{sh} = \frac{j\omega L_p}{1 - \omega^2 L_p C_p} \tag{9.7}$$

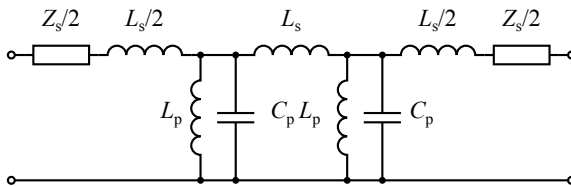


**Fig. 9.11** Equivalent circuit for the modes propagating along the unit cells arranged in the  $x$ -direction. This circuit corresponds to one period of a quarter part of the arrangement of unit cells in a line. Reprinted from Kubo, H., Nishibayashi, K., Yamamoto, T., and Sanada, A., IEICE Trans. Electron., Vol. E96-C, No. 10, p. 1275, 2013. Copyright©2013 IEICE

Using these equations, dispersion curves are calculated for the first and the second LH modes and the first and second RH modes. The curves are plotted by the broken lines in Fig. 9.10 for comparison with the simulation result. Though differences are found between the curves obtained from the two kinds of methods, the two LH modes of the equivalent circuit propagate in the frequency regions near the perspective propagation regions of the two LH modes by simulation, respectively. The circuit describes the characteristics of the NRI material. These results confirm that the RH and LH waves of the material are guided by the slot lines with inductive patterns and capacitive stubs.

The refractive indices are calculated from simulation results of dispersion relations. In Fig. 9.12, the curves denoted by  $\Gamma$ - $X$  are the dispersion relations of the second LH mode propagating in the  $x$ -direction, and the curves denoted by  $\Gamma$ - $M$  are those in the direction tilted by  $45^\circ$ . The difference between refractive indices in the two directions indicates the anisotropy of the material. The anisotropy is small near the  $\Gamma$  point because the cell size  $a$  is sufficiently small compared with the wavelength in the material. The anisotropy becomes large as the phase constant increases.

The refocus characteristics of NRI material lenses have been studied for confirming sub-wavelength resolution [17–19]. The flat lens in Fig. 9.13 is made of the 2D bulk-type NRI material, where unit cells cut to half height are arranged in the form of 15 rows and 9 columns on a copper plate. The unit cells are covered with a brass plate when the propagation characteristics are measured. Around the flat lens, metal strips are soldered on the copper plate for converting between an incident wave from the outside and the LH mode.

The layout of the system for measuring the wave field through the flat lens is illustrated in Fig. 9.14. The source is 54 mm away from the lens. From the source

**Fig. 9.12** Refractive index of 2D bulk-type NRI material composed of slot lines for  $a = 12$ ,  $d = 8$ ,  $g = 2$ ,  $\ell = 12$ ,  $w_b = 42$  mm, and  $\varepsilon_r = 2.0$ . The solid lines show the refractive index for the second LH modes propagating in the  $x$ -direction, and the broken lines show the refractive index for the second LH modes propagating in the direction tilted by  $45^\circ$ . Reprinted from Kubo, H., Nishibayashi, K., Yamamoto, T., and Sanada, A., IEICE Trans. Electron., Vol. E96-C, No. 10, p. 1276, 2013. Copyright©2013 IEICE

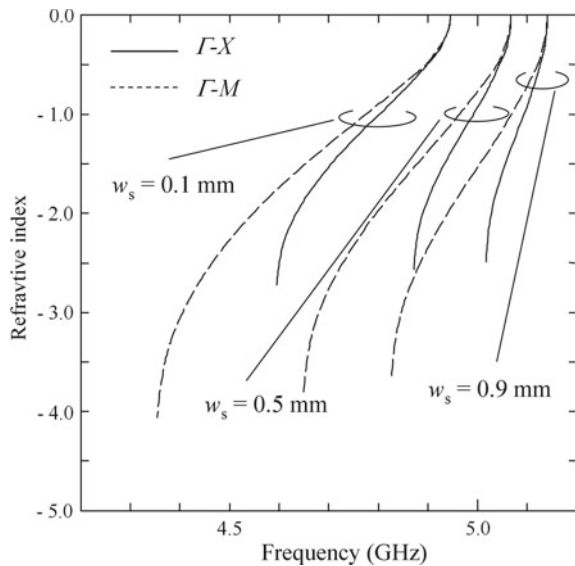


**Fig. 9.13** Photograph of a flat lens made of 2D bulk-type NRI material for  $a = 12$ ,  $d = 8$ ,  $g = 2$ ,  $\ell = 12$ ,  $w_b = 42$ ,  $w_s = 0.1$  mm, and  $\epsilon_r = 2.0$ . Metal patterns are also formed on the top of the unit cells for contacting with the upper brass plate. Reprinted from Kubo, H., Nishibayashi, K., Yamamoto, T., and Sanada, A., *IEICE Trans. Electron.*, Vol. E96-C, No. 10, p. 1278, 2013. Copyright©2013 IEICE

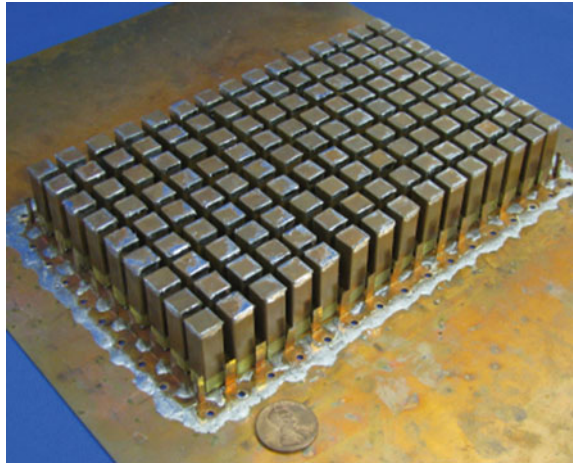
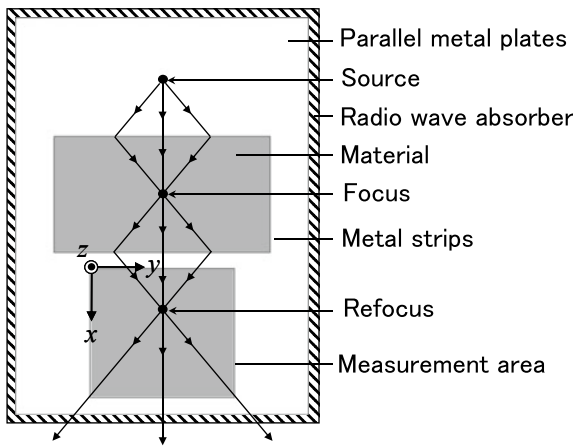


**Fig. 9.14** Layout of a source point, the flat lens made of the 2D bulk-type NRI material, and the area for measuring the electric field of the wave through the lens. Reprinted from Kubo, H., Nishibayashi, K., Yamamoto, T., and Sanada, A., *IEICE Trans. Electron.*, Vol. E96-C, No. 10, p. 1278, 2013. Copyright©2013 IEICE



point, a cylindrical wave is excited by a probe, a  $z$  polarized wave propagates in the parallel plates, and the wave is incident into the lens. The electric field of the wave through the lens is observed at the measurement area at 4.84 GHz.

The measured field distributions are depicted in Figs. 9.15 and 9.16. The origin is 15 mm away from the edge of the lens. The magnitude distribution shows that the field is large in the area of  $23 \text{ mm} < x < 78 \text{ mm}$  and  $48 \text{ mm} < y < 65 \text{ mm}$ . The phase distribution shows that the equiphase lines are almost parallel to the  $y$ -axis in the area of  $45 \text{ mm} < x < 60 \text{ mm}$ . Equiphase lines around the area indicate that the wave focuses at the area and expands to the lower area. The program for depicting the phase chart does not normally operate in the area where the phase crosses the branch cut from  $-\pi$  to  $\pi$ , so that the phase distribution changes rapidly from  $\pi$  to  $-\pi$  near  $x = 10, 60$ , and  $110 < x < 130 \text{ mm}$ . It is wrong of the distribution to vary from blue to green and from green to red there. It is correct to jump from blue to red.

**Fig. 9.15** Magnitude of an electric field distribution of the wave through the flat lens made of the 2D bulk-type NRI material. The origin is 15 mm away from the edge of the outer unit cell of the lens in the  $x$ -direction. Reprinted from Nishibayashi, K., Kubo, H., and Sanada, A., Proceedings of the 2010 IEICE General Conference, C-2-107, p. 150, 2010. Copyright©2010 IEICE

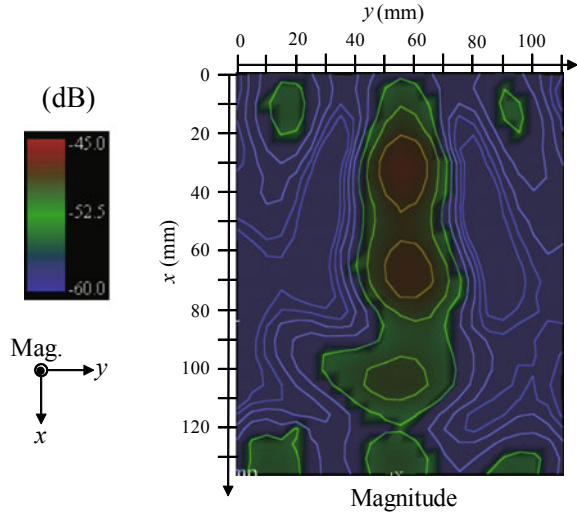
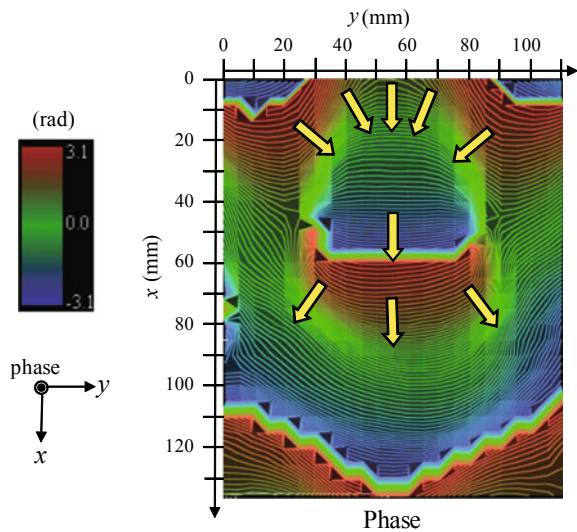


**Fig. 9.16** Phase of an electric field distribution of the wave through the flat lens made of the 2D bulk-type NRI material. The origin is 15 mm away from the edge of the outer unit cell of the lens in the  $x$ -direction. Reprinted from Nishibayashi, K., Kubo, H., and Sanada, A., Proceedings of the 2010 IEICE General Conference, C-2-107, p. 150, 2010. Copyright©2010 IEICE



The electric field distributions of the waves through the lens are measured for excitation by two sources with the same phase. The two sources are separated by  $d_{sour}$ . Figures 9.17 and 9.18 show the magnitude and the phase distributions for  $d_{sour} = 60$  mm, respectively. Taking account also of the phase distribution, the centers of two refocus points are estimated on the magnitude distribution. The two centers are denoted by the arrows, and the distance between them is about 60 mm.

In the same way, magnitude and phase distributions are depicted for  $d_{sour} = 40$  and 30 mm in Figs. 9.19, 9.20, 9.21, and 9.22, respectively. The distance between the

**Fig. 9.17** Magnitude of an electric field distribution of the wave through the flat lens made of the 2D bulk-type NRI material. The wave is excited by two sources with the same phase. The two sources are 60 mm apart

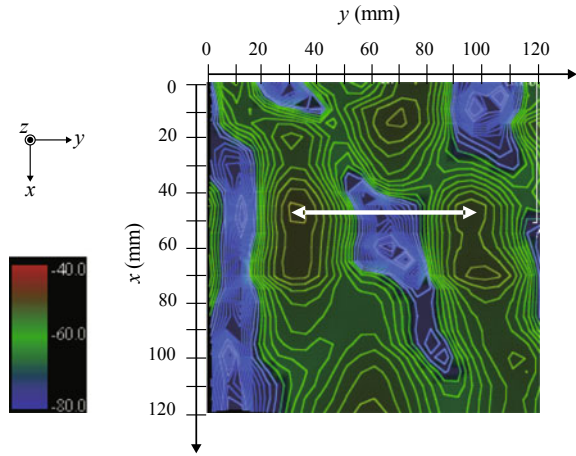
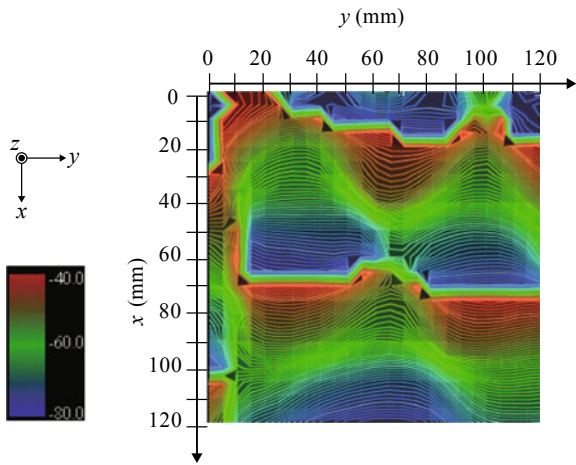


**Fig. 9.18** Phase of an electric field distribution of the wave through the flat lens made of the 2D bulk-type NRI material. The wave is excited by two sources with the same phase. The two sources are 60 mm apart

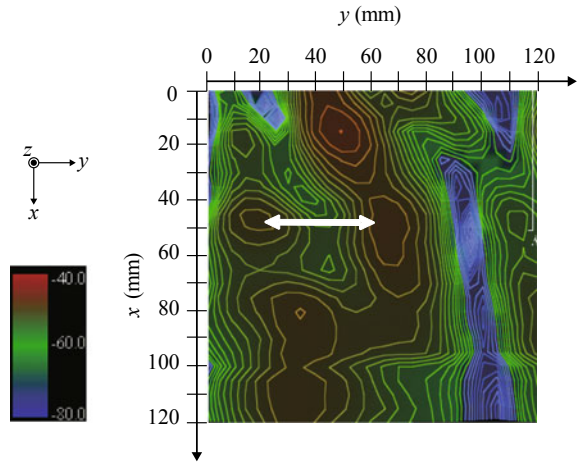


two centers is about 40 mm when  $d_{sour} = 40$  mm. As center points are indistinct when  $d_{sour} = 30$  mm, arrows are drawn by inferring only from the magnitude distribution.

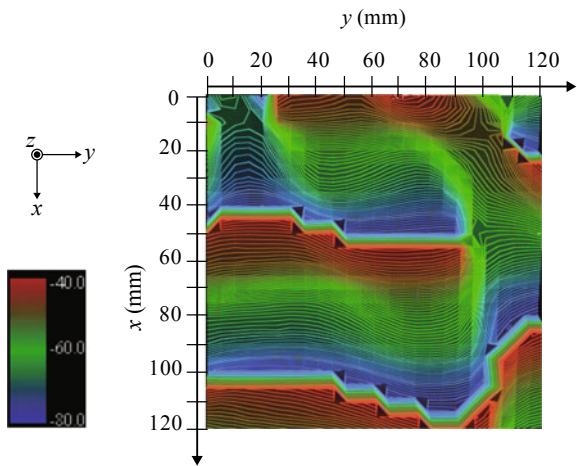
### 9.3.2 Hexagonal Lattice Arrangement

Figure 9.23a shows a structure acting as a 2D bulk-type NRI material composed of dielectric cylinders with metal patterns. The metal patterns have the same roles as those on the prisms of the 2D bulk-type NRI material in the previous subsection. The cylinders are arranged in the form of a hexagonal lattice in the  $x$ - $y$  plane to improve the anisotropy. The refractive indices and anisotropic factor for  $z$ -polarized waves are

**Fig. 9.19** Magnitude of an electric field distribution of the wave through the flat lens made of the 2D bulk-type NRI material. The wave is excited by two sources with the same phase. The two sources are 40 mm apart



**Fig. 9.20** Phase of an electric field distribution of the wave through the flat lens made of the 2D bulk-type NRI material. The wave is excited by two sources with the same phase. The two sources are 40 mm apart



plotted in Fig. 9.24.  $\Gamma$ -K and  $\Gamma$ -M denote the directions in the wavenumber space as shown in the figure. The refractive indices are calculated from the wavenumber. The isotropy factor is defined here by the following equation:

$$\frac{n_{\Gamma-M} - n_{\Gamma-K}}{n_{\Gamma-M}} \tag{9.8}$$

where  $n_{\Gamma-K}$  and  $n_{\Gamma-M}$  denote the refractive indices in each direction. Anisotropy is improved compared with the NRI material composed of prisms arranged in the form of a square lattice. The anisotropy factor is small near the frequency where the refractive indices are equal to 1.



**Fig. 9.21** Magnitude of an electric field distribution of the wave through the flat lens made of the 2D bulk-type NRI material. The wave is excited by two sources with the same phase. The two sources are 30 mm apart

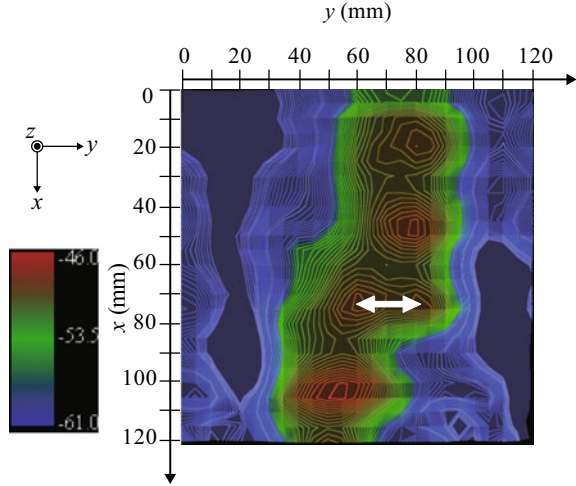
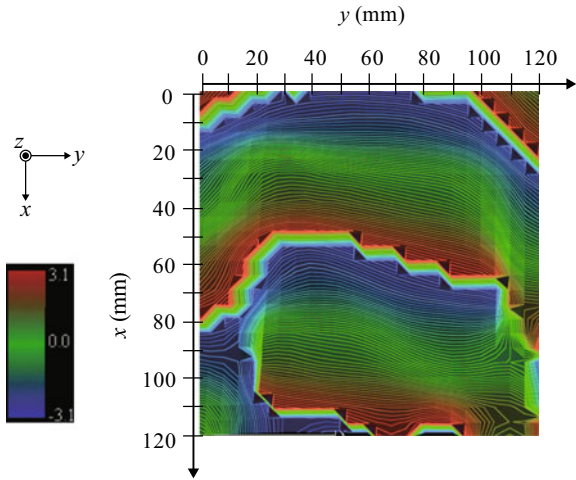


**Fig. 9.22** Phase of an electric field distribution of the wave through the flat lens made of the 2D bulk-type NRI material. The wave is excited by two sources with the same phase. The two sources are 30 mm apart



In Fig. 9.25, transmission characteristics are plotted for a  $z$ -polarized wave propagating in the  $x$ -direction in the material composed of five layers of unit cells. To transform the incident wave into the wave guided in the material, dielectric cylinders with a metal strip pattern are arranged beside the unit cells of the input and the output. The wave is transmitted from 4.08 to 4.49 GHz where the LH mode exists in the material.

The flat lens in Fig. 9.26 is made of 2D bulk-type NRI material composed of slot lines on cylinders, where 218 of unit cells cut to half height are arranged in the form of a hexagonal lattice on a copper plate. Dielectric cylinders with a metal strip for conversion are put around the unit cells. The unit cells are covered with a brass plate when the propagation characteristics are measured. A wave propagating between

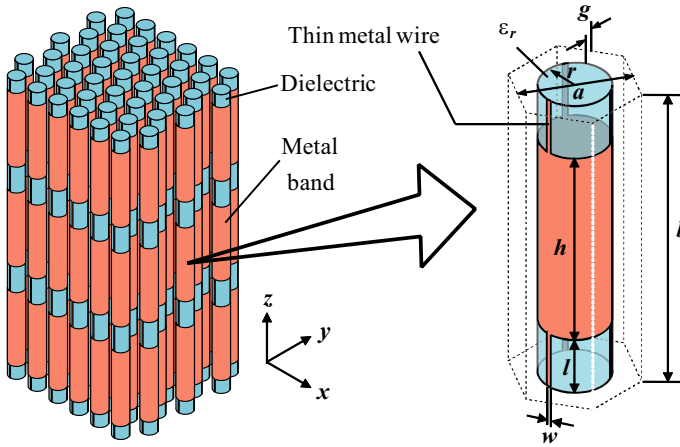


**Fig. 9.23** Structure of 2D bulk-type NRI material composed of slot lines on cylinders arranged in the form of a hexagonal lattice. The figure shows the overall structure (L) and a unit cell (R). Reprinted from Fukushima, T., Kubo, H., Sanada, A., and Yamamoto, T., Proceedings of the 2011 IEICE Society Conference, C-2-77, p. 115, 2011. Copyright©2011 IEICE

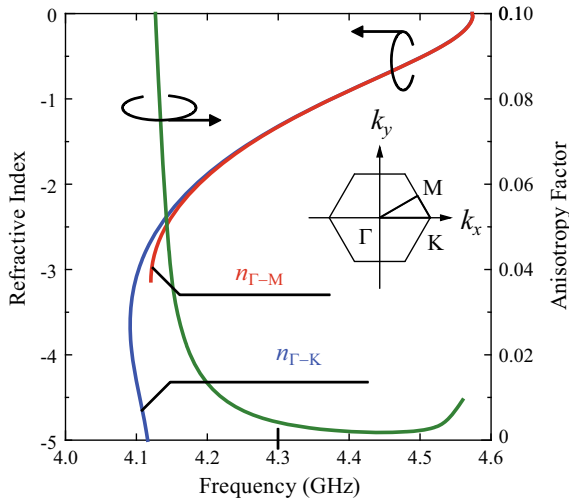


**Fig. 9.24** Frequency characteristics of the refractive index and anisotropy factor of 2D bulk-type NRI material composed of slot lines on cylinders for  $a = 13.4$ ,  $b = 54.4$ ,  $w = 0.1$ ,  $h = 40.0$ ,  $\ell = 7.0$ ,  $r = 5.2$ ,  $g = 1.5$  mm, and  $\epsilon_r = 2.0$ . The refractive index is calculated from the phase constant of waves propagating in the  $x$ -direction or in the direction tilted from  $x$ -axis by  $30^\circ$ . Reprinted from Fukushima, T., Kubo, H., Sanada, A., and Yamamoto, T., Proceedings of the 2011 IEICE Society Conference, C-2-77, p. 115, 2011. Copyright©2011 IEICE



**Fig. 9.25** Transmission characteristics of 2D bulk-type NRI material composed of slot lines on cylinders for  $a = 13.4$ ,  $b = 54.4$ ,  $w = 0.1$ ,  $h = 40.0$ ,  $\ell = 7.0$ ,  $r = 5.2$ ,  $g = 1.5$  mm, and  $\epsilon_r = 2.0$ . A plane wave is incident into five layers of unit cells in the  $x$ -direction. Transformers are set at both ends

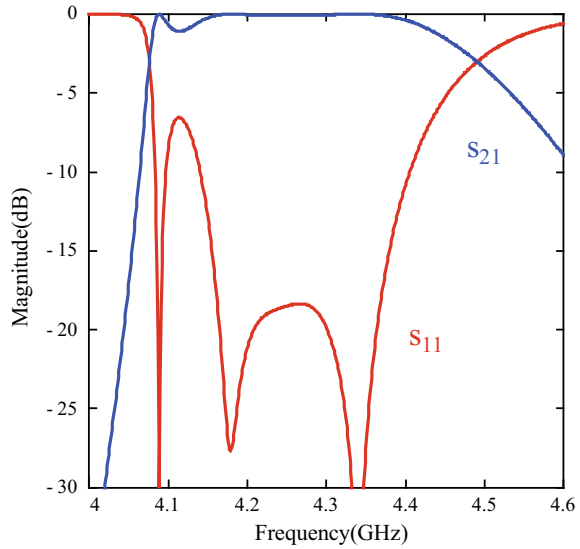
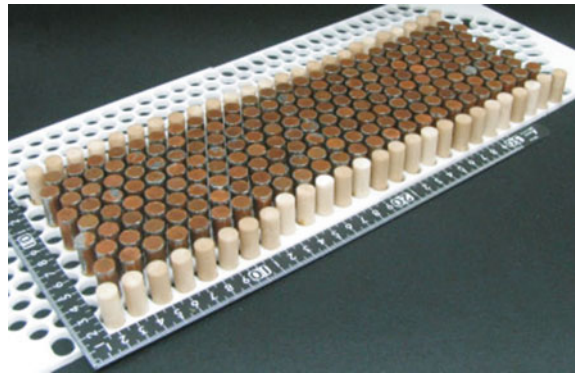


**Fig. 9.26** Photograph of the 2D bulk-type NRI material composed of slot lines on cylinders. Metal patterns are also formed on the top of the cylinders for contacting with the upper brass plate. Reprinted from Yamamoto, T., Kubo, H., Fukushima, T., and Sanada, A., IEICE Transactions (Japanese Edition), Vol. J99-C, No. 12, p. 584, 2016. Copyright©2016 IEICE



the upper plate and the lower plate is excited by a probe located at a point 46 mm away from the lens. The electric field of the wave through the lens is observed in the measurement area at 4.30 GHz. The measured field distributions are depicted in Figs. 9.27 and 9.28.

The origin is 24 mm away from the edge of the lens in the  $y$ -direction. The field is maximum at  $x = 25$ ,  $y = 78$  mm. The equiphase line at  $x = 20$  mm is almost straight parallelly to the  $y$ -axis. The equiphase lines in the areas  $x < 20$  mm and  $x > 20$  mm are curved in an arc shape. These lines indicate that the wave focuses near the point and expands to the lower area. Also in these figures, the program for depicting the phase chart does not normally operate at the area where the phase crosses the branch cut from  $-180$  to  $180^\circ$ , so that black zones are found in  $30 < y < 60$  mm and in  $90 < y < 100$  mm. It is wrong that the phase of  $-180^\circ$  is colored in black. It is correct to change from blue to red.

**Fig. 9.27** Magnitude of an electric field distribution of the wave through the flat lens made of the 2D bulk-type NRI material composed of slot lines on cylinders. The wave is excited by a source located 46 mm away from the lens. The origin is 14 mm away from the lens in the  $x$ -direction. Reprinted from Yamamoto, T., Kubo, H., Fukushima, T., and Sanada, A., IEICE Transactions (Japanese Edition), Vol. J99-C, No. 12, p. 585, 2016. Copyright©2016 IEICE

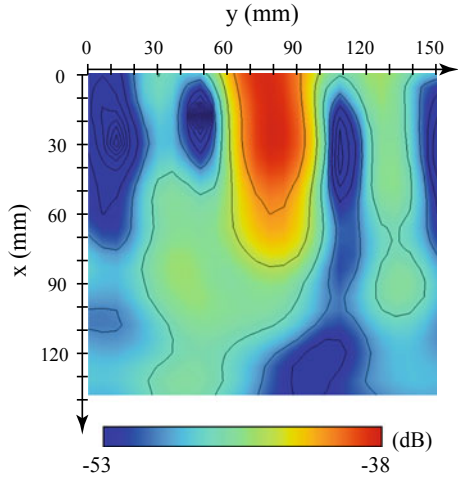
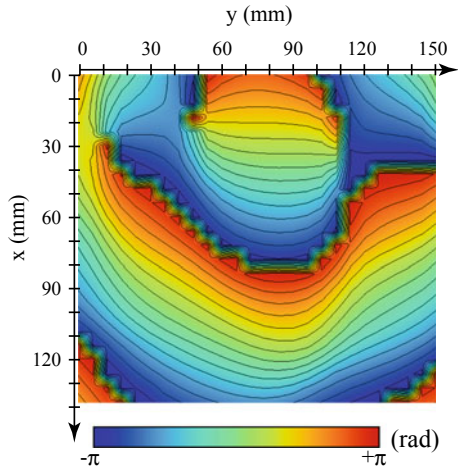


**Fig. 9.28** Phase of an electric field distribution of the wave through the flat lens made of 2D bulk-type NRI material composed of slot lines on cylinders. Reprinted from Yamamoto, T., Kubo, H., Fukushima, T., and Sanada, A., IEICE Transactions (Japanese Edition), Vol. J99-C, No. 12, p. 585, 2016. Copyright©2016 IEICE



## References

1. D. Sievenpiper, L. Zhang, R.F.J. Broas, N.G. Alexopolous, E. Yablonovitch, High-impedance electromagnetic surfaces with a forbidden frequency band. *IEEE Trans. Microw. Theor. Tech.* **47**, 2059–2074 (1999)
2. D.R. Smith, W.J. Padilla, D.C. Vier, S.C. Nemat-Nasser, S. Schultz, Composite medium with simultaneously negative permeability and permittivity. *Phys. Rev. Lett.* **84**, 4184–4187 (2000)
3. R. Maeques, J. Mukai, F. Mesa, F. Medina, Left-handed-media simulation and transmission of EM waves in subwavelength split-ring-resonator-loaded metallic waveguide. *Phys. Rev. Lett.* **89**(18), 183901-1-183901-4 (2002)
4. J.B. Pendry, D. Schurig, D.R. Smith, Controlling electromagnetic fields. *Science* **312**, 1780–1782 (2006)

5. H. Kubo, T. Yoshida, A. Sanada, T. Yamamoto, Propagation characteristics on the left-handed mode in the material composed of metal strips put alternately on front and back sides. *IEICE Trans. Electron.* **E-95C**, 1658–1661 (2012)
6. A.A. Oliner, A Periodic-structure negative-refractive-index medium without resonant elements, in *IEEE-APS/URSI International Symposium Digest*, vol. 2, p. 41 (2002)
7. C. Caloz, T. Itoh, Application of the transmission line theory of left-handed (LH) materials to the realization of a microstrip LH transmission line, in *IEEE-APS International Symposium Digest*, pp. 412–415 (2002)
8. A.K. Iyer, G.V. Eleftheriades, Negative refractive index media using periodically L-C loaded transmission lines. *IEEE-MTT International Symposium Digest*, pp. 1067–1070 (2002)
9. C. Caloz, T. Itoh, Transmission line approach of left-handed (LH) materials and microstrip implementation of an artificial LH transmission line. *IEEE Trans. Antennas Propagat.* **52**, 115–1166 (2004)
10. A. Sanada, C. Caloz, T. Itoh, Characteristics of the composite right/left-handed transmission lines. *IEEE Microw. Wirel. Compon. Lett.* **14**, 68–70 (2004)
11. A. Grbic, G.V. Eleftheriades, Experimental verification of backward wave radiation from a negative refractive index metamaterial. *J. Appl. Phys.* **92**, 5930–5935 (2002)
12. H. Kubo, K. Nishibayashi, T. Yamamoto, A. Sanada, New negative refractive index material composed of dielectric prisms with metal patterns. *IEICE Trans. Electron.* *E-96C*, 1273–1280 (2013)
13. T. Fukushima, H. Kubo, A. Sanada, T. Yamamoto, Negative index material composed of cylinders with a metal pattern, in *Proceedings of the Asia-Pacific Microwave Conference*, pp. 530–533 (2011)
14. H. Kubo, H. Iida, A. Sanada, A Sheet-type metamaterial with rejection characteristics in a frequency range, in *2009 Asia-Pacific Microwave Conference Proceedings*, Singapore, CD-ROM (2009)
15. R.E. Chaddock, The application of lumped element techniques to high frequency hybrid integrated circuits. *Radio Electron. Eng.* **44**, 414–420 (1974)
16. R.E. Collin, *Foundations for Microwave Engineering*, Chap. 8 (McGraw-Hill, New York, 1992)
17. A. Grbic, G.V. Eleftheriades, Overcoming the diffraction limit with a planar left-handed transmission-line lens. *Phys. Rev. Lett.* **92**, 117403-1-117403-4 (2004)
18. A. Sanada, C. Caloz, T. Itoh, Planar distributed structures with negative refractive index. *IEEE Trans. Microw. Theor. Tech.* **52**, 1252–1263 (2004)
19. Y. Sato, T. Ueda, Y. Kado, T. Itoh, Design of isotropic 3-D multilayered CRLH metamaterial structures using conductive mesh plates and dielectric resonator, in *Proceedings of Asia-Pacific Microwave Conference*, pp. 526–529 (2011)

# Chapter 10

## Functional Composites of Discharge Plasmas and Solid Metamaterials



Osamu Sakai and Akinori Iwai

**Abstract** Discharge plasmas are composed of electrons and ions, and their permittivity is dynamic and tunable. Conventional metamaterials are composed of designed functional microstructures of solid materials, and become extraordinary wave media such as negative-permeability materials. The composites of the plasmas and the metamaterials are well mixed to show dynamic properties coming from plasmas and extraordinary outputs based on metamaterials. Here, we describe their theoretical basis and topical features observed in microwave experiments. Beyond properties of tunability, such composite “plasma metamaterials” work well as nonlinear and high-energy-carrier metamaterials, unlike conventional solid-state metamaterials.

### 10.1 Introduction

#### 10.1.1 Roles of Discharge Plasmas in Metamaterial Structure

Plasmas and metamaterials are composites of a huge number of individual units. Metamaterials in a conventional definition (without plasmas) are composed of microstructures whose sizes are much smaller than the wavelength of a given electromagnetic wave [1, 2]. Usually, the microstructure as a unit with the same shape forms a spatially periodic structure, and it is called a metamaterial (or metasurface, when its structure is two-dimensional [3]). Mathematical integral effects occur over space compared with the wavelength scale result in extraordinary outputs as averaged wave parameters in permittivity and permeability [4]. Discharge plasmas are composed of negatively charged electrons and positive ions, and internal free electrons with electron density  $n_e$  in a quasi-steady state affect parameters like permittivity [5]. Their

---

O. Sakai (✉) · A. Iwai  
The University of Shiga Prefecture, Hikone, Japan  
e-mail: [sakai.o@e.usp.ac.jp](mailto:sakai.o@e.usp.ac.jp)

A. Iwai  
Kyoto University, Kyoto, Japan

collective effects via Coulomb's forces between individual charged particles ensure charge neutrality over the size called the Debye length.

Although they are both composites, metamaterials and plasmas have very different features in structures. Metamaterials' configurations are robust; microstructures are usually metallic, and they are installed on supporters like insulator plates. The structure has a large volume fraction of vacancy.

On the other hand, the shape of plasma is flexible and adjustable. In plasmas, free electrons move freely with their kinetic energy, and rather immobile positive ions compensate electrons electrically. Then, the external shape of plasma and profiles of their internal  $n_e$  are controllable for a period with more than a time scale like particle diffusion time and depend on the consumption of the external power that generates and sustains plasmas. For instance, we successfully created a two-dimensional photonic-crystal-like structure that consists of  $17 \times 21$  columns of lengthy plasmas with 2.5-mm spatial periodicity; we never used any capillaries to confine plasmas. We can insert plasmas in the vacant space inside the metamaterials, which is one of the promising configurations as composites of plasmas and metamaterials [6].

Then, what are the advantages of plasmas in solid-state metamaterial structures? So far, most studies have been performed for controlling permittivity  $\varepsilon$ , whereas permeability  $\mu$  is designed by conventional metamaterial configurations. We note that  $\varepsilon$  is a *microscopic* one that depends on  $n_e$ ; free electrons work against electric fields of propagating electromagnetic waves. Then, its harmony with macroscopic  $\mu$  yields refractive index  $N$  and wave impedance  $Z$ . Several reports including experimental results have suggested that  $N$  can be negative by composites of plasmas and metamaterials [6, 7]. This composite has variable  $\varepsilon$  with fixed  $\mu$ . Unlike other tunable metamaterials that usually include small additional elements with tunability, we can directly change  $\varepsilon$  in this dynamic metamaterial. This fact can lead to nonlinearity in such metamaterials with historical heritage of nonlinear physics pursued in plasma science [8, 9].

In this chapter, we review previous studies and rich findings on several aspects of plasma metamaterials. After surveying the previous studies, we investigate  $\varepsilon$  and  $\mu$  in this type of metamaterial. Then, we touch on recent progress of plasma metamaterials, in particular, with tunability and nonlinearity.

### 10.1.2 Previous Studies on Plasma Metamaterials

There have been a huge number of studies on electromagnetic waves propagating in plasmas for several decades, since they include charged particles of electrons and ions that respond to them in various manners. Consequently,  $\varepsilon$  of plasmas takes various values, and becomes a tensor in cases where we apply an external magnetic field to plasmas; such reviews are found in older textbooks [10–12].

In this chapter, we focus on scalar  $\varepsilon$ , which is sufficiently unique to other wave media whose materials are solids, liquids, and gases. In 1990, there was a proposal stating that plasmas work as tools to control electromagnetic waves, such as reflectors

and absorbers [13]. In this proposal, plasmas are bulk materials, like plates and spheres. After that, a few reports pointed out functions of periodic plasma structures [14, 15], and they are called plasma photonic crystals [16]. As we will address later in Sect. 10.3.1, they show a number of attractive features like flexible bandgaps. Here, plasmas play roles on variable  $\varepsilon$  from  $+1$  to  $0$ , but another role of negative  $\varepsilon$  was recently pointed out [17]. Bandgaps are observed both in one-dimensional and two-dimensional plasma photonic crystals. Spatially, periodic structure also works as a wave media in a similar manner to surface plasmon polaritons.

$\varepsilon$  in plasmas can be easily negative in microwave frequencies if  $n_e$  is sufficiently high, and this property has been used in generation of surface-wave plasmas [18]. Thus, one may think that this property can be applied to obtain negative- $N$  materials by installation of negative- $\varepsilon$  plasmas and negative- $\mu$  metamaterials. After theoretical prediction on this concept [19], a few experimental studies verified negative- $N$  states in a composite of negative- $\varepsilon$  plasmas and negative- $\mu$  metamaterials, in which  $\varepsilon$  and  $N$  are dynamic and tunable [7, 20]; here, we call this composite *plasma metamaterial*. Recently, this concept has been extended to get dynamic metasurfaces using microplasma installation to functional surfaces [21]. Mainly, plasma metamaterials are being studied in this chapter.

## 10.2 Permittivity, Permeability, and Refractive Index in Plasma Metamaterial

Propagation of electromagnetic waves can be comprehended by refractive index  $N$ . When  $N$  is large, their wavelength  $\lambda$  becomes short, and vice versa. On the interface of multiple media, the impedance  $Z$  plays a crucial role; the transmission and reflection coefficients of electromagnetic waves depend on  $Z$ .

$\varepsilon$  and  $\mu$  are constituents of  $N$  and  $Z$ , and are displayed in Fig. 10.1 for various materials. Natural bulk materials have very limited values of  $\varepsilon$  and  $\mu$ ;  $\varepsilon$  is usually more than  $+1$ , and some solids like ferromagnetic materials show large positive  $\varepsilon$  values. Extraordinary cases are observed in metals in the photon range and in plasmas in the microwave range. Metamaterials studied so far have represented successful regulations of  $\varepsilon$  and  $\mu$  using elaborate designs of metallic and/or dielectric materials that *macroscopically* (or via spatial integration) create extraordinary values including those with a negative sign.

The point at which plasma metamaterials distinguish themselves from the other metamaterials is  $\varepsilon$ , which is less than  $+1$ , including negative values with very smooth continuity. In addition, these values of  $\varepsilon$  are achieved by *microscopic* properties from free electrons, unlike the metamaterials in which  $\varepsilon$  is macroscopically negative. Another point that is unique but requires careful design of configuration in plasma metamaterials is spatial merging of plasma and solid components for supporting metamaterials that *macroscopically* control  $\mu$ , as shown in Fig. 10.2. Metamaterials like double split ring resonators (DSRRs) usually form as metallic patterns on

**Fig. 10.1**  $\epsilon - \mu$  map for various materials. Dotted data points are experimentally obtained [26]. Reproduced with permission from Sakai et al., *Plasma Sources Sci. Technol.*, **Vol. 25**: 055019-1-10. Copyright 2016 IOP Publishing

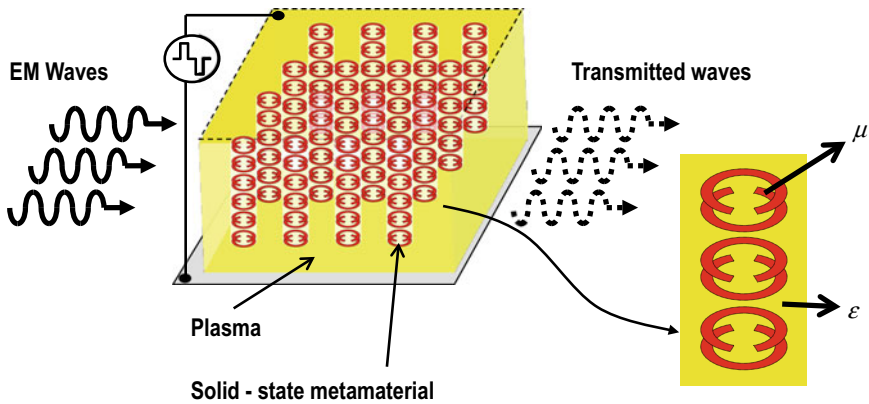
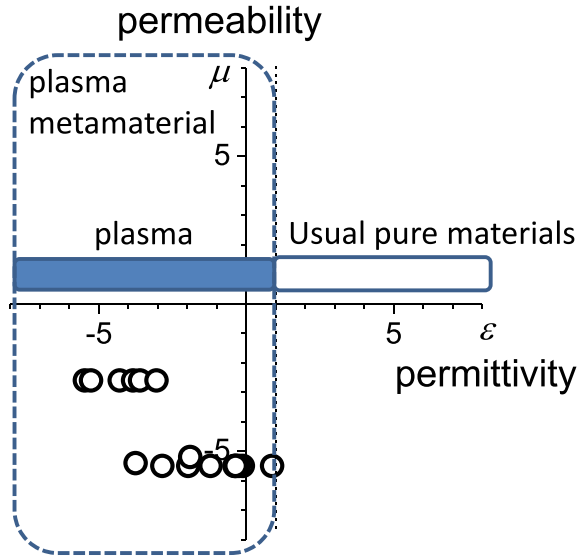


**Fig. 10.2** Conceptual view of composite of discharge plasma and solid metamaterial [6]. Reproduced with permission from Sakai et al., *Plasma Sources Sci. Technol.*, **Vol. 21**: 013001-1-18. Copyright 2012 IOP Publishing

dielectric plates, between which sufficient vacancies for plasma generations exist. Then, we have to be careful of effects of plasmas on  $\mu$  and those of metamaterials on  $\epsilon$ , and we have to confirm successful integration of these two parameters coming from microscopic and macroscopic values.

### 10.2.1 Permittivity

$\varepsilon$ , where we define it as relative permittivity in plasma, represents a response of media against electric field  $\mathbf{E}$ . When  $\mathbf{E}$  of an electromagnetic wave is in a plasma, free electrons with density  $n_e$ , which is not in dielectric dipole but free to yield external current, respond against  $\mathbf{E}$ . Instead of direct consideration of the constitution equation given by  $\mathbf{D} = \varepsilon\varepsilon_0\mathbf{E}$  using electric displacement field  $\mathbf{D}$  (whose vector notation with spatial directionality is  $\mathbf{D}$ ) and vacuum permittivity  $\varepsilon_0$ , we start from Ampere's law as with

$$\nabla \times \mathbf{H} = \varepsilon_0 \frac{\partial \mathbf{E}}{\partial t} + \mathbf{J}, \quad (10.1)$$

where  $\mathbf{H}$  is magnetic field, and  $t$  is time.  $\mathbf{J}$  is external current density by free electrons. When we take a component  $\tilde{X}$  via Fourier transform of a time evolution in such a manner as  $X = \tilde{X} \exp\{i(\omega t - kx)\}$  at a frequency  $\omega/2\pi$  with  $i = \sqrt{-1}$ , (10.1) becomes

$$\nabla \times \tilde{\mathbf{H}} = i\omega\varepsilon_0\tilde{\mathbf{E}} + \tilde{\mathbf{J}} = i\omega\varepsilon\varepsilon_0\tilde{\mathbf{E}}, \quad (10.2)$$

where  $k$  is wavenumber at a spatial position  $x$ .  $\varepsilon$  in plasma arises not from conductivity current but from displacement current, as shown in the following. Using the plasma frequency  $\omega_{pe}$ , where

$$\omega_{pe}^2 = \frac{e^2 n_e}{\varepsilon_0 m_e} \quad (10.3)$$

and  $e$  is elementary charge and  $m_e$  is electron mass, from momentum balance in plasma, the current density is deduced as

$$\frac{\partial \mathbf{J}}{\partial t} + \nu_m \mathbf{J} = \varepsilon_0 \omega_{pe}^2 \mathbf{E}, \quad (10.4)$$

where the first term of (10.4) on the left-hand side represents the displacement current and the second term is for the conductive one. The conversion of (10.4) to component at  $\omega/2\pi$  leads to the expression

$$(i\omega + \nu_m)\tilde{\mathbf{J}} = \varepsilon_0 \omega_{pe}^2 \tilde{\mathbf{E}}. \quad (10.5)$$

Then, from (10.2) and (10.5), we can derive

$$i\omega\varepsilon_0\tilde{\mathbf{E}} + \frac{\varepsilon_0\omega_{pe}^2}{i\omega + \nu_m}\tilde{\mathbf{E}} = i\omega\varepsilon\varepsilon_0\tilde{\mathbf{E}}, \quad \varepsilon = 1 + \frac{\omega_{pe}^2}{i\omega(i\omega + \nu_m)} = 1 - \frac{\omega_{pe}^2}{\omega^2(1 - i\nu_m/\omega)}. \quad (10.6)$$

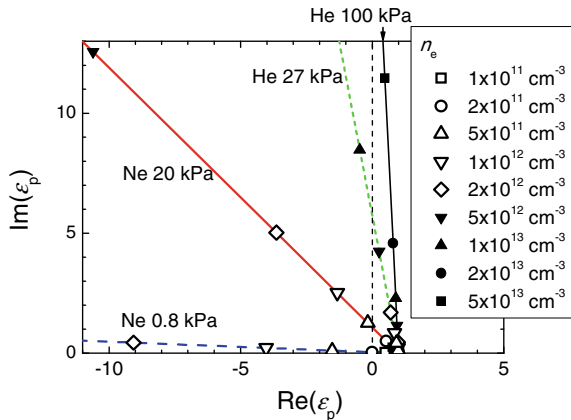


$\text{Re}(\varepsilon)$  shown in (10.6) arises from the displacement component given in (10.4), and it becomes negative as  $n_e$  increases. This implies that  $\mathbf{E}$  is the accelerating force in the electron momentum balance and drives electrons mainly with phase separation by  $\pi/2$  between  $\mathbf{E}$  and  $\mathbf{J}$  once it exists in plasma. Another point we should address here using Fig. 10.3 is a significant amount of  $\text{Im}(\varepsilon)$  as a source of conduction current and energy losses, which work as an attenuation term.

From a practical point of view, we can measure values of  $\varepsilon$  in plasma metamaterials, unlike conventional metamaterials. As shown in (10.6),  $\varepsilon$  is a function of  $n_e$  and  $v_m$ , where  $v_m$  depends on gas pressure and electron temperature  $T_e$  [22]. Gas pressure is easily measurable by an externally installed sensor on a chamber wall, and  $n_e$  and  $T_e$  can be measured by a Langmuir probe, which is a tiny metallic needle that collects a very small amount of current from the plasma at various bias voltages [23]. On the other hand,  $\varepsilon$  in conventional metamaterials should be estimated via parameter retrieval method [24] which assumes a homogeneous medium and is based on macroscopic averaging. Then, plasma metamaterials can be a tool to understand the detailed effects of  $\varepsilon$  in metamaterials.

When plasmas are adjacent to solid metamaterials that induce abnormal  $\mu$ , there is no change in  $\varepsilon$  except the periphery region on the solid surface in which sheaths exist [5]. The thickness of the sheaths is usually negligible in plasma metamaterials, and  $n_e$  and consequently,  $\varepsilon$  are still measurable. The substantial values of  $\varepsilon$  will be average ones weighed by spatial occupancy ratio between plasmas and solids. If plasmas are adjacent to solid metamaterials that induce abnormal  $\mu$ , both effects are superposed. Beyond such linear superposition, more complicated effects might arise from plasma-metamaterial composites, which are described in Sect. 10.2.2.

**Fig. 10.3** Variable  $\varepsilon$ , which is a complex value, depending on electron density  $n_e$  and gas pressure  $p$  [6]. Reproduced with permission from Sakai et al., *Plasma Sources Sci. Technol.*, Vol. 21: 013001-1-18. Copyright 2012 IOP Publishing



### 10.2.2 Permeability

Permeability  $\mu$  in plasma metamaterials is usually controlled by additional solid materials immersed in plasma. For instance, DSRRs and double-helix metallic wires work as abnormal metamaterials that can be with plasmas [7, 25, 26]. At some future stage, structured plasmas will create abnormal- $\mu$  metamaterials [6], but there have been no specific ideas proposed to achieve them in experiments.

When we put abnormal- $\mu$  metamaterials in plasmas, the values of  $\mu$  may change due to conductivity in plasmas. That is, from a point of view based on electromagnetics,  $\mu$  may change when the integral space that is defined to derive the equivalent value of  $\mu$  [4] contains plasmas that are sources of external current  $\mathbf{J}$  in (10.1).

This phenomenon is understandable using equivalent circuits with additional components by plasmas [25]. Figure 10.4a shows that the effects of plasmas are not only additional resistors but also capacitors with diodes due to the presence of sheaths on the surface of solids of metamaterials. When we apply a set of experimental parameters that are possible in real situations, the resonance frequency changes within 10% of initial values as shown in Fig. 10.4b. One thing that is also applicable for all metamaterials is that reactance circuits composed of inductances and capacitances have certain resonances in every design [19], and this model analysis indicates that design of negative  $\mu$  using equivalent circuits is powerful even if plasmas exist.

### 10.2.3 Refractive Index

Refractive index or dielectric constant  $N$  is a typical measure of propagating electromagnetic waves, and the formula

$$N = \sqrt{\varepsilon}\sqrt{\mu}, \quad (10.7)$$

can be derived from the wave equation based on (10.1) (Ampere's law) and the equation of Faraday's law if  $\varepsilon$  and  $\mu$  are uniform in a given medium [6]. General interpretation of parameters in metamaterials is based on the same assumption, and this formula for  $N$  is also applicable for plasma metamaterials. Here, however, to investigate effects of plasmas and metamaterials more carefully in a situation similar to an experimental setup, we use the dispersion relation of one-dimensional periodic structures [19], given as

$$\cos ka = \cos \frac{N\omega d_n}{c} \cos \frac{N_d\omega d_d}{c} - \frac{1}{2} \left( \frac{Z}{Z_d} + \frac{Z_d}{Z} \right) \sin \frac{N\omega d_n}{c} \sin \frac{N_d\omega d_d}{c}, \quad (10.8)$$

where  $a$  is periodic length of the one-dimensional structure,  $d_n$  and  $d_d$  are thickness of the plasma-metamaterial composite and that of dielectric, respectively,  $N_d$  and  $Z_d$  are refractive index and wave impedance in the dielectric layer, respectively, and  $c$

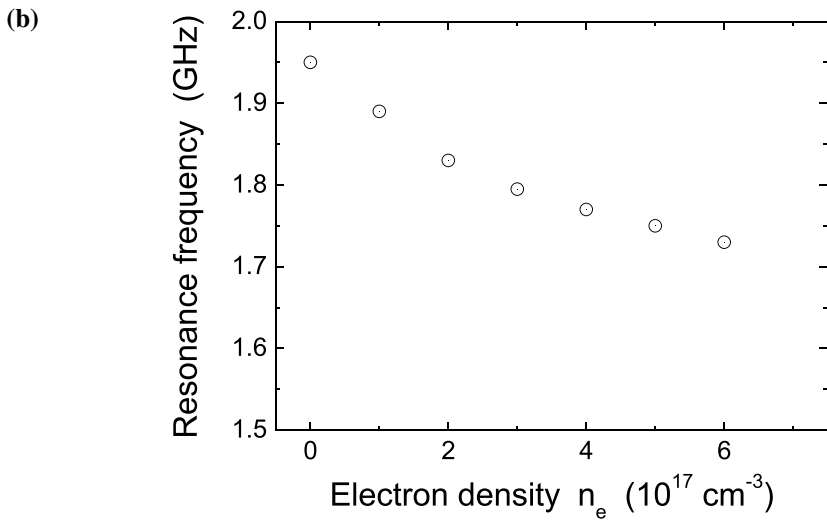
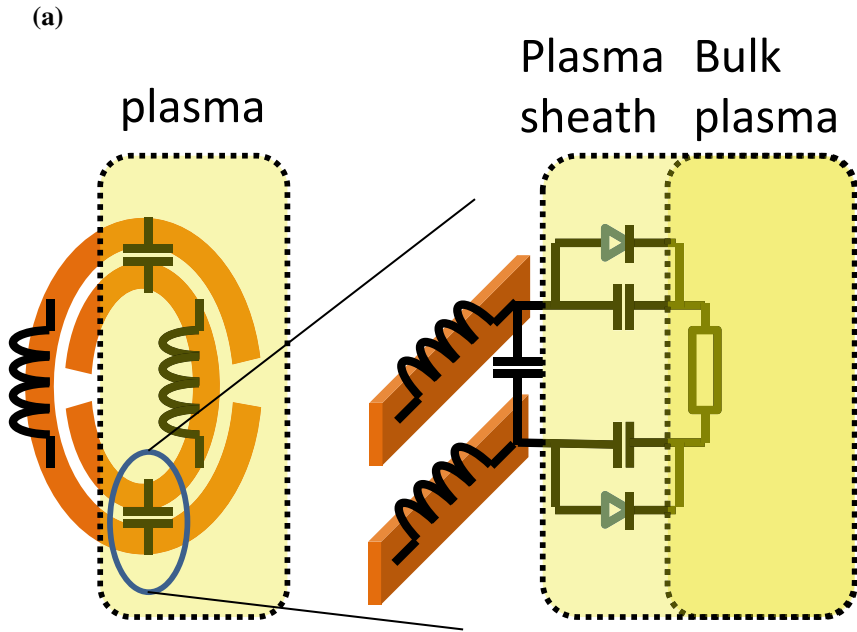


**Fig. 10.4** **a** Enlarged view of contact region between plasma and metamaterial (DSRR) with equivalent circuit [25]. **b** Change of resonance frequency of DSRR by increasing contact plasma with  $n_e$ . Reproduced with permission from Iwai and Sakai et al., *Appl. Phys. Express*, **Vol. 8**: 056201-1-4. Copyright 2015 The Japan Society of Applied Physics

is velocity of light. This dispersion relation handles spatial variation of  $\epsilon$  and  $\mu$  with suitable boundary conditions on each interface. Usually, such dispersion relations are investigated to see the effects of bandgaps, but we here study  $N$  at frequencies much lower than the bandgaps and with a much longer wavelength than the spatial periodic length, as shown in Fig. 10.5a.

**Fig. 10.5** Theoretical plots of  $\epsilon$ ,  $\mu$ ,  $N$ , and  $k$  in one-dimensional plasma-metamaterial composite in dielectric periodic gap as a function of  $\omega/2\pi$  [19]. Reproduced with permission from Adamovich and Sakai et al., *Phys. Plasmas*, **Vol. 17**: 123504-1-9. Copyright 2010 American Institute of Physics

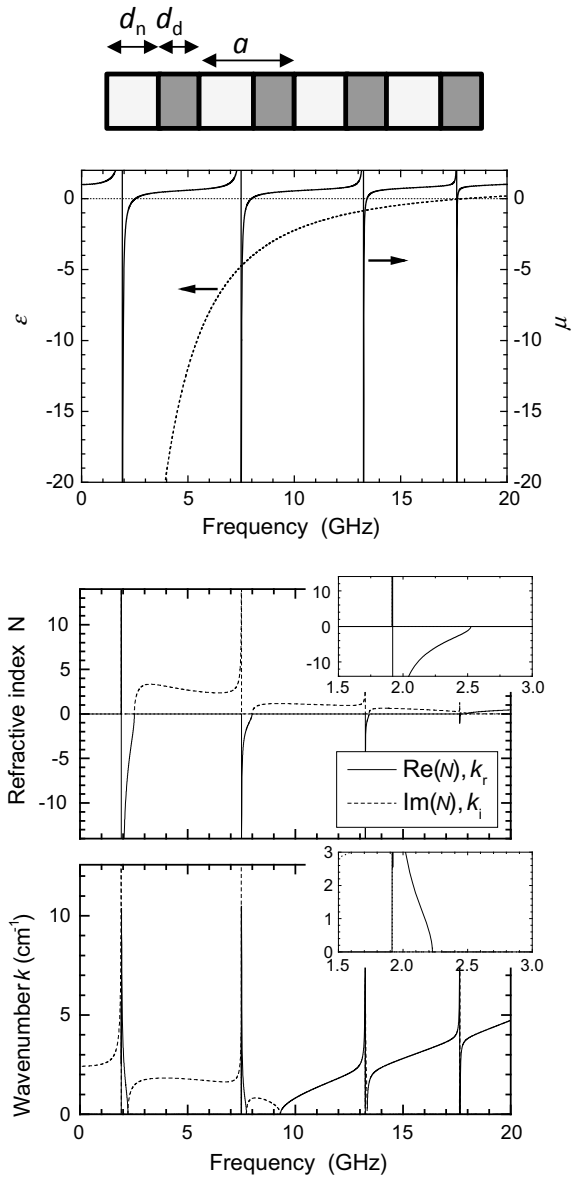
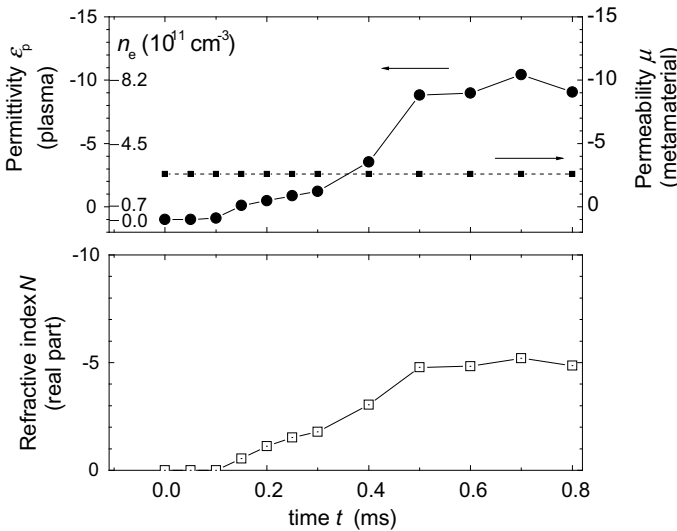


Figure 10.5b, c shows one typical example of wave parameters in plasma metamaterials with collisionless plasma, with  $\text{Im}(\varepsilon) = 0$ . This example indicates that, when  $\varepsilon$  and  $\mu$  are both negative,  $N$  becomes negative, which is consistent with (10.7). Further calculations shown in [19] demonstrate that, since plasma metamaterials can take various complex  $\varepsilon$ ,  $N$  can become negative with suitable negative  $\mu$  even if  $\text{Re}(\varepsilon)$  is positive. This condition is summarized as follows:

$$\arg(\varepsilon) + \arg(\mu) > \pi. \tag{10.9}$$

In one experiment in which DSRRs were installed in plasma space, the negative- $N$  state was successfully observed, as shown in Fig. 10.6. Since  $n_e$  is time-variant in plasmas,  $\varepsilon$  has time evolutions monitored by Langmuir probe measurement.  $\mu$  is drawn as a constant value in Fig. 10.6, which is a value measured via parameter retrieval method [24] with deformation from the initial value, although we confirmed that it is still in the negative polarity regardless of plasma effects.

We mentioned in Sect. 10.1 that  $\varepsilon$  is determined microscopically while  $\mu$  is defined macroscopically. However, plasma itself has a discrete structure composed of charged particles, whose sizes are also much smaller than the wavelength; this is by the definition of metamaterials. Although the sizes of charged particles and the unit sizes of metamaterials are different by several orders, they are both in the criteria of metamaterials, and they are well merged in plasmas metamaterials whose  $N$  is expressed as (10.7).



**Fig. 10.6**  $\varepsilon$ ,  $\mu$ , and  $N$  observed in experiments of plasma-metamaterial composite, with their time evolutions [35]. Reprinted from [35] by The Author(s) licensed under CC BY 3.0

## 10.3 Aspects Emerging in Plasma Metamaterials

### 10.3.1 Dynamic/Tunable Properties

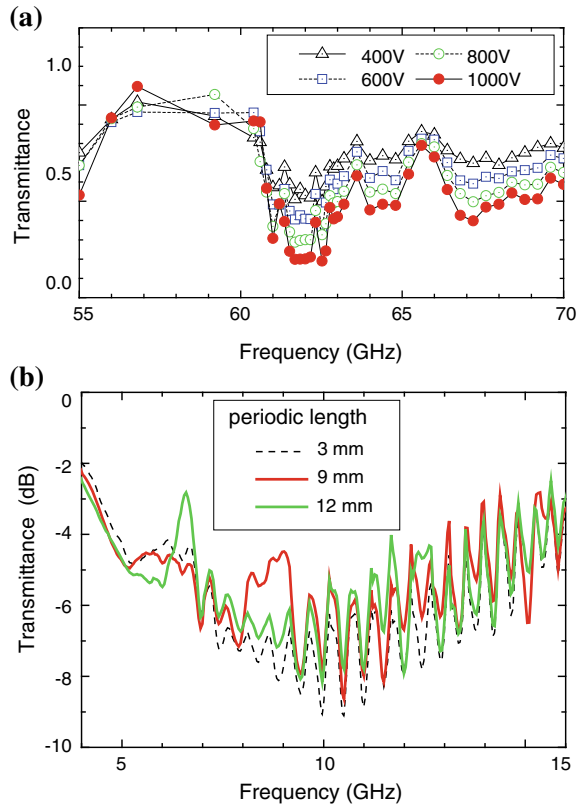
The dynamic properties are quite drastic in plasma metamaterials. There have been a number of proposals to make metamaterials dynamic, such as those in which photoconductive layers are activated by lasers [27]. However, the dynamic range of  $\varepsilon$ , for instance, from  $+1$  to  $-20$  in plasma metamaterials is so large that most metamaterials cannot work in a similar manner. This word “dynamic” can be replaced by those like “tunable” and “reconfigurable,” both of which are quite attractive points that are usually difficult to achieve, both by metamaterials and conventional pure materials.

The tunability often means shift of frequency properties due to the change in  $\text{Re}(\varepsilon)$ . Plasma metamaterials also offer this role in tunability, but they can also serve as adjustable attenuators, due to the change of  $\text{Im}(\varepsilon)$  via gas-pressure variations described in Sect. 10.2.1. That is, plasma metamaterials make metamaterials not only tunable as scalar filters but as *vector (phasor)* filters in wave complex plane. Also, the dynamic property includes drastic transitions caused by nonlinearity, which will be discussed in Sect. 10.3.2.

Dynamic properties were observed in plasma photonic crystals, in which  $\varepsilon$  and its spatial patterns can be deformed in time; this is a good illustration of how plasmas work as functional electromagnetic wave devices. Figure 10.7 displays various flexible modes of plasma photonic crystals. Figure 10.7a shows the wave attenuation in one bandgap of the  $\Gamma$ - $X$  direction in the two-dimensional square lattice, where this band gap is the lowest one at  $\omega a/2\pi c \sim 0.5$  with  $a = 2.5$  mm [28]; the plane-wave expansion method well predicts the bandgap frequency as 61–63 GHz [29]. Higher discharge voltage for plasma generation leads to lower value  $\varepsilon$  in comparison with the surrounding gas space in which  $\varepsilon \sim +1$ , enhancing the attenuation with larger  $\text{Im}(N)$  in the bandgap. Figure 10.7b shows the varying frequency of the lowest bandgap of the one-dimensional structure on the coplanar waveguide, by changing spatial periodicity of turn-on plasma columns [30–33]. We observed clear frequency shifts of the band path region according to the spatial periodicity; this is not a bandgap itself but a transmission band just below the bandgap due to electric field localization outside the lossy plasma.

A varying negative- $N$  material using a plasma-metamaterial composite is achieved as shown in Fig. 10.6. Microwave bulk plasma makes  $\varepsilon$  negative, and DSRR array makes  $\mu$  negative. As described in Sect. 10.2.3, the confirmation of two negative values is by separate measurements, and the reflection measurement of propagating microwaves confirms simultaneous achievement of these values and consequently a negative- $N$  value [26]. This configuration enables us to obtain negative- $N$  material, without states with positive  $\varepsilon$  and negative  $\mu$ , since the plasma generation is in the nonlinear scheme described in Sect. 10.3.2. Another example of negative- $N$  plasma metamaterial is investigated by measurement of elements in the scattering matrix  $S_{21}$ , which represents transmitting signals through the device under test. In this configuration, we can observe both positive- and negative- $\varepsilon$  plasmas with negative- $\mu$

**Fig. 10.7 a** Transmittance of waves propagating in two-dimensional structure of plasma columns [28]. With fixed structure, discharge voltage to generate plasmas is a variable for regulation. Reproduced with permission from Sakaguchi and Sakai et al., *J. Appl. Phys.*, **Vol. 101**: 073305-1-7. Copyright 2007 American Institute of Physics. **b** Transmittance of wave propagation in one-dimensional structure of plasma columns on coplanar waveguide [30]. With fixed discharge voltage, periodic length of turn-on plasma columns is a variable for regulation. Reproduced with permission from Sakai et al., *Plasma Phys. Contr. Fusion*, **Vol. 49**: B453–B463. Copyright 2007 IOP Publishing



metamaterial because plasma generation is in the linear scheme in the total system in which plasma generation is by low-frequency high discharge voltage.

### 10.3.2 Nonlinear Properties

Nonlinearity exists in various aspects and manners in science and technology. For instance, nonlinear dynamics is stability analysis using differential equations and can demonstrate processes in bifurcations and chaos. Nonlinear wave theory explains wave summation and division and leads to nonlinear photonics. Both nonlinearities are more or less significant when two factors exist: non-locality (through something transported, in terms of position vector  $\mathbf{r}$ ) and memory (in which the past events affect the current states, in terms of  $t$ ) effects. Nonlinear metamaterials have nonlinear components inside, and show various extraordinary properties beyond conventional metamaterials.

Plasma metamaterials can be nonlinear metamaterials, partly because plasmas are nonlinear media in terms of parameter dynamics and wave propagation due to their nonlocal and memory effects. Owing to addition of changes in wave propagation via abnormal  $\mu$  values, plasma metamaterials exhibit various features of nonlinear dynamics and photonics. The fundamental formulae that can describe the origin of nonlinearity in plasmas are the particle continuum equation and the momentum balance equation as in [33]:

$$\frac{\partial n_e(\mathbf{r}, t)}{\partial t} + \nabla \cdot (n_e(\mathbf{r}, t)\mathbf{v}_e(\mathbf{r}, t)) = n_e(\mathbf{r}, t)\mathbf{v}_e(\mathbf{r}, t)\alpha\left(\frac{E(\mathbf{r}, t)}{p}\right) - \beta n_e^2(\mathbf{r}, t), \tag{10.10}$$

$$m_e n_e(\mathbf{r}, t) \left\{ \frac{\partial \mathbf{v}_e(\mathbf{r}, t)}{\partial t} + (\mathbf{v}_e(\mathbf{r}, t) \cdot \nabla) \mathbf{v}_e(\mathbf{r}, t) \right\} = -n_e(\mathbf{r}, t)e\mathbf{E}(\mathbf{r}, t) - \nabla p_e(\mathbf{r}, t) - m_e n_e(\mathbf{r}, t)\mathbf{v}_e(\mathbf{r}, t)v_m, \tag{10.11}$$

where  $\mathbf{v}_e$  is electron fluid velocity,  $p$  is gas pressure,  $\beta$  is recombination coefficient, and  $p_e$  is electron pressure.  $\alpha$  is ionization coefficient that has a form including the exponential function. In addition,  $\mathbf{E}$  and  $\mathbf{H}$  in (10.1) and (10.2),  $\varepsilon$  in (10.6), and  $N$  in (10.7) also depend on  $\mathbf{r}$  and  $t$ . That is, parameters related to nonlinearity are  $n_e$ ,  $\mathbf{v}_e$ ,  $\mathbf{E}$ , and  $\mathbf{H}$  ( $\varepsilon$  and  $N$  are dependent on  $n_e$ ). In short, the network of this nonlinear system is displayed in Fig. 10.8.

Then, what are the effects of  $\mu$  on this system?  $\varepsilon$  and  $\mu$  work together in Ampere’s law and Faraday’s law. A negative sign of  $\varepsilon$  makes reversed direction of  $\mathbf{H}$ , giving rise to a negative sign of  $\mu$  in propagating waves.  $n_e$  of negative- $\varepsilon$  plasma should be higher than that of positive- $\varepsilon$  plasma, possible in a high  $E$  space; furthermore,  $n_e$  contains a term of  $\exp(E)$ , which is more highly nonlinear than  $E^2$  (for instance, in Kerr’s effect). The relation between  $n_e$  and  $E$  is nonlinear as shown in Fig. 10.8, and consequently,  $\varepsilon$  and  $N$  are in a strong nonlinear system.

More precisely, there should be the state with  $\varepsilon = +1$ , certainly in the case of a vacuum with  $n_e = 0$  and  $E = 0$  (no propagating waves), but the states with  $\varepsilon = 0 - +1$  should not exist when  $\mu < 0$ , since the waves that generate plasmas should be present. The working point with parameters of  $E$  and  $\varepsilon$  experiences a jump from the state with  $\varepsilon = +1$  to that with  $\varepsilon > 1$ . Details are shown in [33], and shown in Fig. 10.9 as a schematic drawing. Figure 10.9 clearly shows this jump or

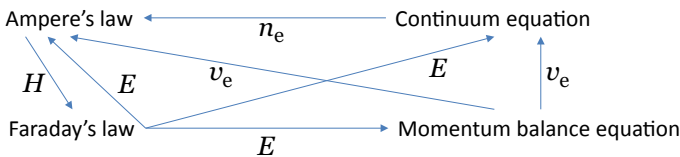
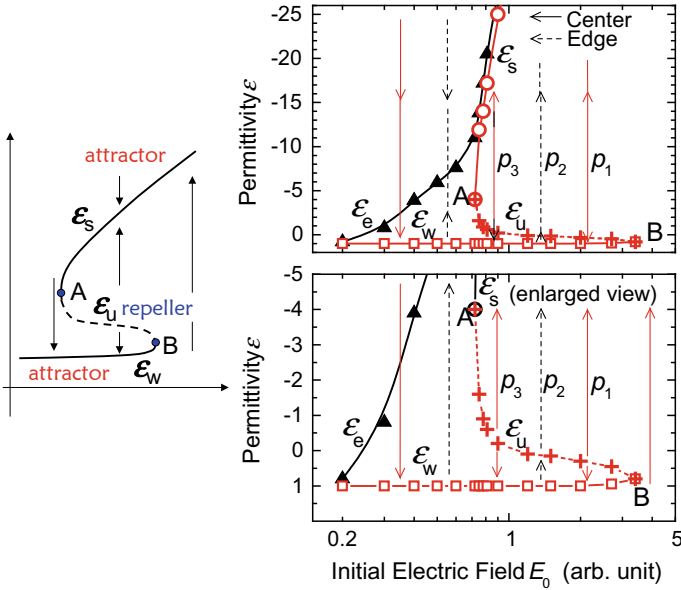


Fig. 10.8 Theoretical display of processes among equations with key parameters





**Fig. 10.9** Theoretical analysis on bifurcation diagram of  $\varepsilon$  in plasma-metamaterial composite as a function of injected microwave  $E$ . Inset displays a simplified model [33]. Reproduced with permission from Sakai, *J. Appl. Phys.*, **Vol. 109**: 084914-1-6. Copyright 2011 American Institute of Physics

the saddle-node bifurcation in the terminology of nonlinear dynamics.

With Fig. 10.9, we can point out what this analysis indicates from another point of view. In the case with negative  $\mu$ ,  $\varepsilon$  is unlimited with increasing  $E$ . This unlimited value of  $\varepsilon$  leads to the concept of high-energy metamaterials, as described in Sect. 10.3.3.

### 10.3.3 Properties as Energy Carriers

Materials usually show some phase transitions from gas to liquid or from liquid to gas due to their internal energy (provided from their external boundary area). On the other hand, metamaterials do not have such properties and show extraordinary parameters only for propagating electromagnetic waves. Due to its fixed spatial design to assure the extraordinary parameters, we hardly expect phase transitions in a metamaterial that induce drastic change of its configuration, but some analogical (and hopefully abnormal) dependence on its internal energy is promising in a metamaterial. Researchers are currently interested in heat flux control via some effects analogically similar to electromagnetic metamaterials [34], and energy may be a keyword to open a new category in metamaterial science.

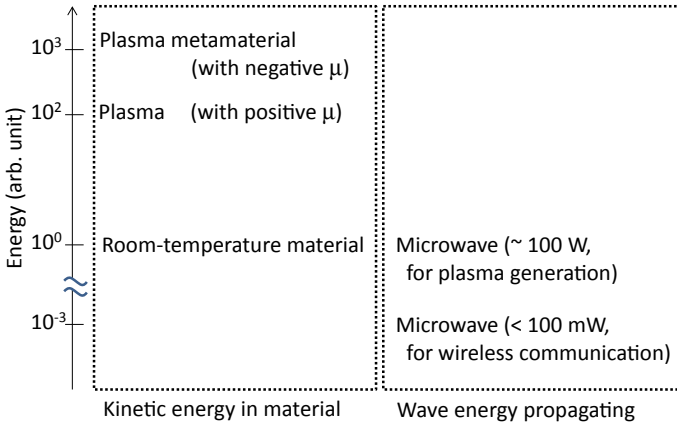


**Fig. 10.10** Energy levels of various materials and propagating waves

Plasma metamaterials are interesting research targets for studying such features. As we have investigated in Sect. 10.3.2, a transition phenomenon is possible in plasma metamaterials when we observe values of  $\epsilon$  and  $N$ , and transition is from low- to high- $n_e$  states, where high values of  $n_e$  mean high internal energy since the internal energy in plasmas is roughly a product of  $n_e$  and electron temperature  $T_e$  (except completely ionized high-temperature plasmas like fusion-oriented ones in which ion temperature is almost equal to  $T_e$ ). Furthermore, as we confirmed in Sect. 10.3.2, when we make  $\mu$  negative and launch electromagnetic waves with large amplitude  $E$ , we can expect generation of high- $n_e$  plasma with unlimited large negative values of  $\epsilon$ .

Here, we estimate how much energy is stored in a plasma metamaterial in comparison with energy of electromagnetic waves [26]. A conventional metamaterial contains energy of a propagating wave as a wave medium that supports wave propagation. Some designed wave media such as wave cavities can store it effectively, and they re-emit or convert it into another energy carrier. A nonlinear plasma metamaterial can store the wave energy as internal kinetic energy ( $n_e \times T_e$ ). Assume wave propagation inside a microwave waveguide for 2.45 GHz, whose cross section is  $\sim 50 \times 100 \text{ mm}^2$ . Microwave energy propagates at velocity  $v = c\beta/k$ , where  $\beta$  is wavenumber in the waveguide with the plasma metamaterial, whereas  $k$  is that in the free space with phase velocity  $c$ . Its energy density per unit length along the waveguide is  $\sim 10^{-8} \text{ J cm}^{-1}$ . On the other hand, the density of the internal kinetic energy in negative- $\mu$  plasma metamaterial is  $\sim 10^{-5} \text{ J cm}^{-1}$ , by three orders larger than the wave propagating energy density. Conventional plasma with both positive values of  $\epsilon$  and  $\mu$  has a smaller internal energy by one order, and the internal kinetic energy of hundreds-of-K materials (near the room temperature) is three orders lower than that of the negative- $\mu$  plasma metamaterial; the internal kinetic energy of hundreds-of-K materials is at a similar level to that of propagating waves. All of the energy levels are summarized in Fig. 10.10. That is, plasma metamaterials have high energy and

“phase” transition, which is a quite rich research target that bridges conventional metamaterials and conventional pure materials.

## 10.4 Concluding Remarks

In this chapter, we studied the effects of discharge plasmas when we use them in configurations of metamaterials. Plasmas have variable  $\varepsilon$ , in both its real and imaginary parts, and they match with solid metamaterials whose  $\mu$  is extraordinary. Negative- $\varepsilon$  plasmas and negative- $\mu$  metamaterials make  $N$  negative, which is a different scheme for negative  $N$  from conventional metamaterials. Flexible  $\varepsilon$  in plasma metamaterials achieves flexible- $N$  materials, which leads to nonlinear metamaterials that exhibit bifurcations of  $\varepsilon$ . It also yields high-energy metamaterials that work as energy storage whose energy density is several orders higher than those of conventional metamaterials.

## References

1. A. Sihvola (ed.), *Advances in Electromagnetics of Complex Media and Metamaterials* (Kluwer, Dordrecht, 2002)
2. L. Solymar, E. Shamonina, *Waves in Metamaterials* (Oxford University Press, Oxford, 2009)
3. A.V. Kildishev, A. Boltasseva, V.M. Shalaev, Planar photonics with metasurfaces. *Science* **339**, 1232009-1–1232009-6 (2013)
4. J.B. Pendry, A.J. Holden, D.J. Robbins, W.J. Stewart, Magnetism from conductors and enhanced nonlinear phenomena. *IEEE Trans. Microw. Theory Tech.* **47**, 2075–2084 (1999)
5. M.A. Lieberman, A.J. Lichtenberg, *Principles of Plasma Discharges and Materials Processing* (Wiley, New York, 1994)
6. O. Sakai, K. Tachibana, Plasmas as metamaterials: a review. *Plasma Sources Sci. Technol.* **21**, 013001-1–013001-18 (2012)
7. O. Sakai, J. Maeda, T. Shimomura, K. Urabe, Functional composites of plasmas and metamaterials: flexible waveguides, and variable attenuators with controllable phase shift. *Phys. Plasmas* **20**, 073506-1–073506-9 (2015)
8. O. Sakai, Y. Yasaka, R. Itatani, High radial confinement mode induced by dc limiter biasing in the HIEI tandem mirror. *Phys. Rev. Lett.* **70**, 4071–4074 (1994)
9. J.L. Walsh, F. Iza, N.B. Janson, M.G. Kong, Chaos in atmospheric-pressure plasma jets. *Plasma Sources Sci. Technol.* **21**, 034008-1–034008-8 (2012)
10. T.H. Stix, *The Theory of Plasma Waves* (McGraw-Hill, New York, 1962)
11. V.L. Ginzburg, *The Propagation of Electromagnetic Waves in Plasma* (Pergamon Press, Oxford, 1964)
12. D.G. Swanson, *Plasma Waves* (Academic Press, Boston, 1989)
13. R.J. Vidmar, On the use of atmospheric pressure plasmas as electromagnetic reflectors and absorbers. *IEEE Trans. Plasma Sci.* **18**, 733–741 (1990)
14. J. Faith, S.P. Kuo, J. Huang, Frequency downshifting and trapping of an electromagnetic wave by a rapidly created spatially periodic plasma. *Phys. Rev. E* **55**, 1843–1851 (1997)
15. D.K. Kalluri, *Electromagnetics of Complex Media* (CRC Press, Boca Raton, 1998)
16. H. Hojo, A. Mase, Dispersion relation of electromagnetic waves in one-dimensional plasma phonic crystals. *J. Plasma Fusion Res.* **80**, 89–90 (2004)

17. B. Wang, M.A. Cappelli, A plasma photonic crystal bandgap device. *Appl. Phys. Lett.* **108**, 161101-1–161101-4 (2016)
18. A.W. Trivelpiece, R.W. Gould, Surface charge waves in cylindrical plasma columns. *J. Appl. Phys.* **30**, 1784–1793 (1959)
19. O. Sakai, T. Shimomura, K. Tachibana, Negative refractive index designed in a periodic composite of lossy microplasmas and microresonators. *Phys. Plasmas* **17**, 123504-1–123504-9 (2010)
20. A. Iwai, Y. Nakamura, O. Sakai, Enhanced generation of a second-harmonic wave in a composite of metamaterial and microwave plasma with various permittivities. *Phys. Rev. E* **92**, 033105 (2015)
21. P. K. Singh, J. Hopwood, S. Sonkusale, Metamaterials for remote generation of spatially controllable two dimensional array of microplasma. *Sci. Reports.* **4**, 5964-1-5 (2014)
22. Y.P. Razer, *Gas Discharge Physics* (Springer-Verlag, Berlin, 1991)
23. I.H. Hutchinson, *Principles of Plasma Diagnostics* (Cambridge University Press, Cambridge, 1987)
24. D.R. Smith, D.C. Vier, Th Koschny, C.M. Soukoulis, Electromagnetic parameter retrieval from inhomogeneous metamaterials. *Phys. Rev. E* **71**, 036617-1–036617-11 (2005)
25. A. Iwai, Y. Nakamura, O. Sakai, Experimental observation and model analysis of second-harmonic generation in a plasma-metamaterial composite. *Appl. Phys. Express.* **8**, 056201-1-4 (2015)
26. O. Sakai, Y. Nakamura, A. Iwai, S. Iio, Negative-permittivity plasma generation in negative-permeability space with high-energy metamaterials. *Plasma Sources Sci. Technol.* **25**, 055019-1–055019-10 (2016)
27. I.V. Shadrivov, P.V. Kapitanova, S.I. Maslovski, Y.S. Kivshar, Metamaterials controlled with light. *Phys. Rev. Lett.* **109**, 083902-1–083902-4 (2012)
28. T. Sakaguchi, O. Sakai, K. Tachibana, Photonic bands in two-dimensional microplasma arrays. II. Band gaps observed in millimeter and sub-terahertz ranges. *J. Appl. Phys.* **101**, 073305-1–073305-7 (2007)
29. O. Sakai, T. Sakaguchi, K. Tachibana, Photonic bands in two-dimensional microplasma arrays. I. Theoretical derivation of band structures of electromagnetic waves. *J. Appl. Phys.* **101**, 073304-1–073304-9 (2007)
30. O. Sakai, T. Sakaguchi, T. Naito, D.-S. Lee, K. Tachibana, Characteristics of metamaterials composed of microplasma arrays. *Plasma Phys. Contr. Fusion.* **49**, B453–B463 (2007)
31. T. Naito, O. Sakai, K. Tachibana, Experimental verification of complex dispersion relation in lossy photonic crystals. *Appl. Phys. Express* **1**, 066003-1–066003-3 (2008)
32. O. Sakai, T. Naito, K. Tachibana, Experimental and numerical verification of microplasma assembly for novel electromagnetic media. *Phys. Plasmas.* **17**, 057102-1-9 (2010)
33. O. Sakai, Transition between positive and negative permittivity in field-dependent metamaterial. *J. Appl. Phys.* **109**, 084914-1–084914-6 (2011)
34. M. Kadic, T. Buckmann, R. Schittny, M. Wegener, Metamaterials beyond electromagnetism. *Rep. Prog. Phys.* **76**, 126501-1-34 (2013)
35. I. Adamovich, S.D. Baalrud, A. Bogaerts, P.J. Bruggeman, M. Cappelli, V. Colombo, U. Czarnetzki, U. Ebert, J.G. Eden, P. Favia, D.B. Graves, S. Hamaguchi, G. Hieftje, M. Hori, I.D. Kaganovich, U. Kortshagen, M.J. Kushner, N.J. Mason, S. Mazouffre, S. Mededovic Thagard, H.-R. Metelmann, A. Mizuno, E. Moreau, A.B. Murphy, B.A. Niemira, G.S. Oehrlein, Z. Lj Petrovic, L.C. Pitchford, Y.-K. Pu, S. Rauf, O. Sakai, S. Samukawa, S. Starikovskaia, J. Tennyson, K. Terashima, M.M. Turner, M.C.M. van de Sanden, A. Vardelle, The 2017 plasma roadmap: low temperature plasma science and technology. *J. Phys. D Appl. Phys.* **50**, 232001-1–232001-46 (2017)

# Chapter 11

## Meta-atoms Emulating Quantum Systems



Toshihiro Nakanishi and Masao Kitano

**Abstract** Electromagnetic property of a medium can be derived from electric and/or magnetic response of constituent atoms or molecules. If an artificial structure called meta-atom is designed to show the same response for the incidence of electromagnetic waves, the assembly of the meta-atoms, or metamaterial, is expected to exhibit the same functionality as that of the atomic medium. In this chapter, we focus on metamaterials mimicking electromagnetically induced transparency (EIT) effect, which has been extensively investigated in atomic systems composed of three-level atoms. We start with an analogy between a two-level atom and a meta-atom with a single resonant mode as a simplest example. Next, we provide rigorous analogy between an atomic medium with three-level atoms showing EIT effects and the metamaterial composed of coupled resonator-based meta-atoms, comparing the atomic response derived from Schrödinger equations of the quantum system and the response of the meta-atom derived from the circuit equations of its circuit model. Based on the coupled resonator model, several examples of metamaterials showing EIT-related effects such as sharp transparency and slow propagation are introduced. We also introduce a tunable metamaterial, which realizes storage of electromagnetic waves in the same way as the atomic EIT system.

### 11.1 Introduction

Metamaterials often include resonant structures to materialize unique electromagnetic characteristics, such as negative refraction, high nonlinearity. The individual constituents, or “meta-atoms,” with a single resonant mode behave as artificial two-

---

T. Nakanishi (✉) · M. Kitano  
Department of Electronic Science and Engineering,  
Kyoto University, Kyoto 615-8510, Japan  
e-mail: [t-naka@kuee.kyoto-u.ac.jp](mailto:t-naka@kuee.kyoto-u.ac.jp)

M. Kitano  
e-mail: [kitano@kuee.kyoto-u.ac.jp](mailto:kitano@kuee.kyoto-u.ac.jp)

© Springer Nature Singapore Pte Ltd. 2019  
K. Sakoda (ed.), *Electromagnetic Metamaterials*, Springer Series  
in Materials Science 287, [https://doi.org/10.1007/978-981-13-8649-7\\_11](https://doi.org/10.1007/978-981-13-8649-7_11)

level atoms, which resonantly absorb electromagnetic waves oscillating at the resonant frequency. If two resonant meta-atoms are closely placed, the resonant line splits into two levels in a similar way to a diatomic molecule forming bonding and anti-bonding levels. The coupled meta-atoms can also be considered as artificial three-level atoms with two absorption lines. These coupled meta-atoms, which emulate the molecules or multi-level atoms, can be expected to show more versatile functionalities than the meta-atoms with a single resonant mode. Here, as an example of unusual effects observed in three-level atoms, we focus on an electromagnetically induced transparency (EIT) effect [1], which renders an opaque medium transparent in a narrow spectral region. The EIT effect in an atomic system acts to dramatically decelerate the group velocity of light [2] and even to stop light pulses in the medium [3, 4]. The sharp transparency and slow propagation unique to the EIT effect were demonstrated in metamaterials in microwave regions [5, 6], and various types of metamaterials have been proposed and experimentally demonstrated to emulate the EIT effect in various frequency ranges, including terahertz [7–10] and optical ranges [11–15]. Recently, storage of electromagnetic waves has also been achieved in a metamaterial in a similar way to that in the atomic EIT system [16].

In Sect. 11.2, we show an analogy between two-level atoms and singly resonant meta-atoms, which are described by the circuit model based on an  $LC$  resonator. In Sect. 11.3, we explicitly derive an analogy between the atomic EIT effect in three-level atoms and the EIT-like effect in meta-atoms composed of coupled resonant modes. In both analogies, the atomic systems are analyzed by solving the Schrödinger equation, while the metamaterials are analyzed by the circuit equations, which well describe the meta-atoms. In spite of the completely different systems, the susceptibilities of the atomic media and the metamaterial counterparts are written in the same forms. This fact means that two systems respond to the electromagnetic waves in exactly the same way in the long wavelength limit, where homogenization of the medium can be employed.

## 11.2 Two-Level Atoms and Their Classical Model

### 11.2.1 Linear Response of Two-Level Atoms

The simplest example of a quantum system is a two-level system interacting with external fields, such as atomic excitation by an oscillating electric or magnetic field, spin precession by a static magnetic field. In this section, we consider the atomic transition between two levels by electric fields  $E = E_p \cos \omega t$  as shown in Fig. 11.1a. We assume that a ground state  $|1\rangle$  and an excited  $|2\rangle$  state are connected with an electric dipole moment, whose operator is defined as  $\hat{p}_p = p_p|2\rangle\langle 1| + \text{H.c.}$  Assuming the origin of the energy is at the ground level  $|1\rangle$  for simplicity, we can write the Hamiltonian of the system as

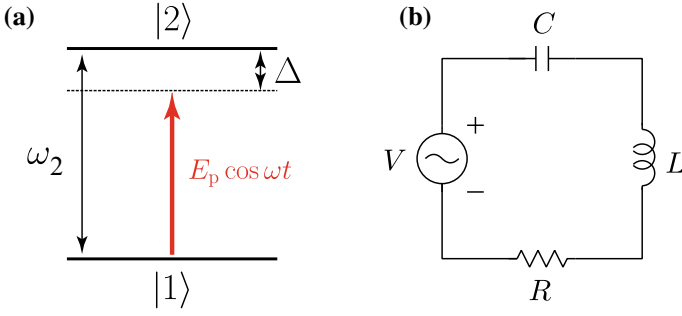


**Fig. 11.1** **a** Two-level system interacting with oscillating fields. **b** Circuit model

$$\hat{H} = -\hat{p}_p E_p \cos \omega t + \hbar \omega_2 |2\rangle\langle 2|, \quad (11.1)$$

where  $E_p \cos \omega t$  is the electric field and  $\omega_2$  is the transition frequency. For near-resonance cases, where the detuning  $\Delta \equiv \omega_2 - \omega$  is less than the linewidth  $\gamma_2$ , rotating wave approximation can be applied, and we obtain

$$\hat{H} = -\frac{\hbar \Omega_p}{2} e^{-i\omega t} |2\rangle\langle 1| - \frac{\hbar \Omega_p^*}{2} e^{i\omega t} |1\rangle\langle 2| + \hbar \omega_2 |2\rangle\langle 2|, \quad (11.2)$$

with  $\Omega_p \equiv p_p E_p / \hbar$ , which is called Rabi frequency [17]. If the state is given by  $|\psi\rangle = C_1(t)|1\rangle + C_2(t)|2\rangle$ , the Schrödinger equation yields

$$\frac{d}{dt} \begin{pmatrix} C_1 \\ C_2 \end{pmatrix} = -i \begin{pmatrix} 0 & -\frac{\Omega_p^*}{2} e^{i\omega t} \\ -\frac{\Omega_p}{2} e^{-i\omega t} & \omega_2 \end{pmatrix} \begin{pmatrix} C_1 \\ C_2 \end{pmatrix}. \quad (11.3)$$

The effect of the decay at  $|2\rangle$  can be phenomenologically introduced as follows:

$$\frac{d}{dt} \begin{pmatrix} C_1 \\ C_2 \end{pmatrix} = -i \begin{pmatrix} 0 & -\frac{\Omega_p^*}{2} e^{i\omega t} \\ -\frac{\Omega_p}{2} e^{-i\omega t} & \omega_2 - i\frac{\gamma_2}{2} \end{pmatrix} \begin{pmatrix} C_1 \\ C_2 \end{pmatrix}. \quad (11.4)$$

**Weak-field approximation** If the field is weak enough to satisfy  $|\Omega_p| \ll \gamma_2$ , it is fairly assumed that only the ground state  $|1\rangle$  is occupied, i.e.,  $C_1(t) = 1$ .<sup>1</sup> Under this condition, (11.4) is reduced to

$$\frac{dC_2}{dt} = -\left(i\omega_2 + \frac{\gamma_2}{2}\right) C_2 + i\frac{\Omega_p}{2} e^{-i\omega t}. \quad (11.5)$$

<sup>1</sup>Phase factor can be ignored because the origin of the energy level is at  $|1\rangle$ .

In a rotating frame defined as  $\tilde{C}_2 = e^{i\omega t} C_2$ , the above relation can be written as

$$\frac{d\tilde{C}_2}{dt} = -\left(i\Delta + \frac{\gamma_2}{2}\right)\tilde{C}_2 + i\frac{\Omega_p}{2}, \quad (11.6)$$

where  $\Delta = \omega_2 - \omega$ . The steady-state solution can be easily derived from  $d\tilde{C}_2/dt = 0$  as

$$\tilde{C}_2(t) = \frac{i\Omega_p}{2} \frac{1}{i\Delta + \frac{\gamma_2}{2}}, \quad C_2(t) = \frac{i\Omega_p}{2} \frac{1}{i\Delta + \frac{\gamma_2}{2}} e^{-i\omega t}. \quad (11.7)$$

**Susceptibility of atomic media** The electric dipole moment per atom is given by

$$\begin{aligned} p_0 &\equiv \langle \psi | \hat{p}_p | \psi \rangle = p_p^* C_1^*(t) C_2(t) + \text{c.c.} \\ &= \tilde{p}_p e^{-i\omega t} + \text{c.c.} \end{aligned} \quad (11.8)$$

where

$$\tilde{p}_p \equiv \frac{i|p_p|^2}{2\hbar} \frac{E_p}{i\Delta + \frac{\gamma_2}{2}}. \quad (11.9)$$

If the medium is composed of two-level atoms with a density  $N$ , the total electric polarization is  $p_p N$ . The complex susceptibility  $\chi$  is obtained from  $\tilde{p}_p N = \varepsilon_0 \chi E_p$ , and the real part  $\chi'$  and imaginary part  $\chi''$  are derived from (11.7) as

$$\chi' = \text{Re} \left[ \frac{i|p_p|^2 N}{2\varepsilon_0 \hbar} \frac{1}{i\Delta + \frac{\gamma_2}{2}} \right] = \frac{|p_p|^2 N}{2\varepsilon_0 \hbar} \frac{\Delta}{\Delta^2 + \left(\frac{\gamma_2}{2}\right)^2}, \quad (11.10)$$

$$\chi'' = \text{Im} \left[ \frac{i|p_p|^2 N}{2\varepsilon_0 \hbar} \frac{1}{i\Delta + \frac{\gamma_2}{2}} \right] = \frac{|p_p|^2 N}{2\varepsilon_0 \hbar} \frac{\frac{\gamma_2}{2}}{\Delta^2 + \left(\frac{\gamma_2}{2}\right)^2}, \quad (11.11)$$

respectively. The absorption spectrum related with  $\chi''$  shows a Lorentzian profile with a width of  $\gamma_2$ . During the derivation, we have assumed weak-field approximation  $|\Omega_p| \ll \gamma_2$ , ignoring saturation effects. Therefore, the derived susceptibilities represent the linear response of the medium.



## 11.2.2 Circuit Analogy of the Two-Level System

The differential equation (11.5) can be regarded as the equation of motions for a harmonic oscillator with a resonant frequency  $\omega_2$  driven by an external force rotating at  $\omega$ . The circuit analogy can be an  $LC$  resonator driven by an external voltage source as shown in Fig. 11.1b. The evolution of the  $LC$  resonator is governed by

$$L \frac{d^2 i}{dt^2} + R \frac{di}{dt} + \frac{i}{C} = \frac{d}{dt}(\tilde{v} \cos \omega t). \quad (11.12)$$

If the amplitude  $\tilde{v}$  of the external voltage source changes slowly enough to satisfy  $|\frac{d\tilde{v}}{dt}| < \omega$ , the current envelope  $\tilde{i}$ , which is defined through  $i = \tilde{i} e^{-i\omega t} + \text{c.c.}$ , also varies slowly. By applying slow varying envelope approximation and using a near-resonance condition,  $\omega_2 + \omega \sim 2\omega$ , (11.12) is reduced to

$$\frac{d\tilde{i}}{dt} = -\left(i\Delta + \frac{R}{2L}\right)\tilde{i} + \frac{\tilde{v}}{2L}, \quad (11.13)$$

where we use the same definition  $\Delta = \omega_2 - \omega$  as introduced in the previous section. Comparing (11.6) and (11.13), we can find that the  $LC$  resonator is described by the same differential equation as the quantum two-level system, by assuming  $\gamma_2 = R/L$  and  $\Omega_p = -i\tilde{v}/L$ . The current in steady state can be easily obtained as

$$\tilde{i} = \frac{1}{i\Delta + \frac{\gamma_2}{2}} \frac{\tilde{v}}{2L}. \quad (11.14)$$

Here, we introduce a complex power, which is given by

$$P_c = \tilde{v}^* \tilde{i} = \frac{|\tilde{v}|^2}{2L} \frac{1}{i\Delta + \frac{\gamma_2}{2}}. \quad (11.15)$$

The real part and imaginary parts of  $P_c$  are

$$P_r \equiv \text{Re}[P_c] = \frac{|\tilde{v}|^2}{2L} \frac{\frac{\gamma_2}{2}}{\Delta^2 + \left(\frac{\gamma_2}{2}\right)^2}, \quad P_i \equiv \text{Im}[P_c] = -\frac{|\tilde{v}|^2}{2L} \frac{\Delta}{\Delta^2 + \left(\frac{\gamma_2}{2}\right)^2}. \quad (11.16)$$

The real (imaginary) part of  $P_c$  corresponds to the imaginary (real) part of the complex susceptibility. It is natural because the real part of  $P_c$  represents the energy dissipation in the resistor and shows a Lorentzian profile with a width of  $\gamma_2 = R/L$ .

The correspondences between the quantum system for driven two-level atoms and its circuit model are summarized in Table 11.1.

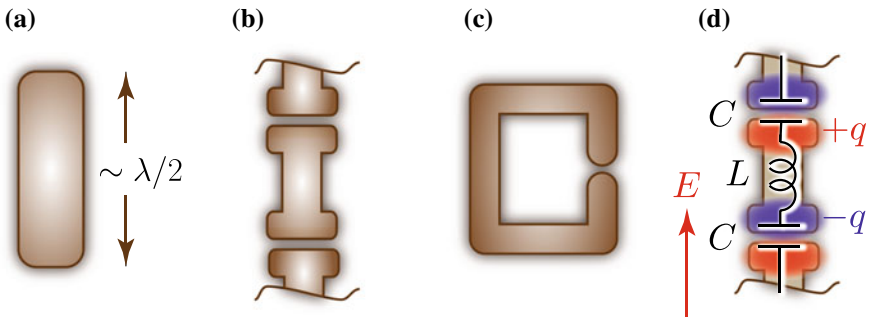
**Table 11.1** Correspondence between the two-level system in a driving field and an  $LC$  resonator driven by an external voltage source

Driven two-level system	Driven $LC$ resonator
Transition frequency: $\omega_2$	Resonant frequency: $1/\sqrt{LC}$
External field: $E_p \cos \omega t$	External voltage source: $\tilde{v} \cos \omega t$
Amplitude for $ 2\rangle$ : $C_2$	Current in the resonator: $i$
Decay rate for $ 2\rangle$ : $\gamma_2$	Dissipation rate: $R/L$
Absorption: $\text{Im}[\chi]$	Dissipated power: $\text{Re}[P_c]$

### 11.2.3 Metamaterial Analogy of the Two-Level System

The constituents of the metamaterial that resonates at a specific frequency can be regarded as artificial atoms (meta-atoms) analogous to the two-level atoms, because the circuit models of the meta-atoms are well described by  $LC$  resonators. There are various kinds of resonant meta-atoms, such as dipole resonators, cut-wire structures, and split-ring resonators as shown in Fig. 11.2a, b, c, respectively. Here, we take a cut-wire structure as a typical example of metamaterials with electric dipole oscillation. As shown in Fig. 11.2d, the metallic parts and the gaps between the cut wires can be regarded as inductors and capacitors, respectively. In the presence of electric field  $E$  aligned along the cut-wire structure, electric charges  $\pm q$  accumulated at both ends of the bar structure form an electric dipole  $p = qd$ , where  $d$  represents the effective dipole length determined by the charge distribution. For an oscillating field with the complex amplitude  $\tilde{E}$ , the same relation can be assumed as  $\tilde{p} = \tilde{q}d$ , where  $\tilde{p}$  and  $\tilde{q}$  are the complex amplitudes of the electric dipole and the charges, respectively. From  $i = dq/dt$ , the complex amplitude of the current,  $\tilde{i}$ , is represented as

$$\tilde{i} = -i\omega\tilde{q}. \quad (11.17)$$

**Fig. 11.2** Various meta-atoms. **a** Dipole resonator. **b** Cut-wire structure. **c** Split-ring resonator. **d** Circuit model for cut-wire structure

The voltage applied to each unit cell with a length  $l$  can be roughly estimated as  $\tilde{v} = \tilde{E}l$ . Hence, (11.14) gives

$$\tilde{p} = i \frac{ld}{2\omega L} \frac{1}{i\Delta + \frac{\gamma_2}{2}} \tilde{E}. \tag{11.18}$$

For the meta-atom density of  $N$ , we can obtain the electric susceptibility of the metamaterial as follows:

$$\chi = \frac{\tilde{p}N}{\epsilon_0 \tilde{E}} = i \frac{ldN}{2\epsilon_0 \omega L} \frac{1}{i\Delta + \frac{\gamma_2}{2}}. \tag{11.19}$$

The susceptibilities of two-level atoms and the metamaterial are the same except for the coefficients, and it is possible to identify the metamaterial composed of artificial atoms like cut wires with a medium composed of two-level atoms.

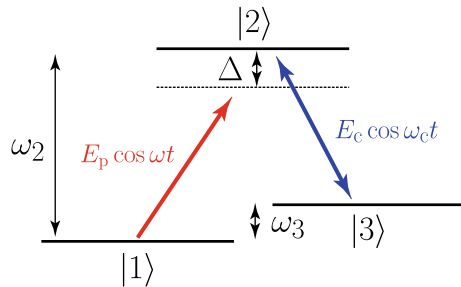
### 11.3 EIT Effect and Its Classical Model

#### 11.3.1 EIT Effect in Three-Level Atoms

In this section, we consider EIT effects in three-level atoms with two ground states,  $|1\rangle$  and  $|3\rangle$ , and a common excited state  $|2\rangle$  as shown in Fig. 11.3. The dipole moments for  $|1\rangle \rightarrow |2\rangle$  and  $|3\rangle \rightarrow |2\rangle$  are defined as  $\hat{p}_p = p_p|2\rangle\langle 1| + \text{H.c.}$  and  $\hat{p}_c = p_c|2\rangle\langle 3| + \text{H.c.}$ , respectively. We assume that a probe field,  $E_p \cos \omega t$ , induces the transition from  $|1\rangle$  to  $|2\rangle$  with a detuning  $\Delta (= \omega_2 - \omega)$ , and the other field  $E_c \cos \omega_c t$ , called the control field, connects the transition between  $|3\rangle$  and  $|2\rangle$  with no detuning,  $\omega_c = \omega_2 - \omega_3$ . The Hamiltonian of the system is given by

$$\hat{H} = -\hat{p}_p E_p \cos \omega t - \hat{p}_c E_c \cos \omega_c t + \hbar\omega_2|2\rangle\langle 2| + \hbar\omega_3|3\rangle\langle 3|. \tag{11.20}$$

**Fig. 11.3** Three-level system interacting with probe and control light



For near-resonance cases, rotating wave approximation can be applied, and we obtain

$$\hat{H} = -\frac{\hbar\Omega_p}{2}e^{-i\omega t}|2\rangle\langle 1| - \frac{\hbar\Omega_p^*}{2}e^{i\omega t}|1\rangle\langle 2| - \frac{\hbar\Omega_c}{2}e^{-i\omega_c t}|2\rangle\langle 3| - \frac{\hbar\Omega_c^*}{2}e^{i\omega_c t}|3\rangle\langle 2| + \hbar\omega_2|2\rangle\langle 2| + \hbar\omega_3|3\rangle\langle 3|, \quad (11.21)$$

where Rabi frequencies are defined as  $\Omega_p \equiv p_p E_p/\hbar$  and  $\Omega_c \equiv p_c E_c/\hbar$ . If the state is given by  $|\psi\rangle = C_1(t)|1\rangle + C_2(t)|2\rangle + C_3(t)|3\rangle$ , the Schrödinger equation yields

$$\frac{d}{dt} \begin{pmatrix} C_1 \\ C_2 \\ C_3 \end{pmatrix} = -i \begin{pmatrix} 0 & -\frac{\Omega_p^*}{2}e^{i\omega t} & 0 \\ -\frac{\Omega_p}{2}e^{-i\omega t} & \omega_2 - i\frac{\gamma_2}{2} & -\frac{\Omega_c}{2}e^{-i\omega_c t} \\ 0 & -\frac{\Omega_c^*}{2}e^{i\omega_c t} & \omega_3 - i\frac{\gamma_3}{2} \end{pmatrix} \begin{pmatrix} C_1 \\ C_2 \\ C_3 \end{pmatrix}, \quad (11.22)$$

where the effects of the decay at  $|2\rangle$  and  $|3\rangle$  are phenomenologically introduced in the same way as the derivation of (11.4). We can assume that the decay rate at the excited state  $|2\rangle$  is much larger than that at the ground state  $|3\rangle$ , i.e.,  $\gamma_2 \gg \gamma_3$ .

**Weak-field approximation** If the probe field is weak enough to satisfy  $|\Omega_p| \ll \gamma_2$ ,  $|\Omega_c|$ , we can assume  $C_1(t) = 1$ . Under this condition, (11.22) becomes

$$\frac{d}{dt} \begin{pmatrix} C_2 \\ C_3 \end{pmatrix} = - \begin{pmatrix} i\omega_2 + \frac{\gamma_2}{2} & -i\frac{\Omega_c}{2}e^{-i\omega_c t} \\ -i\frac{\Omega_c^*}{2}e^{i\omega_c t} & i\omega_3 + \frac{\gamma_3}{2} \end{pmatrix} \begin{pmatrix} C_2 \\ C_3 \end{pmatrix} + \frac{i}{2} \begin{pmatrix} \Omega_p e^{-i\omega t} \\ 0 \end{pmatrix}. \quad (11.23)$$

In a rotating frame defined as  $\tilde{C}_2 = e^{i\omega t} C_2$  and  $\tilde{C}_3 = e^{i\omega t} e^{-i\omega_c t} C_3$ , the above relation can be written as

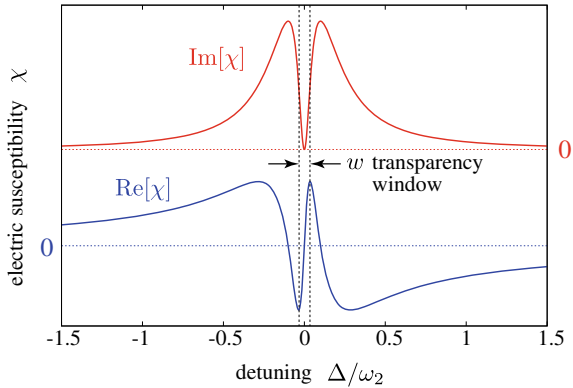
$$\frac{d}{dt} \begin{pmatrix} \tilde{C}_2 \\ \tilde{C}_3 \end{pmatrix} = - \begin{pmatrix} i\Delta + \frac{\gamma_2}{2} & -i\frac{\Omega_c}{2} \\ -i\frac{\Omega_c^*}{2} & i\Delta + \frac{\gamma_3}{2} \end{pmatrix} \begin{pmatrix} \tilde{C}_2 \\ \tilde{C}_3 \end{pmatrix} + \frac{i}{2} \begin{pmatrix} \Omega_p \\ 0 \end{pmatrix}. \quad (11.24)$$

The steady-state solution can be easily derived from  $d\tilde{C}_2/dt = d\tilde{C}_3/dt = 0$  as

$$\tilde{C}_2 = \frac{i\Omega_p}{2} \frac{i\Delta + \frac{\gamma_3}{2}}{\left(i\Delta + \frac{\gamma_2}{2}\right)\left(i\Delta + \frac{\gamma_3}{2}\right) + \left|\frac{\Omega_c}{2}\right|^2}. \quad (11.25)$$

**Susceptibility of EIT media** As in Sect. 11.2.1, the complex susceptibility for the probe light is derived as

**Fig. 11.4** Electric susceptibility of atomic EIT medium for  $\gamma_2 = 0.5\omega_2$ ,  $\gamma_3 = 0$ ,  $\Omega_c = 0.2\omega_2$ . Imaginary part (top) and real part (bottom). Reprinted with permission from [18]. Copyright 2018 Springer Nature



$$\chi = \frac{i|p_p|^2 N}{2\epsilon_0 \hbar} \frac{i\Delta + \frac{\gamma_3}{2}}{\left(i\Delta + \frac{\gamma_2}{2}\right) \left(i\Delta + \frac{\gamma_3}{2}\right) + \left|\frac{\Omega_c}{2}\right|^2}. \tag{11.26}$$

The spectral shape of the susceptibility for ideal case  $\gamma_3 = 0$  is illustrated in Fig. 11.4. The absorption spectrum represented by the imaginary part of the susceptibility shows sharp transparency in a broad absorption line. In addition to the absorption profile, the refractive index related to the real part of the susceptibility is extremely modified in the transparency window, and the group velocity of the light is dramatically reduced. The width of the transparency window is proportional to  $|\Omega_c|^2$ , or the intensity of the control light. The storage of light can be achieved through the dynamic modulation of the group velocity controlled by changing the intensity of the control light.

### 11.3.2 Circuit Analogy of EIT Effects

In 2002, Alzar it et al. proposed a method to mimic EIT effects using coupled harmonic oscillators [19]. In this section, we deal with weakly coupled  $LC$  resonators with a resonant frequency of  $\omega_2 = 1/\sqrt{LC}$  as shown in Fig. 11.5a, b, which represent a magnetically coupled resonator and an electrically coupled resonator, respectively. For the time being, we will consider the magnetically coupled resonator, which is almost the same as the electrically coupled resonator. We assume that the resonator directly driven by the external voltage oscillating at  $\omega$  has a low quality (low Q) factor while the other has a high quality (high Q) factor, i.e.,  $R \gg r$ . The circuit equation is given by

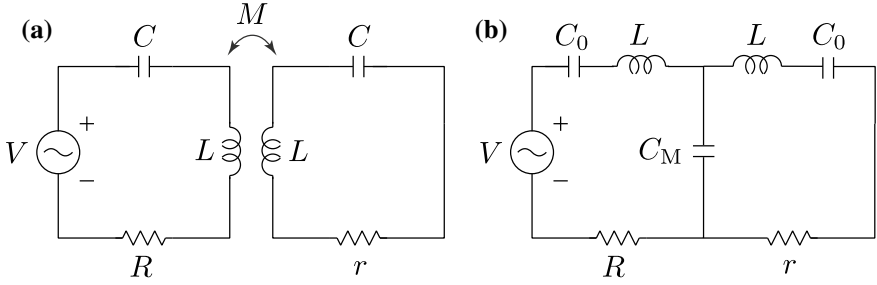


**Fig. 11.5** Circuit model of atomic EIT system. **a** Magnetically coupled resonator. **b** Electrically coupled resonator

$$L \frac{d^2 i_1}{dt^2} + R \frac{di_1}{dt} + \frac{i_1}{C} + M \frac{d^2 i_2}{dt^2} = \frac{d}{dt} (\tilde{v} \cos \omega t), \quad (11.27)$$

$$L \frac{d^2 i_2}{dt^2} + r \frac{di_2}{dt} + \frac{i_2}{C} + M \frac{d^2 i_1}{dt^2} = 0, \quad (11.28)$$

where  $i_1$  and  $i_2$  are currents in the low Q resonator and high Q resonator, respectively. Through the same procedure to derive (11.13) in Sect. 11.2.2, we obtain

$$\frac{d}{dt} \begin{pmatrix} \tilde{i}_1 \\ \tilde{i}_2 \end{pmatrix} = - \begin{pmatrix} i\Delta + \frac{R}{2L} & -i\frac{\kappa\omega}{2} \\ -i\frac{\kappa\omega}{2} & i\Delta + \frac{r}{2L} \end{pmatrix} \begin{pmatrix} \tilde{i}_1 \\ \tilde{i}_2 \end{pmatrix} + \frac{1}{2} \begin{pmatrix} \tilde{v} \\ \frac{L}{r} \\ 0 \end{pmatrix}, \quad (11.29)$$

where the coupling coefficient and the detuning are introduced as  $\kappa = M/L$  and  $\Delta = \omega_2 - \omega$ , respectively. In the derivation, we assume a weak coupling limit  $\kappa \ll 1$ . By comparing (11.24) with (11.29), it is obvious that the currents in the circuit model are governed by the same differential equations as those for quantum states in the atomic three-level system. Then, the steady-state solution is derived as

$$\tilde{i}_1 = \frac{\tilde{v}}{2L} \frac{i\Delta + \frac{\gamma_3}{2}}{\left(i\Delta + \frac{\gamma_2}{2}\right) \left(i\Delta + \frac{\gamma_3}{2}\right) + \left|\frac{\Omega_c}{2}\right|^2}, \quad (11.30)$$

by using  $\gamma_2 = R/L$ ,  $\gamma_3 = r/L$ ,  $\Omega_c = \kappa\omega$ , and  $\Omega_p = -i\tilde{v}/L$ .

The complex power for the current in the low Q resonator is given as

$$P_c = \tilde{v}^* \tilde{i}_1 = \frac{|\tilde{v}|^2}{2L} \frac{i\Delta + \frac{\gamma_3}{2}}{\left(i\Delta + \frac{\gamma_2}{2}\right) \left(i\Delta + \frac{\gamma_3}{2}\right) + \left|\frac{\Omega_c}{2}\right|^2}. \quad (11.31)$$

**Table 11.2** Correspondence between the atomic EIT system and its circuit model

Atomic EIT system	Coupled resonator model
Transition frequency: $\omega_2$	Resonant frequency: $1/\sqrt{LC}$
External field: $E_p \cos \omega t$	External voltage source: $\tilde{v} \cos \omega t$
Amplitude for $ 2\rangle$ : $C_2$	Current in low Q resonator: $i_1$
Amplitude for $ 3\rangle$ : $C_3$	Current in high Q resonator: $i_2$
Decay rate for $ 2\rangle$ : $\gamma_2$	Dissipation rate of low Q resonator: $R/L$
Decay rate for $ 3\rangle$ : $\gamma_3$	Dissipation rate of high Q resonator: $r/L$
Rabi frequency by control light: $\Omega_c$	Coupling of the resonators: $\kappa\omega$ or $1/\omega C_M L$
Absorption of probe light: $\text{Im}[\chi]$	Dissipated power: $\text{Re}[P_c]$

The real part of  $P_c$  represents the dissipation and corresponds to the imaginary part of the susceptibility  $\chi$  expressed by (11.26) for an atomic EIT medium. As a result, the dissipation in the circuit is suppressed in a narrow spectral region. The width of the low dissipation region is proportional to  $\Omega_c^2 = \kappa^2 \omega^2$ , and smaller coupling  $\kappa$  results in a narrower low dissipation region.<sup>2</sup>

In the case of the electrically coupled resonator shown in Fig. 11.5b, the circuit equation is given by

$$L \frac{d^2 i_1}{dt^2} + R \frac{di_1}{dt} + \frac{i_1}{C} + \frac{i_2}{C_M} = \frac{d}{dt}(\tilde{v} \cos \omega t), \quad (11.32)$$

$$L \frac{d^2 i_2}{dt^2} + r \frac{di_2}{dt} + \frac{i_2}{C} + \frac{i_1}{C_M} = 0, \quad (11.33)$$

where  $1/C = 1/C_0 + 1/C_M$ . Equation (11.29) is replaced with

$$\frac{d}{dt} \begin{pmatrix} \tilde{i}_1 \\ \tilde{i}_2 \end{pmatrix} = - \begin{pmatrix} i\Delta + \frac{R}{2L} & \frac{i}{2\omega C_M L} \\ \frac{i}{2\omega C_M L} & i\Delta + \frac{r}{2L} \end{pmatrix} \begin{pmatrix} \tilde{i}_1 \\ \tilde{i}_2 \end{pmatrix} + \frac{1}{2} \begin{pmatrix} \tilde{v} \\ \frac{\tilde{v}}{L} \\ 0 \end{pmatrix}. \quad (11.34)$$

This expression has the same form as (11.29) except for the coupling term. Hence, we redefine  $\Omega_c = -1/\omega C_M L$ , and the electrically coupled resonator can be regarded as identical to the magnetically coupled resonator.

The correspondences between the quantum EIT system and its circuit model are summarized in Table 11.2.

<sup>2</sup> $\Omega_c = \kappa\omega$  is obviously frequency dependent, though it can be considered nearly constant  $\kappa\omega_2$  in the weak coupling limit  $\kappa \ll 1$ .

### 11.3.3 Metamaterial Analogy of EIT Effects

The EIT effects can be materialized with metamaterials composed of meta-atoms that are described by the circuit model provided in the previous section. In the circuit model, two resonators with different quality factors are coupled and only the resonator with a low Q factor is excited. On the other hand, the metamaterial emulating the EIT effects, called an EIT metamaterial, consists of meta-atoms with two resonant structures, or two resonant modes, with different quality factors, and only the resonator with low Q factor is excited by external electromagnetic waves. In the presence of the coupling between the two resonators, which we refer to as EIT coupling, the EIT effects including narrow-band transparency and slow light propagation are materialized.

Before showing realistic structures of the EIT metamaterials, we provide an overview of the EIT-like effects in metamaterials with the concept model shown in Fig. 11.6a. The left (right) circle corresponds to a low Q (high Q) resonator, and the antenna symbolically represents the function of receiving external electromagnetic waves. It should be noted that the high Q resonator cannot be directly excited by the external fields. The resonant mode with the low Q factor is called “radiative mode” or “bright mode,” and the one with the high Q factor is called “trapped mode” or “dark mode.” As shown in Fig. 11.6b, without the EIT coupling the energy in the radiative mode excited by the external fields is rapidly consumed due to high dissipation in the low Q resonator, and consequently, the propagating waves are absorbed in the metamaterial. On the other hand, in the presence of the EIT coupling, as shown in Fig. 11.6c, the metamaterial is rendered transparent, because the energy received through the radiative mode is transferred to the trapped mode with low losses via the EIT coupling. In addition to the transparency, the propagation is slowed down in the metamaterial owing to the temporal storage in the trapped mode.

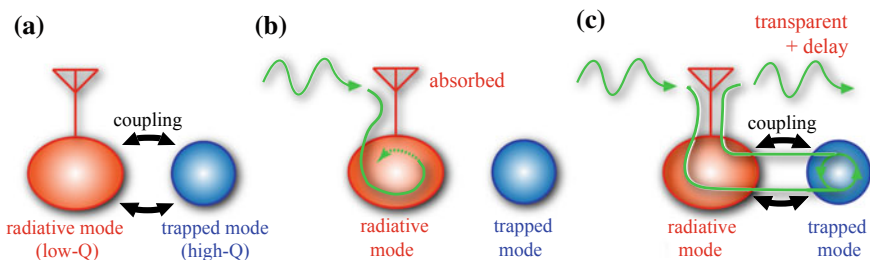


**Fig. 11.6** **a** Concept model of EIT metamaterial. **b** Coupling is turned off. **c** Coupling is turned on. Reprinted with permission from [18]. Copyright 2018 Springer Nature



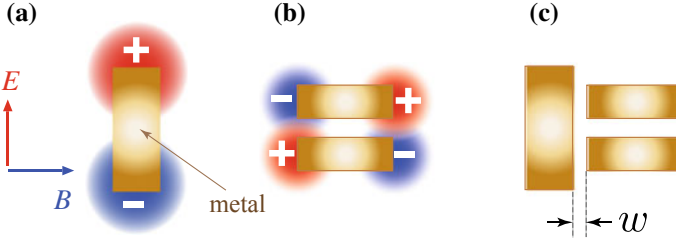


**Fig. 11.7** a Dipole antenna. b Pair of strips. c Composite structure

### 11.3.3.1 EIT-like Effect in Coupled Resonator-Based Metamaterials

In actual EIT metamaterials, electric dipole resonance is often used as a radiative mode, because electric dipole oscillation effectively interacts with far-field or propagating waves. In other words, the stored energy in the resonant mode is quickly released into propagating waves, and the quality factor as a resonator is relatively low due to the radiation dissipation. On the other hand, lower dissipative resonance such as magnetic dipole resonance and electric quadrupole resonance can be used for a trapped mode.

As a typical example of the EIT metamaterials, the proposal by Zhang's group [20] is shown in Fig. 11.7. Their EIT metamaterial is comprised of two elements: a dipole antenna shown in Fig. 11.7a and a pair of stripes shown in Fig. 11.7b. The polarization of the incident electromagnetic field is also shown on the left-hand side of Fig. 11.7a. As shown in Fig. 11.7a, electric dipole resonance in the dipole antenna is induced by oscillating electric fields, when half of the wavelength is adjusted around the length of the antenna. Hence, this resonance serves as a radiative mode.

On the other hand, the pair of stripes has an electric quadrupole resonance mode as shown in Fig. 11.7b and serves as a trapped mode. It should be noted that the incident electromagnetic field does not directly excite the quadrupole resonance in the long wavelength limit. The resonance frequencies for the radiative mode and the trapped mode are tuned to be the same by adjusting the dimensions of the structure. In order to observe EIT-like effects, the radiative mode and the trapped mode are coupled with each other by placing two structures close together, as shown in Fig. 11.7c.

The circuit model of a “meta-atom” for the metamaterial is expressed by the electrically coupled resonators, as shown in Fig. 11.5b, and the current  $\tilde{i}_1$  in the dipole antenna can be expressed by (11.30). As described in Sect. 11.2.3, the dipole moment  $\tilde{p}$  is proportional to the current  $\tilde{i}_1$  in the dipole antenna, and the resulting susceptibility of the metamaterial with the meta-atom density of  $N$  becomes

$$\chi = i \frac{ldN}{\varepsilon_0\omega} \frac{\tilde{i}_1}{\tilde{v}} = i \frac{ldN}{2\varepsilon_0\omega L} \frac{i\Delta + \frac{\gamma_3}{2}}{\left(i\Delta + \frac{\gamma_2}{2}\right) \left(i\Delta + \frac{\gamma_3}{2}\right) + \left|\frac{\Omega_c}{2}\right|^2}, \quad (11.35)$$

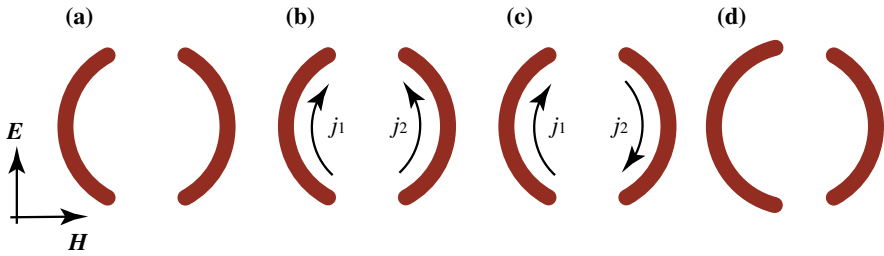


**Fig. 11.8** **a** Symmetric split ring. **b** Radiative mode. **c** Trapped mode. **d** Asymmetric split ring. Reprinted with permission from [18]. Copyright 2018 Springer Nature

where  $\gamma_2$  and  $\gamma_3$  can be interpreted as the dissipation in the radiative mode and the trapped mode, respectively. As a result, the above expression is written in the same form as the susceptibility of the atomic EIT medium given by (11.26). This fact means that the EIT metamaterial responds to electromagnetic fields in exactly the same way as the atomic EIT medium. It is possible to control the coupling strength  $\Omega_c$  by changing the distance  $w$  between the two structures instead of changing the intensity of the control light for the atomic EIT medium.

### 11.3.3.2 EIT-like Effect in Structural Symmetry-Broken Metamaterial

The sharp transparency in metamaterials was first demonstrated in microwave regions [5, 6]. In this section, we show the operating principle for the metamaterial composed of asymmetric split rings in [5]. As shown in Fig. 11.8a, we start with a metallic symmetric split ring. The structure has two resonant modes, one of which is formed by symmetric currents  $j_1$  and  $j_2$  in two arcs, as shown in Fig. 11.8b, and the other is formed by antisymmetric currents, as shown in Fig. 11.8c. The former mode shows electric dipole resonance, which is directly excited by the electric field  $E$  and has a low Q factor due to the high radiation loss. It works as a radiative mode. On the other hand, the latter mode forms loop current showing magnetic dipole resonance, which has a high Q factor owing to the cancelation of electric dipole radiation from two arcs. This mode cannot be excited by the incident wave and works as a trapped mode. Owing to the symmetric structure, these two resonant modes are eigenmodes and decoupled with each other. Hence, the meta-atoms show no EIT effect.

If the structural symmetry is broken as shown in Fig. 11.8d, the two modes in the asymmetric split rings are coupled and the EIT effect emerges. The EIT-like effects in such symmetry-broken structures have also been widely investigated [9, 21, 22].

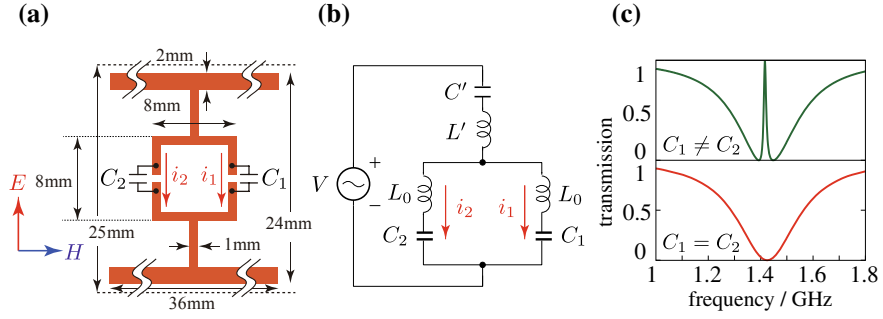


**Fig. 11.9** **a** Structure of a tunable EIT metamaterial. **b** Circuit model. **c** Transmission spectra for  $C_1 = 1.91$  pF,  $C_2 = 2.33$  pF (top) and  $C_1 = C_2 = 2.1$  pF (bottom). Adapted with permission from [16]. Copyrighted by the American Physical Society

### 11.3.3.3 Tuning of EIT-like Effects in Metamaterials

For practical applications, the tunability of EIT-like effects is quite important. The metamaterials whose EIT properties can be controlled have been demonstrated in various ways utilizing phase transition of superconductor [23], photo-carrier excitation in semiconductor [24, 25], and so on. Here, we show a capacitance-tunable EIT metamaterial designed for dynamic switching of an EIT-like effect [16]. Figure 11.9a illustrates the unit cell of a meta-atom, which includes variable capacitances  $C_1$  and  $C_2$  in two arms in the central loop structure. The structure has two resonance modes: one formed by in-phase current  $i_+ = i_1 + i_2$ , which works as a radiative mode, and the other formed by anti-phase current  $i_- = i_1 - i_2$ , which works as a trapped mode. In the same way as the structural symmetry-broken metamaterial introduced in the previous section, this metamaterial shows an EIT-like effect, or sharp transparency, for asymmetric case  $C_1 \neq C_2$ .

Precise analysis can be performed by using the circuit model as shown in Fig. 11.9b. The inductance  $L'$ ,  $2L_0$ , and the capacitance  $C'$ , respectively, correspond to the inductance of the metallic structure excluding the loop structure, the loop inductance, and the capacitance between neighboring cells. By introducing the radiation loss in the radiative (trapped) mode as  $R$  ( $r$ ), the circuit equation can be obtained as

$$L \frac{d^2 i_+}{dt^2} + R \frac{di_+}{dt} + \frac{i_+}{C_+} + \frac{i_-}{\Delta C} = \frac{d}{dt} (2\bar{v} \cos \omega t), \quad (11.36)$$

$$L_0 \frac{d^2 i_-}{dt^2} + r \frac{di_-}{dt} + \frac{i_-}{C_-} + \frac{i_+}{\Delta C} = 0. \quad (11.37)$$

where we define  $L = 2L' + L_0$  and

$$\frac{1}{C_+} = \frac{2}{C'} + \frac{1}{2C_1} + \frac{1}{2C_2}, \quad \frac{1}{C_-} = \frac{1}{2C_1} + \frac{1}{2C_2}, \quad \frac{1}{\Delta C} = \frac{1}{2C_1} - \frac{1}{2C_2}. \quad (11.38)$$

The resonant frequency for  $i_+$  is tuned to that for  $i_-$ . It is confirmed that these equations (11.36) and (11.37) are written in the same forms as (11.32) and (11.33). Consequently, the electric susceptibility shows the EIT characteristics expressed as (11.35), assuming a coupling strength of

$$|\Omega_c| = \frac{1}{\omega\sqrt{LL_0}} \frac{1}{\Delta C}. \quad (11.39)$$

It is noted that  $|\Omega_c|$ , which is zero for symmetric case  $C_1 = C_2$ , grows larger with increasing asymmetry. Figure 11.9c shows the transmission spectra computed for the symmetric case  $C_1 = C_2 = 2.1$  pF (bottom) and the asymmetric case  $C_1 = 1.91$  pF,  $C_2 = 2.33$  pF (top). As expected, the sharp transparency unique to the EIT effect can be observed for the asymmetric case. The dynamic tunability of the EIT effect in this metamaterial enables us to achieve the storage of electromagnetic waves in a similar way to the atomic EIT systems. Recently, the design of this metamaterial has been extended to implement a true EIT effect in the sense that the transparency for an electromagnetic wave is induced by the incidence of an auxiliary electromagnetic wave [26], and the storage of electromagnetic waves in the metamaterial has been demonstrated in exactly the same way as light storage in the atomic EIT medium [27].

## 11.4 Conclusion

We have provided rigorous analogies between atomic systems and metamaterials, comparing the Schrödinger equations and circuit equations derived from the circuit models of the meta-atoms. The derived susceptibilities in both systems were written in the same expression, which means that the atomic medium and the artificial metamaterial had no difference in their response to the electromagnetic waves. The meta-atoms with a resonant mode showed a Lorentzian absorption profile like two-level atoms, and the meta-atoms based on coupled resonators showed a sharp transparency unique to the EIT effect, which was found in the three-level system. Switchable EIT metamaterials were also mentioned.

In addition to the electromagnetic wave storage introduced in Sect. 11.3.3.3, there are various other applications of the EIT-like metamaterials. The sharp transparency sensitive to the surrounding environment can be applied to accurate sensing [28]. It can also be used for frequency selective excitation of highly localized plasmonic modes [29].

**Acknowledgements** This research was financially supported by JSPS KAKENHI Grants No. 22560041, No. 22109004, No. 25790065, and No. 25287101.

## References

1. S. Harris, Phys. Today **50**, 36 (1997)
2. L.V. Hau, S.E. Harris, Z. Dutton, C.H. Behroozi, Nature **397**(6720), 594 (1999)
3. D. Phillips, A. Fleischhauer, A. Mair, R. Walsworth, M. Lukin, Phys. Rev. Lett. **86**(5), 783 (2001)
4. C. Liu, Z. Dutton, C.H. Behroozi, L.V. Hau, Nature **409**(6819), 490 (2001)
5. V.A. Fedotov, M. Rose, S.L. Prosvirnin, N. Papasimakis, N.I. Zheludev, Phys. Rev. Lett. **99**(14), 147401 (2007)
6. N. Papasimakis, V.A. Fedotov, N.I. Zheludev, S.L. Prosvirnin, Phys. Rev. Lett. **101**(25), 253903 (2008)
7. S.Y. Chiam, R. Singh, C. Rockstuhl, F. Lederer, W. Zhang, A. Bettiol, Phys. Rev. B **80**(15), 153103 (2009)
8. Z. Li, Y. Ma, R. Huang, R. Singh, J. Gu, Z. Tian, J. Han, W. Zhang, Opt. Express **19**(9), 8912 (2011)
9. R. Singh, I.A.I. Al-Naib, Y. Yang, D. Roy Chowdhury, W. Cao, C. Rockstuhl, T. Ozaki, R. Morandotti, W. Zhang, Appl. Phys. Lett. **99**(20), 201107 (2011)
10. X. Liu, J. Gu, R. Singh, Y. Ma, J. Zhu, Z. Tian, M. He, J. Han, W. Zhang, Appl. Phys. Lett. **100**(13), 131101 (2012)
11. N. Liu, L. Langguth, T. Weiss, J. Kästel, M. Fleischhauer, T. Pfau, H. Giessen, Nat. Mater. **8**(9), 758 (2009)
12. J. Zhang, S. Xiao, C. Jeppesen, A. Kristensen, N.A. Mortensen, Opt. Express **18**(16), 17187 (2010)
13. W. Huang, Q. Wang, X. Yin, C. Huang, H. Huang, Y. Wang, Y. Zhu, J. Appl. Phys. **109**(11), 114310 (2011)
14. R. Hokari, Y. Kanamori, K. Hane, J. Opt. Soc. Am. B **31**(5), 1000 (2014)
15. Y. Yang, I.I. Kravchenko, D.P. Briggs, J. Valentine, Nat. Commun. **5**, 5753 (2014)
16. T. Nakanishi, T. Otani, Y. Tamayama, M. Kitano, Phys. Rev. B **87**(16), 161110 (2013)
17. M. Scully, M. Zubairy, *Quantum Optics* (Cambridge University Press, Cambridge, 1997)
18. E. Kamenetskii, A. Sadreev, A. Miroshnichenko, *Fano Resonances in Optics and Microwaves* (Springer, Switzerland, 2018)
19. C.L. Garrido Alzar, M.A.G. Martinez, P. Nussenzveig, Am. J. Phys. **70**(1), 37 (2002)
20. S. Zhang, D.A. Genov, Y. Wang, M. Liu, X. Zhang, Phys. Rev. Lett. **101**(4), 047401 (2008)
21. M. Kang, H.X. Cui, Y. Li, B. Gu, J. Chen, H.T. Wang, J. Appl. Phys. **109**(1), 014901 (2011)
22. Y. Tamayama, K. Yasui, T. Nakanishi, M. Kitano, Phys. Rev. B **89**(7), 075120 (2014)
23. C. Kurter, P. Tassin, L. Zhang, T. Koschny, A. Zhuravel, A. Ustinov, S. Anlage, C. Soukoulis, Phys. Rev. Lett. **107**(4), 043901 (2011)
24. J. Gu, R. Singh, X. Liu, X. Zhang, Y. Ma, S. Zhang, S.A. Maier, Z. Tian, A.K. Azad, H.T. Chen, A.J. Taylor, J. Han, W. Zhang, Nat. Commun. **3**, 1151 (2012)
25. F. Miyamaru, H. Morita, Y. Nishiyama, T. Nishida, T. Nakanishi, M. Kitano, M.W. Takeda, Sci. Rep. **4**, 4346 (2014)
26. T. Nakanishi, M. Kitano, Phys. Rev. Appl. **4**(2), 024013 (2015)
27. T. Nakanishi, M. Kitano, Appl. Phys. Lett. **112**(20), 201905 (2018)
28. Z.G. Dong, H. Liu, J.X. Cao, T. Li, S.M. Wang, S.N. Zhu, X. Zhang, Appl. Phys. Lett. **97**(11), 114101 (2010)
29. S. Zhang, Z. Ye, Y. Wang, Y. Park, G. Bartal, M. Mrejen, X. Yin, X. Zhang, Phys. Rev. Lett. **109**(19), 193902 (2012)

**Part IV**  
**Chiral and Non-reciprocal**  
**Metamaterials**

# Chapter 12

## Dispersion Relation in Chiral Media: Credibility of Drude–Born–Fedorov Equations



Kikuo Cho

**Abstract** Dispersion relation of electromagnetic field in a chiral medium is discussed from the viewpoint of constitutive equations to be used as a partner of Maxwell equations. The popular form of Drude–Born–Fedorov (DBF) constitutive equations is compared with the one which is a simplified form of the first-principles macroscopic constitutive equations. Both of them describe [A] the dependence of the phase velocity of the EM wave in chiral media on the circular polarizations. However, there arises a decisive difference in the dispersion curve in the resonant region of chiral, left-handed character, as to [B] the ability of reproducing the linear crossing at  $k = 0$ , which is derived from the first-principles theory. DBF equations are a phenomenology applicable only to A but not to B.

### 12.1 Introduction

Symmetry plays an important role in the electromagnetic (EM) response of matter. It is revealed in the form of susceptibilities relating electric and magnetic polarization ( $\mathbf{P}$  and  $\mathbf{M}$ ) with source EM field. In high-symmetry case,  $\mathbf{P}$  and  $\mathbf{M}$  consist of the contributions of independent groups of excitations belonging to different irreducible representations of the symmetry group in consideration. This allows us to treat electric and magnetic properties of matter independently. However, when a medium lacks in certain mirror symmetry, i.e., the case of chiral symmetry, some (or all the) components of  $\mathbf{P}$  and  $\mathbf{M}$  belong to the same irreducible representation, so that they can be induced by both electric and magnetic source fields. In addition, there can also be a mixing between electric dipole (E1) and electric quadrupole (E2) transitions.

The study of chiral symmetry in the EM response of matter has a long history (Introduction of [1]). Chiral substances have been considered as unconventional materials for a long time, but now it attracts much attention as an important source of new materials and phases, providing hot topics in the studies of metamaterials [2], multiferroics [3], and superconductivity [4].

---

K. Cho (✉)

Institute of Laser Engineering, Osaka University, Suita, Osaka 565-0871, Japan  
e-mail: [k-cho@kcc.zaq.ne.jp](mailto:k-cho@kcc.zaq.ne.jp)

© Springer Nature Singapore Pte Ltd. 2019

K. Sakoda (ed.), *Electromagnetic Metamaterials*, Springer Series  
in Materials Science 287, [https://doi.org/10.1007/978-981-13-8649-7\\_12](https://doi.org/10.1007/978-981-13-8649-7_12)

189

In spite of its long history, theoretical description of chirality does not seem to be standardized. In the documents of IUPAP and IUPAC dealing with the standard definitions of physical and chemical quantities [5, 6], there is no mentioning about the chiral susceptibilities. Correspondingly, there are two or more different forms of phenomenological constitutive equations in use for macroscopic response. Though the effect of chiral symmetry is expected also in microscopic responses, its first-principles theory has been made only very recently [7, 8]. From the viewpoint that all the different forms of EM response theories should belong to a single hierarchy with logical ranking, one should be able to choose the most appropriate form of the constitutive equations for the macroscopic chiral response on the basis of the microscopic theory.

A typical effect of chirality is the difference in the phase velocity of EM waves for right and left circular polarizations in the off-resonant long-wavelength region. However, this is not the only aspect of our interest in discussing chirality. In fact, the dispersion curves in the resonant region of susceptibility show a remarkable behavior, by which we can select the appropriate form of phenomenological constitutive equations.

Macroscopic EM response of matter is usually calculated by the combination of Maxwell and constitutive equations. The standard form of the latter is

$$\mathbf{D} = \epsilon \mathbf{E} , \quad \mathbf{B} = \mu \mathbf{H} \quad (12.1)$$

with the dielectric constant (permittivity)  $\epsilon$  and permeability  $\mu$ . However, if the medium in consideration has chiral symmetry, these constitutive equations need to be generalized. A popular form of such an extension is

$$\mathbf{D} = \epsilon(\mathbf{E} + \beta \nabla \times \mathbf{E}) , \quad (12.2)$$

$$\mathbf{B} = \mu(\mathbf{H} + \beta \nabla \times \mathbf{H}) , \quad (12.3)$$

which is called Drude–Born–Fedorov equations (DBF equations) [9–12]. The parameter (chiral admittance)  $\beta$  describes the chirality of the medium. This is a phenomenology to be used for uniform and isotropic media. All the coefficients  $\epsilon$ ,  $\mu$ ,  $\beta$  are treated as scalars with a possible dependence on frequency  $\omega$ . In considering the  $\omega$  dependence, however, each of  $\beta\epsilon$  and  $\beta\mu$  should be a single parameter, because linear response coefficients should generally be a superposition of single pole functions. The reason for treating them as scalars instead of tensors is a simplification for parameterization.

However, this is not the only way of generalization. From the viewpoint that the fundamental variables of EM field are  $\mathbf{E}$  and  $\mathbf{B}$  rather than  $\mathbf{E}$  and  $\mathbf{H}$ , both electric and magnetic polarizations  $\mathbf{P}$  and  $\mathbf{M}$  should consist both of the  $\mathbf{E}$ - and  $\mathbf{B}$ -induced components, so that the definition  $\mathbf{D} = \mathbf{E} + 4\pi \mathbf{P}$ ,  $\mathbf{H} = \mathbf{B} - 4\pi \mathbf{M}$  leads to the extension



$$\mathbf{D} = \hat{\epsilon}\mathbf{E} + i\xi\mathbf{B} , \quad (12.4)$$

$$\mathbf{H} = (1/\hat{\mu})\mathbf{B} + i\eta\mathbf{E} , \quad (12.5)$$

where the terms with  $\xi$  and  $\eta$  take care of the chirality. Here also, the parameters  $\hat{\epsilon}$ ,  $\hat{\mu}$ ,  $\xi$ ,  $\eta$  are scalars. For later convenience, let us call them chiral constitutive equations (ChC equations). The first-principles calculation of macroscopic constitutive equations can be put in similar form with tensorial coefficients, as shown below.

As to the difference or similarity of DBF and ChC equations, there is a controversy. There have been arguments in the metamaterials community that DBF and ChC equations are essentially same [13], and also, it is argued that the former can be derived from the latter by assuming the uniformity and isotropy of matter [1] (Sect. 4.4). But there are others finding DBF and ChC equations different. The purpose of this article is to show that there is a clear difference between them leading to the preference of ChC over DBF equations. In view of the fact that DBF equations are frequently used in metamaterials studies and also in recent textbook of standard electromagnetism [12], it will be important to clarify the difference between DBF and ChC equations.

We first note the relation between the parameters of DBF and ChC equations. By means of the relation

$$\nabla \times \mathbf{E} = (i\omega/c)\mathbf{B} , \nabla \times \mathbf{H} = (-i\omega/c)\mathbf{D} , \quad (12.6)$$

DBF equations can be rewritten as

$$\mathbf{D} = \epsilon\mathbf{E} + (i\omega/c)\epsilon\beta\mathbf{B} , \quad (12.7)$$

$$\mathbf{H} = (i\omega/c)\epsilon\beta\mathbf{E} + (1/\mu)[1 - (\omega\beta/c)^2\epsilon\mu]\mathbf{B} . \quad (12.8)$$

If DBF and ChC equations are equivalent, the DBF parameters can be written in terms of the ChC parameters by comparing (12.7) and (12.8) with (12.4) and (12.5) as

$$\hat{\epsilon} = \epsilon , \quad \xi = \eta = (\omega/c)\epsilon\beta , \quad (1/\hat{\mu}) = (1/\mu) - (\omega\beta/c)^2\epsilon . \quad (12.9)$$

This relation will be shown later to lead to a contradiction, which disproves the equivalence of DBF and ChC equations.

The first-principles derivation of micro- and macroscopic constitutive equations is done in the following way [7]. We assume a general form of non-relativistic Hamiltonian (including relativistic correction terms, such as spin-orbit interaction and spin Zeeman term) for many particle systems in an EM field, and calculate the microscopic current density induced by the EM field, which is in general given as a functional of the transverse (T) part of vector potential  $\mathbf{A}^{(T)}$  and the longitudinal (L) external electric field  $\mathbf{E}_{\text{ext}}^{(L)}$ . The integral kernel of the functional is the microscopic susceptibility of separable form with respect to position coordinates. When the relevant quantum mechanical states have spatial extension much less than the wavelength of the EM field, we may apply long-wavelength approximation to the

microscopic current density, which leads to the macroscopic constitutive equations to be used for macroscopic Maxwell equations.

In this macroscopic scheme, we need only a single  $3 \times 3$  tensor to relate induced current density and source EM field, covering all the electric, magnetic, and chiral polarizations of matter. This macroscopic constitutive equation is given in the form [7]

$$\mathbf{J}(\mathbf{k}, \omega) = \chi_{\text{em}}(\mathbf{k}, \omega) \{ \mathbf{A}^{(\text{T})}(\mathbf{k}, \omega) - (ic/\omega) \mathbf{E}_{\text{ext}}^{(L)}(\mathbf{k}, \omega) \}. \quad (12.10)$$

The internal  $\mathbf{L}$  field does not appear in the source field, since it is taken into account as the Coulomb potential in the matter Hamiltonian. The susceptibility  $\chi_{\text{em}}$  is written in terms of the quantum mechanical transition energies and the lower moments of the corresponding transition matrix elements of current density operator.

Using the identity  $\mathbf{J} = -i\omega \mathbf{P} + ic\mathbf{k} \times \mathbf{M}$  in Fourier representation, we can rigorously rewrite the constitutive equation into the form

$$\mathbf{P} = \chi_{\text{eE}} \mathbf{E} + \chi_{\text{eB}} \mathbf{B}, \quad \mathbf{M} = \chi_{\text{mE}} \mathbf{E} + \chi_{\text{mB}} \mathbf{B} \quad (12.11)$$

The four susceptibilities  $\chi_{\text{eE}}, \chi_{\text{eB}}, \chi_{\text{mE}}, \chi_{\text{mB}}$  are again written in terms of the quantum mechanical transition energies and lower transition moments of electric dipole (E1), electric quadrupole (E2), and magnetic dipole (M1) characters. Details are given in Sect. 3.1 of [7]. The lowest order terms of them are

$$\begin{aligned} \chi_{\text{eE}} &= \frac{1}{\omega^2 V} \sum_{\nu} [\bar{g}_{\nu} \bar{\mathbf{J}}_{0\nu} \bar{\mathbf{J}}_{\nu 0} + \bar{h}_{\nu} \bar{\mathbf{J}}_{\nu 0} \bar{\mathbf{J}}_{0\nu}], \\ \chi_{\text{mB}} &= \frac{1}{V} \sum_{\nu} [\bar{g}_{\nu} \bar{\mathbf{M}}_{0\nu} \bar{\mathbf{M}}_{\nu 0} + \bar{h}_{\nu} \bar{\mathbf{M}}_{\nu 0} \bar{\mathbf{M}}_{0\nu}], \\ \chi_{\text{eB}} &= \frac{i}{\omega V} \sum_{\nu} [\bar{g}_{\nu} \bar{\mathbf{J}}_{0\nu} \bar{\mathbf{M}}_{\nu 0} + \bar{h}_{\nu} \bar{\mathbf{J}}_{\nu 0} \bar{\mathbf{M}}_{0\nu}], \\ \chi_{\text{mE}} &= \frac{-i}{\omega V} \sum_{\nu} [\bar{g}_{\nu} \bar{\mathbf{M}}_{0\nu} \bar{\mathbf{J}}_{\nu 0} + \bar{h}_{\nu} \bar{\mathbf{M}}_{\nu 0} \bar{\mathbf{J}}_{0\nu}], \end{aligned} \quad (12.12)$$

$$\bar{g}_{\nu} = \frac{1}{E_{\nu 0} - \hbar\omega - i0^+} - \frac{1}{E_{\nu 0}}, \quad \bar{h}_{\nu} = \frac{1}{E_{\nu 0} + \hbar\omega + i0^+} - \frac{1}{E_{\nu 0}}, \quad (12.13)$$

where  $V$  is the volume of the cell for periodic boundary condition to define  $\mathbf{k}$ , and  $\bar{\mathbf{J}}_{0\nu}$  and  $\bar{\mathbf{M}}_{0\nu}$  are the E1 and M1 transition moments, respectively, of current density and (orbital and spin) magnetization operators between the matter eigenstates  $|0\rangle$  (ground state) and  $|\nu\rangle$  with transition energy  $E_{\nu 0}$  between them. (E2 moments appear in the  $\bar{\mathbf{J}}_{\mu\nu}$  terms in the next higher order.) Chiral symmetry allows the existence of the transitions with mixed (E1 and M1) or (E1 and E2) character, leading to the  $O(k^1)$  terms in  $\chi_{\text{em}}$ .

Though there appear four susceptibilities, the single susceptibility nature is intact, since the rewriting of (12.10) into (12.11) is reversible. Combining the new form of

constitutive equations with the definition of  $\mathbf{D}$  and  $\mathbf{H}$ , we obtain

$$\mathbf{D} = \mathbf{E} + 4\pi\mathbf{P} = (1 + 4\pi\chi_{eE})\mathbf{E} + 4\pi\chi_{eB}\mathbf{B} , \quad (12.14)$$

$$\mathbf{H} = \mathbf{B} - 4\pi\mathbf{M} = (1 - 4\pi\chi_{mB})\mathbf{B} - 4\pi\chi_{mE}\mathbf{E} . \quad (12.15)$$

If we replace the parameters of these equations as

$$1 + 4\pi\chi_{eE} \rightarrow \hat{\epsilon} , \quad 4\pi\chi_{eB} \rightarrow i\xi , \quad -4\pi\chi_{mE} \rightarrow i\eta , \quad 1 - 4\pi\chi_{mB} \rightarrow \frac{1}{\hat{\mu}} , \quad (12.16)$$

we get ChC equations. It should also be noted that the poles of  $\chi_{mB}$ , i.e., the magnetic transition energies, are, not the poles, but the zeros of  $\hat{\mu}$ . This is due to the definition of  $\chi_{mB}$ ,  $\mathbf{M} = \chi_{mB}\mathbf{B}$  as required in the first-principles approach, in contrast to the conventional one  $\mathbf{M} = \chi_m\mathbf{H}$ . In this way, ChC equations are very close to the first-principles theory. In contrast, such a microscopic support does not exist for DBF equations. The scalar character of  $\hat{\epsilon}$ ,  $\hat{\mu}$ ,  $\xi$ ,  $\eta$  is due to the approximation to neglect the off-diagonal terms of the original tensor expressions and the assumption of isotropy in the plane perpendicular to  $\mathbf{k}$ .

## 12.2 Dispersion Equation

In order to show the difference between DBF and ChC equations, it is sufficient to give a single example. For this purpose, we compare the dispersion relations obtained from DBF and ChC equations.

### 12.2.1 Case of DBF Equations

If we solve DBF equations and (12.6) for  $\nabla \times \mathbf{H}$  and  $\nabla \times \mathbf{E}$ , we obtain

$$\nabla \times \mathbf{H} = a\mathbf{H} + b\mathbf{E} , \quad (12.17)$$

$$\nabla \times \mathbf{E} = d\mathbf{H} + e\mathbf{E} , \quad (12.18)$$

where

$$a = e = -\epsilon\mu\beta/\Delta , \quad b = -ic\epsilon/\omega\Delta , \quad d = +ic\mu/\omega\Delta , \quad (12.19)$$

and  $\Delta = \epsilon\mu\beta^2 - c^2/\omega^2$ . From (12.6)–(12.8), and  $\nabla \cdot \mathbf{B} = 0$ , both  $\mathbf{E}$  and  $\mathbf{H}$  are transverse, so that

$$\nabla \times \nabla \times \mathbf{E} = k^2\mathbf{E} , \quad \nabla \times \nabla \times \mathbf{H} = k^2\mathbf{H} \quad (12.20)$$

for Fourier components. Then, by operating  $\nabla \times$  to (12.17) and (12.18), we obtain a set of homogeneous linear equations of  $\mathbf{H}$ ,  $\mathbf{E}$ . The condition for the existence of non-trivial solution gives us the dispersion equation

$$\det|k^2 \mathbf{1} - \mathcal{A}^2| = 0, \quad (12.21)$$

where  $\mathcal{A}$  is a  $2 \times 2$  matrix with the components  $a, b, d, e$

$$\mathcal{A} = \begin{bmatrix} a & b \\ d & e \end{bmatrix}. \quad (12.22)$$

This dispersion equation can be rewritten as

$$\det|k\mathbf{1} + \mathcal{A}| = 0 \quad \text{or} \quad \det|k\mathbf{1} - \mathcal{A}| = 0, \quad (12.23)$$

so that the solution is

$$k = \pm a \pm \sqrt{bd}, \quad (12.24)$$

with all the combinations of  $\pm$  being allowed, which finally leads to a compact expression

$$\frac{ck}{\omega} = \pm \frac{\sqrt{\epsilon\mu}}{1 \pm (\omega\beta/c)\sqrt{\epsilon\mu}}. \quad (12.25)$$

This gives a dispersion curve with two branches. In homogeneous isotropic media, the two modes correspond to right and left circular polarizations. It should be noted that the condition for the existence of real solution is  $\epsilon\mu \geq 0$ . This means that the left-handed medium is defined in the same way as in non-chiral medium, in contrast to the case of ChC equations shown below.

### 12.2.2 Case of ChC Equations

A same way of solution is possible in this case, too. After eliminating  $\mathbf{D}$ ,  $\mathbf{B}$  from the ChC equations, the solution for  $\nabla \times \mathbf{H}$ ,  $\nabla \times \mathbf{E}$  has a same form as the one, where  $a, b, d, e$  of previous subsection are replaced with the following  $f, g, h, j$ , respectively

$$f = (\omega/c)\xi\hat{\mu}, \quad (12.26)$$

$$g = -i(\omega/c)(\hat{\epsilon} + \hat{\mu}\xi\eta), \quad (12.27)$$

$$h = i(\omega/c)\hat{\mu}, \quad (12.28)$$

$$j = (\omega/c)\hat{\mu}\eta. \quad (12.29)$$

Further transformation of the equations of  $\nabla \times \mathbf{H}$ ,  $\nabla \times \mathbf{E}$  into a set of homogeneous equations of  $\mathbf{E}$ ,  $\mathbf{H}$  allows us to obtain the dispersion equation, as the condition for the existence of non-trivial solution,

$$\frac{ck}{\omega} = \pm \frac{1}{2} [\hat{\mu}(\eta + \xi) \pm \sqrt{\{\hat{\mu}(\eta + \xi)\}^2 + 4\hat{\epsilon}\hat{\mu}}], \quad (12.30)$$

where we take all the combinations of  $\pm$ . The condition for real solutions is

$$\{\hat{\mu}(\eta + \xi)\}^2 + 4\hat{\epsilon}\hat{\mu} \geq 0, \quad (12.31)$$

which is less restrictive than non-chiral case.

## 12.3 Discussions

First of all, we note that, for both DBF and ChC equations, the well-known result of  $(ck/\omega)^2 = \epsilon\mu$  is obtained in the absence of chirality ( $\beta = 0$  and  $\xi = 0, \eta = 0$ ). Also both of the constitutive equations exhibit the typical behavior of chiral medium, i.e., the existence of the two branches with polarization-dependent refractive indices. In the nonresonant region, both of them could be used to fit experimental results via appropriate choice of parameter values.

### 12.3.1 Resonant Region of Left-Handed Chiral Medium

A decisive difference appears in resonant region. An example will be the left-handed behavior emerging in the neighborhood of a chiral resonance with E1-M1 mixed character. Such a case has been treated by the first-principles theory of macroscopic constitutive equation [7] (Sects. 3.8.1 and 4.1.1). It shows a pair of dispersion curves for left and right circularly polarized modes, which have a linear crossing at  $k = 0$ . It will be a test for the phenomenologies whether such a linear crossing can be realized or not by choosing parameter values.

The dispersion equation in the first-principles macroscopic formalism is

$$0 = \det \left[ \frac{c^2 k^2}{\omega^2} \mathbf{1} - \left[ \mathbf{1} + \frac{4\pi c}{\omega^2} \chi_{\text{em}}^{(\text{T})}(\mathbf{k}, \omega) \right] \right], \quad (12.32)$$

where  $\chi_{\text{em}}^{(\text{T})}(\mathbf{k}, \omega)$  is the T component of susceptibility tensor (Sect. 2.5 of [7]). Let us choose a chiral form of susceptibility tensor  $\chi_{\text{em}}^{(\text{T})}$  as

$$\mathbf{1} + \frac{4\pi c}{\omega^2} \chi_{\text{em}}^{(\text{T})} = (\epsilon_{\text{b}} + a' + c'k^2) \mathbf{1} + \begin{bmatrix} 0 & ib'k \\ -ib'k & 0 \end{bmatrix}, \quad (12.33)$$

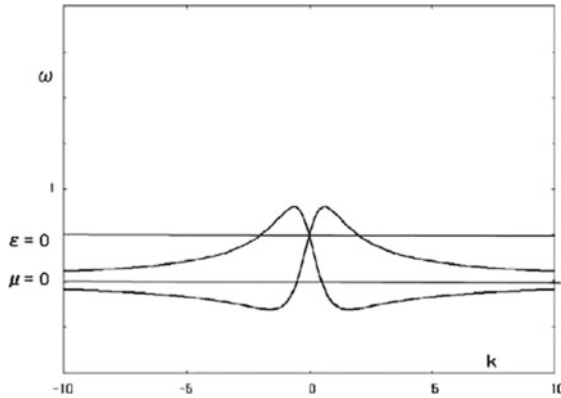


**Fig. 12.1** Dispersion curves of a chiral left-handed medium for the model in the text. Both ordinate and abscissa are normalized by the frequency of the pole as  $\omega/\omega_0$  and  $ck/\omega_0$ . Two horizontal lines show the frequencies of  $\epsilon = 0$  and  $\mu = 0$ . Reprinted by permission of Springer-Verlag GmbH, part of Springer Nature, Springer, 1st edn. [7] Copyright 2010, and 2nd edn. [14] Copyright 2018

where the terms with  $a', b', c'$  represent the contribution of a pole  $\sim 1/(\omega_0 - \omega)$  with mixed (E1, M1) character, while  $\epsilon_b$  is the background dielectric constant due to all the other resonances. We assume that the resonance with mixed E1 and M1 characters occurs in the frequency region of  $\epsilon_b < 0$ , i.e., a chiral version of left-handed medium. The off-diagonal elements of  $\chi_{em}^{(T)}$  become the diagonal elements of  $\chi_{eM}^{(T)}$  and  $\chi_{mE}^{(T)}$  according to the rigorous rewriting process given in [7], and these diagonal elements correspond to  $\hat{\xi}$  and  $\hat{\eta}$  of ChC equations.

The dispersion equation for this model is written as

$$\left(\frac{ck}{\omega}\right)^2 = \bar{\epsilon}\bar{\mu} \pm \bar{\beta}\bar{\mu} \frac{ck}{\omega}, \tag{12.34}$$

and its solution is given as

$$\frac{ck}{\omega} = \pm \frac{1}{2} \left[ \pm \bar{\beta}\bar{\mu} + \sqrt{\bar{\beta}^2\bar{\mu}^2 + 4\bar{\epsilon}\bar{\mu}} \right], \tag{12.35}$$

where we take all the combinations of  $\pm$ , and

$$\bar{\beta} = \omega b'/c, \quad \bar{\epsilon} = \epsilon_b + a', \quad \bar{\mu} = 1/[1 - (\omega/c)^2 c']. \tag{12.36}$$

Noting that  $b'$  is a chiral parameter corresponding to  $\xi, \eta$  of the ChC equations, we see that this equation is the same type as (12.30), but not as (12.25). An example of this dispersion relation is given in Fig. 12.1. The characteristic behavior of the dispersion curves is a linear crossing at  $k = 0$  (Fig. 4.1 of [7]).

In order to check whether the dispersion equations (12.25) and (12.30) have this typical behavior of “linear crossing at  $k = 0$ ”, we focus on the behavior of the dispersion equations near  $k = 0$ . Since both of the dispersion equations are given in the

form “ $ck/\omega = F(\omega)$ ,” we only need to examine how the function  $F(\omega)$  approaches zero in each case.

The microscopic model of left-handed chiral medium given above consists of a matter excitation level with (E1, M1) mixed character in the frequency range of  $\epsilon_b < 0$ . This means that all of  $\chi_{eE}, \chi_{eB}, \chi_{mE}, \chi_{mB}$  have a common pole (at  $\omega = \omega_0$ ), and the background part of  $\chi_{eE}$  is largely negative in the frequency range of interest to make  $\epsilon_b < 0$ . Namely,  $\hat{\epsilon}, 1/\hat{\mu}, \xi, \eta$  of ChC equations have a common pole at  $\omega = \omega_0$  and  $\hat{\epsilon} = \epsilon_b + \bar{a}/(\omega_0 - \omega)$ . It may appear that the RHS of (12.30) becomes zero for the frequency satisfying  $\hat{\mu} = 0$  or  $\hat{\epsilon} = 0$ . However, as mentioned before, the zero of  $\hat{\mu}$  corresponds to the pole of M1 transition, which in this case is common to the pole of  $\xi$  and  $\eta$ . Therefore, the zero of  $\hat{\mu}$  is canceled in the product  $\hat{\mu}(\xi - \eta)$ . Thus, the only remaining possibility of zero arises from  $\hat{\epsilon} = 0$ . The  $\omega$  dependence of the RHS of (12.30) near zero point can be found by rewriting it as

$$\frac{ck}{\omega} = \pm \frac{2\hat{\epsilon}\hat{\mu}}{\hat{\mu}(\xi + \eta) \pm \sqrt{\{\hat{\mu}(\xi + \eta)\}^2 + 4\hat{\epsilon}\hat{\mu}}}. \quad (12.37)$$

At the frequency satisfying  $\hat{\epsilon} = 0$ , i.e.,  $\epsilon_b + a' = 0$ , all of  $\hat{\mu}, \xi, \eta$  remain finite. While the numerator goes to zero, one of the  $\pm$  combinations in the denominator remains finite, so that the whole expression becomes zero for this combination. This occurs for both signs of  $\pm$  in front of the whole expression. For negative  $\epsilon_b$  and positive numerator of the pole  $\sim 1/(\omega_0 - \omega)$ ,  $\epsilon_b + a' = 0$  occurs at  $\omega = \omega_z < \omega_0$  and in its neighborhood  $\hat{\epsilon} \sim (\omega - \omega_z)$ . This shows that the RHS of (12.30) behaves like  $\sim(\omega - \omega_z)$ , which means the linear crossing of the two branches. Note also that  $\omega_z$  lies inside the frequency range of (12.31).

Now, we check whether the same behavior is obtained for DBF equations by assuming (12.9), from which we obtain

$$\frac{1}{\mu} = \frac{1}{\hat{\mu}} + \frac{\xi^2}{\hat{\epsilon}}, \quad \frac{\omega^2 \beta^2}{c^2} \epsilon \mu = 1 - \frac{\mu}{\hat{\mu}}. \quad (12.38)$$

This shows that  $1/\mu$  has the same pole as  $1/\hat{\mu}$  at  $\omega = \omega_0$ , so that the factor  $\mu/\hat{\mu}$  on the RHS of the second equation does not have the pole at  $\omega = \omega_0$  via cancellation. Therefore, there is no chance for the denominator of the RHS of (12.25) to diverge. Hence, the only possibility of its becoming zero comes from the factor  $\sqrt{\epsilon\mu}$  on the numerator. In view of the fact that the zeros of  $\epsilon, \mu$  occur at different  $\omega$ 's, e.g., at  $\omega_{z1}$  and  $\omega_{z2}$  ( $\omega_{z1} > \omega_{z2}$ ), the  $\omega$  dependence of  $\sqrt{\epsilon\mu}$  should be  $\sim\sqrt{\omega_{z1} - \omega}$  or  $\sim\sqrt{\omega - \omega_{z2}}$  in the neighborhood of the zeros. Therefore, no linear crossing is possible in the DBF dispersion curves. The two zeros are the boundaries of the region of left-handed behavior.

One might argue that other type of  $\omega$  dependence than (12.9) could lead to the linear crossing behavior. But one cannot freely give the  $\omega$  dependence even as a phenomenology. Linear susceptibilities should be a sum of single pole functions. In the absence of the first-principles theory for DBF equations, it would be quite difficult to give an appropriate model on a reliable basis.

### 12.3.2 *Conventionality Versus Logical Consistency*

DBF equations have been popularly used in the macroscopic argument of chiral systems, especially in the field of metamaterials research. As long as they are used for nonresonant phenomena as a practical tool, there is not much to say against it, except for the difficulty in assigning microscopic meaning to the parameter  $\beta$ . However, the restriction to the nonresonant phenomena does not seem to be widely recognized, to the knowledge of the present author. In fact, there are examples of its use for resonant phenomena [15, 16]. The constitutive equations in these papers are  $\mathbf{D} = \epsilon\mathbf{E} - i\xi\mathbf{H}$ ,  $\mathbf{B} = \mu\mathbf{H} + i\xi\mathbf{E}$ . They are not quite DBF equations but of the same type, in the sense that they lead to the dispersion equation  $(ck/\omega) = \pm(\sqrt{\epsilon\mu} \pm \xi)$ , which is unable to reproduce the linear crossing discussed above.

From the qualitative difference of the two dispersion equations (12.25) and (12.30) in resonant region, and from the fact that DBF equations have no support from microscopic theory in contrast to ChC equations, it is highly recommended to use ChC equations rather than DBF equations. As we show in this note, ChC equations can be handled as easily as DBF equations and are consistent with the microscopically derived macroscopic constitutive equation. If one dares to stay with DBF equations, one should keep the validity limit in mind.

## 12.4 Conclusion

The DBF equations, popularly used as the constitutive equations of chiral media, are shown to have a limited range of applicability; i.e., they should not be used in resonant region, where a qualitatively erroneous result can arise. On the other hand, the ChC equations, consistent with the first-principles microscopic constitutive equations, can be used for both resonant and nonresonant problems.

**Acknowledgements** This work is supported by Grant-in-Aid for scientific research on Innovative Areas Electromagnetic Metamaterials of MEXT Japan (Grant No. 22109001).

## References

1. O.N. Singh, A. Lakhtakia, *Electromagnetic Fields in Unconventional Materials and Structures* (Wiley, 2000)
2. Z.F. Li, M. Mutlu, E. Ozbay, *J. Opt.* **15**, 023001 (2013)
3. Review articles in *Nat. Mater.* **6**(1) (2007)
4. C. Kallin, A.J. Berlinsky, *J. Phys. Condens. Matter* **21**, 164210 (2009)
5. IUPAP document, *Physica* **146A**, 1 (1987)
6. E.R. Cohen, et al. (eds.), *Quantities, Units and Symbols in Physical Chemistry*, 3rd edn. (RSC Publishing, 2007)
7. K. Cho, *Reconstruction of Macroscopic Maxwell Equations*, 1st edn. (Springer, Berlin, Heidelberg, 2010)



8. K. Cho, *J. Phys. Condens. Matter* **20**, 175202 (2008)
9. P. Drude, *Lehrbuch der Optik* (S. Hirzel, Leipzig, 1912)
10. M. Born, *Optik* (Springer, Heidelberg, 1933)
11. F.I. Fedorov, *Opt. Spectrosc.* **6**, 49 (1959); *ibid.* **6**, 237 (1959)
12. Y.B. Band, *Light and Matter* (Wiley, 2006)
13. N. Engheta, private commun
14. K. Cho, *Reconstruction of Macroscopic Maxwell Equations*, 2nd edn. (Springer, Berlin, Heidelberg, 2018), p. 103
15. P-G. Luan, Y-T Wang, S. Zhang, X. Zhang, *Optics Lett.* **36**, 675 (2011)
16. S. Tomita, K. Sawada, A. Porokhnyuk, T. Ueda, *Phys. Rev. Lett.* **113**, 235501 (2014)

# Chapter 13

## Surface Waves of Isotropic Chiral Metamaterials



Hiroshi Miyazaki and Yoji Jimba

**Abstract** Phase diagrams of the surface electromagnetic waves in isotropic chiral metamaterials in contact with either the vacuum or metal are presented over a wide range of permittivity, permeability, and chiral parameters. Chirality is found to reduce the localized nature of the surface wave and modify strongly the surface wave phase diagrams. Exact analytical treatment of the chirality is presented which enables us to determine the surface wave phase diagrams and their boundaries completely.

### 13.1 Introduction

Metamaterials are artificial optical structures composed of periodic optical elements called meta-atoms whose sizes are much smaller than the relevant wavelength [1–3]. Owing to the freedom of geometrical structures and composite materials, one can design their optical functionality over a wide range such as negative permittivity or permeability. Metamaterials with both negative permittivity and permeability are known to exhibit left-handedness and support the backward waves where the phase velocity is in opposite direction to the energy flow [4]. This leads to various curious optical responses such as negative refraction, super lens, optical cloaking, negative Doppler effect, and negative Cerenkov effect. Backward waves can also be created by the artificial chiral meta-atoms having no mirror symmetric optical structure [5–8]. Although natural chiral materials have already been known back to the nineteenth centuries, their chirality is too small to support left-handedness [9, 10]. However, the concept of meta-atoms enables us to create metamaterials having huge values of chirality. Chiral metamaterials allow much easy realization of negative refraction as they require no negative permittivity and permeability. In addition, it can draw out much fascinating proposals such as chiral vacuum and circular beam splitters [11].

---

H. Miyazaki (✉)

Department of Applied Physics, Tohoku University, Sendai 980-8579, Japan  
e-mail: [hmiyazak@olive.apph.tohoku.ac.jp](mailto:hmiyazak@olive.apph.tohoku.ac.jp)

Y. Jimba

College of Engineering, Nihon University, Koriyama 963-8642, Japan

© Springer Nature Singapore Pte Ltd. 2019

K. Sakoda (ed.), *Electromagnetic Metamaterials*, Springer Series  
in Materials Science 287, [https://doi.org/10.1007/978-981-13-8649-7\\_13](https://doi.org/10.1007/978-981-13-8649-7_13)

201

In spite of these intriguing proposals, there arises soaring technological difficulty of dimensionality. While tremendous efforts have still been devoted to create three-dimensional metamaterials by using sophisticated modern technology, growing interest has recently been provoked, instead, to the two-dimensional metamaterials called meta-surfaces because of their feasibility of fabrication [12]. To utilize the optical functionality of meta-surfaces, it is indispensable to study the electromagnetic waves localized at the meta-surfaces which are natural extensions of famous surface plasmons studied years ago by Sommerfeld [13] and Richie [14]. Shadrivov et al. [15] and later Kats et al. [16] have pointed out that the backward surface waves can be realized at the interfaces between the positive and negative index metamaterials. Jin et al. have studied the existence of surface polaritons on the surface of a half-space of chiral metamaterials [17]. They pointed out that the surface polaritons can exist for sufficiently large values of chiral parameter. In this paper, we report the results of the detailed investigation of surface waves on the chiral metamaterials' surfaces [18]. Phase diagrams are presented for the existence of the surface waves over a wide range of parameters. Perturbative treatment of the chirality is presented and is shown to have certain limitations even for much smaller values of chirality. This difficulty leads us to develop the exact analytical treatment of the chirality, which enables us to give a thorough description of the phase diagrams.

## 13.2 Models and Formulations

Characteristic feature of the chiral media is the simultaneous excitation of the electric and magnetic polarizations due to the applied fields. This is best described by the constitutive relations:

$$\mathbf{D}(\mathbf{r}) = \varepsilon\varepsilon_0\mathbf{E}(\mathbf{r}) + i\kappa\sqrt{\varepsilon_0\mu_0}\mathbf{H}(\mathbf{r}), \quad \mathbf{B}(\mathbf{r}) = \mu\mu_0\mathbf{H}(\mathbf{r}) - i\kappa\sqrt{\varepsilon_0\mu_0}\mathbf{E}(\mathbf{r}), \quad (13.1)$$

where  $\kappa$  is the chirality parameter, and  $\varepsilon$  and  $\mu$  are the relative permittivity and permeability of the chiral medium. We assume positive values of  $\kappa$  for simplicity of discussion. Let us briefly describe the electromagnetic waves in a uniform chiral medium. We combine (13.1) with the Maxwell equations and assume the time and spatial dependence of electromagnetic fields as  $\exp(i\mathbf{k} \cdot \mathbf{r} - i\omega t)$ . This leads to the following equations for the amplitudes of the electromagnetic fields:

$$\mathbf{H} = \frac{i\kappa}{\mu Z_0}\mathbf{E} + \frac{\mathbf{k} \times \mathbf{E}}{\omega\mu\mu_0}, \quad \mathbf{D} = \varepsilon_0\left(\varepsilon - \frac{\kappa^2}{\mu}\right)\mathbf{E} + \frac{i\kappa}{\omega\mu Z_0}\mathbf{k} \times \mathbf{E}, \quad (13.2)$$

where  $Z_0$  is the vacuum impedance. By assuming  $\mathbf{k} = (0, k, 0)$ , we obtain the expression for  $k$  as

$$k = k^\pm = \sqrt{\varepsilon_0\mu_0}\omega(\sqrt{\varepsilon\mu} \pm \kappa), \quad (13.3)$$

and the following relations:

$$E_x = \pm i E_z, H_x = \frac{\sqrt{\varepsilon\mu}}{\mu Z_0} E_z, E_y = H_y = 0, H_z = \mp i \frac{\sqrt{\varepsilon\mu}}{\mu Z_0} E_z. \quad (13.4)$$

Here, we assume positive value of  $\sqrt{\varepsilon\mu}$  for  $\varepsilon < 0$  and  $\mu < 0$ , and + and -, respectively, represent the right- and left-rotating waves. Since the Poynting vector has positive y-component for  $\varepsilon > 0$  and  $\mu > 0$ , the left-rotating wave becomes the backward wave for  $\kappa > \sqrt{\varepsilon\mu}$  because of the negative value of  $k^-$ . In the chiral medium, therefore, the backward wave can exist without assuming simultaneous negative values of  $\varepsilon$  and  $\mu$ .

Let us formulate the surface electromagnetic waves between two semi-infinite chiral media. We assume that the chiral medium with  $(\varepsilon_j, \mu_j, \kappa_j)$  occupies the region  $x < 0$  for  $j = 1$  and  $x > 0$  for  $j = 2$ . The surface wave is assumed to localize near the  $yz$  plane and propagates along the  $y$ -direction with the propagation constant  $\beta$ . Since the uniform chiral medium has right- and left-rotating waves, the surface wave can be expressed as:

$$\begin{aligned} \mathbf{E}^1 &= \mathbf{E}^{1+} \exp(k_x^{1+} x + i\beta y) + \mathbf{E}^{1-} \exp(k_x^{1-} x + i\beta y) \quad : \quad x < 0, \\ \mathbf{E}^2 &= \mathbf{E}^{2+} \exp(-k_x^{2+} x + i\beta y) + \mathbf{E}^{2-} \exp(-k_x^{2-} x + i\beta y) \quad : \quad x > 0, \end{aligned} \quad (13.5)$$

where  $k_x^{j\pm} = \sqrt{\beta^2 - (k^{j\pm})^2}$ , and  $k^{j\pm}$  is given by  $k^{j\pm} = \sqrt{\varepsilon_0 \mu_0} \omega (\sqrt{\varepsilon_j \mu_j} \pm \kappa_j)$ . From the localization condition, we have  $\text{Re}(k_x^{j\pm}) > 0$ . By substituting (13.5) into the Maxwell equations, we obtain the relations between each component of the surface waves as

$$\begin{aligned} E_x^{j\pm} &= \frac{\pm i \beta}{k^{j\pm}} E_z^{j\pm}, \quad E_y^{j\pm} = \pm (-1)^j \frac{k_x^{j\pm}}{k^{j\pm}} E_z^{j\pm}, \quad H_x^{j\pm} = \frac{\sqrt{\varepsilon_j \mu_j} \beta}{Z_0 \mu_j k^{j\pm}} E_z^{j\pm}, \\ H_y^{j\pm} &= (-1)^{j-1} \frac{\sqrt{\varepsilon_j \mu_j} i k_x^{j\pm}}{Z_0 \mu_j k^{j\pm}} E_z^{j\pm}, \quad H_z^{j\pm} = \mp \frac{i \sqrt{\varepsilon_j \mu_j}}{Z_0 \mu_j} E_z^{j\pm}. \end{aligned} \quad (13.6)$$

It is straightforward to derive the following eigenvalue equation from the continuity condition of the tangential components of surface waves at the interface:

$$(1 + Z_r)^2 (Q^{1+} + Q^{2+})(Q^{1-} + Q^{2-}) = (1 - Z_r)^2 (Q^{1+} - Q^{2-})(Q^{1-} - Q^{2+}), \quad (13.7)$$

where  $Z_r = \mu_2 \sqrt{\varepsilon_1 \mu_1} / \mu_1 \sqrt{\varepsilon_2 \mu_2}$  and  $Q^{j\pm}$  is defined as

$$P^{j\pm} \equiv \frac{k_x^{j\pm}}{\beta}, \quad \alpha^{j\pm} \equiv \sqrt{\varepsilon_j \mu_j} \pm \kappa_j, \quad Q^{j\pm} \equiv \frac{P^{j\pm}}{\alpha^{j\pm}}. \quad (13.8)$$

Hereafter, we will use the dimensionless parameter  $\bar{\omega} = \omega\sqrt{\epsilon_0\mu_0}/\beta$  instead of  $\omega$ .

### 13.3 Numerical Results

The phase diagram of surface waves can be obtained by solving (13.7) for  $\bar{\omega}$  which satisfies the condition  $\text{Re}(P^{j\pm}) > 0$ . It is easy to show from (13.7) that the phase diagram satisfies the following scaling rule:  $\epsilon_j \rightarrow a \cdot \epsilon_j, \mu_j \rightarrow b \cdot \mu_j, \kappa_j \rightarrow \sqrt{ab} \cdot \kappa_j, \bar{\omega} \rightarrow \bar{\omega} / \sqrt{ab}$  with  $a \cdot b > 0$ . In this paper, we will mainly study the phase diagrams where medium I is non-chiral. For such occasions, the scaling rule allows us to treat only two cases; that is, the chiral medium I is either the vacuum or lossless metal having  $\epsilon_1 = -1, \mu_1 = 1$ .

As a preliminary, we explain the phase diagrams for non-chiral medium II in contact with the vacuum or lossless metal shown in Fig. 13.1a and b, respectively. Here, the horizontal and vertical axes represent  $\epsilon_2$  and  $\mu_2$  of the medium II. In what follows, we will use the notations  $\epsilon$  and  $\mu$  instead of  $\epsilon_2$  and  $\mu_2$  except the cases to be notified. The black and light gray regions indicate the surface wave regions with the positive and negative energy flow along the  $y$  direction, respectively. No surface wave is allowed for the white regions. Since we assume  $\beta$  to be positive, the black and light gray regions mean, respectively, the right-handed (forward wave) and left-handed (backward wave) regions. These regions are separated by the boundaries

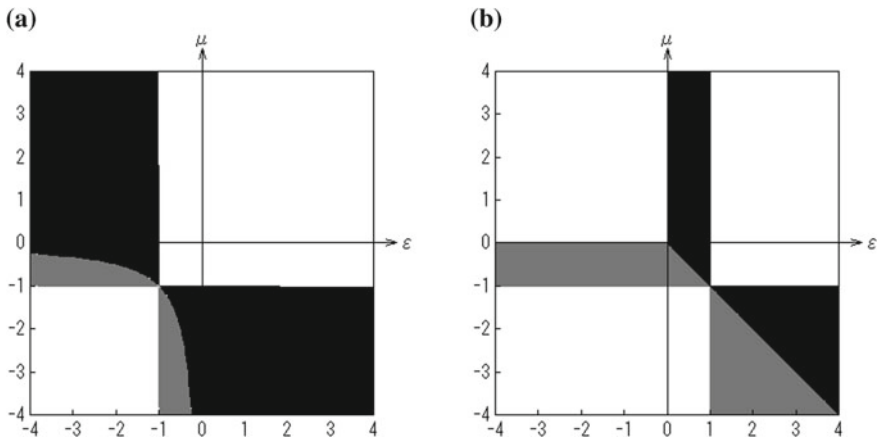


**Fig. 13.1** Phase diagrams of surface waves for non-chiral metamaterial in contact with **a** the vacuum and **b** lossless metal with  $\epsilon_1 = -1, \mu_1 = 1$ , and  $\kappa_1 = 1$ . Black and light gray regions, respectively, indicate the right-handed and left-handed surface wave regions. No surface waves are allowed for the white regions

$\varepsilon\mu = 1$  in Fig. 13.1a and  $\varepsilon + \mu = 0$  in Fig. 13.1b. There are no surface wave when  $\varepsilon$  and  $\mu$  have the same sign with those in the medium I.

These phase diagrams can be explained from (13.7). For non-chiral medium II in contact with the vacuum, (13.7) is simplified as:

$$\frac{P}{\varepsilon} + P_0 = 0: TM, \quad \frac{P}{\mu} + P_0 = 0: TE, \quad (13.9)$$

where  $P_0 = \sqrt{1 - \bar{\omega}^2}$  and  $P = \sqrt{1 - \varepsilon\mu\bar{\omega}^2}$ . TM and TE represent, respectively, the transverse magnetic and electric fields. By solving (13.9) for  $\bar{\omega}$ , we obtain

$$\bar{\omega}^2 = \frac{\varepsilon^2 - 1}{\varepsilon(\varepsilon - \mu)}: TM, \quad \bar{\omega}^2 = \frac{\mu^2 - 1}{\mu(\mu - \varepsilon)}: TE, \quad (13.10)$$

provided that  $\varepsilon < 0$  for TM,  $\mu < 0$  for TE, and the following conditions are satisfied:

$$1 > \bar{\omega}^2 > 0, \quad 1 > \varepsilon\mu\bar{\omega}^2. \quad (13.11)$$

Since  $\bar{\omega}$  means the surface wave velocity normalized by the vacuum light velocity, conditions (13.11) mean that the surface wave can only exist when its velocity is smaller than the velocities of the bulk electromagnetic waves in the surrounding media. As for the phase boundaries, it is easy to see that the condition  $\bar{\omega}^2 > 0$  gives rise to the phase boundaries  $\varepsilon = -1$ ,  $\mu = -1$ , while the boundary  $\varepsilon\mu = 1$  between left-handed and right-handed regions stems from the vanishing damping factor  $P_0 = P = 0$ .

When the non-chiral medium is in contact with lossless metal, the TE part of (13.9) and the definition of  $P$  remain unchanged while  $P_0$  is replaced by  $P_0 = \sqrt{1 + \bar{\omega}^2}$  and the TM part of (13.8) changes as  $P/\varepsilon - P_0 = 0$ . Correspondingly,  $\bar{\omega}^2$  is given as

$$\bar{\omega}^2 = \frac{1 - \varepsilon^2}{\varepsilon(\varepsilon + \mu)}: TM, \quad \bar{\omega}^2 = \frac{1 - \mu^2}{\mu(\mu + \varepsilon)}: TE, \quad (13.12)$$

provided that  $\varepsilon > 0$  for TM and  $\mu < 0$  for TE. Since there is no bulk wave in lossless metal, the condition  $1 > \bar{\omega}^2$  drops out in (13.11). These conditions lead to the phase diagram shown in Fig. 13.1b. Here, all the boundaries result from the condition  $\bar{\omega}^2 > 0$  in contrast to the case in Fig. 13.1a.

Let us study the surface waves of chiral medium in contact with the vacuum. Figure 13.2a–d shows the phase diagrams for  $\kappa = 0.2, 0.5, 1.0, 1.5$  in medium II. As is seen, the chirality brings about the gap between the left-handed and right-handed regions. With the increase of  $\kappa$ , the left-handed region moves away from the origin with the simultaneous shrinkage. This shrinkage is also observed for the right-handed regions in the third quadrant which approach to the origin and finally vanish at  $\kappa = 1$ . On the other hand, the right-handed regions in the second and fourth quadrants become wide with the increase of  $\kappa$ . It is interesting to observe that there

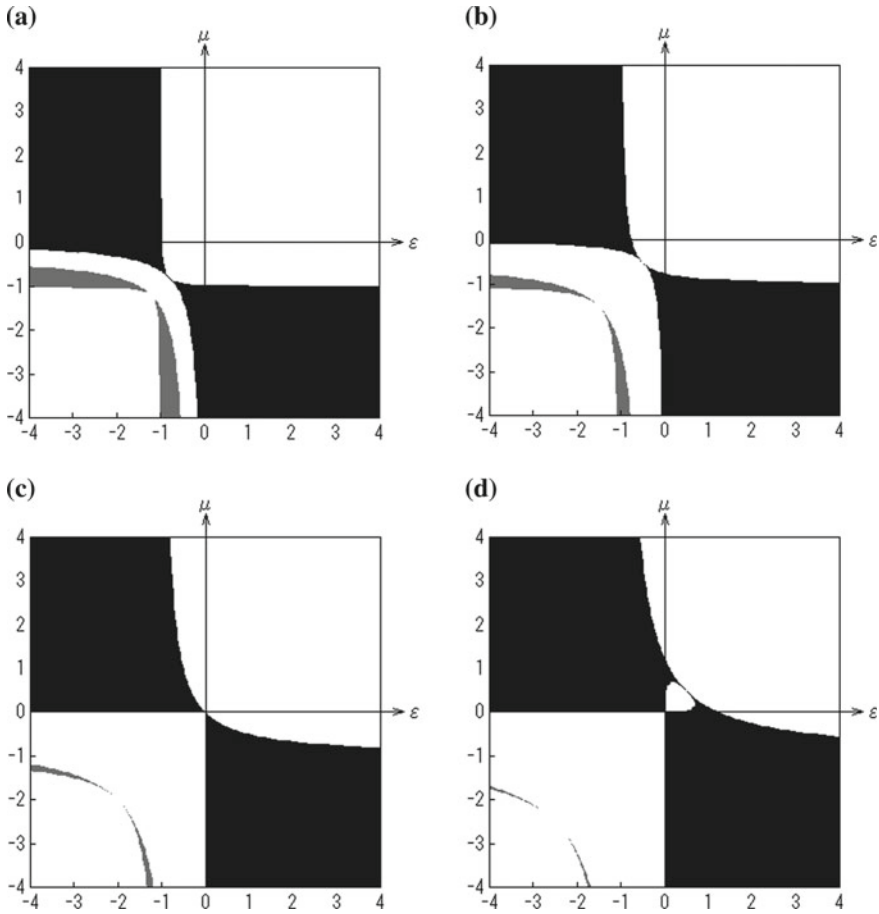


**Fig. 13.2** Phase diagrams of surface waves for chiral metamaterial in contact with the vacuum. Chiral parameters  $\kappa$  are taken as **a** 0.2, **b** 0.5, **c** 1.0, and **d** 1.5. Black and light gray regions, respectively, represent the right-handed and left-handed surface wave states

appear the right-handed regions in the first quadrant when  $\kappa$  exceeds unity. With further increase of  $\kappa$ , these regions leave the origin.

Detailed numerical calculation shows that the energy flow in the vacuum layer is in the positive  $y$  direction irrespective of the values of  $\kappa$ ; that is, the energy flow is right-handed. In contrast, the energy flow is always left-handed in the chiral medium in the second, third, and fourth quadrants. The handedness of the surface wave is determined by the sum of these energy flows. The negative flow in the chiral medium is the strongest for  $\epsilon \mu > 1$  in the third quadrant. This negative flow overcomes the positive flow in the vacuum layer and results in the left-handed surface waves. In the second or fourth quadrants, the negative flow is the strongest near  $\epsilon = -1$  or  $\mu = -1$  and decreases rapidly for larger negative  $\epsilon$  or  $\mu$ . In contrast to the third

quadrant, however, the positive flow in the vacuum layer surpasses the negative flow in the chiral medium and results in the right-handed surface waves. The situation in the first quadrant for  $\kappa \geq 1$  is complicated. The energy flow in the vacuum layer is always positive while that in the chiral medium shows both direction depending on the values of  $\varepsilon$  and  $\mu$ . It is positive for small values of  $\varepsilon$  or  $\mu$ , but is negative for larger values of  $\varepsilon$  and  $\mu$ . The sum of the energy flow is positive as a whole.

In Fig. 13.3a–d, we show the phase diagrams for  $\kappa = 0.2, 0.5, 1.0, 1.5$  when the chiral medium is in contact with lossless metal of  $\varepsilon_1 = -1, \mu_1 = 1$ . For all values of  $\kappa$ , the surface waves are right-handed or left-handed for  $\varepsilon + \mu > 0$  or  $\varepsilon + \mu < 0$ , respectively. With the increase of  $\kappa$ , the surface wave regions in the first and third quadrants shrink and move away from the origin, while that in the fourth quadrant

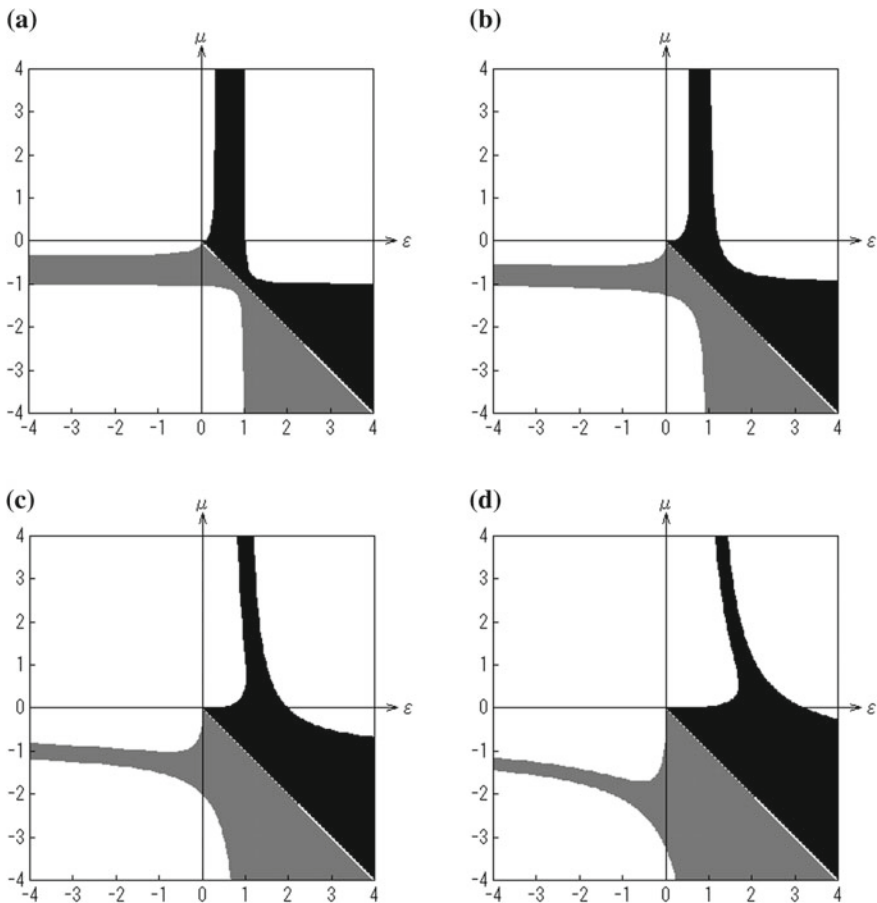


**Fig. 13.3** Phase diagrams of surface waves for chiral metamaterial in contact with lossless metal with  $\varepsilon_1 = -1, \mu_1 = 1$ , and  $\kappa_1 = 1$ . Chiral parameters  $\kappa$  are chosen as **a** 0.2, **b** 0.5, **c** 1.0, and **d** 1.5. Black and light gray regions, respectively, indicate the right-handed and left-handed surface wave states



become expanded and tend to occupy the whole area of the quadrant. There is no surface waves in the second quadrant irrespective of the values of  $\kappa$ . The energy flows in lossless metal and chiral medium are found to be almost in reverse direction. The flow in the chiral medium is right-handed or left-handed for the first or third quadrant, respectively. In the region  $\varepsilon + \mu > 0$  in the fourth quadrant, it is right-handed near the origin and becomes left-handed away from the origin. The flow for  $\varepsilon + \mu < 0$  in the fourth quadrant is in completely reverse direction to that for  $\varepsilon + \mu > 0$ .

Let us study the effect of the chirality of medium I. Figure 13.4a–d shows the phase diagrams when the medium I has the parameters  $\varepsilon_1 = 1$ ,  $\mu_1 = 1$ ,  $\kappa_1 = 0.5$ . Corresponding values of chiral parameter  $\kappa_2$  are chosen as  $\kappa_2 = 0.2, 0.5, 1.2, 2.0$ . Compared to the cases of the vacuum, we observe for  $\kappa_2 = 0.2$  that the right-handed

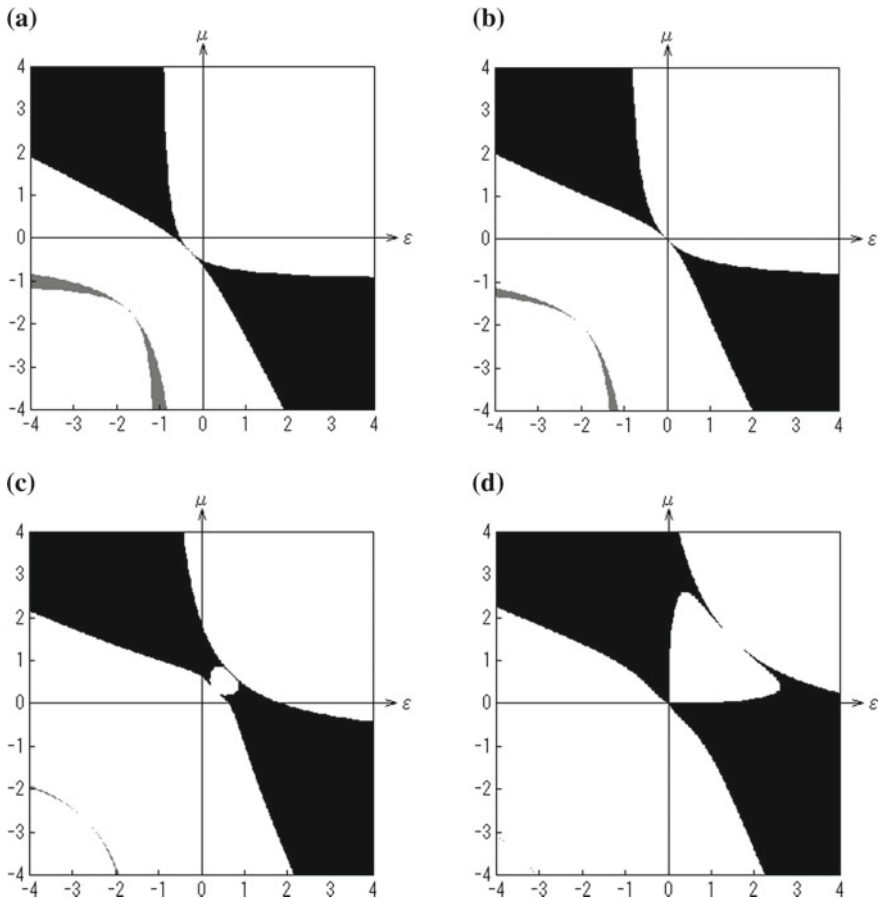


**Fig. 13.4** Phase diagrams of surface waves at the interface between two semi-infinite chiral metamaterials. Upper chiral metamaterial layer has the fixed parameters  $\varepsilon_1 = 1$ ,  $\mu_1 = 1$ , and  $\kappa_1 = 0.5$ . Chiral parameters  $\kappa_2$  for lower metamaterial layer are taken as **a** 0.2, **b** 0.5, **c** 1.2, and **d** 2.0. Black and light gray regions, respectively, indicate the right-handed and left-handed surface wave regions

regions decrease drastically in the second and fourth quadrants while the left-handed regions remain almost unchanged. With the increase of  $\kappa_2$ , the right-handed regions gradually shift to the upper right direction and pass the origin at  $\kappa_2 = 0.5$ . With further increase of  $\kappa_2$ , the central part near the origin becomes expanded and split as shown in Fig. 13.4c. For  $\kappa_2 = 2.0$  in Fig. 13.4d, the lower boundary in the first quadrant moves back to the origin while the upper boundary shifts further to the upper right direction. In contrast, the introduction of chirality in lossless metal exhibits no such drastic change of the phase diagrams. In general, the effect of chirality brings about the non-local term  $\nabla \times \mathbf{E}$  to the electric displacement  $\mathbf{D}$ . This non-locality tends to weaken the localized nature of the surface waves and results in the shrinkage of the surface wave regions. However, the effect of chirality is no simple as we observe the re-entrant appearance of the surface states when the medium I has the chirality as shown in Fig. 13.4. In the next section, we will discuss the effect of chirality based on (13.7).

### 13.4 Perturbative Treatment of Chirality

Let us first discuss the effect of chirality from the perturbative point of view. For simplicity of discussion, we assume no chirality for medium I. When the medium I is the vacuum,  $\alpha^{1\pm} = 1$  and  $Q^{1\pm} = P^{1\pm} = P_0 = \sqrt{1 - \bar{\omega}^2}$ . Substitution of these expressions into (13.7) yields the following equation:

$$F(\varepsilon, \mu, \kappa, \bar{\omega}) = Q^+ Q^- + P_0^2 + \frac{(\varepsilon + \mu)}{2\sqrt{\varepsilon\mu}} P_0 (Q^+ + Q^-) = 0, \quad (13.13)$$

where we denote  $Q^{2\pm}$  as  $Q^\pm$ . Since this equation is even in  $\kappa$ , we expand  $F$  to second order in  $\kappa$ :

$$F(\varepsilon, \mu, \kappa, \bar{\omega}) \cong F_0(\varepsilon, \mu, \bar{\omega}) + \kappa^2 F_2(\varepsilon, \mu, \bar{\omega}), \quad (13.14)$$

where  $F_0$  and  $F_2$  are given as

$$\begin{aligned} F_0(\varepsilon, \mu, \bar{\omega}) &= [1 + \varepsilon\mu - 2\varepsilon\mu\bar{\omega}^2 + (\varepsilon + \mu)R(\varepsilon, \mu, \bar{\omega})]/(\varepsilon\mu), \\ F_2(\varepsilon, \mu, \bar{\omega}) &= \frac{1}{2} \frac{2(1 - \varepsilon\mu\bar{\omega}^2)(1 - 3\varepsilon\mu\bar{\omega}^2) + (\varepsilon + \mu)(2 - 3\varepsilon\mu\bar{\omega}^2)R(\varepsilon, \mu, \bar{\omega})}{\varepsilon^2\mu^2(1 - \varepsilon\mu\bar{\omega}^2)^2}. \end{aligned} \quad (13.15)$$

Here,  $R$  is given by  $R(\varepsilon, \mu, \bar{\omega}) = \sqrt{(1 - \bar{\omega}^2)(1 - \varepsilon\mu\bar{\omega}^2)}$ . By solving  $F_0(\varepsilon, \mu, \bar{\omega}) = 0$  for  $\bar{\omega}$ , we obtain the solutions (13.10). Denoting these non-chiral solutions as  $\bar{\omega}_0$ , we expand  $F_0$  to first order in  $\Delta\bar{\omega} = \bar{\omega} - \bar{\omega}_0$  while  $\bar{\omega}$  in  $F_2$  is replaced by  $\bar{\omega}_0$ . From the expansion, we obtain the perturbative solution for  $\Delta\bar{\omega}$ . By using the approximation

formula  $\bar{\omega}^2 = (\bar{\omega}_0 + \Delta\bar{\omega})^2 \cong \bar{\omega}_0^2 + 2\bar{\omega}_0\Delta\bar{\omega}$ , we have the following perturbative expressions for  $\bar{\omega}$ :

$$\bar{\omega}_{TM}^2 = \frac{\varepsilon^2 - 1}{\varepsilon(\varepsilon - \mu)} - \frac{(3\varepsilon^2 - 1)\kappa^2}{(\varepsilon\mu - 1)(\varepsilon - \mu)\varepsilon^3}, \bar{\omega}_{TE}^2 = \frac{\mu^2 - 1}{\mu(\mu - \varepsilon)} - \frac{(3\mu^2 - 1)\kappa^2}{(\varepsilon\mu - 1)(\mu - \varepsilon)\mu^3}. \tag{13.16}$$

These results are valid in the third quadrant while the expressions for  $\bar{\omega}_{TM}$  and  $\bar{\omega}_{TE}$  are also valid in the second and fourth quadrants, respectively. When the medium I is lossless metal, we have to replace  $(\varepsilon + \mu)$  in (13.13) by  $(\mu - \varepsilon)$ . In addition,  $P_0$  should read  $P_0 = \sqrt{1 + \bar{\omega}^2}$ . Similar procedure leads to the following expressions for  $\bar{\omega}$ :

$$\bar{\omega}_{TM}^2 = \frac{1 - \varepsilon^2}{\varepsilon(\varepsilon + \mu)} + \frac{(3\varepsilon^2 - 1)\kappa^2}{(\varepsilon\mu + 1)(\varepsilon + \mu)\varepsilon^3}, \bar{\omega}_{TE}^2 = \frac{1 - \mu^2}{\mu(\varepsilon + \mu)} + \frac{(3\mu^2 - 1)\kappa^2}{(\varepsilon\mu + 1)(\mu + \varepsilon)\mu^3}. \tag{13.17}$$

Notice that the expression for  $\bar{\omega}_{TM}$  is valid for the first and fourth quadrants while that for  $\bar{\omega}_{TE}$  is valid for the third and fourth quadrants.

By using the condition (13.11) for  $\bar{\omega}$  in (13.16) or (13.17), we obtain the phase diagram for the chiral medium in contact with the vacuum or lossless metal as shown in Fig. 13.5a or b, respectively. The chiral parameter  $\kappa$  is chosen as  $\kappa = 0.2$ . The black and light gray regions indicate the TM and TE surface waves, respectively (note the difference of the definition of color regions in, e.g., Fig. 13.1). By comparing Fig. 13.5a with the exact phase diagram in Fig. 13.2a, we observe that the effect of

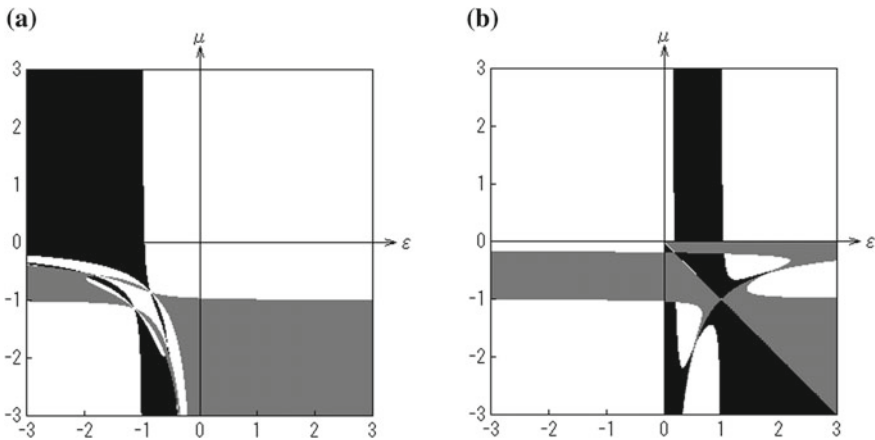


**Fig. 13.5** Phase diagrams of surface waves of chiral metamaterials in contact with **a** the vacuum and **b** lossless metal obtained from the perturbative treatment of the chirality. Chiral parameter is taken as  $\kappa = 0.2$ . Black and light gray regions, respectively, represent the TM and TE surface wave modes. Note the overlap regions of TM and TE modes in (b)

chirality is well reproduced near the boundaries  $\varepsilon = -1$  or  $\mu = -1$ . However, the gap region between the right-handed and left-handed waves around  $\varepsilon\mu = 1$  in the third quadrant shows strange behavior. Although we observe the opening of gap, there appear peculiar unphysical surface modes within the gap region. This is also the case of lossless metal in Fig. 13.5b where there appear unphysical surface waves near the axes and  $\varepsilon\mu = -1$  in the fourth quadrant. These unphysical solutions originate from the divergent factors in the denominators of the second terms in (13.16) and (13.17). Thus, although the perturbation theory of the chirality provides certain guidelines, it breaks down in some regions. These observations drive us to seek for more powerful treatment of the chirality as shown in the next section.

### 13.5 Analytical Treatment of Chirality

By analyzing (13.7), we found the exact treatment of the phase diagrams when the medium I is non-chiral. We will first show the results for the chiral medium in contact with the vacuum. When medium I is the vacuum, (13.7) becomes (13.13). Let us rewrite (13.13) in a form:

$$Q^+ Q^- + P_0^2 = -\frac{(\varepsilon + \mu)}{2\sqrt{\varepsilon\mu}} P_0(Q^+ + Q^-), \quad (13.18)$$

and square both sides. Then, we obtain the following equation for  $\bar{\omega}$ :

$$Q^{+2} Q^{-2} - \frac{(\varepsilon + \mu)^2}{4\varepsilon\mu} P_0^2(Q^{+2} + Q^{-2}) + P_0^4 = \frac{(\varepsilon - \mu)^2}{2\varepsilon\mu} P_0^2 Q^+ Q^-. \quad (13.19)$$

Since  $Q^+$  and  $Q^-$  have square roots, we can remove them by further taking the square of both sides. By appropriately arranging various terms, we arrive at the following quadratic equation for  $\Omega \equiv \bar{\omega}^2$ :

$$a(\varepsilon, \mu, \kappa)\Omega^2 + b(\varepsilon, \mu, \kappa)\Omega + c(\varepsilon, \mu, \kappa) = 0, \quad (13.20)$$

where  $a(\varepsilon, \mu, \kappa)$ ,  $b(\varepsilon, \mu, \kappa)$ , and  $c(\varepsilon, \mu, \kappa)$  are, respectively, given as:

$$\begin{aligned} a(\varepsilon, \mu, \kappa) &= -\varepsilon\mu(\varepsilon - \mu)^2 \left[ (\varepsilon\mu - \kappa^2)^2 - (\varepsilon + \kappa)(\mu + \kappa) \right] \\ &\quad \left[ (\varepsilon\mu - \kappa^2)^2 - (\varepsilon - \kappa)(\mu - \kappa) \right], \\ b(\varepsilon, \mu, \kappa) &= \varepsilon\mu(\varepsilon - \mu)^2 \\ &\quad \left\{ (\varepsilon\mu - \kappa^2)^4 - (\varepsilon\mu + \kappa^2) \left[ (\varepsilon\mu - \kappa^2)^2 + \varepsilon\mu + \kappa^2 - 1 \right] - 2\kappa^2(\varepsilon^2 + \mu^2) \right\}, \end{aligned}$$

$$c(\varepsilon, \mu, \kappa) = \varepsilon\mu \left[ (\varepsilon + 1)(\mu + 1) - \kappa^2 \right] \left[ (\varepsilon - 1)(\mu - 1) - \kappa^2 \right] \\ \left[ \varepsilon\mu(\varepsilon\mu - 1)^2 - \varepsilon\mu\kappa^2(2\varepsilon\mu - \kappa^2) - \kappa^2(\varepsilon^2 + \mu^2) \right]. \quad (13.21)$$

Although these expressions seem complicated, we found it straightforward to derive the analytical results from the elementary considerations. First of all, all the functions  $a(\varepsilon, \mu, \kappa)$ ,  $b(\varepsilon, \mu, \kappa)$ , and  $c(\varepsilon, \mu, \kappa)$  are invariant for the exchange of  $\varepsilon$  and  $\mu$ . Therefore, the phase diagram should be mirror symmetric with respect to the line  $\varepsilon = \mu$ . It is obvious that the solution  $\Omega \equiv \bar{\omega}^2$  of (13.20) can be regarded as a surface wave only if the following four conditions are satisfied: (a)  $\Omega$  should be real, (b)  $\Omega$  should further be positive and gives positive values to  $P_0$  and  $P^\pm$ , (c)  $\Omega$  should satisfy (13.18), and (d)  $\Omega$  should further satisfy (13.19). The latter two conditions stem from squaring both sides. Now, the condition (a) is easily obtained from the following expression for the discriminant of (13.20):

$$D = \varepsilon^2\mu^2(\varepsilon^2 - \mu^2)^2(\varepsilon\mu - \kappa^2)^2[\varepsilon\mu - (\kappa + 1)^2]^3[\varepsilon\mu - (\kappa - 1)^2]^3. \quad (13.22)$$

Therefore, the condition (a) becomes

$$[\varepsilon\mu - (\kappa + 1)^2][\varepsilon\mu - (\kappa - 1)^2] \geq 0. \quad (13.23)$$

Let us discuss the conditions (b), (c), and (d) in the first and third quadrants. The condition (b) turns out to be the following existence conditions of the solutions  $\Omega^+$  and  $\Omega^-$  of (13.20) which automatically include (13.23). The positive solution  $\Omega^+$  can satisfy the condition (b) only when  $c(\varepsilon, \mu, \kappa) \leq 0$  or the following three conditions should simultaneously be satisfied:

$$\sqrt{\varepsilon\mu} + \kappa \leq 1, \left[ (\varepsilon + 1)(\mu + 1) - \kappa^2 \right] \left[ (\varepsilon - 1)(\mu - 1) - \kappa^2 \right] \leq 0, \\ \varepsilon\mu(\varepsilon\mu - 1)^2 - \varepsilon\mu\kappa^2(2\varepsilon\mu - \kappa^2) - \kappa^2(\varepsilon^2 + \mu^2) \leq 0 \quad (13.24)$$

Equation (13.24) also represents the condition for the negative solution  $\Omega^-$  satisfying (b). The condition (c) is shown to be  $\kappa \geq \sqrt{\varepsilon\mu}$  and  $\kappa + \sqrt{\varepsilon\mu} \geq 1$  for the first quadrant. As for the third quadrant, it is (1)  $\kappa \geq \sqrt{\varepsilon\mu}$  and  $\kappa + \sqrt{\varepsilon\mu} \geq 1$  or (2)  $\sqrt{\varepsilon\mu} \geq \kappa$ . These conditions cover the region near the origin of the third quadrant for  $\kappa \leq 1/2$  while they further include the region near the origin in the first quadrant and the exterior region of the third quadrant for  $\kappa \geq 1/2$ . The condition (d) turns out to impose the restriction  $\varepsilon\mu \leq \kappa^2$  on the condition (13.24) for  $\Omega^-$ . As for  $\Omega^+$ , the condition (d) gives two regions: [1]  $f(\varepsilon, \mu, \kappa) \geq 0$ ,  $\varepsilon\mu \geq \kappa^2$ , and  $\varepsilon\mu \geq (\kappa + 1)^2$ , [2] (1)  $\varepsilon\mu \geq \kappa^2$ ,  $\varepsilon\mu \leq (1 - \kappa)^2$ , and  $0 \leq \kappa \leq 1$  or (2)  $f(\varepsilon, \mu, \kappa) \leq 0$ ,  $\varepsilon\mu \leq (1 - \kappa)^2$ , and  $\kappa \geq 1$ . Here,  $f(\varepsilon, \mu, \kappa)$  is defined as:

$$f(\varepsilon, \mu, \kappa) = \varepsilon\mu(\varepsilon\mu - \kappa^2)^4 - 2\varepsilon\mu(\varepsilon\mu + \kappa^2)(\varepsilon\mu - \kappa^2)^2 + (\varepsilon^3 - \kappa^2\mu)(\mu^3 - \kappa^2\varepsilon). \quad (13.25)$$

In the case of the second and fourth quadrants, it is easy to show from  $\varepsilon\mu \leq 0$  that (13.23) is automatically satisfied. The condition (b) is given by (1)  $c(\varepsilon, \mu, \kappa) \leq 0$ , or (2)  $a(\varepsilon, \mu, \kappa) \geq 0$ ,  $b(\varepsilon, \mu, \kappa) \geq 0$ ,  $c(\varepsilon, \mu, \kappa) \geq 0$ , and  $(\varepsilon\mu - \kappa^2)^2 \geq \varepsilon\mu + \kappa^2$ . These conditions can further be simplified as  $(\varepsilon + 1)(\mu + 1) \leq \kappa^2$  or  $(\varepsilon - 1)(\mu - 1) \leq \kappa^2$ . The conditions (c) and (d) turn out to be simple:  $\varepsilon + \mu \leq 0$  for  $\Omega^+$  and  $\varepsilon + \mu \geq 0$  for  $\Omega^-$ .

Now, we discuss the case of chiral medium in contact with lossless metal. In this case, (13.18) is replaced by

$$Q^+ Q^- - P_0^2 = \frac{(\varepsilon - \mu)}{2\sqrt{\varepsilon\mu}} P_0 (Q^+ + Q^-), \quad (13.26)$$

We square both sides and arrive at the following equation for  $\bar{\omega}$ :

$$Q^{+2} Q^{-2} - \frac{(\varepsilon - \mu)^2}{4\varepsilon\mu} P_0^2 (Q^{+2} + Q^{-2}) + P_0^4 = \frac{(\varepsilon + \mu)^2}{2\varepsilon\mu} P_0^2 Q^+ Q^-. \quad (13.27)$$

We take the square of both sides further, and obtain again the following quadratic equation for  $\Omega \equiv \bar{\omega}^2$ :

$$a'(\varepsilon, \mu, \kappa)\Omega^2 + b'(\varepsilon, \mu, \kappa)\Omega + c'(\varepsilon, \mu, \kappa) = 0, \quad (13.28)$$

where  $a(\varepsilon, \mu, \kappa)$ ,  $b'(\varepsilon, \mu, \kappa)$ , and  $c'(\varepsilon, \mu, \kappa)$  are, respectively, given as:

$$\begin{aligned} a'(\varepsilon, \mu, \kappa) &= \varepsilon\mu(\varepsilon + \mu)^2 \left[ (\varepsilon\mu - \kappa^2)^4 + 2(\varepsilon\mu + \kappa^2)(\varepsilon\mu - \kappa^2)^2 + (\varepsilon^2 + \kappa^2)(\mu^2 + \kappa^2) \right], \\ b'(\varepsilon, \mu, \kappa) &= \varepsilon\mu(\varepsilon + \mu)^2 \\ &\quad \left\{ (\varepsilon\mu - \kappa^2)^4 + (\varepsilon\mu + \kappa^2) \left[ (\varepsilon\mu - \kappa^2)^2 - \varepsilon\mu - \kappa^2 - 1 \right] + 2\kappa^2(\varepsilon^2 + \mu^2) \right\}, \\ c'(\varepsilon, \mu, \kappa) &= \varepsilon\mu \left[ (\varepsilon - 1)(\mu + 1) - \kappa^2 \right] \left[ (\varepsilon + 1)(\mu - 1) - \kappa^2 \right] \\ &\quad \left[ \varepsilon\mu(\varepsilon\mu - \kappa^2 + 1)^2 - \kappa^2(\varepsilon - \mu)^2 \right]. \end{aligned} \quad (13.29)$$

As in the case of the vacuum, we found it straightforward to derive the analytical results by the elementary considerations. For this case, all the functions  $a'(\varepsilon, \mu, \kappa)$ ,  $b'(\varepsilon, \mu, \kappa)$ , and  $c'(\varepsilon, \mu, \kappa)$  are invariant against the exchange of  $(\varepsilon, \mu) \rightarrow (-\mu, -\varepsilon)$ . Therefore, the phase diagram should be mirror symmetric with respect to the line  $\varepsilon + \mu = 0$ . The condition (a) for the real solution is given by the following expression for the discriminant of (13.28):

$$D = \varepsilon^2 \mu^2 (\varepsilon^2 - \mu^2)^2 (\varepsilon\mu - \kappa^2)^2 \left[ \varepsilon^2 \mu^2 - 2\varepsilon\mu\kappa^2 + 2\varepsilon\mu + (\kappa^2 + 1)^2 \right]^3 > 0. \quad (13.30)$$

It is easy to show that this condition is automatically satisfied for all values of  $\varepsilon$ ,  $\mu$ , and  $\kappa$ . Therefore, we have only to concentrate on the remaining three conditions: (b) the solutions should be positive and give the positive values to  $P^\pm$ , (c) the solutions should satisfy (13.26), and (d) they should also satisfy (13.27).

Let us again start with the first and third quadrants. The condition (b) for the existence of both solutions  $\Omega^+$  and  $\Omega^-$  turns out to be  $(\varepsilon + 1)(\mu - 1) \leq \kappa^2$ ,  $(\varepsilon - 1)(\mu + 1) \leq \kappa^2$ , and  $\varepsilon\mu(\varepsilon\mu - \kappa^2 + 1)^2 \geq \kappa^2(\varepsilon - \mu)^2$  for  $\kappa \leq 1$  while the case of  $\kappa \geq 1$  needs additional condition  $\varepsilon\mu \geq \kappa^2 - 1$  to the above conditions. These conditions stem from the requirement  $c'(\varepsilon, \mu, \kappa) \geq 0$  and  $b'(\varepsilon, \mu, \kappa) \leq 0$ . The solutions  $\Omega^+$  have the additional existence region satisfying  $c'(\varepsilon, \mu, \kappa) \leq 0$ . Under these conditions, the solutions  $\Omega^+$  satisfy (13.26) for (1)  $\sqrt{\varepsilon\mu} \geq \kappa$  and  $(\varepsilon - \mu)g(\varepsilon, \mu, \kappa) \leq 0$  or (2)  $\sqrt{\varepsilon\mu} \leq \kappa$  and  $\varepsilon \geq \mu$ . Here,  $g(\varepsilon, \mu, \kappa)$  is given by

$$g(\varepsilon, \mu, \kappa) = \left[ (\varepsilon\mu - \kappa^2)^2 + (\varepsilon + \kappa)(\mu + \kappa) \right] \left[ (\varepsilon\mu - \kappa^2)^2 + (\varepsilon - \kappa)(\mu - \kappa) \right]. \quad (13.31)$$

They also satisfy (13.27) for  $(\varepsilon\mu - \kappa^2)h(\varepsilon, \mu, \kappa) \geq 0$  where  $h(\varepsilon, \mu, \kappa)$  is given as

$$h(\varepsilon, \mu, \kappa) = \varepsilon\mu(\varepsilon\mu - \kappa^2)^4 + (\varepsilon^3 - \kappa^2\mu)(\mu^3 - \kappa^2\varepsilon) + 2\varepsilon\mu(\varepsilon\mu + \kappa^2)(\varepsilon\mu - \kappa^2)^2 \quad (13.32)$$

As for the solutions  $\Omega^-$ , (13.26) and (13.27) are satisfied, respectively, for  $\varepsilon \geq \mu$  and  $\varepsilon\mu \geq \kappa^2$ . The conditions for the second and fourth quadrants are simple. The condition (b) turns out to be  $c'(\varepsilon, \mu, \kappa) \geq 0$ , or equivalently,  $[(\varepsilon + 1)(\mu - 1) - \kappa^2][(\varepsilon - 1)(\mu + 1) - \kappa^2] \geq 0$ . Equation (13.26) can only be satisfied by the negative solutions  $\Omega^-$  and is written as  $\varepsilon \geq \mu$ . Equation (13.27) is satisfied for all the regions of second and fourth quadrants.

Figure 13.6a and b shows the phase diagrams obtained analytically for chiral medium in contact with the vacuum for  $\kappa = 0.5$  and  $\kappa = 1.5$ , respectively, while Fig. 13.6c is the phase diagram for chiral medium in contact with lossless metal for  $\kappa = 0.5$ . Let us first discuss the case of  $\kappa = 0.5$  in Fig. 13.6a. For this value of  $\kappa$ , the first quadrant is excluded because of the condition (c). The black, light gray, and dark gray regions in the third quadrant together show the existence regions of the solutions  $\Omega^+$  and  $\Omega^-$ . All these regions in the third quadrant satisfy the condition (c). The regions satisfying the additional condition (d) for  $\Omega^+$  and  $\Omega^-$  are, respectively, indicated by the black and light gray regions. Therefore, these two regions near and away from the origin are the surface wave regions. The boundaries for these regions near the origin are given by  $(\varepsilon + 1)(\mu + 1) = \kappa^2$  and  $\varepsilon\mu = (\kappa - 1)^2$ , while those away from the origin are given by  $(\varepsilon + 1)(\mu + 1) = \kappa^2$  and  $f(\varepsilon, \mu, \kappa) = 0$ . The existence regions of the solutions  $\Omega^+$  and  $\Omega^-$  in the second and fourth quadrants are indicated by the sum of the black, light gray, and dark gray regions. The regions for  $\Omega^+$  and  $\Omega^-$  which satisfy the additional conditions (c) and (d) are indicated by light gray and black below and above the line  $\varepsilon + \mu = 0$ , respectively. Thus, these two

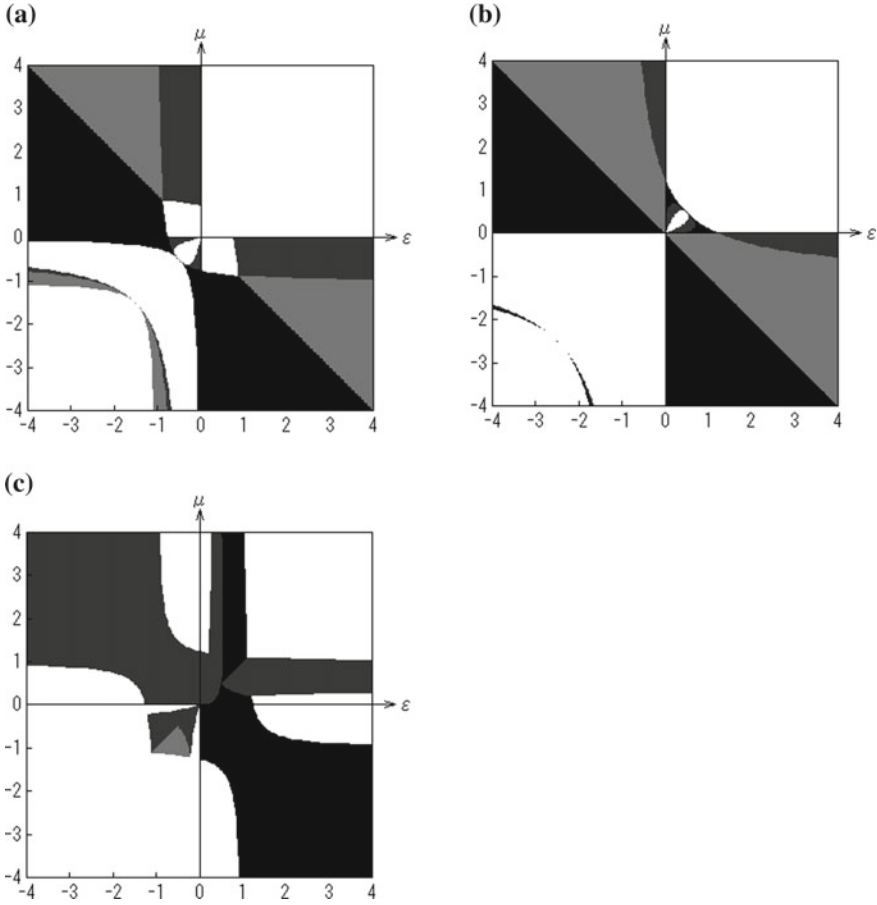


**Fig. 13.6** Phase diagrams of surface waves of chiral metamaterials derived from the analytical treatment of the chirality. Metamaterial with **a**  $\kappa = 0.5$  and **b**  $\kappa = 1.5$  is in contact with the vacuum. In **c** metamaterial with  $\kappa = 0.5$  is in contact with lossless metal. Meaning of each region is given in the text

regions in the second and fourth quadrant are the regions of surface waves. Their boundaries are given by the axes and  $(\epsilon + 1)(\mu + 1) = \kappa^2$ .

Let us deal with the case of the first and third quadrants for  $\kappa = 1.5$  in Fig. 13.6b. The condition (c) allows for the region  $\sqrt{\epsilon\mu} \leq \kappa$  in the first quadrant while it gives the region  $\sqrt{\epsilon\mu} \geq \kappa$  in the third quadrant. The dark gray and black regions show the existence regions of the solutions  $\Omega^+$ . There is no allowed region for the solutions  $\Omega^-$  in these two quadrants. The regions satisfying the additional condition (d) for  $\Omega^+$  are painted by black near the origin in the first quadrant and away from the origin in the third quadrant. These are the regions for the surface waves. They are surrounded by the boundaries  $(\epsilon + 1)(\mu + 1) = \kappa^2$  and  $f(\epsilon, \mu, \kappa) = 0$ . As for the second and fourth quadrants, the whole regions allow for the solutions  $\Omega^+$  and  $\Omega^-$  as shown



by the black, light gray, and dark gray. The regions for  $\Omega^+$  and  $\Omega^-$  which satisfy the additional conditions (c) and (d) are the same as in the case of  $\kappa = 0.5$ . Thus, the light gray and black regions in the second and fourth quadrant are the regions of surface waves which is surrounded by the axes and  $(\varepsilon + 1)(\mu + 1) = \kappa^2$ .

As is noticed below (13.29), the phase diagram for chiral medium in contact with lossless metal is mirror symmetric with respect to the line  $\varepsilon + \mu = 0$ . We utilize this symmetry in Fig. 13.6c and use the first and third quadrants to show the existence regions of the solutions  $\Omega^+$  and  $\Omega^-$ , respectively. The dark gray and black regions in the first quadrant show the existence regions of the solutions  $\Omega^+$ , while the dark and light gray regions in the third quadrant show those for the solutions  $\Omega^-$ . Additional conditions (c) and (d) are satisfied for black and light gray regions by  $\Omega^+$  and  $\Omega^-$  in the respective quadrant. These black and light gray areas are the existence regions of surface waves. We can see that the surface wave region is almost occupied by the  $\Omega^+$  solutions with a tiny region of  $\Omega^-$  solutions. The correct phase diagrams in these quadrants are obtained by combining the black and light gray regions in the first and third quadrants according to the mirror symmetry. In a similar way, the existence regions for the solutions in the second and fourth quadrants are given by the dark gray and black areas in Fig. 13.6c. Additional conditions (c) and (d) exclude the second quadrant and allow the black region as surface wave region. All the boundaries are given  $(\varepsilon - 1)(\mu + 1) = \kappa^2$  and  $h(\varepsilon, \mu, \kappa) = 0$ . Thus, the analytical solutions exactly reproduce the surface wave regions numerically obtained in Fig. 13.3.

## 13.6 Summary

We have studied the phase diagrams of the surface electromagnetic waves for systems composed mainly of the chiral medium in contact with either the vacuum or lossless metal. Numerical simulations were carried out to obtain the phase diagrams of the surface states for various parameters. It turns out that the introduction of the chirality generally reduces the surface wave regions because of its non-local nature. For sufficiently large values of chirality, however, there appear new surface states in the first quadrant. The perturbative treatment of the chirality is presented to analyze the phase diagrams, which turns out to be insufficient because of the divergent terms. More powerful analysis of the phase diagrams is developed based on the exact treatment of the chirality. This enables us to identify all the boundaries of the phase diagrams. Further extension of the exact treatment to the surface waves of bianisotropic chiral metamaterials will be presented elsewhere.

**Acknowledgements** The authors acknowledge sincere thanks to the late Professor Hangyo at Osaka University for fruitful discussion and valuable comments. We would also be very grateful to T. Sato at Nikon Corporation, Japan, for enlightening discussions. This work is supported by the Grant-in-Aid for Scientific Research on Innovative Areas: “Electromagnetic Metamaterials” (No. 22109003) awarded by the Ministry of Education, Culture, Sports, Science and Technology, Japan.

## References

1. J.B. Pendry, A.J. Holden, D.J. Robbins, W.J. Stewart, *IEEE Trans. Microw. Theory Tech.* **47**, 2075 (1999)
2. J.P. Pendry, *Phys. Rev. Lett.* **85**, 3966 (2000)
3. J.P. Pendry, *Nature* **423**, 22 (2003)
4. V.G. Veselago, *Soviet Phys. Uspekhi* **10**, 509 (1968)
5. I.V. Lindell, A.H. Sihvola, S.A. Tretyakov, A.J. Viitanen, *Electromagnetic Waves in Chiral and Bi-isotropic Media* (Artech House, Norwood, MA, 1994)
6. J.P. Pendry, *Science* **306**, 1353 (2004)
7. S.A. Tretyakov, A.H. Sihvola, L. Jylha, *Photonics Nanostructures Fundam. Appl.* **3**, 107 (2005)
8. B. Wang, J. Zhou, T. Koschnby, M. Kafesaki, C.M. Soukoulis, *J. Opt. A: Pure Appl. Opt.* **11** 114003 (2009)
9. D.F. Arago, *Mem. Inst.* **1**, 93 (1811)
10. J.B. Biot, *Mem. Acad. Sci.* **2**, 41 (1817)
11. Y. Tamayama, T. Nakanishi, K. Sugiyama, M. Kitano, *Opt. Express* **16**, 20869 (2008)
12. A.A. Maradudin, *Structured Surfaces as Optical Metamaterials* (Cambridge Univ. Press, New York, NY, 2011)
13. A. Sommerfeld, *Ann. Phys. Chemie* **303**, 233 (1899)
14. R.H. Ritchie, *Phys. Rev.* **106**, 874 (1957)
15. I.V. Shadrivov, A.A. Sukhorukov, Y.S. Kivshar, A.A. Zharov, A.D. Boardman, P. Egan, *Phys. Rev. E* **69** 016617 (2004)
16. A.V. Kats, S. Savel'ev, V.A. Yampol'skii, F. Nori, *Phys. Rev. Lett.* **98** 073901 (2007)
17. Y. Jin, J. He, S. He, *Phys. Lett. A* **351**, 354 (2006)
18. T. Sato, Y. Jimba, H. Miyazaki, *Trans. Mater. Res. Soc. Jpn.* **38**, 493 (2013)

# Chapter 14

## Magneto-chiral Metamolecules for Microwaves



Satoshi Tomita, Kei Sawada, Hiroyuki Kurosawa and Tetsuya Ueda

**Abstract** This chapter overviews magneto-chiral (MCh) effects for the X-band microwaves by a single metamolecule consisting of a copper chiral structure and a ferrite rod. The directional birefringence due to the MCh effects is induced at the resonant optical activity frequencies by applying a weak DC magnetic field of 1 mT and increased with the magnetic field. The nonreciprocal differences in refractive indices by the MCh effects are evaluated to be  $10^{-3}$  at 200 mT, which is much larger than that observed in natural chiral molecules at the visible frequencies. Moreover, the enhanced MCh effects can be obtained at ferromagnetic resonance frequencies by the ferrite rod in the metamolecule. The present study paves the way toward the realization of synthetic gauge fields for electromagnetic waves and the emergence of *meta material-science* using microwave metamaterials. Furthermore, higher frequencies including the visible region are accessible by our concept, in which an interaction between magnetism and chirality in the metamaterials is realized without intrinsic electronic interactions.

---

S. Tomita (✉)

Nara Institute of Science and Technology, 8916-5 Takayama, Ikoma,  
Nara 630-0192, Japan  
e-mail: [tomita@tohoku.ac.jp](mailto:tomita@tohoku.ac.jp)

K. Sawada

RIKEN SPring-8 Center, 1-1-1 Kouto, Sayo, Hyogo 679-5148, Japan  
e-mail: [sawada@spring8.or.jp](mailto:sawada@spring8.or.jp)

H. Kurosawa

National Institute of Information and Communications Technology,  
588-2 Iwaoka, Kobe, Hyogo 651-2492, Japan  
e-mail: [kurosawa.hiroyuki@nict.go.jp](mailto:kurosawa.hiroyuki@nict.go.jp)

T. Ueda

Kyoto Institute of Technology, Matsugasaki, Sakyo, Kyoto 606-8585, Japan  
e-mail: [ueda@kit.ac.jp](mailto:ueda@kit.ac.jp)

© Springer Nature Singapore Pte Ltd. 2019

K. Sakoda (ed.), *Electromagnetic Metamaterials*, Springer Series  
in Materials Science 287, [https://doi.org/10.1007/978-981-13-8649-7\\_14](https://doi.org/10.1007/978-981-13-8649-7_14)

## 14.1 Introduction

Symmetry breaking is a key in electromagnetic response of matter [1]. Let us suppose an optical activity, in which the polarization plane of a linearly polarized electromagnetic wave gradually rotates as it passes through a medium. The break in space-inversion symmetry in chiral structures like sugars, amino-acids, and proteins causes reciprocal structural optical activity, referred to as natural optical activity [2, 3]. Broken time-reversal symmetry in magnetized materials, on the other hand, leads to nonreciprocal magnetic optical activity; that is to say, magneto-optical (MO) effects. When both symmetries are simultaneously broken, in other words, MO effects and natural optical activities are combined within a material; electromagnetic waves experience the directional birefringence independent of polarizations, namely the magnetochiral (MCh) effect [4–7]. The MCh effect is promising for new functional optical elements such as a nonreciprocal “one-way mirror”, and also very much interested in terms of homochirality [8] that is a big question in biology and biochemistry. The effect is, however, very small owing to weak coupling between magnetism and chirality in natural materials even under strong magnetic fields [9–12]. For example, the MCh effects in the visible region by optically active molecular liquids highlight directional variations in refractive indices to be  $10^{-8}$  at 5 T [13] and  $10^{-10}$  at 100 mT [14]. Therefore, it becomes important and interesting to enhance the MCh coupling using artificial structures [15, 16].

Metamaterials are artificially structured materials, which are composed of unit cells much smaller than the wavelength of electromagnetic waves and designed to interact with and control electromagnetic waves [17]. An important feature of metamaterials is an independent control of electric and magnetic responses that gives rise to interesting phenomena, for example, a negative index of refraction [17] and invisible cloak [18]. Such phenomena are realized by tuning independently the electric permittivity ( $\epsilon$ ) and magnetic permeability ( $\mu$ ). This independent control is traced back to the absence of an intrinsic electronic interaction between  $\epsilon$  and  $\mu$  in man-made structures. Even without the interaction, electromagnetic waves “regard”  $\epsilon$  and  $\mu$  combined together as a fictitious interaction: a refractive index  $n = \sqrt{\epsilon}\sqrt{\mu}$  and wave impedance  $\eta = \sqrt{\mu\mu_0/\epsilon\epsilon_0}$ , where  $\epsilon_0$  and  $\mu_0$  are, respectively, the electric permittivity and magnetic permeability of vacuum.

In this chapter, we demonstrate a fictitious interaction between magnetism and chirality as the MCh effect. Most studies on directional birefringence [9, 13, 14, 19–23] have been devoted so far to realizing and enhancing intrinsic electronic interactions such as magneto-electric resonances. However, we reveal that the MCh effect occurs in the artificial structure—metamolecule—without using such intrinsic electronic interactions. A large MCh effect by the single metamolecule consisting of a ferrite rod—magnetic meta-atom—and a metallic chiral structure—chiral meta-atom—is directly observed at the X-band microwave frequencies under a very weak DC magnetic field of 1 mT [24]. The effect increases as the magnetic field increases. The nonreciprocal differences in the real and imaginary parts of refractive indices due to the MCh effects are evaluated to be  $10^{-3}$  at 200 mT. Furthermore, the MCh

effects can be enhanced using magnetic resonance in the magnetic meta-atom [25]. The present study opens a door toward the realization of synthetic gauge fields, e.g., effective magnetic fields for electromagnetic waves [26, 27], and can be a pioneer in the development of new physics, named *meta material-science* using metamaterials [28–30].

## 14.2 Theory

We derive here the MCh effects from viewpoints of the symmetry breakings. Let us consider dispersion relation,  $\omega = \omega_{L,R}(\mathbf{k})$ , where L and R denote left- and right-handed circular polarizations, respectively. The two circular polarizations are defined as eigenstates of angular momentum in this chapter. The time-reversal operation transforms the dispersion as  $\omega_{L,R}(\mathbf{k}) \rightarrow \omega_{R,L}(-\mathbf{k})$ . A system with the time-reversal symmetry satisfies the following relation,

$$\begin{aligned}\omega_L(\mathbf{k}) &= \omega_R(-\mathbf{k}), \\ \omega_R(\mathbf{k}) &= \omega_L(-\mathbf{k}).\end{aligned}\tag{14.1}$$

Similarly, if a system has the space-inversion symmetry, the dispersion satisfies the relation,

$$\begin{aligned}\omega_L(\mathbf{k}) &= \omega_L(-\mathbf{k}), \\ \omega_R(\mathbf{k}) &= \omega_R(-\mathbf{k}).\end{aligned}\tag{14.2}$$

Therefore, under the symmetry breakings of the time-reversal and/or the space-inversion, (14.1) and (14.2) are not the case. Especially, if a system lacks both the time-reversal and the space-inversion symmetries, unpolarized electromagnetic waves can have directional dependence, namely the MCh effects. In Fig. 14.1, schematics of these properties are summarized together with corresponding optical phenomena and dispersion relations.

Based on these discussions, we explicitly derive the refractive index of an MCh medium from Maxwell equations,

$$\nabla \times \mathbf{E}(\mathbf{r}, t) = -\frac{\partial \mathbf{B}(\mathbf{r}, t)}{\partial t},\tag{14.3}$$

$$\nabla \times \mathbf{H}(\mathbf{r}, t) = \frac{\partial \mathbf{D}(\mathbf{r}, t)}{\partial t},\tag{14.4}$$

where  $\mathbf{E}$ ,  $\mathbf{B}$ ,  $\mathbf{H}$ , and  $\mathbf{D}$  are the electric field, the magnetic field, the magnetic field strength, and the electric flux density, respectively [28]. The constitutive equations of the chiral media with magnetism are written as [31]

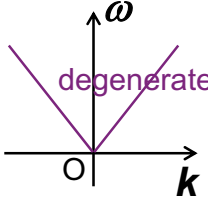
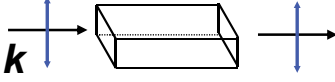
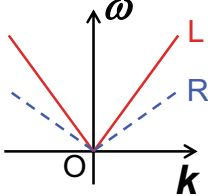
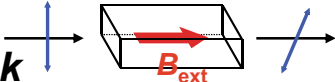
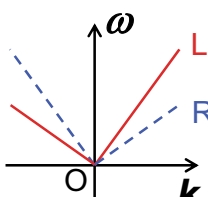
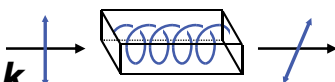
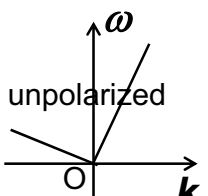
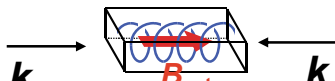
Broken symmetry	Dispersion	Phenomenon
None		<p>Conventional propagation</p> 
Time-reversal symmetry		<p>Magnetic optical activity (Magneto-optical effect)</p> 
Space-inversion symmetry		<p>Structural optical activity (Natural optical activity)</p> 
Time-reversal symmetry & Space-inversion symmetry		<p>Magneto-chiral effects</p> 

Fig. 14.1 Broken symmetries in matter and optical phenomena with dispersion relations

$$\mathbf{D}(\mathbf{r}, t) = \epsilon_0 \hat{\epsilon} \mathbf{E}(\mathbf{r}, t) - i \frac{\hat{\xi}}{c} \nabla \times \mathbf{H}(\mathbf{r}, t), \tag{14.5}$$

$$\mathbf{B}(\mathbf{r}, t) = \mu_0 \hat{\mu} \mathbf{H}(\mathbf{r}, t) + i \frac{\hat{\xi}}{c} \nabla \times \mathbf{E}(\mathbf{r}, t), \tag{14.6}$$

where the parameters,  $\hat{\epsilon}$ ,  $\hat{\mu}$ ,  $\hat{\xi}$  are, respectively, the electric permittivity, the magnetic permeability, and the chirality tensors of the medium. The permeability tensor  $\hat{\mu}$ , which is described by

$$\hat{\boldsymbol{\mu}} = \begin{pmatrix} \mu_{xx} & -i\kappa & 0 \\ i\kappa & \mu_{yy} & 0 \\ 0 & 0 & \mu_{zz} \end{pmatrix}, \quad (14.7)$$

plays a major role to characterize electromagnetic interactions in the microwave region, while the permittivity is assumed to be a scalar,  $\hat{\boldsymbol{\varepsilon}} = \varepsilon \hat{\mathbf{1}}$ . On the off-diagonal component, MO parameter  $\kappa$  is proportional to the external magnetic field and gives the MO effects such as Faraday rotation. The chirality tensor  $\hat{\boldsymbol{\xi}}$  represents an effect of structural chirality that breaks the space-inversion symmetry. We suppose that the chiral axis is parallel to the  $z$ -direction. The chirality tensor is thus written as

$$\hat{\boldsymbol{\xi}} = \begin{pmatrix} 0 & 0 & 0 \\ 0 & 0 & 0 \\ 0 & 0 & \xi \end{pmatrix}. \quad (14.8)$$

This means that the electric field in the  $z$ -direction induces the  $z$ -component of the magnetic field, and vice versa.

Now, we consider plane waves of  $\mathbf{E}$ ,  $\mathbf{B}$ ,  $\mathbf{H}$  and  $\mathbf{D} \propto e^{i\mathbf{k}\cdot\mathbf{r}-i\omega t}$ . Equations (14.3) and (14.4) become

$$\mathbf{k} \times \mathbf{E}(\mathbf{r}) = \omega \mathbf{B}(\mathbf{r}), \quad (14.9)$$

$$\mathbf{k} \times \mathbf{H}(\mathbf{r}) = -\omega \mathbf{D}(\mathbf{r}). \quad (14.10)$$

Let us write  $\mathbf{E}$  and  $\mathbf{B}$  in terms of  $\mathbf{H}$ . From (14.5) and (14.10), the electric field is written as

$$\mathbf{E} = \frac{1}{\varepsilon_0 \varepsilon} \left[ \frac{-1}{\omega} \mathbf{k} \times \mathbf{H} + i \frac{\hat{\boldsymbol{\xi}}}{c} \mathbf{H} \right], \quad (14.11)$$

where position dependence is omitted for simplicity. Substituting this representation of the electric field as (14.11) into (14.6), we get

$$\mathbf{B} = \mu_0 \hat{\boldsymbol{\mu}} \mathbf{H} + i \frac{1}{c \varepsilon_0 \varepsilon} \hat{\boldsymbol{\xi}} \left[ \frac{-1}{\omega} \mathbf{k} \times \mathbf{H} + i \frac{\hat{\boldsymbol{\xi}}}{c} \mathbf{H} \right]. \quad (14.12)$$

From (14.11) and (14.12) combined with (14.9), the wave equation is written to be

$$-\mathbf{k} \times (\mathbf{k} \times \mathbf{H}) + i \frac{\omega}{c} \mathbf{k} \times (\hat{\boldsymbol{\xi}} \mathbf{H}) + i \frac{\omega}{c} \hat{\boldsymbol{\xi}} (\mathbf{k} \times \mathbf{H}) = \frac{\omega^2}{c^2} \varepsilon \hat{\boldsymbol{\mu}} \mathbf{H} - \frac{\omega^2}{c^2} \hat{\boldsymbol{\xi}}^2 \mathbf{H}. \quad (14.13)$$

To realize the MCh effect, we break the time-reversal symmetry by applying an external magnetic field to the  $z$ -direction. The external field gives the off-diagonal components of the magnetic permeability  $\hat{\boldsymbol{\mu}}$  as in (14.7) to be nonzero. Moreover, let us recall here that the  $z$ -component of the electric field induces that of the magnetic field, and vice versa, owing to  $\hat{\boldsymbol{\xi}}$  with chiral axis in the  $z$ -direction as shown in (14.8).

In this case, it is convenient to separate the propagation direction into the transverse and the longitudinal components to be  $\mathbf{k} = (k_t, k_z)$ . Given that  $\mu_{xx} = \mu_{yy} = \mu_{zz} = \mu$  in (14.13), the dispersion relation, namely the index ellipsoid, is obtained to be

$$\frac{k_t^2}{(n_t^\pm)^2} + \frac{k_z^2}{(n_z^\pm)^2} = \frac{\omega^2}{c^2}, \quad (14.14)$$

where

$$n_t^\pm = \sqrt{\varepsilon}\sqrt{\mu} \pm \frac{1}{4}\sqrt{\frac{\varepsilon}{\mu}}\kappa \pm \frac{\xi \operatorname{sgn}(k_t)}{2} + \frac{1}{4}\xi \operatorname{sgn}(k_t) \frac{\kappa}{\mu}. \quad (14.15)$$

This is the refractive index of an MCh medium for transverse propagation, in which the sign  $\pm$  represents polarization states [28].

The refractive index as shown in (14.15) consists of four terms that have different physical meanings as follows: The first term in the right-hand side is a conventional dispersion without symmetry breakings. The second term is accompanied by  $\kappa$  under the magnetic field that breaks the time-reversal symmetry. This term thus represents the MO effect and depends on polarization states. The third term has directional dependence and represents structural optical activity by the chirality  $\xi$  that breaks the space-inversion symmetry. This term also depends on polarization states. The fourth term is what we are looking for in this article; that is to say, the MCh effect. Notably, this term is independent of polarization states but depends on propagation directions, represented by  $\operatorname{sgn}(k_t)$ . Such properties are caused by the simultaneous breaking of the time-reversal and the space-inversion symmetries, as summarized in Fig. 14.1.

Our derivation here implies that the MCh effect is realized without an explicit coupling between the MO effect and the structural optical activity. Even without the coupling, electromagnetic waves feel  $\kappa$  and  $\xi$  combined together as an interaction. This situation is very similar to the conventional refractive index, namely the first term in the right-hand side of (14.15), which can be modified using metamaterials [17, 18]. In this way, metamaterials associated with a combination of  $\kappa$  and  $\xi$  may boost MCh effects by several orders of magnitude. Consequently, the MCh effect causes directional birefringence, resulting in the difference between transmission coefficients of microwaves from the top and the bottom of the metamaterial.

### 14.3 Metamolecule Preparation and Measurement Setup

The MCh metamolecule is embodied by using an yttrium-iron-garnet ferrite square pillar and copper (Cu) chiral structure as shown in Fig. 14.2a [24, 25]. As shown in the left part, a Cu wire of 0.55 mm in diameter is coiled clockwise four times round a thread groove of the right-handed screw to form the right-handed chiral meta-atom. The cross-section and length of the ferrite magnetic meta-atom are 1.5 mm  $\times$  1.5



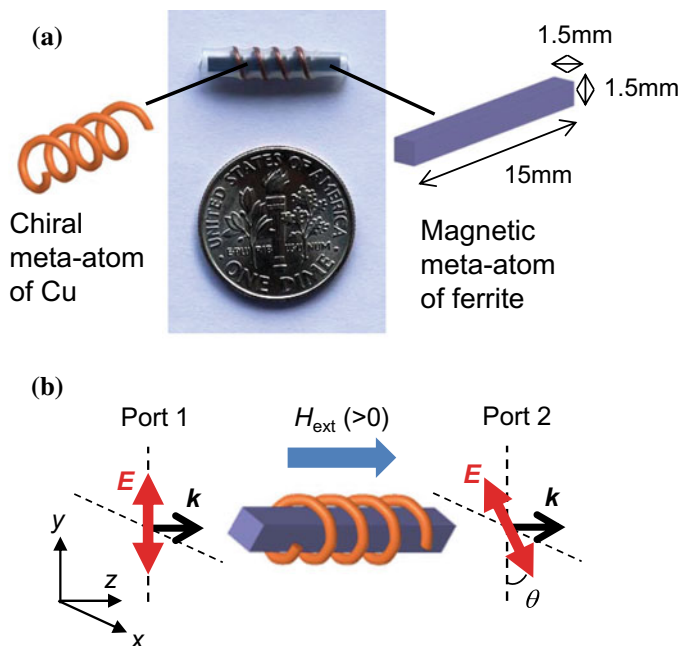


**Fig. 14.2** **a** Center: A photograph of the MCh metamolecule. Diameter of the coin in the photo is 17.91 mm. Illustrations of Cu chiral meta-atom (left) and ferrite magnetic meta-atom (right). **b** A schematic of configurations in the microwave measurements of  $S_{21}$  of the MCh metamolecule. Reprinted figure with permission from [24], Copyright 2014 by the American Physical Society

mm and 15 mm, respectively, as illustrated on the right-hand side. The ferrite pillar is well insulating. The magnetic meta-atom is inserted in the chiral meta-atom for constructing a metamolecule. The metamolecule is fixed in a thermal-contraction tube.

A single metamolecule is put into a WR-90 waveguide, which is terminated at both the ends by Agilent 281A adaptors. Two adaptors are connected via waveguide so that the polarization plane of an electric field of the fundamental  $TE_{10}$  mode in an adaptor is parallel to that in the other adaptor. Because AC magnetic fields of microwaves in the waveguide are parallel to the chiral axis of the MCh metamolecule, structural optical activities are excited.

The single metamolecule in the waveguide is placed between two poles of an electromagnet for applying DC magnetic fields. The external DC magnetic field is applied in the  $z$ -direction as shown in Fig. 14.2b. The magnetic field  $\mu_0 H_{\text{ext}}$  is monitored by using a Gauss meter equipped with a Hall element.  $\mu_0 H_{\text{ext}} > 0$  ( $\mu_0 H_{\text{ext}} < 0$ ) corresponds to the magnetic field direction from port 1 to port 2 (port 2 to port 1). An X-band microwave source is Agilent PNA N5224 vector network analyzer. We measure S-parameters of  $S_{21}$  and  $S_{12}$  corresponding, respectively, to transmission coefficients from port 1 to port 2 and from port 2 to port 1 simultaneously [24, 25].

## 14.4 Magneto-chiral Effects Under Weak Magnetic Fields

### 14.4.1 Transmission Spectra of Chiral and Magnetic Meta-atoms

Figure 14.3a illustrates an amplitude spectrum of  $S_{21}$  in frequencies from 6 to 12 GHz through only the Cu chiral meta-atom under  $\mu_0 H_{\text{ext}} = 0$  mT in the waveguide. The measurements are valid in the pass-band above 6.6 GHz, which is the cut-off frequency of the waveguide. We observe a salient notch at 9.4 GHz. The notch is attributed to resonance in the chiral meta-atom, referred to as chiral resonance in

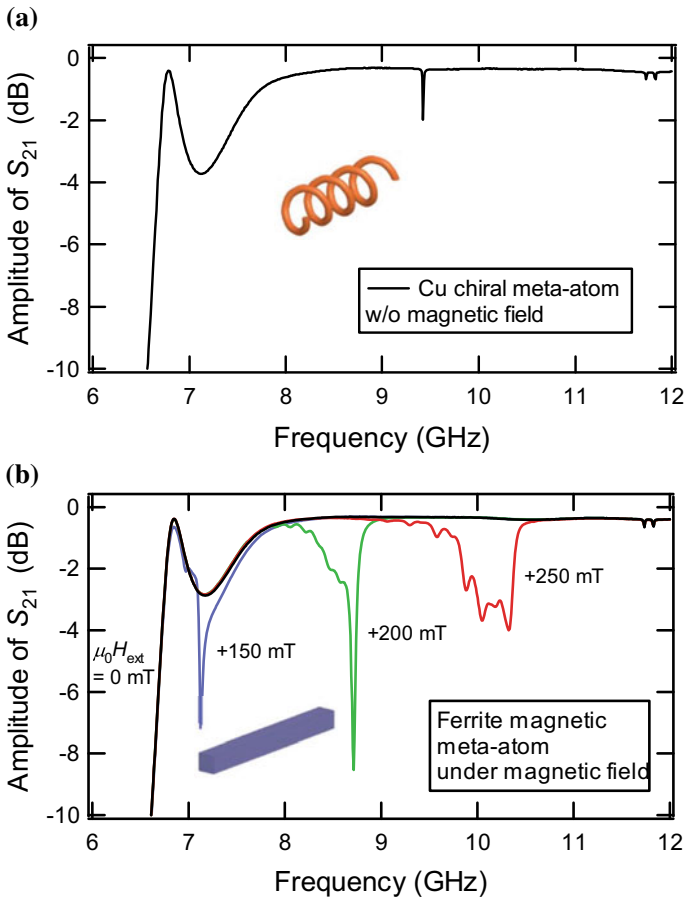


**Fig. 14.3** **a** Transmission  $S_{21}$  amplitude spectrum of Cu chiral meta-atom in the waveguide without the external DC magnetic field. **b** Transmission  $S_{21}$  amplitude spectra of ferrite magnetic meta-atom in the waveguide under  $\mu_0 H_{\text{ext}} = 0$  mT, +150 mT, +200 mT, and +250 mT. Reprinted figure with permission from [24], Copyright 2014 by the American Physical Society

this article. The chiral resonance gives rise to the enhanced optical activity [32]. The spectrum of the chiral structure under nonzero  $\mu_0 H_{\text{ext}}$  is identical as that shown in Fig. 14.3a.

Amplitude spectra of  $S_{21}$  of the ferrite magnetic meta-atom in the waveguide are shown in Fig. 14.3b. Under  $\mu_0 H_{\text{ext}} = 0$  mT, a feature-less spectrum is observed from 7 to 12 GHz. In contrast, a large notch appears at 7.1 GHz when  $\mu_0 H_{\text{ext}} = +150$  mT is applied by using the electromagnet. This notch shifts to a higher frequency at approximately 8.7 and 10.3 GHz by increasing  $\mu_0 H_{\text{ext}}$  to +200 mT and +250 mT, respectively. The features shifting upward with an increase in  $\mu_0 H_{\text{ext}}$  is caused by the ferromagnetic resonance (FMR) of the magnetic meta-atom.

### 14.4.2 Magnetochiral Effects by a Single Metamolecule

By combining the ferrite magnetic meta-atom with the Cu chiral meta-atom and applying  $\mu_0 H_{\text{ext}}$ , both time-reversal and space-inversion symmetries can be broken [24]. This simultaneous breaking leads to the emergence of the MCh effects as demonstrated in Fig. 14.4. Figure 14.4a, c, e show amplitude spectra of  $S_{21}$  (solid curves) and  $S_{12}$  (dotted curves) of the metamolecule under  $\mu_0 H_{\text{ext}} = 0$  mT, +10 mT, and +180 mT, respectively. Figure 14.4b, d, f are corresponding phase spectra. Under  $\mu_0 H_{\text{ext}} = 0$  mT, we see a salient notch at 10.2 GHz and additional weak notch at 7.5 GHz in Fig. 14.4a. The phase spectra in Fig. 14.4b show weak dispersion-type features at these frequencies. These are chiral resonances due to the Cu chiral meta-atom. The insets in Fig. 14.4a, b show enlarged spectra at the chiral resonant at approximately 10 GHz. The inset highlights that  $S_{21}$  and  $S_{12}$  spectra are identical at  $\mu_0 H_{\text{ext}} = 0$  mT, i.e., reciprocal in the presence of the time-reversal symmetry.

The MCh effect is manifested in the amplitude difference and phase difference of transmitted microwaves. Indeed, under  $\mu_0 H_{\text{ext}} = +10$  mT, transmission  $S_{21}$  (solid curve) and  $S_{12}$  (dotted curve) spectra at the chiral resonance are not identical as in Fig. 14.4c, d, whether the incident directions of microwaves are parallel or anti-parallel to the DC magnetic field. Notably, FMR by the ferrite meta-atom is located at a very low frequency of about 1 GHz under  $\mu_0 H_{\text{ext}} = +10$  mT. Nevertheless, we observe a finite difference between  $S_{21}$  and  $S_{12}$  spectra at the chiral resonance in Fig. 14.4c, d.

Figure 14.4e, f show transmission  $S_{21}$  (solid) and  $S_{12}$  (dotted) spectra under  $\mu_0 H_{\text{ext}} = +180$  mT. We notice in the inset that the difference around 10 GHz increases. Moreover, FMR in the magnetic meta-atom results in complicated features at approximately 8 GHz, which shift to a higher frequency with a further increase in  $\mu_0 H_{\text{ext}}$ . Significant amplitude and phase differences between  $S_{21}$  and  $S_{12}$  are observed at FMR frequency.

Further evidence of the MCh effects by the metamolecule is shown in Fig. 14.5. Figures 14.5a and 14.5b are, respectively, the differences in phases and in amplitudes between  $S_{21}$  and  $S_{12}$  under  $\mu_0 H_{\text{ext}}$  from  $-200$  to  $+200$  mT. A feature-less spectrum is

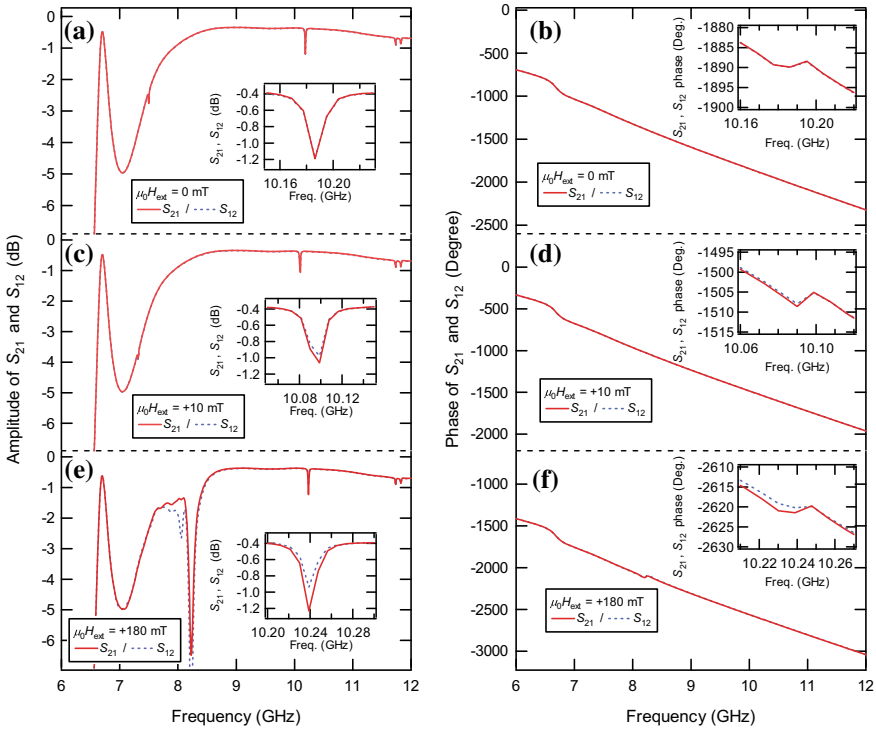


**Fig. 14.4** Experimentally observed transmission  $S_{21}$  (solid) and  $S_{12}$  (dotted) amplitude spectra (a), (c), (e) and phase spectra (b), (d), (f) of the single MCh metamolecule under the external DC magnetic fields of 0 mT [(a) and (b)], +10 mT [(c) and (d)], and +180 mT [(e) and (f)]. Insets: enlarged spectra at the chiral resonance at approximately 10 GHz. Reprinted figure with permission from [24], Copyright 2014 by the American Physical Society

obtained with  $\mu_0 H_{\text{ext}} = 0$  mT. With  $\mu_0 H_{\text{ext}} = +1$  mT, a signal due to the MCh effects emerges at a chiral resonance frequency at approximately 10 GHz. Notably, a very weak magnetic field of +1 mT is enough to induce the MCh effects. As the magnetic field increases, the MCh effect at approximately 10 GHz becomes large and shifts. Differential spectra with  $\mu_0 H_{\text{ext}} < 0$  are also shown in the lower half of Fig. 14.5. The appearance and frequency shift of the MCh effects are very similar to those in  $\mu_0 H_{\text{ext}} > 0$ ; whereas, the polarity of MCh effects is flipped with the direction of the magnetic field.

### 14.4.3 Nonreciprocal Differences in Refractive Indices

In Fig. 14.6a, we plot a graph of the phase difference, that is evaluated as a half value of the peak-to-peak variation at the chiral resonance around 10 GHz (triangles), versus  $\mu_0 H_{\text{ext}}$ . The amplitude difference (circles) is also plotted in Fig. 14.6b. The

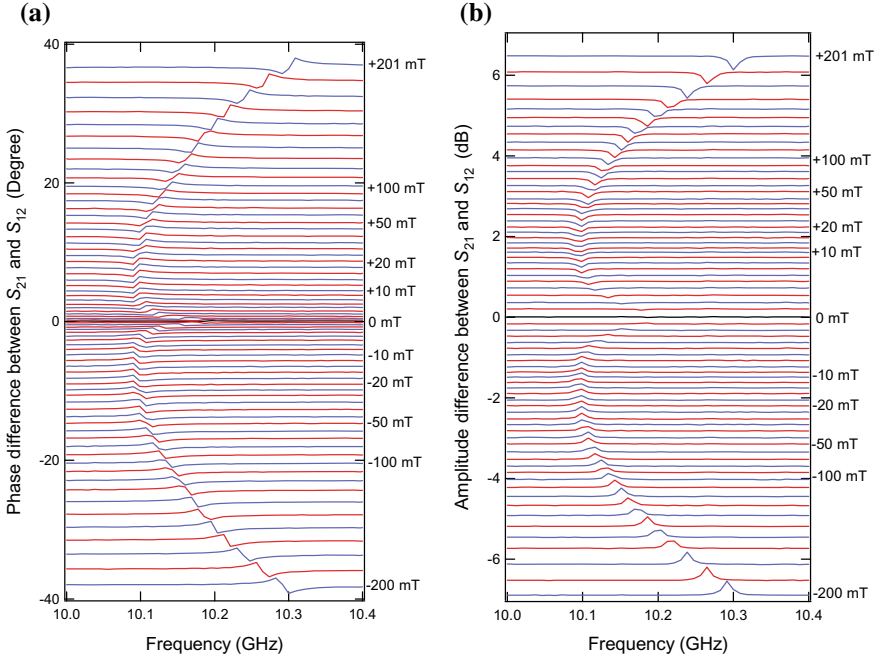


**Fig. 14.5** Differences in **a** phases and **b** amplitudes between  $S_{21}$  and  $S_{12}$  at approximately 10 GHz of the MCh metamolecule under DC magnetic fields from  $-200$  to  $+200$  mT. Reprinted figure with permission from [24], Copyright 2014 by the American Physical Society

MCh effect appears at  $\mu_0 H_{\text{ext}} = 1$  mT, rapidly grows with the magnetic field up to  $\mu_0 H_{\text{ext}} = 10$  mT, and increases monotonically with  $\mu_0 H_{\text{ext}}$ . The continuous increase in the MCh effect is consistent with (14.15), which theoretically indicates that the MCh effect increases with the MO effect. The MO effects are proportional to the effective magnetization of the metamolecule [33]. Under the unsaturated regime, the magnetization is a function of  $\mu_0 H_{\text{ext}}$ . A rapid increase in the MCh effects at a very low  $\mu_0 H_{\text{ext}}$  below 10 mT is thus traced back to the soft magnetic nature of the ferrite magnetic meta-atom in the metamolecule that was observed by a magnetometer [24].

We evaluate the difference in refractive indices obtained by the MCh effects. The phase and amplitude differences in the transmission coefficients as shown in Fig. 14.6 can be converted into the nonreciprocal differences in the real and imaginary parts of refractive indices  $\Delta n'$  and  $\Delta n''$ , respectively. Let us consider the 1-D structure composed of the single metamolecule inserted in a rectangular waveguide. We describe  $\Delta n'$  and  $\Delta n''$  between forward ( $S_{21}$ ) and reverse ( $S_{12}$ ) propagations of unpolarized waves

$$\Delta n = n_{1 \rightarrow 2} - n_{2 \rightarrow 1} = \Delta n' + i \Delta n''. \quad (14.16)$$

$\Delta n$  is a Lorentz-type function of the operational frequency and is related to the phase and amplitude of the complex transmission coefficients as follows:

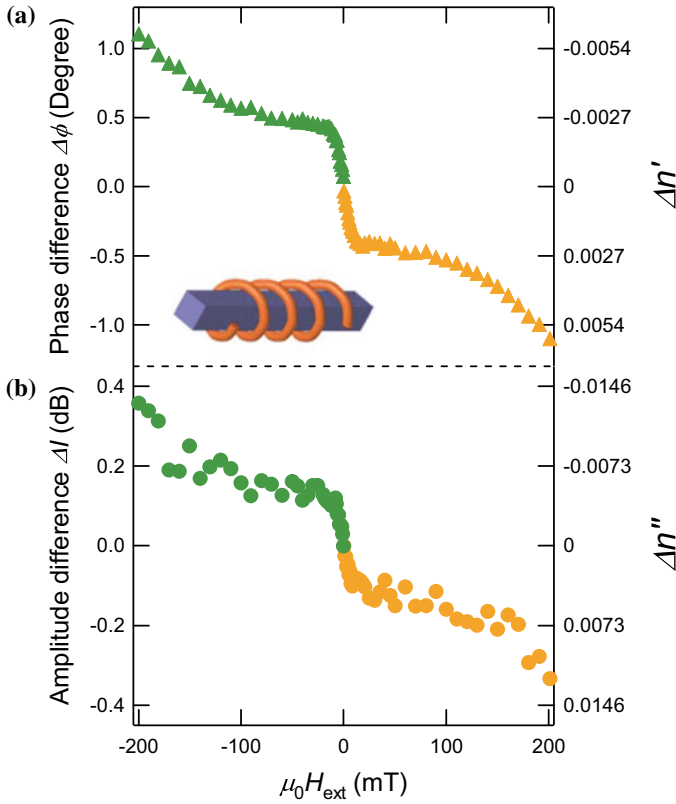


**Fig. 14.6** Differences in **a** phases and **b** amplitudes are plotted as a function of  $\mu_0 H_{\text{ext}}$ . Evaluated differences in the index of refraction are also indicated from the right axes. Reprinted figure with permission from [24], Copyright 2014 by the American Physical Society

$$\Delta n' = -\frac{c}{2\pi fl} \Delta\phi \simeq -47.7 \times \frac{\Delta\phi}{fl}, \quad (14.17)$$

$$\Delta n'' = -\frac{c}{40\pi(\log_{10} e) fl} \Delta I \simeq -5.50 \times \frac{\Delta I}{fl}, \quad (14.18)$$

where  $\Delta\phi$  corresponds to the phase difference  $\angle S_{21} - \angle S_{12}$  in radian,  $\Delta I$  the amplitude difference  $|S_{21}| - |S_{12}|$  in decibel at the MCh effects. The frequency  $f$  is measured in GHz, and  $l$  denotes the total length of the metamolecule measured in millimeters.

At  $\mu_0 H_{\text{ext}} = +200$  mT, we find from Fig. 14.6 that the maximum values of  $\Delta\phi$  and  $\Delta I$  are  $\Delta\phi \sim -1.0^\circ = -0.017$  radian and  $\Delta I \sim -0.4$  dB. From (14.17) and (14.18), with  $l = 15$  mm and  $f = 10$  GHz, we evaluate  $\Delta n' \simeq 5.4 \times 10^{-3}$  and  $\Delta n'' \simeq 1.5 \times 10^{-2}$  maxima [24] as indicated from the right axes of Fig. 14.6a, b. The success of the direct observation of the MCh effects in this study is attributed to

several advantages for the microwave metamolecule: the structural optical activity is enhanced through the chiral resonance in the Cu chiral meta-atom [32], the magnetic response of the ferrite magnetic meta-atom is massive at microwave frequencies [34], and the microwave phase and amplitude can be directly measured using the network analyzer. The manifestation of the real part of the nonreciprocal index difference  $\Delta n'$  and the monotonic increase with  $\mu_0 H_{\text{ext}}$  verifies the MCh effect. The values of  $\Delta n'$  and  $\Delta n''$  of the single metamolecule are not yet significantly large. However, larger responses are expected by combining FMR with the chiral resonance as shown in the following and by assembling metamolecules into metamaterials. Furthermore, it should be mentioned that higher frequencies including the visible region are accessible by our concept of the interaction between magnetism and chirality in metamaterials [35–37].

## 14.5 Enhanced Magnetochiral Effects Under Strong Magnetic Fields

In the previous section, we demonstrated the emergence of large MCh effects under weak magnetic fields below  $\pm 200$  mT. The MCh effect was associated with the chiral resonance in the chiral meta-atom. However, the interaction of the chiral resonance with the ferrite FMR by the ferrite meta-atom remained to be addressed. By applying strong magnetic fields, FMR approaches the chiral resonance frequencies. This motivates a further enhancement of MCh effects [25].

Figure 14.7a shows experimentally observed differences between  $S_{21}$  and  $S_{12}$  of phase spectra at various  $\mu_0 H_{\text{ext}}$  up to  $\pm 400$  mT. Figure 14.7b shows corresponding amplitude difference spectra. A ferrite square pillar is replaced by a ferrite cylinder in the measurements under a strong magnetic field. However, this change in the magnetic meta-atom shape does not result in significant changes in the experimental results. The upper halves of Fig. 14.7a, b show MCh signals with  $\mu_0 H_{\text{ext}} > 0$ . When  $\mu_0 H_{\text{ext}} = +11$  mT, a weak signal associated with the chiral resonance emerges at 8.9 GHz in Fig. 14.7a. A weak dip is observed at the same frequency in corresponding amplitude difference spectra (Fig. 14.7b). An increase in  $\mu_0 H_{\text{ext}}$  leads to a blue shift and an enhancement of the MCh signals at the chiral resonance.

When  $\mu_0 H_{\text{ext}} = +201$  mT, the MCh signals associated with FMR appear at approximately 8.5 GHz in Fig. 14.7. The MCh signals due to FMR shift to higher frequencies and become large as  $\mu_0 H_{\text{ext}}$  increases. This shift of FMR is accompanied by a further blue shift of the MCh signals caused by the chiral resonance. The blue shift of the MCh signals due to the chiral resonance is explained by the effective  $\mu$  in the waveguide [28]. Under  $\mu_0 H_{\text{ext}} = +250$  mT, FMR is overlapped to the chiral resonance around 9 GHz, bringing about splitting of the chiral resonance. At  $\mu_0 H_{\text{ext}} = +280$  mT, we observe a signal at approximately 8.3 GHz, a slightly lower frequency

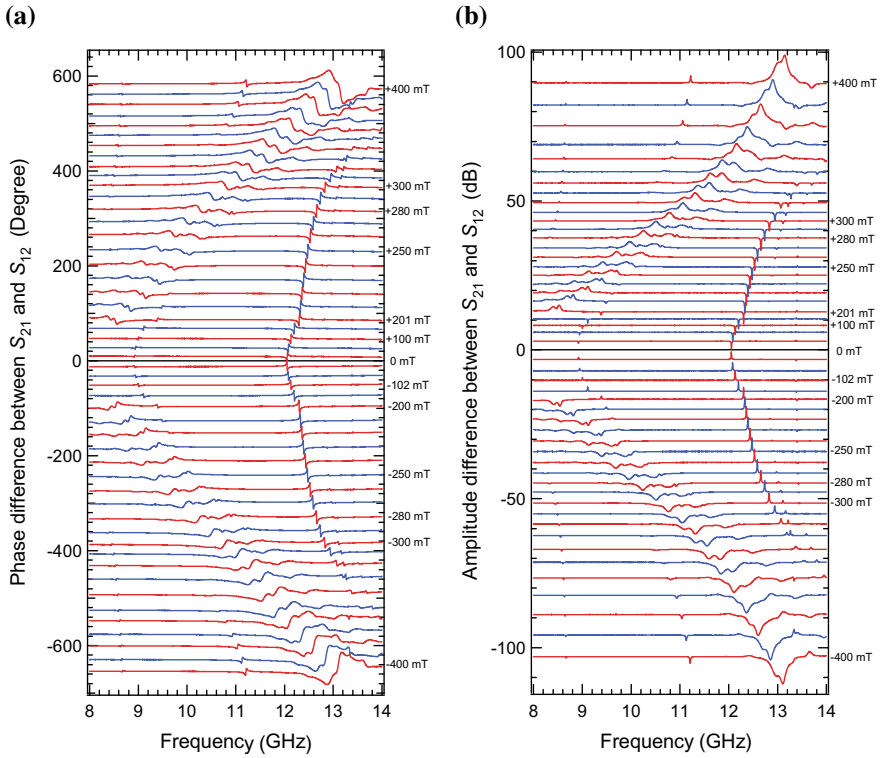


**Fig. 14.7** Experimentally observed **a** phase and **b** amplitude differences between  $S_{21}$  and  $S_{12}$  from 8 to 14 GHz of the MCh metamolecule under DC magnetic fields up to  $\pm 400$  mT. Reprinted figure with permission from [25], Copyright 2017 by the American Physical Society

below 9 GHz. Notably, the polarity of the MCh signal due to the chiral resonance is inverted. The polarity reversal after being passed by FMR is further evidence of the MCh effect, which is proportional to the product of  $\xi$  and  $\kappa$ , because  $\kappa$  flips its sign in the vicinity of FMR [28].

The MCh signals due to FMR in Fig. 14.7a, b become significant at  $\mu_0 H_{\text{ext}} = +400$  mT. The maximum values of phase and amplitude differences associated with FMR at approximately 13 GHz under +400 mT were  $20.8^\circ$  and 9.11 dB, respectively [25]. The nonreciprocal differences in the real and imaginary parts of refractive indices due to the enhanced MCh effect at the FMR frequency are evaluated to be  $\Delta n' \simeq -8.9 \times 10^{-2}$  and  $\Delta n'' \simeq -2.6 \times 10^{-1}$  under +400 mT [25, 28]. Differential spectra for the reversed direction of the external DC magnetic field ( $\mu_0 H_{\text{ext}} < 0$ ) are also shown in the lower halves of Fig. 14.7a, b. Whereas the appearance and frequency shift of signals are very similar to those in  $\mu_0 H_{\text{ext}} > 0$ , the polarity of the MCh signals is flipped with the direction of the magnetic field.



## 14.6 Conclusions and Perspectives

In conclusion, we demonstrated MCh effects at the X-band microwave frequency by a single metamolecule consisting of a Cu chiral meta-atom combined with a ferrite magnetic meta-atom under an external DC magnetic field. The MCh effects were induced by a very weak magnetic field of 1 mT and increased with the magnetic field. The nonreciprocal differences in the real and imaginary parts of refractive indices due to the MCh effects were increased up to  $\Delta n' \simeq 5.4 \times 10^{-3}$  and  $\Delta n'' \simeq 1.5 \times 10^{-2}$  by applying +200 mT [24]. Furthermore, the MCh effects were enhanced using FMR in the metamolecule up to  $\Delta n' \simeq -8.9 \times 10^{-2}$  and  $\Delta n'' \simeq -2.6 \times 10^{-1}$  under +400 mT [25].

The present study paves the way to the realization of synthetic gauge fields, e.g., effective magnetic fields for electromagnetic waves. The “Lorentz force” by synthetic gauge fields for light is expected to be observed in non-uniform metamaterials consisting of the MCh metamolecules. Furthermore, the symmetry arguments used here for electromagnetism can be applied to the electrical charge transport. The electrical counterpart of the optical MCh effect is referred to as the electrical MCh effect [38]. These new avenues of analogy between lights and electrons lead to a new research field, namely *meta material-science* using metamaterials [28–30].

**Acknowledgements** We thank M. Hangyo, K. Sakoda, and A. Porokhnyuk for valuable discussion. The authors acknowledge financial support of this work by JSPS/MEXT KAKENHI (No. 22109002, No. 22109005, No. 26287065, and No. 17K19034).

## References

1. E. Hecht, *Optics* (Pearson Education Limited, 2013)
2. J.A. Kong, *Electromagnetic Wave Theory* (EMW Publishing, 2005)
3. N. Berova, K. Nakanishi, R.W. Woody, *Circular Dichroism: Principles and Applications*, 2nd edn. (Wiley-VCH, 2000)
4. N.B. Baranova, Y.V. Bogdanov, B.Y. Zel'dovich, *Opt. Commun.* **22**, 243 (1977)
5. V.A. Markelov, M.A. Novikov, A.A. Turkin, *Pis'ma Zh. Eksp. Teor. Fiz.* **25**, 404 (1977) [*JETP Lett.* **25**, 378 (1977)]
6. G. Wagnière, M. Meier, *Chem. Phys. Lett.* **93**, 78 (1982)
7. L.D. Barron, J. Vrbancich, *Mol. Phys.* **51**, 715 (1984)
8. G.L.J.A. Rikken, E. Raupach, *Nature* **405**, 932 (2000)
9. G.L.J.A. Rikken, E. Raupach, *Nature* **390**, 493 (1997)
10. G.L.J.A. Rikken, E. Raupach, *Phys. Rev. E* **58**, 5081–5084 (1998)
11. V. Krstić, S. Roth, M. Burghard, K. Kern, G.L.J.A. Rikken, *J. Chem. Phys.* **117**, 11315 (2002)
12. V.A. Sautenkov, Y.V. Rostovtsev, H. Chen, P. Hsu, G.S. Agarwal, M.O. Scully, *Phys. Rev. Lett.* **94**, 233601 (2005)
13. P. Kleindienst, G.H. Wagnière, *Chem. Phys. Lett.* **288**, 89 (1998)
14. M. Vallet, R. Ghosh, A. Le Floch, T. Ruchon, F. Bretenaker, J.-Y. Thépot, *Phys. Rev. Lett.* **87**, 183003 (2001)
15. S. Eslami, J.G. Gibbs, Y. Rechkemmer, J. van Slageren, M. Alarcón-Correa, T.-C. Lee, A.G. Mark, G.L.J.A. Rikken, P. Fischer, *ACS Photon.* **1**, 1231 (2014)

16. G. Armelles, A. Cebollada, H.Y. Feng, A. García-Martín, D. Meneses-Rodríguez, J. Zhao, H. Giessen, *ACS Photon.* **2**, 1272 (2015)
17. D.R. Smith, J.B. Pendry, M.C.K. Wiltshire, *Science* **305**, 788 (2004)
18. D. Schurig, J.J. Mock, B.J. Justice, S.A. Cummer, J.B. Pendry, A.F. Starr, D.R. Smith, *Science* **314**, 977 (2006)
19. C. Train, R. Gheorghie, V. Krstić, L.-M. Chamoreau, N.S. Ovanesyan, G.L.J.A. Rikken, M. Gruselle, M. Verdaguer, *Nature Mater.* **7**, 729–734 (2008)
20. I. Kézsmárki, N. Kida, H. Murakawa, S. Bordács, Y. Onose, Y. Tokura, *Phys. Rev. Lett.* **106**, 057403 (2011)
21. S. Bordács, I. Kézsmárki, D. Szaller, L. Demkó, N. Kida, H. Murakawa, Y. Onose, R. Shimano, T. Rööm, U. Nagel, S. Miyahara, N. Furukawa, Y. Tokura, *Nature Phys.* **8**, 734–738 (2012)
22. M. Mochizuki, S. Seki, *Phys. Rev. B* **87**, 0134403 (2013)
23. I. Kézsmárki, D. Szaller, S. Bordács, V. Kocsis, Y. Tokunaga, Y. Taguchi, H. Murakawa, Y. Tokura, H. Engelkamp, T. Rööm, U. Nagel, *Nature Commun.* **5**, 3203 (2014)
24. S. Tomita, K. Sawada, A. Porokhnyuk, T. Ueda, *Phys. Rev. Lett.* **113**, 235501 (2014)
25. S. Tomita, H. Kurosawa, K. Sawada, T. Ueda, *Phys. Rev. B* **95**, 085402 (2017)
26. K. Sawada, N. Nagaosa, *Phys. Rev. Lett.* **95**, 237402 (2005)
27. K. Fang, Z. Yu, S. Fan, *Nature Photon.* **6**, 782 (2012)
28. S. Tomita, H. Kurosawa, T. Ueda, K. Sawada, *J. Phys. D Appl. Phys.* **51**, 083001 (2018)
29. S. Tomita, K. Sawada, S. Nagai, A. Sanada, N. Hisamoto, T. Ueda, *Phys. Rev. B* **96**, 165425 (2017)
30. N. Hisamoto, T. Ueda, K. Sawada, S. Tomita, *Phys. Rev. B* **97**, 085105 (2018)
31. O.N. Singh, A. Lakhtakia (eds.), *Electromagnetic Fields in Unconventional Materials and Structures* (Wiley-Interscience, 2004)
32. K.F. Lindman, *Ann. Phys.* **368**, 621 (1920)
33. C.L. Hogan, *Bell Syst. Tech. J.* **31**, 1 (1952)
34. T. Ueda, S. Yamamoto, Y. Kado, T. Itoh, *IEEE Trans. Microw. Theory Tech.* **60**, 3043 (2012)
35. T. Kodama, S. Tomita, N. Hosoiito, H. Yanagi, *Appl. Phys. A* **122**, 41 (2016)
36. T. Kodama, S. Tomita, T. Kato, D. Oshima, S. Iwata, S. Okamoto, N. Kikuchi, O. Kitakami, N. Hosoiito, H. Yanagi, *Phys. Rev. Appl.* **6**, 024016 (2016)
37. T. Kodama, Y. Kusanagi, S. Okamoto, N. Kikuchi, O. Kitakami, S. Tomita, N. Hosoiito, H. Yanagi, *Phys. Rev. Appl.* **9**, 054025 (2018)
38. G.L.J.A. Rikken, J. Fölling, P. Wyder, *Phys. Rev. Lett.* **87**, 236602 (2001)

# Chapter 15

## Dispersion Engineering of Nonreciprocal Metamaterials



Tetsuya Ueda and Tatsuo Itoh

**Abstract** Nonreciprocal metamaterials using normally magnetized ferrite microstrip lines are reviewed, showing derivation of formula for the phase-shifting nonreciprocity based on the eigenmode solution in terms of the effective magnetization in ferrite and asymmetric boundary condition for the wave-guiding structures. Dispersion engineering of the nonreciprocity is also discussed for potential applications to leaky wave antennas with wide steering angles and reduced beam squint.

### 15.1 Introduction

*Metamaterials* are artificial electromagnetic media that are composed of small elements compared to the wavelength, referred to as *unit cell*, and provide macroscopic responses to external electric or magnetic source fields forming the constitutive relation with permittivity, permeability, and conductivity, as *effective medium* [1–3]. They are expected to realize new electromagnetic phenomena or functionalities that are impossible or very difficult to achieve only with materials existing in nature, such as negative refractive indices, cloaking techniques, and so forth.

Among various kinds of metamaterials, composite right-/left-handed (CRLH) transmission lines are one of the most comprehensive and practically useful concepts to concisely model complex physical phenomena and to design configuration of metamaterials, based on circuit theory [1]. In this chapter, we focus on nonreciprocal transmission appearing in the CRLH metamaterials.

*Nonreciprocity* to be discussed here means exhibition of differences in transmission coefficients of circuits/components or wave-guiding structures in two opposite

---

T. Ueda (✉)

Electrical Engineering and Electronics, Kyoto Institute  
of Technology, Matsugasaki Sakyo-ku, Kyoto 606-8585, Japan  
e-mail: [ueda@kit.ac.jp](mailto:ueda@kit.ac.jp)

T. Itoh

Electrical Engineering Department, University of California,  
Los Angeles, 405 Hilgard Ave., Los Angeles, CA 90095-1594, USA

propagation directions. In a combination of metamaterials with the nonreciprocity, nonreciprocal metamaterials have been studied to explore exotic electromagnetic phenomena and to create state-of-the-art circuits/components with transmission characteristics depending on directions of wave propagation.

In general, nonreciprocal transmission characteristic stems from a combination of two factors; one is *broken time-reversal symmetry*, and another is *broken spatial inversion symmetry*. To realize the broken time-reversal symmetry, natural gyrotropic media, such as ferromagnetic media and ferrites in microwave region [4, 5], or magneto-optic media in optical region [6, 7] are conventionally used. Recently, the use of active devices such as PIN diodes, field effect transistors, or time-varying switches based on semiconductor circuit technology has also been proposed and developed as artificial Faraday-effect structures operating without magnets [8, 9]. These gyrotropic materials are characterized by a rotational axis corresponding to magnetization vector in gyromagnetic media. Both natural and artificial materials with broken time-reversal symmetry play the same role in constructing off-diagonal components in permeability or permittivity tensors.

It is noted that not only broken time-reversal symmetry but also broken spatial inversion symmetry plays an important role in designing magnitude of the nonreciprocal characteristics. The geometrical asymmetry is achieved by making the wave-guiding structures asymmetric with respect to the plane including the gyrotropic axis and propagation direction. Of course, when the wave-guiding structures are symmetric with respect to the plane, nonreciprocal transmission characteristics disappear even if there exist broken time-reversal symmetries.

In the remainder of the Introduction, we briefly summarize a history and recent progress of nonreciprocal CRLH metamaterials and their applications to microwave circuits and antennas. The early work on both nonreciprocal electromagnetic band gap structures [10, 11] and nonreciprocal metamaterials [12–16] is focused and is still now focusing mainly on nonreciprocity appearing in magnitude of transmission coefficients for the artificial electromagnetic structures including gyrotropic materials for applications to isolators and circulators. For these cases, the selection of propagation direction along the structures determines whether wave propagation is permitted or prohibited just like isolators.

On the other hand, one of the most outstanding and intrinsic properties of metamaterials originates from phase gradient of fields for traveling waves in the structures, i.e., wavenumber vectors, as can be easily understood by terminologies, such as positive/negative refractive indices, right-/left-handed, forward/backward wave propagation, and so forth. Recently, from a viewpoint of phase gradient, CRLH metamaterials with phase-shifting nonreciprocity in the transmission coefficients were proposed and demonstrated [17–19]. Ideally, such metamaterials show transparency for both propagation directions, but with different refractive indices. With the use of such nonreciprocal CRLH metamaterials, we can have a situation where left-handed mode propagation with negative refractive index is dominant in one direction of the transmitted power, while right-handed mode propagation with positive refractive index is dominant in the opposite power direction at the same frequencies. In the

special cases, we can have exactly the same wavenumber vector for two different guided modes carrying their electromagnetic powers in the opposite directions.

Such nonreciprocal CRLH metamaterials were implemented into leaky wave antennas. Most of conventional nonreciprocal leaky wave antennas permitted electromagnetic wave radiation only for one propagation direction along the transmission lines, because they used nonreciprocal magnitude of transmission coefficients, whereas the leaky wave radiation from phase-shifting nonreciprocal CRLH metamaterials permits electromagnetic wave radiation for both transmitted power directions, but has asymmetric leaky wave beam directions [17, 20].

For leaky wave antennas based on the phase-shifting nonreciprocal CRLH metamaterials, radiation gain can be enhanced by constructive interference of far fields between primary leaky wave radiation from incident signals propagating along the transmission line to the terminal and secondary leaky wave radiation that are converted from residual signals which does not contribute to primary radiation and goes back to the input port after the reflection at the terminal [21].

At specific frequencies on the dispersion curves of the nonreciprocal CRLH transmission lines, unidirectional wavenumber vectors can be achieved for two different transmitted power directions. This condition corresponds to the operational frequency at the intersection of two dispersion curves whose slopes have opposite signs. The condition can also be found at lower or higher cutoff frequencies of the band gaps in the dispersion curves. The situation can be realized by shifting the geometrical axis of dispersion curves for conventional CRLH metamaterials to the right or left in the horizontal direction with respect to the vertical frequency axis. The relation of refractive indices for two propagation directions can be understood from the fact that tangent of each dispersion curve at the operational frequency is related to the group velocity, i.e., transmitted power direction, and that wavenumber vector is associated with the phase velocity.

By using nonreciprocal CRLH lines with unidirectional wavenumber vectors, a new type of transmission line resonator, referred to as *pseudo-traveling wave resonator*, has been proposed and demonstrated [22, 23]. Unique and fascinating features of the resonators are as follows; in the first place, the resonant frequency does not depend on the resonator's size, but on the dispersion curves of the transmission lines employed in the resonators that are designed with configuration parameters of the unit cell. Second, in the field profile on the resonator, the amplitude distribution is uniform and phase distribution varies linearly with the position in the longitudinal direction. The gradient of phase distribution, or wavenumber vectors, on the resonator is tunable independently of the resonant condition. Thus, the pseudo-traveling wave resonator has size-independent resonant frequency and the field profile analogous to traveling waves with arbitrarily tunable wavenumber vector on the resonator.

With the use of tunable gradient of phase distribution, pseudo-traveling wave resonators were implemented into beam scanning antennas [23]. The beam direction can be continuously controlled by tuning the nonreciprocity of the CRLH transmission lines employed in the resonator, for example, by changing an externally applied dc magnetic field to magnetic medium in the nonreciprocal transmission line. The beam can be steered even by altering the geometrical asymmetry of the wave-guiding struc-

tures [24], for example, by electronically tuning a pair of the electrical lengths for double inserted stubs on both sides of the transmission line. The pseudo-traveling wave resonators with tunable gradient of phase distribution were implemented to compact and highly efficient leaky wave antennas with automatic power-recycling system in order to handle the beam scanning or to switch the rotation direction of circularly polarized antennas [25, 26]. However, steering beam angle is determined by the magnitude of the nonreciprocity. To make the circuit size compact, enhancement of tunable range for the nonreciprocity is desired. In addition to the steering angles, beam steering antennas suffers from beam squint problems, where the beam direction varies with the operational frequency. To reduce the beam squint, it is necessary to design the dispersion of phase-shifting nonreciprocity of the CRLH metamaterials [27–29].

In this chapter, we will review the basic theory on how to design the nonreciprocity and their dispersion of the CRLH metamaterials. As an example, we consider typical ferrite-based nonreciprocal metamaterials for convenience. It is noted that the design concept discussed here covers not only the ferrite-based metamaterials, but also non-magnet gyrotropic metamaterials, from the viewpoint of designing waveguide geometries. We begin with typical permeability tensor for gyrotropic materials. Asymmetric admittance surfaces on sidewalls of the wave-guiding structures are introduced to simply model the condition of broken spatial inversion symmetry [27–29]. Nonreciprocal eigenmode analysis and some numerical simulation results are given along with the approximate formula for the nonreciprocity, which will give us a good insight into physical meanings of electromagnetic phenomena and dispersive behavior of nonreciprocal CRLH metamaterials.

## 15.2 Permittivity/Permeability Tensors for Gyrotropic Medium Due to Broken Time-Reversal Symmetry

### 15.2.1 Permeability Tensor for Microwaves in Ferrites

In microwave/millimeter wave region, ferrites, i.e., ferrimagnetic media are well-known as magnetically tunable and gyromagnetic materials, for applications to tunable and nonreciprocal circuits/devices [4, 5], such as isolators and circulators. The gyrotropic characteristics of ferrites originate microscopically from spin, magnetic behavior of electrons. When an external dc magnetic field is applied to the ferrite that is sufficiently large for the magnetization to be saturated and a microwave signal is injected in it, the magnetization vector  $\mathbf{M}$  shows the precession about the axis of the applied dc magnetic field, as shown in Fig. 15.1a. The dynamic equation for the precession of the magnetization is expressed by the following [4, 5, 30, 31]

$$\frac{d\mathbf{M}}{dt} = -\gamma\mu_0\mathbf{M} \times \mathbf{H} - \alpha_m \frac{\mathbf{M}}{M_S} \times \frac{d\mathbf{M}}{dt} \quad (15.1)$$

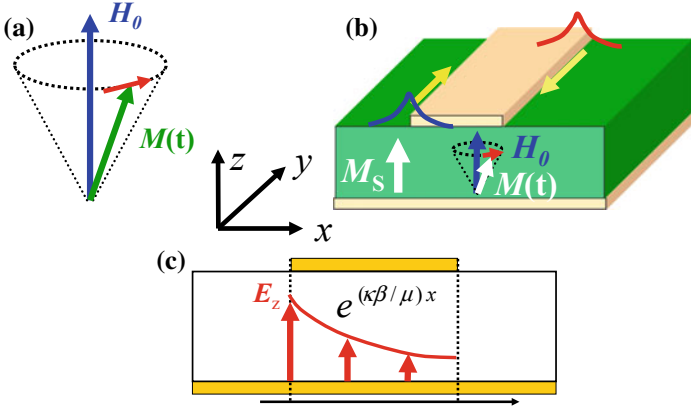


**Fig. 15.1** Schematic of **a** precession for magnetization in ferrite, **b** perspective view of normally magnetized ferrite microstrip line, and **c** field profile along the strip width

where  $\gamma$  is a gyromagnetic ratio between angular momentum and the magnetic dipole moment for electronic spin, and the quantity  $\alpha_m$  is a damping constant for the precession of magnetization due to magnetic loss. In the following, we assume that the direction of the applied dc magnetic field and the induced magnetization is in the  $z$ -axis for simplicity. When the incident microwave signal is small and nonlinear effect of the ferrite material is negligible, linearization approximation is assumed on the above (15.1) under the steady-state condition, leading to the relation of complex amplitudes between magnetization and magnetic field components in the microwave region. As a result, the constitutive relation for microwave components in complex phasor representation using a time-varying factor  $e^{j\omega t}$  is expressed by

$$\begin{aligned} \tilde{\mathbf{B}} &= \mu_0 \hat{\mu} \tilde{\mathbf{H}} \\ \hat{\mu} &= \begin{pmatrix} \mu & j\kappa & 0 \\ -j\kappa & \mu & 0 \\ 0 & 0 & 1 \end{pmatrix} \end{aligned} \quad (15.2)$$

$$\mu = \frac{\tilde{\omega}_\perp^2 - \omega^2}{\tilde{\omega}_h^2 - \omega^2}, \quad \kappa = \frac{\omega\omega_m}{\tilde{\omega}_h^2 - \omega^2} \quad (15.3)$$

where  $\tilde{\mathbf{B}}$  and  $\tilde{\mathbf{H}}$  are complex amplitudes of microwave components of the magnetic flux density and magnetic field, respectively, and  $\hat{\mu}$  is Polder tensor, or a relative permeability tensor, and

$$\begin{aligned} \omega_h &= \gamma\mu_0 H_0, \quad \omega_m = \gamma\mu_0 M_S, \\ \tilde{\omega}_h &= \omega_h + j\omega\alpha_m = \gamma\mu_0(H_0 + j\Delta H/2), \quad \tilde{\omega}_\perp = \sqrt{\tilde{\omega}_h(\tilde{\omega}_h + \omega_m)}. \end{aligned} \quad (15.4)$$

The quantities  $H_0$  and  $M_S$  denote the internal dc magnetic field and saturation magnetization in ferrites, respectively, and  $\Delta H = 2\omega\alpha_m/\gamma\mu_0$ , a half width of magnetic loss for the applied dc field to the ferrite material. It is noted that gyrotropic characteristics appear in the off-diagonal component  $\kappa$  of the permeability tensor in (15.2). In what follows, we will treat not only saturated magnetization for sufficiently large applied dc magnetic fields to the ferrite, but also the unsaturated magnetization for low applied dc magnetic fields. Even in the latter cases, we can describe behavior of wave propagation using (15.2)–(15.4), by replacing the saturation magnetization  $M_S$  by the effective magnetization  $M_{ef}$ .

### 15.2.2 Permittivity Tensor in Gyro-electric Medium

In optical region, materials in itself do not react directly against the alternating magnetic field components of the light wave, but may respond to the electric field component through the dynamics of electric polarization. In magneto-optic media under the application of dc magnetic field along the  $z$ -direction, the gyrotropic characteristics appear in the off-diagonal component  $\kappa_e$  of the permittivity tensor in the following [6, 7],

$$\tilde{\mathbf{D}} = \varepsilon_0 \hat{\varepsilon} \tilde{\mathbf{E}} \Leftrightarrow \hat{\varepsilon} = \begin{pmatrix} \varepsilon_1 & j\kappa_e & 0 \\ -j\kappa_e & \varepsilon_1 & 0 \\ 0 & 0 & \varepsilon_2 \end{pmatrix} \quad (15.5)$$

Permittivity tensors analogous to (15.5) can also be found in microwave/millimeter wave propagation in low-temperature semiconductors or ionized materials with cyclotron motion of electrons under the applied dc magnetic field in the  $z$ -direction. By taking into account dual relation of fields with symmetry in Maxwell equations, we can treat permittivity tensors in (15.5) in the same manner as permeability tensors in (15.2). In what follows, we consider only ferrite medium in microwave region with permeability tensor in gyromagnetic medium. Of course, we can translate the following discussion on permeability tensor in microwave region into permittivity tensor in magneto-optic medium based on the dual relation.

### 15.2.3 Field Displacement Effect in Transversely Magnetized Wave-Guiding Structures

When the electric field for an incident wave is parallel to the gyromagnetic axis of ferrite materials and they are set to be in the transverse direction, the field profile of the propagating wave on the cross section can be switched by changing the propagation directions, referred to as *field displacement effect*, which will serve to appearance of



the nonreciprocity. In this section, we consider the fundamental mode propagating along a microstrip line with a normally magnetized ferrite substrate as a specific case in order to understand the field displacement effect.

We begin with Maxwell's equations,

$$\begin{aligned}\nabla \times \tilde{\mathbf{E}} &= -j\omega\tilde{\mathbf{B}} \\ \nabla \times \tilde{\mathbf{H}} &= j\omega\tilde{\mathbf{D}}\end{aligned}\quad (15.6)$$

along with the constitution relation (15.2)–(15.4) for gyromagnetic medium with the axis in the  $z$ -direction.

The geometry under consideration and the coordinate system is shown in Fig. 15.1. In Fig. 15.1, the gyromagnetic axis is set to the  $z$ -direction, normal to the ferrite substrate, and propagation direction is in the  $y$ -direction. For simplicity, we assume that the field profile in the  $z$ -direction along thickness of the substrate is almost uniform, i.e.,  $\partial/\partial z = 0$ , since the thickness is much smaller than the wavelength. Assuming the field profile of the guided wave mode along the microstrip line proportional to  $\exp(-j\beta y)$  with a phase constant  $\beta$ , the differential equations (15.6) for wave propagation in ferrite are described in the Cartesian coordinates system and reduce to

$$\begin{aligned}-j\beta\tilde{E}_z &= -j\omega\mu_0(\mu\tilde{H}_x + j\kappa\tilde{H}_y) \\ -\frac{\partial\tilde{E}_z}{\partial x} &= -j\omega\mu_0(-j\kappa\tilde{H}_y + \mu\tilde{H}_x) \\ -j\beta\tilde{H}_z &= j\omega\varepsilon_0\varepsilon_r\tilde{E}_x \\ -\frac{\partial\tilde{H}_z}{\partial x} &= j\omega\varepsilon_0\varepsilon_r\tilde{E}_y\end{aligned}\quad (15.7)$$

Equation (15.7) implies that transverse electric (TE) modes related to the components  $\tilde{E}_z$ ,  $\tilde{H}_x$ ,  $\tilde{H}_y$  are sensitive to the permeability tensor. We have focused only on the TE modes since transverse magnetic (TM) modes with  $\tilde{H}_z$ ,  $\tilde{E}_x$ ,  $\tilde{E}_y$  are insensitive to the dc magnetic field. From (15.7), the 1-D Helmholtz equation is given by

$$\frac{d^2\tilde{E}_z}{dx^2} - K_x^2\tilde{E}_z = 0\quad (15.8)$$

with

$$K_x^2 = \beta^2 - \left(\frac{\omega}{c}\right)\varepsilon_r\mu_{ef}, \quad \mu_{ef} = \frac{\mu^2 - \kappa^2}{\mu}\quad (15.9)$$

where  $\varepsilon_r$  is the dielectric constant of the ferrite, and quantities  $\mu$  and  $\kappa$  are expressed by (15.3). Then, the field profile is assumed from (15.7) to be

$$\begin{aligned}\tilde{E}_z &= A \cosh(K_x x) + B \sinh(K_x x) \\ \tilde{H}_y &= \frac{1}{j\omega\mu_0\mu\mu_{ef}} [A \{\mu K_x \sinh(K_x x) - \kappa\beta \cosh(K_x x)\} \\ &\quad + B \{\mu K_x \cosh(K_x x) - \kappa\beta \sinh(K_x x)\}] \end{aligned} \quad (15.10)$$

where  $A$  and  $B$  are unknown constants. To find the guided modes, we assume perfect magnetic conductors (PMC) on the sidewalls at the strip edges of the center microstrip line, for simplicity, where the tangential component of the magnetic field is zero, that is,

$$\tilde{H}_y = 0 \quad \text{at } x = 0, w \quad (15.11)$$

By applying the boundary conditions to (15.10), we have

$$[(\kappa\beta)^2 - (\mu K_x)^2] \sinh(K_x w) = 0. \quad (15.12)$$

For the fundamental mode, the coefficient of the hyperbolic-sinusoidal function in (15.12) vanishes, and

$$(\kappa\beta)^2 - (\mu K_x)^2 = (\kappa\beta)^2 - \mu^2 \left[ \beta^2 - \left( \frac{\omega}{c} \right) \varepsilon_r \mu_{ef} \right] = 0$$

The following dispersion relation is obtained [32],

$$\beta = \pm \frac{\omega}{c} \sqrt{\varepsilon_r \mu}, \quad (15.13)$$

The mode is referred to as *edge-guided mode*. The reason will be found in its field profile. It is noted that the relation  $A/B = 1$  in (15.10) holds for wave propagation in the  $+y$ -direction with (15.13). Then, the electric field profile of the edge-guided mode in (15.10) reduces to

$$\tilde{E}_z = A \exp \left[ \left( \frac{\kappa\beta}{\mu} \right) x \right] \exp(-j\beta y) \quad (15.14)$$

Therefore, the field profiles have an exponential form along the  $x$ -axis in the transverse direction. The position with the maximum values of the fields can be found at one of the edges of the center microstrip and can be switched by the selection of the propagation direction, that is, the sign of  $\beta$ , as confirmed in (15.14). This phenomenon is well known as *field displacement effect*. In Fig. 15.1c, the microstrip line structure provides the symmetric geometry with respect to the plane holding two vectors; the magnetization vector in the ferrite,  $\mathbf{M}$ , and the wavenumber vector,  $\boldsymbol{\beta}$ . In such cases, the structure shows the reciprocal transmission characteristics. On the other hand, to be discussed later, when a stub is inserted only on one side of the edges of the center microstrip so that the geometry has the asymmetry with respect to the same plane, the

field was concentrated on either side of the strip edge where the stubs are inserted or the opposite side. As a result, the normally magnetized ferrite microstrip lines with asymmetric geometry show the nonreciprocal transmission characteristics.

### 15.3 Introduction to Asymmetric Admittance Surfaces Equivalent to Broken Spatial Inversion Symmetry

In this section, we introduce asymmetric admittance surfaces in simplified waveguiding structures as boundary conditions in order to provide broken spatial inversion symmetry. The schematic of the transverse cross section of the geometry under consideration is shown in Fig. 15.2. It is composed of a ferrite block with height  $d$  and width  $w$  that is placed at the center, two metallic plates at the top and bottom, two different admittance surfaces at the right and left, and the ferrite is magnetized normal to the metallic plates. We assume that the fundamental mode propagates in the  $y$ -direction and has the electric field component in the  $z$ -direction. Then, the electric field component is parallel to the axis of the gyromagnetic anisotropy in ferrite. We can implement such a simplified model to understand physical meanings of wave propagation and roughly estimate dispersion characteristics of normally magnetized ferrite microstrip lines with stubs.

When the thickness of the ferrite substrate is much smaller than the wavelength, variation of the field distribution along the thickness is negligible. Then, the dominant mode is simplified to TE mode. In microstrip lines, the admittance surfaces are placed as virtual boundary condition on the sidewalls at the strip edges. A pair of admittance surfaces  $Y_1$  and  $Y_2$  are defined at  $x = 0$ , and  $w$ , as a ratio of the magnetic field component to the electric field that can be observed from the ferrite region to outside in the following [27, 28],

$$Y_1 = H_y/E_z \text{ at } x = 0 \tag{15.15}$$

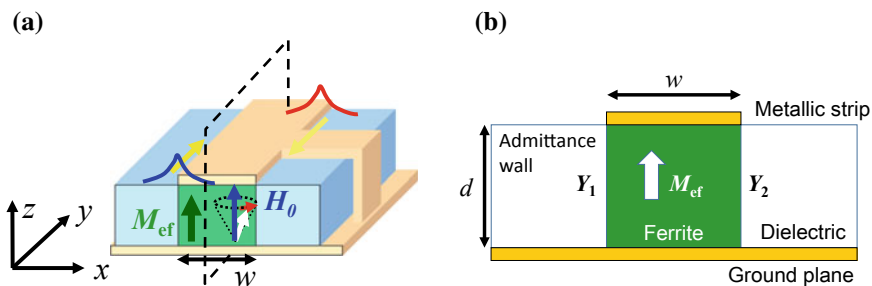


**Fig. 15.2** Schematic of **a** perspective view and **b** cross section of a simplified model for asymmetric insertion of stubs in normally magnetized ferrite microstrip line

and

$$Y_2 = -H_y/E_z \text{ at } x = w, \quad (15.16)$$

Stubs inserted at both edges of the microstrip line determine specific values of the admittances  $Y_1$  and  $Y_2$ . When no stubs are inserted, perfect magnetic conductors may be assumed as the admittance boundaries with  $Y_1 = Y_2 = 0$ .

## 15.4 Analysis of Nonreciprocal Edge-Guided Modes

In order to find eigenmode solution to asymmetric wave-guiding structure with normally magnetized ferrite substrate, we return to the Helmholtz equation (15.8) and the field profile (15.10). By imposing asymmetric boundary conditions (15.15) and (15.16) on the model in Fig. 15.2b, the generalized dispersion relation is obtained in the following [28],

$$\Phi(\omega, \beta, \kappa) = \cot(k_x w) - \frac{(\omega/c)^2 \mu (\tilde{Y}_1 \tilde{Y}_2 \kappa + \varepsilon_r) - \beta^2}{j(\omega/c) \mu k_x (\tilde{Y}_1 + \tilde{Y}_2)} - \frac{\beta \kappa (\tilde{Y}_1 - \tilde{Y}_2)}{\mu k_x (\tilde{Y}_1 + \tilde{Y}_2)} = 0 \quad (15.17)$$

with normalized admittance surfaces,

$$\tilde{Y}_1 = Y_1/Y_0, \quad \tilde{Y}_2 = Y_2/Y_0, \quad Y_0 = \sqrt{\varepsilon_o/\mu_o} \quad (15.18)$$

$$k_x^2 = -K_x^2 = \varepsilon_r \mu_{ef} \left( \frac{\omega}{c} \right)^2 - \beta^2, \quad (15.19)$$

The first and second terms in (15.17) are even function of the phase constant  $\beta$  due to the fact that  $k_x$  is also even function as seen from (15.19), whereas the third term is explicitly an odd function. Therefore, (15.17) varies with the sign of  $\beta$ , i.e., selection of propagation direction, which leads to nonreciprocal transmission where the magnitude of phase constant differs depending on the propagation direction.

For specific cases without stubs inserted,  $Y_1 = Y_2 = 0$ . The dispersion relation (15.17) becomes even function and reduces to (15.13), which results in reciprocal transmission of the edge-guided mode.

## 15.5 Formula for Nonreciprocity Appearing in Phase Constant

In the previous section, we have derived generalized nonreciprocal dispersion relation (15.17) by introducing asymmetric admittances on the sidewalls of the transverse cross section in the normally magnetized ferrite microstrip lines. The nonreciprocity appearing in the phase constant can be estimated in an implicit manner by directly solving the transcendental equation (15.17). In order to understand the mechanism of the nonreciprocity, it is more instructive and useful to explicitly express the nonreciprocity, in terms of the configuration parameters, such as magnetic properties of the ferrite and asymmetry of the waveguide. In the remainder of this section, we will show the derivation of the approximate formula for the nonreciprocity [28].

The nonreciprocity manifests itself due to the appearance of off-diagonal components in Polder's tensor  $\kappa$  in (15.2). In what follows, we assume that the magnitude of  $\kappa$  is small since the operational frequency of interest is set up far away from the ferromagnetic resonant frequencies of the ferrite. Then, we can regard the off-diagonal component  $\kappa$  as a perturbation to the dispersion relation.

We begin with the reciprocal case of (15.17) under the assumption  $\kappa = 0$ , and find the phase constant  $\beta = \beta_1$  as the zeroth-order approximation. Next, we regard  $\Phi$  in (15.17) as a function of  $\kappa$  and  $\beta = \beta_1 + \Delta\beta_{NR}$ , where  $\Delta\beta_{NR}$  represents a perturbation of phase constant, i.e., phase-shifting nonreciprocity induced by  $\kappa$ . In the vicinity of  $\beta = \beta_1$  and  $\kappa = 0$ , total derivative of the dispersion relation  $\Delta\Phi$  is approximately given in the lowest order by

$$\Delta\Phi = \Phi(\omega, \beta_1 + \Delta\beta_{NR}, \kappa) - \Phi(\omega, \beta_1, 0) = \left. \frac{\partial\Phi}{\partial\beta} \right|_{\substack{\kappa=0 \\ \beta=\beta_1}} \cdot \Delta\beta_{NR} + \left. \frac{\partial\Phi}{\partial\kappa} \right|_{\substack{\kappa=0 \\ \beta=\beta_1}} \cdot \kappa = 0$$

Thus, we can express phase-shifting nonreciprocity  $\Delta\beta_{NR}$  as

$$\Delta\beta_{NR} = -\kappa \left. \frac{\partial\Phi}{\partial\kappa} \right|_{\substack{\kappa=0 \\ \beta=\beta_1}} / \left. \frac{\partial\Phi}{\partial\beta} \right|_{\substack{\kappa=0 \\ \beta=\beta_1}}. \quad (15.20)$$

From (15.17), we have

$$\Delta\beta_{NR} \approx \frac{-j\kappa(\omega/c)(\tilde{Y}_1 - \tilde{Y}_2)}{\tilde{Y}_1\tilde{Y}_2\left(\frac{\omega}{c}\frac{\mu}{k_{x1}}\right)^2 - j\frac{\omega}{c}\frac{w\mu(\tilde{Y}_1 + \tilde{Y}_2)}{\sin^2(k_{x1}w)} - 1} \quad (15.21)$$

where a variable  $k_{x1}$  in (15.21) satisfies the relation  $k_{x1}^2 = \mu\epsilon_r(\omega/c)^2 - \beta_1^2$ , and it can be approximately expressed from  $\Phi|_{\kappa=0, \beta=\beta_1} = 0$  using Taylor series by

$$k_{x1}^2 \approx \frac{j(\omega/c)\mu w\tilde{Y}_1\tilde{Y}_2 + \tilde{Y}_1 + \tilde{Y}_2}{\left(w^2\frac{(\tilde{Y}_1 + \tilde{Y}_2)}{3} + \frac{w}{j(\omega/c)\mu}\right)}. \quad (15.22)$$

The expression (15.22) can be reduced under the assumption that the operation frequency is much higher than  $\omega_h$  and  $\omega_m$ . Then, the nonreciprocity appearing in the phase constant is given by

$$\Delta\beta_{NR} \approx \frac{(\omega_m/c)(\tilde{Y}_2 - \tilde{Y}_1)}{w\left(\frac{\omega}{c}\right)\frac{(\tilde{Y}_2 + \tilde{Y}_1)}{3} - 2j}. \quad (15.23)$$

For typical cases with the strip width  $w$  much smaller than the wavelength, (15.23) further reduces to

$$\Delta\beta_{NR} \approx \frac{j}{2} \left( \frac{\omega_m}{c} \right) (\tilde{Y}_2 - \tilde{Y}_1) \quad (15.24)$$

It should be emphasized that for lossless cases, admittances on the sidewalls  $\tilde{Y}_1, \tilde{Y}_2$  are purely imaginary, and  $\Delta\beta_{NR}$  takes real values, which means that the nonreciprocity manifests itself only in the phase constant but not in the attenuation constant.

Equation (15.24) reveals the linear dependence of the phase-shifting nonreciprocity  $\Delta\beta_{NR}$  on the magnetization  $M_{ef}$ . In fact, it has been experimentally confirmed that the nonreciprocity of the nonreciprocal CRLH transmission line was approximately proportional to the effective magnetization of the unsaturated ferrite [23]. Equation (15.24) suggests that the use of ferrites with larger  $M_{ef}$  can provide stronger nonreciprocity. It is also found from (15.24) that the nonreciprocity  $\Delta\beta_{NR}$  is proportional to a factor  $(\tilde{Y}_1 - \tilde{Y}_2)$ , the difference of admittances on both sidewalls, which verifies that the geometrical asymmetry of the wave-guiding structure, i.e., broken spatial inversion symmetry, contributes to the nonreciprocity.

## 15.6 Transmission Line Analysis for Composite Structures

In the previous section, nonreciprocal eigenmode solution for wave-guiding structures which is asymmetric on the transverse cross section but uniform in the longitudinal direction was discussed. In this section, we consider composite structures whose unit cell is separated into several sections in the longitudinal direction. A typical example of the normally magnetized ferrite microstrip line periodically and asymmetrically inserted with stubs is shown in Fig. 15.3 [28]. Each unit cell is separated into three sections; two of them are reciprocal sections without stubs, and the other section is nonreciprocal section where stubs are asymmetrically inserted into the center microstrip line. The dispersion relation for such composite structures can be obtained by combining in series the eigenmode solution in each section that was discussed in the previous section, based on the transmission line model.

Circuit parameters in the 1-D nonreciprocal metamaterial structure are expressed by the ABCD matrix for the unit cell, as shown in Fig. 15.3b. The unit cell is composed of two types of sections studied earlier, and its ABCD matrix  $F_{Cell}$  becomes a product

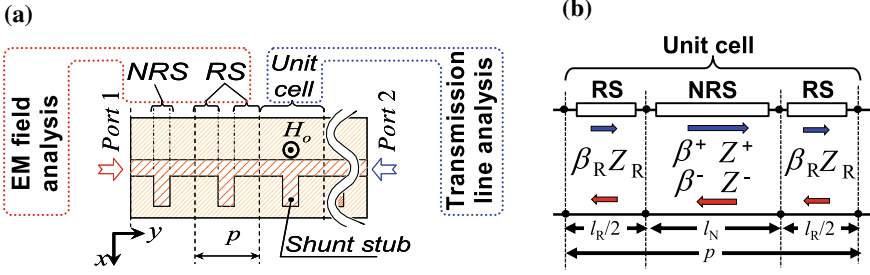


**Fig. 15.3** Unit cell in the periodic metamaterial structure. **a** Top view of the nonreciprocal microstrip line which is composed of reciprocal sections (RS) and a nonreciprocal section (NRS). **b** The transmission line model. Reproduced with permission from [28]. Copyright © 2013 IEICE

of corresponding matrices for reciprocal sections  $F_{RS}$  and for nonreciprocal section  $F_{NRS}$

$$F_{Cell} = F_{RS} F_{NRS} F_{RS} = \begin{bmatrix} A_{Cell} & B_{Cell} \\ C_{Cell} & D_{Cell} \end{bmatrix}$$

In the first place, it is necessary to determine each matrix in each section. The matrix  $F_{RS}$  is a well-known ABCD matrix for conventional transmission lines. On the other hand, the ABCD matrix  $F_{NRS}$  is derived in terms of different propagation constants  $\beta^+$  and  $\beta^-$  in analogy to the transmission line section with nonreciprocal phase constants, where the superscripts “+” and “-” denote directions of wave propagation [17],

$$F_{NRS} = \begin{bmatrix} A_{NRS} & B_{NRS} \\ C_{NRS} & D_{NRS} \end{bmatrix} \quad (15.25)$$

with

$$\begin{aligned} A_{NRS} &= e^{j\Delta\beta_{NR}l_N} \left( \cos(\bar{\beta}_N l_N) + j \frac{\Delta Z_N \sin(\bar{\beta}_N l_N)}{\bar{Z}_N} \right) \\ B_{NRS} &= e^{j\Delta\beta_{NR}l_N} \left( j \bar{Z}_N \left( 1 - \frac{\Delta Z_N^2}{\bar{Z}_N^2} \right) \sin(\bar{\beta}_N l_N) \right) \\ C_{NRS} &= e^{j\Delta\beta_{NR}l_N} \left( j \frac{\sin(\bar{\beta}_N l_N)}{\bar{Z}_N} \right) \\ D_{NRS} &= e^{j\Delta\beta_{NR}l_N} \left( \cos(\bar{\beta}_N l_N) - j \frac{\Delta Z_N \sin(\bar{\beta}_N l_N)}{\bar{Z}_N} \right) \\ \bar{\beta}_N &= (\beta^+ + \beta^-)/2, \Delta Z_N = (Z^+ - Z^-)/2, \bar{Z}_N = (Z^+ + Z^-)/2 \end{aligned} \quad (15.26)$$

where  $Z^+$  and  $Z^-$  are characteristic impedances of the modes with phase constants  $\beta^+$  and  $\beta^-$ , respectively. The quantity  $l_N$  denotes the length of nonreciprocal section. It is noted that the nonreciprocity in the nonreciprocal section is described by  $\Delta\beta_{NR} = (\beta^+ - \beta^-)/2$ . For lossless transmission line, characteristic impedance is reciprocal and  $\Delta Z_N = 0$ . By applying the Floquet-Bloch theorem, that is, periodic boundary condition to the single unit cell in the longitudinal direction, we have

$$\begin{bmatrix} V_1 \\ I_1 \end{bmatrix} = F_{Cell} \begin{bmatrix} V_2 \\ I_2 \end{bmatrix} = \hat{I} e^{j\tilde{\beta}_{MM}p} \begin{bmatrix} V_2 \\ I_2 \end{bmatrix} \quad (15.27)$$

where  $V_i$  and  $I_i$  are voltages and currents at ports  $i$  ( $i = 1, 2$ ) of the unit cell, respectively,  $p$  is the period, and  $\tilde{\beta}_{MM}$  is the complex propagation constant in the whole periodic structure that will be treated in terms of phase and attenuation constants  $\beta_{MM}$  and  $\alpha_{MM}$  as

$$\tilde{\beta}_{MM} = \beta_{MM} - j\alpha_{MM}.$$

Eigenmode analysis of (15.27) allows us to derive a dispersion relation for propagation constant  $\tilde{\beta}_{MM}$  in the metamaterial,

$$\det(F_{Cell}) + e^{j2\tilde{\beta}_{MM}p} - e^{j\tilde{\beta}_{MM}p}(A_{cell} + D_{cell}) = 0. \quad (15.28)$$

For  $\varepsilon$ -negative structures, as shown in Fig. 15.3a, (15.28) becomes

$$\cos(\tilde{\beta}_{MM}p - \Delta\beta_{NR}l_N) = \cos\tilde{\beta}_N l_N \cos\beta_R l_R - \frac{(\bar{Z}_N^2 + Z_R^2) - \Delta Z_N^2}{2\bar{Z}_N \bar{Z}_R} \sin\tilde{\beta}_N l_N \sin\beta_R l_R \quad (15.29)$$

where  $\beta_R$ ,  $l_R$ , and  $Z_R$  are the phase constant, total length, and characteristic impedance of reciprocal sections without stubs, respectively. It is found from left-hand side of (15.29) that the dispersion curves are shifted in the horizontal direction with respect to the frequency axis by

$$\Delta\beta_{MM} = \Delta\beta_{NR} \frac{l_N}{p} \quad (15.30)$$

Equation (15.30) means that the magnitude of the nonreciprocity is determined by a longitudinal fraction of nonreciprocal section in the unit cell.

To validate the transmission line approach along with eigenmode solution that is discussed here, dispersion relation and the approximate formula for the nonreciprocity are compared with numerical simulation results for two cases, epsilon-negative metamaterial and CRLH metamaterials, as shown in Fig. 15.4. For both cases, inductive stubs are periodically inserted at one of center strip edges. The difference between the two is whether the periodically loaded series capacitance is inserted or not.



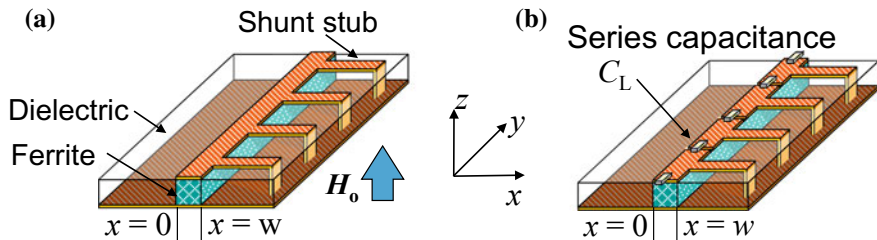


**Fig. 15.4** Schematic of the geometries **a**  $\epsilon$ -negative and **b** CRLH metamaterials. Reproduced with permission from [28]. Copyright © 2013 IEICE

In Fig. 15.5, the dispersion diagram and the nonreciprocity as a function of the frequency are plotted. Figure 15.5a, b represents the dispersion curves for epsilon-negative and CRLH metamaterials, respectively. The solid and broken lines show phase and attenuation constants, respectively, and a dash-dot line denotes the nonreciprocity estimated from (15.24) and (15.30). The calculations are made with yttrium iron garnet (YIG) rod of  $0.8 \text{ mm} \times 0.8 \text{ mm}$  in cross section and 2-mm-length shunt stubs inserted from one side of the structure. The effective magnetization is  $\mu_o M_{ef} = 175 \text{ mT}$ , and the internal dc field is  $\mu_o H_0 = 10 \text{ mT}$ . The values of  $l_R$  and  $l_N$  are 3 mm and 1 mm, respectively. For the CRLH metamaterials in Fig. 15.4b, periodically inserted series capacitance  $C_L = 0.3 \text{ pF}$ .

In Fig. 15.5, numerical simulation results by ANSYS HFSS™ ver.13 based on the finite element method (FEM) are also plotted with dots for comparison. The simulated phase characteristics of S-parameters were converted into the dispersion diagram. The calculations by the transmission line approach are in good agreement with the numerical simulation. For epsilon-negative structure in Fig. 15.5a, visible discrepancy below the cutoff frequency of 6 GHz is found due to the fact that FEM simulation is carried out for finite number of cells. Below the cutoff region, numeri-

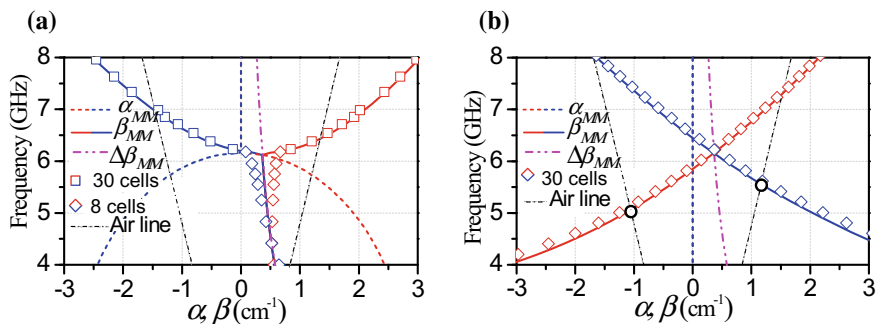


**Fig. 15.5** Comparison of dispersion diagram between the proposed TL approach and numerical simulation. **a**  $\epsilon$ -negative metamaterial. **b** CRLH metamaterial. Reproduced with permission from [28]. Copyright © 2013 IEICE

cal simulation suffers from significant errors due to small amplitude of transmission coefficients for damping modes. It is found from Fig. 15.5a, b that the nonreciprocities  $\Delta\beta$  for both cases are approximately proportional to  $1/\omega$ . The tendency can be confirmed by the formula for the nonreciprocity in (15.24) by substituting the admittances of asymmetrically inserted shunt inductance  $Y_1 = 0$  and  $Y_2 = -j/\omega L_L$  into the equation. It is noted that the present transmission line approach cannot take into account the radiation losses.

## 15.7 Design of Dispersion-Less Nonreciprocity for Antenna Applications

For conventional leaky wave antennas, beam angle  $\theta$  with respect to broadside direction of the transmission line is determined by the phase constant  $\beta$  in the fast wave region, or by the effective refractive index of the line  $n_{\text{ef}}$ , under  $|n_{\text{ef}}| \leq 1$ , and is given in the following,

$$\theta = \sin^{-1} \frac{\beta}{\beta_0} = \sin^{-1}(n_{\text{ef}}) \quad (15.31)$$

where  $\beta_0$  is the phase constant in free space. As seen from (15.31),  $n_{\text{ef}}$  must be constant with the operational frequency in order to avoid beam squint problem where the beam direction varies with the operational frequency. Unfortunately,  $n_{\text{ef}}$  is intrinsically dispersive, since the phase velocity in the fast wave region exceeds the speed of light in vacuum as well as the group velocity.

On the other hand, beam direction of high-efficient resonant-type leaky wave antennas based on nonreciprocal CRLH metamaterials is given by [23],

$$\theta = \sin^{-1} \frac{\Delta\beta}{\beta_0} = \sin^{-1} \frac{\Delta n_{\text{ef}}}{2} \quad (15.32)$$

In order to make the nonreciprocity proportional to the operational frequency, the admittance difference ( $Y_1 - Y_2$ ) needs to be composed of capacitances, such as with  $Y_1 = 0$  and  $Y_2 = j\omega C_R$  [29]. In addition, we need to insert inductive stubs into shunt branch of the CRLH lines to establish negative permittivity. To eliminate the influence of dispersive inductive stubs on the nonreciprocity, the inductive stubs are inserted so that they have geometrical symmetry with respect to a plane that includes an axis of gyrotropic material and wave propagation direction. In Fig. 15.6, top view of the proposed CRLH transmission line is illustrated. It is composed of a microstrip line-based CRLH transmission line on the hybrid substrate with the thickness  $d = 0.8$  mm including dielectric and ferrite substrates with dielectric constants  $\epsilon_d = 2.6$  and  $\epsilon_f = 15$ , respectively. A normally magnetized ferrite rod is embedded just below the center strip. Series lumped capacitance is periodically loaded in the microstrip line with period  $p$  to establish negative permeability. Capacitive stubs are inserted

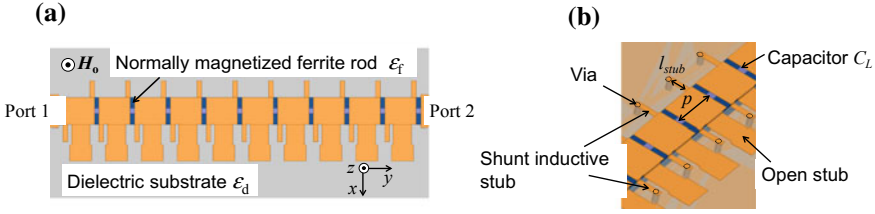


**Fig. 15.6** Proposed geometry of dispersion-free nonreciprocal phase-shifting CRLH transmission Lines. Reprint from [29]. Copyright © 2016 IEEE

only on right-hand side of the center microstrip edges so that the nonreciprocity is approximately proportional to the operational frequency. This situation corresponds to the constant difference of refractive indices between forward and backward propagation directions. In addition, inductive stubs are also inserted in the CRLH line to construct negative permittivity, but the influence on the nonreciprocity should be avoided. Two equivalent short inductive stubs are inserted symmetrically in the unit cell of CRLH line to eliminate the undesired dispersion of the nonreciprocity, as shown in Fig. 15.6.

In Fig. 15.7, the simulated and measured dispersion curves and the phase-shifting nonreciprocity estimated from S-parameters are shown for the cases with positive and negative dc magnetic field. The configuration parameters are as follows; thickness of the substrate including dielectric and ferrite is 0.8 mm. The dielectric constant of dielectric and ferrite substrate is  $\epsilon_d = 2.6$  and  $\epsilon_f = 15$ , respectively. The length of unit cell  $p = 4.0$  mm, the center strip width  $w = 3.0$  mm, and series lumped capacitance  $C_L = 0.5$  pF. Shunt capacitive stubs inserted are composed of the large patch with the dimension  $2.4 \text{ mm} \times 1.8 \text{ mm}$  that is connected to the microstrip line with the length 2.2 mm and width of 2.0 mm. Shorted inductive stubs have the length and width of 1.3 and 0.5 mm. The dimension of a ferrite rectangular rod is  $0.8 \text{ mm} \times 3.0 \text{ mm} \times 40.5 \text{ mm}$ . The magnetic loss of ferrite is  $\mu_0 \Delta H = 5 \text{ mT}$ . The CRLH line was designed so that a band gap between lower and higher pass bands due to single

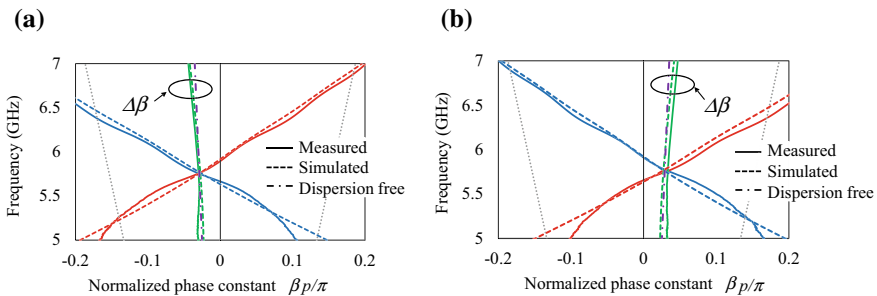


**Fig. 15.7** Simulated and measured dispersion curves and phase-shifting nonreciprocity. **a** Positive applied dc magnetic field. **b** Negative applied dc magnetic field. Reprint from [29]. Copyright © 2016 IEEE

negative conditions is small. In the simulation setup, the effective magnetization was  $\pm 170$  mT, and an externally applied dc magnetic field in the experiment was  $\pm 135$  mT. In this case, the measured nonreciprocity  $\Delta\beta$  is approximately proportional to the operational frequency corresponding to oblique beam angle at  $\pm 10^\circ$  with respect to broadside direction in a relatively wideband ranging from 5 to 7 GHz. As can be predicted from the configuration, linearity of the nonreciprocity is restricted at low frequency due to ferromagnetic resonance of ferrite and at high frequency due to dispersion of distributed capacitive shunt stubs.

## 15.8 Summary

In this chapter, dispersion engineering of nonreciprocal CRLH metamaterials was briefly introduced and reviewed, based on a combination of eigenmode solution and transmission line approach.

## References

1. C. Caloz, T. Itoh, *Electromagnetic Metamaterials: Transmission Line Theory and Microwave Applications* (Wiley, New Jersey, 2006)
2. G.V. Eleftheriades, K.G. Balmain, *Negative Refraction Metamaterials: Fundamental Principles and Applications* (IEEE Press, Wiley, New Jersey, 2005)
3. N. Engheta, R.W. Ziolkowski, *Metamaterials: Physics and Engineering Explorations* (IEEE Press, Wiley, New Jersey, 2006)
4. B. Lax, K. Button, *Microwave Ferrites and Ferrimagnetics* (McGraw-Hill, New York, 1962)
5. A.G. Gurevich, G.A. Melkov, *Magnetization Oscillations and Waves* (CRC Press, Boca Raton, 1996)
6. L.D. Landau, E.M. Lifshitz, L.P. Pitaevski, *Electrodynamics of Continuous Media*, 2nd edn. (Butterworth Heinemann Ltd., 1995)
7. D.D. Stancil, *Theory of Magnetostatic Waves* (Springer, 1993)
8. T. Kodera, D.L. Sounas, C. Caloz, Artificial Faraday rotation using a ring metamaterial structure without static magnetic field. *Appl. Phys. Lett.* **99**(3), 031114 (2011)
9. B.-I. Popa, S.A. Cummer, Nonreciprocal active metamaterials. *Phys. Rev. B* **85**(205101), 2 (2012)
10. A. Figotin, I. Vitebskiy, Electromagnetic unidirectionality in magnetic photonic crystals. *Phys. Rev. B* **67**(165210), 1–20 (2003)
11. M.B. Stephanson, K. Sertel, J.L. Volakis, Frozen modes in coupled microstrip lines printed on ferromagnetic substrates. *IEEE Microw. Wirel. Compon. Lett.* **18**(5), 305–307 (2008)
12. M. Tsutsumi, T. Ueda, Nonreciprocal left-handed microstrip lines using ferrite substrate, in *IEEE MTT-S International Microwave Symposium Digest*, pp. 249–252, June 2004
13. T. Ueda, M. Tsutsumi, Left-handed transmission characteristics of ferrite microstrip lines without series capacitive load. *IEICE Trans. Electron* **E89-C**, 1318–1323 (2006)
14. T. Ueda, M. Tsutsumi, Nonreciprocal left-handed transmission characteristics of microstrip lines on the ferrite substrate. *IET Proc. Microw. Antennas Propag.* **1**(2), 349–354 (2007)
15. T. Kodera, C. Caloz, Uniform ferrite-loaded open waveguide structure with CRLH response and its application to a novel backfire-to-endfire leaky-wave antenna. *IEEE Trans. Microw. Theory Tech.* **57**(4), 784–795 (2009)

16. N. Apaydin, K. Sertel, J.L. Volakis, Nonreciprocal and magnetically scanned leaky-wave antenna using coupled CRLH lines. *IEEE Trans. Antennas Propag.* **62**(6), 2954–2961 (2014)
17. T. Ueda, K. Horikawa, M. Akiyama, M. Tsutsumi, Nonreciprocal phase-shift composite right/left handed transmission lines and their application to leaky wave antennas. *IEEE Trans. Antennas Propag.* **57**(7), 1995–2005 (2009)
18. T. Ueda, M. Akiyama, Nonreciprocal phase-shift composite right/left handed transmission lines using ferrite-rod-embedded substrate. *IEEE Trans. Magn.* **45**(10), 4203–4206 (2009)
19. H. Kishimoto, T. Ueda, Y. Kado, Experimental demonstration of nonreciprocal phase-shift composite right/left handed transmission lines with ferrite-rod-embedded substrate. *IEEE Trans. Magn.* **47**(10), 3724–3727 (2011)
20. K. Horikawa, T. Ueda, M. Akiyama, Beam steering of leaky wave radiation from nonreciprocal phase-shift composite right/left handed transmission lines. *IEICE Trans. Electron.* **E93-C**(7), 1089–1097 (2010)
21. K. Horikawa, T. Ueda, M. Akiyama, Influence of reflected waves at a terminal of nonreciprocal phase-shift CRLH transmission lines on the leaky wave radiation, in *Proceedings of Asia-Pacific Microwave Conference*, pp. 151–154, Dec 2009
22. T. Ueda, H. Kishimoto, Pseudo-traveling wave resonator based on nonreciprocal phase-shift composite right/left handed transmission lines, in *IEEE MTT-S International Microwave Symposium Digest*, pp. 41–44, May 2010
23. T. Ueda, S. Yamamoto, Y. Kado, T. Itoh, Pseudo-traveling wave resonator with magnetically tunable phase gradient of fields and its applications to beam steering antennas. *IEEE Trans. Microw. Theory Tech.* **60**(10), 3043–3054 (2012)
24. T. Ueda, J. Fukuda, Y. Kado, T. Itoh, Nonreciprocal phase-shift CRLH transmission lines using geometrical asymmetry with periodically inserted double shunt stubs, in *Proceedings of 42nd European Microwave Conference*, pp. 570–573, Oct 2012
25. A. Porokhnyuk, T. Ueda, Y. Kado, T. Itoh, Beam antenna with circular polarization rotation switching based on passive components, in *Proceedings of 44th European Microwave Conference*, pp. 327–330, Oct 2014
26. K. Ninomiya, T. Ueda, A. Porokhnyuk, T. Itoh, Demonstration of circularly-polarized leaky-wave antenna based on pseudo-traveling wave resonance, in *Proceedings of 45th European Microwave Conference*, pp. 450–453, Sept 2015
27. A. Porokhnyuk, T. Ueda, Y. Kado, T. Itoh, Design of nonreciprocal CRLH metamaterial for non-squinting leaky-wave antenna, in *IEEE MTT-S International Microwave Symposium Digest*, vol. TH1H-1, pp. 1–3, June 2013
28. A. Porokhnyuk, T. Ueda, Y. Kado, T. Itoh, Mode analysis of phase-constant nonreciprocity in ferrite-embedded CRLH metamaterials. *IEICE Trans. Electron.* **E96-C**(10), 1263–1272, Oct 2013
29. T. Ueda, K. Ninomiya, K. Yoshida, T. Itoh, Design of dispersion-free phase-shifting nonreciprocity in composite right/left handed metamaterials, in *IEEE MTT-S International Microwave Symposium Digest*, vol. TH2G-1, pp. 1–4, May 2016
30. R.E. Collin, *Foundations for Microwave Engineering*, 2nd edn. (IEEE Press)
31. D.M. Pozar, *Microwave Engineering*, 4th edn. (Wiley, 2012)
32. M.E. Hines, Reciprocal and nonreciprocal modes of propagation in ferrite strip line and microstrip devices. *IEEE Trans. Microw. Theory Tech.* **19**(5), 442–451 (1971)

**Part V**  
**Novel Aspects**

# Chapter 16

## Photonic Dirac Cones and Relevant Physics



Kazuaki Sakoda

**Abstract** In this chapter, we derive a necessary and sufficient condition for materializing the photonic Dirac cone, which is an isotropic linear dispersion relation, on the  $\Gamma$  point of periodic metamaterials and photonic crystals by the  $\mathbf{k} \cdot \mathbf{p}$  perturbation theory and the group theory. We analyze the coupling between the Dirac-cone modes in metamaterials/photonic crystal slabs and the free-space modes by the Green function method, and prove that the propagation direction of the Dirac-cone modes in the slab can be controlled by the polarization of the incident wave. We further analyze the shapes of dispersion curves of the slab modes in the presence of diffraction loss and show that the group velocity of the slab modes exceeds the light velocity in free space. This problem of superluminal propagation is often found for non-Hermitian systems. Finally, we extend our discussion to electronic waves and prove that we can also materialize the Dirac cone on the  $\Gamma$  point of periodically modulated quantum wells.

### 16.1 Introduction

The Dirac cone is originally an idea to describe the energy spectrum of massless particles. It is characterized by the isotropic linear dependence of their energy on their momentum. A similar energy spectrum was discovered in the dispersion relation of periodic metamaterials in the Brillouin zone center by the transmission line theory in the microwave region [1–4]. Such device structures were named composite right/left-handed (CRLH) transmission lines. To materialize the linear dispersion, it was necessary to make two dispersion curves of the CRLH transmission line degenerate in the zone center or the  $\Gamma$  point of the Brillouin zone, by fine-tuning of the device structure.

Later, the materialization condition of the Dirac cone in the dispersion relation of periodic metamaterials and photonic crystals was clarified for general cases by tight-binding approximation [5–7] and the  $\mathbf{k} \cdot \mathbf{p}$  perturbation theory [8, 9].

---

K. Sakoda (✉)  
National Institute for Materials Science, Tsukuba, Japan  
e-mail: [sakoda.kazuaki@nims.go.jp](mailto:sakoda.kazuaki@nims.go.jp)

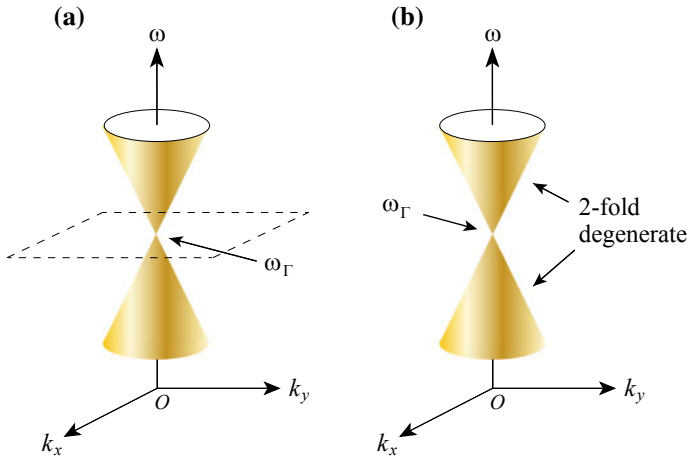


**Fig. 16.1** Examples of the photonic Dirac-cone dispersion relation. **a** Dirac cone with an auxiliary quadratic dispersion surface (broken line) realized, for example, by accidental degeneracy of  $E$  and  $A_1$  modes in the square-lattice metamaterials of the  $C_{4v}$  symmetry. **b** Double Dirac cone realized, for example, by the  $E_1$  and  $E_2$  modes in the triangular-lattice metamaterials of the  $C_{6v}$  symmetry.  $\omega_\Gamma$  is the Dirac point frequency. Reprinted with permission from [13]: Copyright ©2014 by the American Physical Society

Mei et al. [8] discussed the formation of the Dirac cone, the Berry phase, and mapping into the Dirac Hamiltonian for phononic and photonic crystals, while the present author (K. S.) derived the sufficient condition for the Dirac-cone formation [9]. Because the effective refractive index is equal to zero at the vertex of the Dirac cone [10], which is called the *Dirac point*, quite curious phenomena and their applications are expected, which include scatter-free waveguides [11] and lenses of arbitrary shapes [12]. We can also expect novel phenomena like the control of the propagation direction by the polarization of the incident wave [13].

As we shall see in this chapter, for the photonic Dirac cone to be materialized, two electromagnetic eigenmodes with particular symmetry combinations should have the same frequency in the Brillouin zone center by fine-tuning the structure and/or the material parameters (Fig. 16.1). This situation is traditionally called *accidental degeneracy* in solid-state physics.

In Sect. 16.2, we derive a necessary and sufficient condition for the Dirac cone by the  $\mathbf{k} \cdot \mathbf{p}$  perturbation theory and the group theory. We apply it to four examples to completely clarify the symmetry combinations of the degenerate eigenmodes that materialize the Dirac cones. In Sect. 16.3, we apply our theory to slab periodic structures to show that the propagation direction of the Dirac-cone mode in the slab can be controlled by the polarization of the incident wave. In Sect. 16.4, we analyze the dispersion and the propagation speed of the slab Dirac-cone modes with diffraction loss to show that their apparent group velocity can be larger than the light velocity in free space. This problem of superluminal propagation is often found for non-Hermitian systems. In Sect. 16.5, we extend our theory to electronic waves and prove that we



can materialize Dirac cones in the energy band of periodically modulated quantum wells. We show that the electronic effective mass is vanishing at the Dirac point, so we can expect curious phenomena such as divergent electronic mobility.

## 16.2 Dirac-Cone Dispersion Relation

### 16.2.1 Derivation by the $\mathbf{k} \cdot \mathbf{p}$ Perturbation Theory

In this section, we follow the discussion in [9]. We start with two of the four Maxwell equations:

$$\nabla \times \mathbf{E}(\mathbf{r}, t) = -\mu_0 \frac{\partial}{\partial t} \mathbf{H}(\mathbf{r}, t), \quad (16.1)$$

$$\nabla \times \mathbf{H}(\mathbf{r}, t) = \varepsilon_0 \varepsilon(\mathbf{r}) \frac{\partial}{\partial t} \mathbf{E}(\mathbf{r}, t), \quad (16.2)$$

where  $\mathbf{E}$  and  $\mathbf{H}$  stand for the electric field and the magnetic field, respectively.  $\varepsilon_0$  and  $\mu_0$  are permittivity and permeability of free space, respectively. For simplicity, we assume that the dielectric constant  $\varepsilon(\mathbf{r})$  of the system is real and the permeability is equal to that of the free space; that is, we assume that the system is non-magnetic. We also assume that  $\varepsilon(\mathbf{r})$  is periodic so that

$$\varepsilon(\mathbf{r} + \mathbf{a}) = \varepsilon(\mathbf{r}), \quad (16.3)$$

where  $\mathbf{a}$  is the elementary translation vector that describes the periodicity of the system structure. By eliminating  $\mathbf{E}$  from these equations and assuming a harmonic oscillation, we obtain the eigenequation for the magnetic field. Because we are considering a periodic system, the eigenfrequency and the eigenfunction depend on the wave vector  $\mathbf{k}$  in the first Brillouin zone:

$$\mathcal{L} \mathbf{H}_{\mathbf{k}n}(\mathbf{r}) \equiv \nabla \times \left[ \frac{1}{\varepsilon(\mathbf{r})} \nabla \times \mathbf{H}_{\mathbf{k}n}(\mathbf{r}) \right] = \lambda_{\mathbf{k}n} \mathbf{H}_{\mathbf{k}n}(\mathbf{r}), \quad (16.4)$$

where  $n$  is the band index. Operator  $\mathcal{L}$  is defined by the first equality of this equation. The  $\mathbf{k}$  dependent eigenvalue is given by

$$\lambda_{\mathbf{k}n} = \frac{\omega_{\mathbf{k}n}^2}{c^2}, \quad (16.5)$$

where  $\omega_{\mathbf{k}n}$  denotes the eigenangular frequency and  $c$  is the light velocity in free space. According to Bloch's theorem, the eigenfunction,  $\mathbf{H}_{\mathbf{k}n}$ , is a product of an exponential factor and a vector field with lattice translation symmetry:

$$\mathbf{H}_{\mathbf{k}n}(\mathbf{r}) = e^{i\mathbf{k}\cdot\mathbf{r}}\mathbf{u}_{\mathbf{k}n}(\mathbf{r}), \quad (16.6)$$

$$\mathbf{u}_{\mathbf{k}n}(\mathbf{r} + \mathbf{a}) = \mathbf{u}_{\mathbf{k}n}(\mathbf{r}). \quad (16.7)$$

The inner product of two vector fields is defined as follows.

$$\langle \mathbf{H}_1 | \mathbf{H}_2 \rangle \equiv \frac{1}{V} \int_V d\mathbf{r} \mathbf{H}_1^*(\mathbf{r}) \cdot \mathbf{H}_2(\mathbf{r}), \quad (16.8)$$

where  $V$  is the volume on which the periodic boundary condition is imposed [14]. Then, we can prove that  $\mathcal{L}$  defined in (16.4) is a Hermitian operator in the Hilbert space of complex vector fields.

*Proof* For two arbitrary complex vector fields,  $\mathbf{H}_1$  and  $\mathbf{H}_2$ ,

$$\langle \mathbf{H}_1 | \mathcal{L}\mathbf{H}_2 \rangle = \frac{1}{V} \int_V d\mathbf{r} \mathbf{H}_1^*(\mathbf{r}) \cdot \left[ \nabla \times \left\{ \frac{1}{\varepsilon(\mathbf{r})} \nabla \times \mathbf{H}_2(\mathbf{r}) \right\} \right]. \quad (16.9)$$

From well-known vector formula,

$$\nabla \cdot (\mathbf{A} \times \mathbf{B}) = \mathbf{B} \cdot (\nabla \times \mathbf{A}) - \mathbf{A} \cdot (\nabla \times \mathbf{B}), \quad (16.10)$$

$$\begin{aligned} \langle \mathbf{H}_1 | \mathcal{L}\mathbf{H}_2 \rangle &= \frac{1}{V} \int_V d\mathbf{r} \left\{ \nabla \times \mathbf{H}_1^*(\mathbf{r}) \right\} \cdot \left\{ \frac{1}{\varepsilon(\mathbf{r})} \nabla \times \mathbf{H}_2(\mathbf{r}) \right\} \\ &\quad - \frac{1}{V} \int_S dS \left[ \mathbf{H}_1^*(\mathbf{r}) \times \left\{ \frac{1}{\varepsilon(\mathbf{r})} \nabla \times \mathbf{H}_2(\mathbf{r}) \right\} \right]_{\perp}, \end{aligned} \quad (16.11)$$

The second term on the right-hand side is the integral of the normal component of the integrand on the surface of volume  $V$ , which is denoted by  $S$ . This term was derived by Gauss's theorem for the volume integral of the divergence of the vector field. This surface integral is equal to zero due to the periodic boundary condition. By using (16.10) again,

$$\begin{aligned} \langle \mathbf{H}_1 | \mathcal{L}\mathbf{H}_2 \rangle &= \frac{1}{V} \int_V d\mathbf{r} \left[ \nabla \times \left\{ \frac{1}{\varepsilon(\mathbf{r})} \nabla \times \mathbf{H}_1^*(\mathbf{r}) \right\} \right] \cdot \mathbf{H}_2(\mathbf{r}) \\ &= \langle \mathcal{L}\mathbf{H}_1 | \mathbf{H}_2 \rangle. \end{aligned} \quad (16.12)$$

This equation implies that the Hermitian conjugate operator  $\mathcal{L}^\dagger$  is  $\mathcal{L}$  itself. So,  $\mathcal{L}$  is a Hermitian operator.  $\blacksquare$

So, the eigenfunctions of  $\mathcal{L}$  are orthogonal to each other and they form a complete set. We normalize them as

$$\langle \mathbf{H}_{\mathbf{k}n} | \mathbf{H}_{\mathbf{k}'n'} \rangle = \delta_{\mathbf{k}\mathbf{k}'} \delta_{nn'}, \quad (16.13)$$

where  $\delta_{\mathbf{k}\mathbf{k}'}$  and  $\delta_{nn'}$  are Kronecker's delta.

Now, we introduce a new operator  $\mathcal{L}_{\mathbf{k}}$  defined by

$$\mathcal{L}_{\mathbf{k}} \equiv e^{-i\mathbf{k}\cdot\mathbf{r}} \mathcal{L} e^{i\mathbf{k}\cdot\mathbf{r}} = (\nabla + i\mathbf{k}) \times \left[ \frac{1}{\varepsilon(\mathbf{r})} (\nabla + i\mathbf{k}) \times \right]. \quad (16.14)$$

Then,  $\mathbf{u}_{\mathbf{k}n}$  are its eigenfunctions with eigenvalue  $\lambda_{\mathbf{k}n}$ . We can prove as before that  $\mathcal{L}_{\mathbf{k}}$  is a Hermitian operator in the Hilbert space of complex vector fields with lattice translation symmetry. So,  $\{\mathbf{u}_{\mathbf{k}n} | n = 1, 2, \dots\}$  is a complete set. We normalize it as

$$\langle \mathbf{u}_{\mathbf{k}n} | \mathbf{u}_{\mathbf{k}n'} \rangle_0 \equiv \frac{1}{V_0} \int_{V_0} d\mathbf{r} \mathbf{u}_{\mathbf{k}n}^*(\mathbf{r}) \cdot \mathbf{u}_{\mathbf{k}n'}(\mathbf{r}) = \delta_{nn'}, \quad (16.15)$$

where  $V_0$  denotes the volume of the unit cell of the periodic system. Thus, in particular, for  $\mathbf{k} = 0$ ,

$$\{\mathbf{u}_{0n} | n = 1, 2, \dots\} \quad (16.16)$$

is an orthonormal complete set. So, any eigenfunction  $\mathbf{u}_{\mathbf{k}l}$  of operator  $\mathcal{L}_{\mathbf{k}}$  can be expressed by a linear combination of eigenfunctions  $\{\mathbf{u}_{0n}\}$  of operator  $\mathcal{L}_0$ . Thus, by a perturbative calculation, we can obtain  $\lambda_{\mathbf{k}l}$  for small  $\mathbf{k}$  using  $\{\mathbf{u}_{0n}\}$  as a basis set. Because we are interested in the presence of  $\mathbf{k}$ -linear terms, the quadratic term of the perturbation operator  $\Delta\mathcal{L}_{\mathbf{k}}$  can be ignored:

$$\begin{aligned} \Delta\mathcal{L}_{\mathbf{k}} &\equiv \mathcal{L}_{\mathbf{k}} - \mathcal{L}_0 \\ &\approx i\mathbf{k} \times \left[ \frac{1}{\varepsilon(\mathbf{r})} \nabla \times \right] + \nabla \times \left[ \frac{1}{\varepsilon(\mathbf{r})} i\mathbf{k} \times \right]. \end{aligned} \quad (16.17)$$

Our next task is to calculate  $\lambda_{\mathbf{k}n}$  by the first-order perturbation theory. We assume according to the situation of our problem that some of the eigenfunctions on the  $\Gamma$  point,  $\{\mathbf{u}_{0l} | l = 1, 2, \dots, M\}$ , are degenerate and denote their eigenvalue by  $\lambda_{\Gamma}$  ( $= \omega_{\Gamma}^2/c^2$ ). By the degenerate perturbation theory, the first-order solution for  $\mathbf{u}_{\mathbf{k}l}$  ( $l = 1, 2, \dots, M$ ) is obtained by diagonalizing the matrix whose  $ij$  ( $1 \leq i, j \leq M$ ) element is given by

$$C_{ij}^{(\mathbf{k})} \equiv \langle \mathbf{u}_{0i} | \Delta\mathcal{L}_{\mathbf{k}} | \mathbf{u}_{0j} \rangle_0. \quad (16.18)$$

The first-order solution gives eigenvalue corrections linear in  $\mathbf{k}$ . So, if the eigenvalues of matrix  $C_{\mathbf{k}} = (C_{ij}^{(\mathbf{k})})$  are equal to zero, the  $\mathbf{k}$ -linear term is absent and the dispersion curve is quadratic or of a higher order in  $\mathbf{k}$ . This means that there is no Dirac cone.

$C_{ij}^{(\mathbf{k})}$  can be denoted in a slightly different form, which is easier to analyze by group theory.

$$\begin{aligned} C_{ij}^{(\mathbf{k})} &= \frac{1}{V_0} \int_{V_0} d\mathbf{r} \mathbf{u}_{0i}^*(\mathbf{r}) \cdot \left[ i\mathbf{k} \times \left\{ \frac{1}{\varepsilon(\mathbf{r})} \nabla \times \mathbf{u}_{0j}(\mathbf{r}) \right\} \right] \\ &\quad + \frac{1}{V_0} \int_{V_0} d\mathbf{r} \mathbf{u}_{0i}^*(\mathbf{r}) \cdot \left[ \nabla \times \left\{ \frac{1}{\varepsilon(\mathbf{r})} i\mathbf{k} \times \mathbf{u}_{0j}(\mathbf{r}) \right\} \right]. \end{aligned} \quad (16.19)$$

When we define  $\Delta\mathcal{L}$  as

$$\Delta\mathcal{L} \equiv \times \left[ \frac{1}{\varepsilon(\mathbf{r})} \nabla \times \right], \quad (16.20)$$

the first term on the right-hand side of (16.19) can be modified to

$$(\text{The 1st term}) = -i\mathbf{k} \cdot \langle \mathbf{u}_{0i} | \Delta\mathcal{L} | \mathbf{u}_{0j} \rangle_0 \quad (16.21)$$

On the other hand, the second term can be written in the following form by transforming the integral as we did for (16.9).

$$\begin{aligned} (\text{The 2nd term}) &= \frac{1}{V_0} \int d\mathbf{r} \nabla \times \mathbf{u}_{0i}^*(\mathbf{r}) \cdot \left[ \frac{1}{\varepsilon(\mathbf{r})} i\mathbf{k} \times \mathbf{u}_{0j}(\mathbf{r}) \right] \\ &= i\mathbf{k} \cdot \langle \mathbf{u}_{0j} | \Delta\mathcal{L} | \mathbf{u}_{0i} \rangle_0^*. \end{aligned} \quad (16.22)$$

When we define  $\mathbf{P}_{ij}$  by

$$\mathbf{P}_{ij} \equiv \langle \mathbf{u}_{0i} | \Delta\mathcal{L} | \mathbf{u}_{0j} \rangle_0, \quad (16.23)$$

we finally obtain

$$C_{ij}^{(\mathbf{k})} = i\mathbf{k} \cdot (-\mathbf{P}_{ij} + \mathbf{P}_{ji}^*). \quad (16.24)$$

We can examine  $C_{\mathbf{k}}$  using the spatial symmetry of  $\{\mathbf{u}_{0l}\}$ . We assume that the periodic structure that we deal with is invariant by symmetry operations of point group  $\mathcal{G}$ . We denote the symmetry operations and their matrix representations by  $\mathcal{R}$  and  $\mathbf{R}$ , respectively. Then, we can prove [9]

$$\mathbf{k} \cdot \mathbf{P}_{ij} = (\mathbf{R}\mathbf{k}) \cdot \langle \mathcal{R}\mathbf{u}_{0i} | \Delta\mathcal{L} | \mathcal{R}\mathbf{u}_{0j} \rangle_0 \quad (16.25)$$

for any  $\mathcal{R} \in \mathcal{G}$ , where by definition,

$$[\mathcal{R}\mathbf{u}_{0i}](\mathbf{r}) \equiv \mathbf{R}\mathbf{u}_{0i}(\mathbf{R}^{-1}\mathbf{r}). \quad (16.26)$$

Equation (16.25) is very powerful to analyze the structure of matrix  $C^{(\mathbf{k})}$ . Actually, (16.25) relates its different elements to each other, so that the number of independent elements is reduced. In addition, in order for  $C_{ij}^{(\mathbf{k})}$  to be nonzero, the product of  $\mathbf{k}$ ,  $\mathbf{u}_{0i}$ , and  $\mathbf{u}_{0j}$  should contain a term invariant for all  $\mathcal{R} \in \mathcal{G}$ . This condition is expressed in a group theoretical terminology that the product of the three terms should contain the totally symmetric representation. The judgement of whether it contains the totally symmetric representation or not is easily performed by the *reduction* procedure [15]. Some examples will be given in the next four sections.

**Table 16.1** Symmetry combinations that generate Dirac cones by accidental degeneracy for one-dimensional periodic lattices of the  $C_{2v}$  symmetry. Symmetries of the magnetic field of the two modes on the  $\Gamma$  point are given in the left column. Shapes of the dispersion curves are given in the right column, where D denotes the Dirac cone

Mode 1	Mode 2	Dispersion
$A_1$	$B_1$	D
$A_2$	$B_2$	D

## 16.2.2 Examples of Dirac Cones

We first examine the one-dimensional lattice of  $C_{2v}$  symmetry, that is, the symmetry of a rectangle. It is known that there are only four different spatial symmetries for the eigenmodes on the  $\Gamma$  point of the  $C_{2v}$  symmetric structure. They are denoted by  $A_1$ ,  $A_2$ ,  $B_1$ ,  $B_2$ , respectively [15]. By following the reduction procedure, we can tell which combination of eigenmode symmetries may lead to nonzero  $C_{ij}^{(\mathbf{k})}$ . As summarized in Table 16.1,  $C_{ij}^{(\mathbf{k})}$  can be nonzero for the combinations of ( $A_1$ ,  $B_1$ ) modes and ( $A_2$ ,  $B_2$ ) modes.

By examining all symmetry transformations  $\mathcal{R} \in C_{2v}$ , we can prove that matrix  $C^{(\mathbf{k})}$  has the following form for the combination of the  $A_1$  ( $\mathbf{u}_{01}$ ) and  $B_1$  ( $\mathbf{u}_{02}$ ) modes.

$$C^{(\mathbf{k})} = \begin{pmatrix} 0, & bk \\ b^*k, & 0 \end{pmatrix}. \quad (16.27)$$

In (16.27),

$$b = i\mathbf{e} \cdot [-\langle \mathbf{u}_{01} | \Delta\mathcal{L} | \mathbf{u}_{02} \rangle_0 + \langle \mathbf{u}_{02} | \Delta\mathcal{L} | \mathbf{u}_{01} \rangle_0^*], \quad (16.28)$$

where  $\mathbf{e}$  is a unit vector in the direction of the one-dimensional alignment of the unit cells. To derive (16.27), we should examine each matrix element by using (16.25). For example, when we consider the  $180^\circ$  rotation for  $\mathcal{R}$ , we have

$$\mathcal{R}\mathbf{u}_{01} = \mathbf{u}_{01}, \quad (16.29)$$

$$\mathcal{R}\mathbf{u}_{02} = -\mathbf{u}_{02}, \quad (16.30)$$

$$\mathbf{R}\mathbf{k} = -\mathbf{k}. \quad (16.31)$$

So,

$$\mathbf{k} \cdot \mathbf{P}_{11} = -\mathbf{k} \cdot \langle \mathbf{u}_{01} | \Delta\mathcal{L} | \mathbf{u}_{01} \rangle = -\mathbf{k} \cdot \mathbf{P}_{11}, \quad (16.32)$$

$$\mathbf{k} \cdot \mathbf{P}_{22} = -\mathbf{k} \cdot \langle \mathbf{u}_{02} | \Delta\mathcal{L} | \mathbf{u}_{02} \rangle = -\mathbf{k} \cdot \mathbf{P}_{22}. \quad (16.33)$$

Thus,  $\mathbf{k} \cdot \mathbf{P}_{11} = \mathbf{k} \cdot \mathbf{P}_{22} = 0$ , which implies that  $C_{11}^{(\mathbf{k})} = C_{22}^{(\mathbf{k})} = 0$ .

The secular equation to determine the first-order correction,  $\Delta\lambda$ , to the eigenvalue of (16.4) is given by

$$\begin{vmatrix} -\Delta\lambda, & bk \\ b^*k, & -\Delta\lambda \end{vmatrix} = 0. \quad (16.34)$$

Thus, its solutions are given by

$$\Delta\lambda = \pm|b|k, \quad (16.35)$$

which leads to the following dispersion relation in the vicinity of the  $\Gamma$  point by the Taylor expansion with respect to  $k$ :

$$\begin{aligned} \omega_k &= c\sqrt{\lambda_k} = \sqrt{\omega_\Gamma^2 + c^2\Delta\lambda} \\ &\approx \omega_\Gamma \pm \frac{|b|c^2k}{2\omega_\Gamma}. \end{aligned} \quad (16.36)$$

So, there is a one-dimensional Dirac cone. The combination of the  $A_2$  and  $B_2$  mode also yields the Dirac cone, since the same relation as (16.27) holds for them.

Next, we examine the two-dimensional square lattice of  $C_{4v}$  symmetry, that is, the symmetry of a regular square. It is known that there are five symmetries of eigenmodes,  $A_1$ ,  $A_2$ ,  $B_1$ ,  $B_2$ , and  $E$  [15]. The  $E$  modes are doubly degenerate, and the rest are non-degenerate.

Let us first examine the case of the combination of an  $E$  mode and an  $A_1$  mode. From group theory [15], we can assume without loss of generality that one of the two eigenfunctions of the  $E$  mode is transformed like the  $x$ -coordinate and the other like the  $y$ -coordinate by the symmetry operation  $\mathcal{R} \in C_{4v}$ . On the other hand, the  $A_1$  eigenmode is invariant. By examining all symmetry transformations, we can prove that matrix  $C_{\mathbf{k}}$  has the following form:

$$C_{\mathbf{k}} = \begin{pmatrix} 0 & 0 & bk_x \\ 0 & 0 & bk_y \\ b^*k_x & b^*k_y & 0 \end{pmatrix}. \quad (16.37)$$

The secular equation is given by

$$\begin{vmatrix} -\Delta\lambda, & 0, & bk_x \\ 0, & -\Delta\lambda, & bk_y \\ b^*k_x, & b^*k_y, & -\Delta\lambda, \end{vmatrix} = 0, \quad (16.38)$$

whose solutions are

$$\Delta\lambda = 0, \quad \pm|b|k, \quad (16.39)$$

where  $k = \sqrt{k_x^2 + k_y^2}$ . Therefore, two of the three dispersion curves give an isotropic Dirac cone. The linear term is absent for the third mode, so it gives a quadratic dispersion. The same result can also be obtained by the tight-binding approximation [6].

**Table 16.2** Symmetry combinations that generate Dirac cones by accidental degeneracy for the square lattice of the  $C_{4v}$  symmetry. Symmetries of the magnetic field of the two modes on the  $\Gamma$  point are given in the left column. Shapes of the dispersion curves are given in the right column, where D and Q denote Dirac cone and quadratic dispersion surface, respectively

Mode 1	Mode 2	Dispersion
$E$	$A_1, A_2, B_1, B_2$	D + Q

For the combinations of  $(E, A_2)$ ,  $(E, B_1)$ , and  $(E, B_2)$  modes, we can similarly prove that matrix  $C_{\mathbf{k}}$  has the following forms, respectively:

$$\begin{aligned}
 (E, A_2) : C_{\mathbf{k}} &= \begin{pmatrix} 0 & 0 & bk_y \\ 0 & 0 & -bk_x \\ b^*k_y & -b^*k_x & 0 \end{pmatrix}, \\
 (E, B_1) : C_{\mathbf{k}} &= \begin{pmatrix} 0 & 0 & bk_x \\ 0 & 0 & -bk_y \\ b^*k_x & -b^*k_y & 0 \end{pmatrix}, \\
 (E, B_2) : C_{\mathbf{k}} &= \begin{pmatrix} 0 & 0 & bk_y \\ 0 & 0 & bk_x \\ b^*k_y & b^*k_x & 0 \end{pmatrix}. \tag{16.40}
 \end{aligned}$$

We obtain the same secular equation for all these cases as the combination of the  $E$  and  $A_1$  modes. So, there is an isotropic Dirac cone and a quadratic dispersion surface.

Now, we examine the two-dimensional triangular lattice of  $C_{6v}$  symmetry. There are six symmetries of eigenmodes,  $A_1, A_2, B_1, B_2, E_1,$  and  $E_2$  [15]. The  $E_1,$  and  $E_2$  modes are doubly degenerate, and the rest are non-degenerate.

For the combination of an  $E_1$  mode and an  $E_2$  mode, we can prove by examining all transformations  $\mathcal{R} \in C_{6v}$  that matrix  $C_{\mathbf{k}}$  has the following form:

$$C_{\mathbf{k}} = \begin{pmatrix} 0 & 0 & -bk_y & -bk_x \\ 0 & 0 & -bk_x & bk_y \\ -b^*k_y & -b^*k_x & 0 & 0 \\ -b^*k_x & b^*k_y & 0 & 0 \end{pmatrix}, \tag{16.41}$$

where we assumed without loss of generality that the two eigenfunctions of the  $E_1$  mode ( $\mathbf{u}_{01}, \mathbf{u}_{02}$ ) are transformed like  $x$  and  $y$  and those of the  $E_2$  mode ( $\mathbf{u}_{03}, \mathbf{u}_{04}$ ) are transformed like  $xy$  and  $x^2 - y^2$  [15]. The secular equation for the first-order correction can be solved easily, and its solutions are given by

$$\Delta\lambda = \pm|b|k \quad (\text{double roots}). \tag{16.42}$$

**Table 16.3** Symmetry combinations that generate Dirac cones by accidental degeneracy for the triangular lattice of the  $C_{6v}$  symmetry. Shapes of the dispersion curves are given in the right column, where D, DD, and Q denote Dirac cone, double Dirac cones, and quadratic dispersion surface, respectively

Mode 1	Mode 2	Dispersion
$E_1$	$E_2$	DD
$E_1$	$A_1, A_2$	D + Q
$E_2$	$B_1, B_2$	D + Q

So, we have isotropic double Dirac cones with the same slope (Fig. 16.1b). This conclusion agrees with the result of the tight-binding calculation given in [7]. Other mode combinations can be analyzed in a similar manner. The results are summarized in Table 16.3.

Finally, we examine the simple cubic lattice of the  $O_h$  symmetry. There are four kinds of non-degenerate eigenmodes ( $A_{1g}, A_{1u}, A_{2g}$ , and  $A_{2u}$ ), two kinds of doubly degenerate eigenmodes ( $E_g$  and  $E_u$ ), and four kinds of triply degenerate eigenmodes ( $T_{1g}, T_{1u}, T_{2g}$ , and  $T_{2u}$ ) [15].

Let us examine the case of two triply degenerate modes. For the combination of a  $T_{1g}$  mode ( $\mathbf{u}_{01}, \mathbf{u}_{02}, \mathbf{u}_{03}$ ) and a  $T_{1u}$  mode ( $\mathbf{u}_{04}, \mathbf{u}_{05}, \mathbf{u}_{06}$ ),  $C^{(\mathbf{k})}$  has the following structure:

$$C^{(\mathbf{k})} = \begin{pmatrix} 0 & 0 & 0 & 0 & bk_z & -bk_y \\ 0 & 0 & 0 & -bk_z & 0 & bk_x \\ 0 & 0 & 0 & bk_y & -bk_x & 0 \\ 0 & -b^*k_z & b^*k_y & 0 & 0 & 0 \\ b^*k_z & 0 & -b^*k_x & 0 & 0 & 0 \\ -b^*k_y & b^*k_x & 0 & 0 & 0 & 0 \end{pmatrix}, \tag{16.43}$$

which is sufficiently sparse so that we can easily obtain its analytical solutions:

$$\Delta\lambda = \begin{cases} 0 & \text{(double roots),} \\ \pm|b|k & \text{(double roots).} \end{cases} \tag{16.44}$$

So, there are isotropic double Dirac cones with the same slope and two quadratic dispersion surfaces. Other symmetry combinations can be analyzed in a similar manner. The result is listed in Table 16.4.

The analytical results obtained by the degenerate perturbation theory can be confirmed by numerical calculation. For example, we assume a simple cubic lattice of dielectric spheres with a dielectric constant of 12.6 (GaAs). By changing the radius of the spheres, we find several cases of accidental degeneracy among the dispersion curves. Figure 16.2 shows two such examples, which agree with the analytical results listed in Table 16.4.



**Table 16.4** Symmetry combinations that generate Dirac cones by accidental degeneracy for the simple cubic lattice of the  $O_h$  symmetry. Shapes of the dispersion curves are given in the right column, where D, DD, and Q denote Dirac cone, double Dirac cones, and quadratic dispersion surface, respectively

Mode 1	Mode 2	Dispersion
$T_{1g}$	$T_{1u}$	DD + 2Q
$T_{2g}$	$T_{2u}$	DD + 2Q
$T_{1g}$	$T_{2u}$	3D
$T_{2g}$	$T_{1u}$	3D
$T_{1g}, T_{2g}$	$E_u$	2D + Q
$T_{1u}, T_{2u}$	$E_g$	2D + Q
$T_{1u}$	$A_{1g}$	D + 2Q
$T_{1g}$	$A_{1u}$	D + 2Q
$T_{2u}$	$A_{2g}$	D + 2Q
$T_{2g}$	$A_{2u}$	D + 2Q

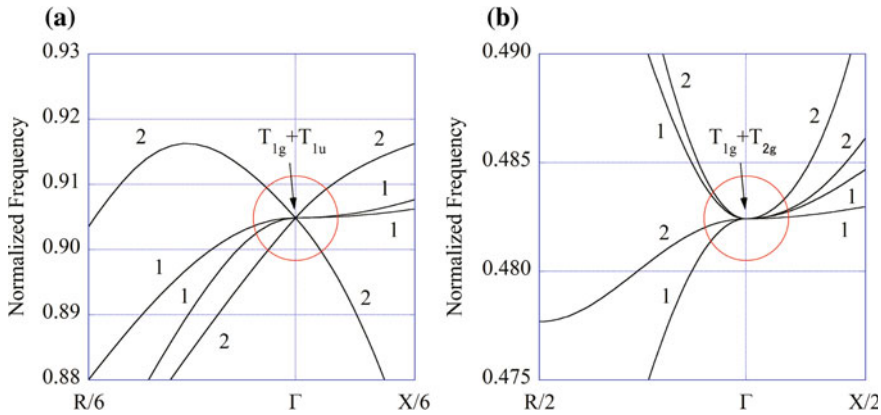


**Fig. 16.2** Dispersion curves of a photonic crystal composed of the simple cubic lattice of dielectric spheres with a dielectric constant of 12.6. The vertical axis is the normalized frequency ( $\omega a/2\pi c$ ), and the horizontal axis is the wave vector in the R ( $= (\pi/a, \pi/a, \pi/a)$ ) and X ( $= (\pi/a, 0, 0)$ ) directions, where R/6, for example, means that the horizontal axis is magnified by six times. The radius of the spheres is 0.160a for (a) and 0.416a for (b). The number associated with each dispersion curve is the multiplicity of the mode. Reprinted with permission from [9]: Copyright ©2012 by The Optical Society

### 16.3 Dirac Cones in the Slab Structure

In this section, we follow the discussion given in [13]. We analyze slab structures composed of a periodic metamaterial or a photonic crystal. They are practically important in the optical frequencies, since they can be fabricated by various lithographic techniques. We show that we can control the propagation direction of the slab mode

by the polarization of the incident wave. We formulate the retarded Green function and analyze the excitation process of the Dirac-cone modes. We apply this method to square and triangular lattices to show the peculiar polarization angle dependence of the propagation direction.

### 16.3.1 Retarded Green Function

By eliminating the electric field from (16.1) and (16.2), we obtain the wave equation for the magnetic field.

$$\mathcal{L}\mathbf{H} \equiv \nabla \times \left[ \frac{1}{\varepsilon(\mathbf{r})} \nabla \times \mathbf{H} \right] = -\frac{1}{c^2} \frac{\partial^2 \mathbf{H}}{\partial t^2}. \quad (16.45)$$

Then, the retarded Green function,  $G(\mathbf{r}, \mathbf{r}', t)$ , for the magnetic field satisfies the following inhomogeneous equation.

$$-\left( \frac{1}{c^2} \frac{\partial^2}{\partial t^2} + \mathcal{L} \right) G(\mathbf{r}, \mathbf{r}', t - t') = \mathbf{I} \delta(\mathbf{r} - \mathbf{r}') \delta(t - t'), \quad (16.46)$$

where  $\mathbf{I}$  is the  $3 \times 3$  unit tensor and  $\delta$  is the Dirac delta function. The retarded Green function is also characterized by the causality:

$$G(\mathbf{r}, \mathbf{r}', t) = 0 \quad (t < 0). \quad (16.47)$$

We introduce the longitudinal eigenfunctions,  $\mathbf{H}_{\mathbf{k}n}^{(L)}$ , in addition to the usual transverse eigenfunctions,  $\mathbf{H}_{\mathbf{k}n}^{(T)}$ . They are characterized by the following equations.

$$\nabla \cdot \mathbf{H}_{\mathbf{k}n}^{(T)} = 0, \quad (16.48)$$

$$\nabla \times \mathbf{H}_{\mathbf{k}n}^{(L)} = 0. \quad (16.49)$$

$\{\mathbf{H}_{\mathbf{k}n}^{(T)}\}$  is a physical solution and is the same as what we have denoted simply by  $\{\mathbf{H}_{\mathbf{k}n}\}$  so far. On the other hand,  $\{\mathbf{H}_{\mathbf{k}n}^{(L)}\}$  is not divergenceless, so it is an unphysical solution. But we still need them to obtain a complete set of eigenfunctions. Then, the retarded Green function for  $t \geq 0$  is given by

$$G(\mathbf{r}, \mathbf{r}', t) = -\frac{c^2}{V} \sum_{\mathbf{k}, n} \left[ \frac{\sin \omega_{\mathbf{k}n} t}{\omega_{\mathbf{k}n}} \mathbf{H}_{\mathbf{k}n}^{(T)}(\mathbf{r}) \otimes \mathbf{H}_{\mathbf{k}n}^{(T)*}(\mathbf{r}') + t \mathbf{H}_{\mathbf{k}n}^{(L)}(\mathbf{r}) \otimes \mathbf{H}_{\mathbf{k}n}^{(L)*}(\mathbf{r}') \right]. \quad (16.50)$$

In this equation,  $\mathbf{A} \otimes \mathbf{B}$  is a tensor whose  $(ij)$  element is given by  $A_i B_j$ . Equation (16.50) was derived from the completeness of  $\{\mathbf{H}_{\mathbf{k}n}^{(T)}\}$  and  $\{\mathbf{H}_{\mathbf{k}n}^{(L)}\}$ . For the details of its derivation, the reader may consult [13].

The solution of the general inhomogeneous equation with a source term  $\mathbf{F}$ ,

$$-\left(\frac{1}{c^2} \frac{\partial^2}{\partial t^2} + \mathcal{L}\right) \mathbf{H}(\mathbf{r}, t) = \mathbf{F}(\mathbf{r}, t), \quad (16.51)$$

is given by the convolution

$$\mathbf{H}(\mathbf{r}, t) = \int_V d\mathbf{r}' \int_{-\infty}^{\infty} dt' G(\mathbf{r}, \mathbf{r}', t - t') \mathbf{F}(\mathbf{r}', t'), \quad (16.52)$$

which can be proved by substituting (16.52) into (16.51) and using (16.46).

### 16.3.2 Coupling with an Incident Plane Wave

We examine the excitation process of Dirac-cone modes by an incident plane wave, which we denote by  $\mathbf{H}_{\text{in}}$ :

$$\mathbf{H}_{\text{in}}(\mathbf{r}, t) = \mathbf{H}_0 e^{i(\mathbf{k}_0 \cdot \mathbf{r} - \omega t)}. \quad (16.53)$$

In this equation,  $\mathbf{k}_0$  and  $\omega$  are the wave vector and the angular frequency of the incident plane wave from free space, respectively. So,

$$\omega = c|\mathbf{k}_0|. \quad (16.54)$$

To use the formulation derived in the last section, we introduce a uniform distribution of magnetic dipoles oscillating in phase,  $\mathbf{P}_m(\mathbf{r}, t)$ , which generate the incident plane wave,  $\mathbf{H}_{\text{in}}$ .

$$\mathbf{P}_m(\mathbf{r}, t) = \mathbf{d}_m \delta(z - z_0) e^{i(\kappa_x x + \kappa_y y) + (-i\omega + \delta)t}, \quad (16.55)$$

where Cartesian coordinates are defined as shown in Fig. 16.3a.  $z_0 (> 0)$  defines the plane where the oscillating magnetic dipoles are located and is assumed to be much larger than the wavelength. For simplicity, we assume that  $\mathbf{d}_m$  is oriented in the  $xy$  plane. We denote its tilt angle against the  $x$ -axis by  $\theta$  (Fig. 16.4). Positive infinitesimal  $\delta$  in (16.55) assures the adiabatic switching of the oscillation.  $\kappa_x$  and  $\kappa_y$  are the  $x$  and  $y$  components of the wave vector of the incident wave  $\mathbf{k}_0$ :

$$\mathbf{k}_0 = \left( \kappa_x, \kappa_y, -\sqrt{\omega^2/c^2 - \kappa_x^2 - \kappa_y^2} \right). \quad (16.56)$$

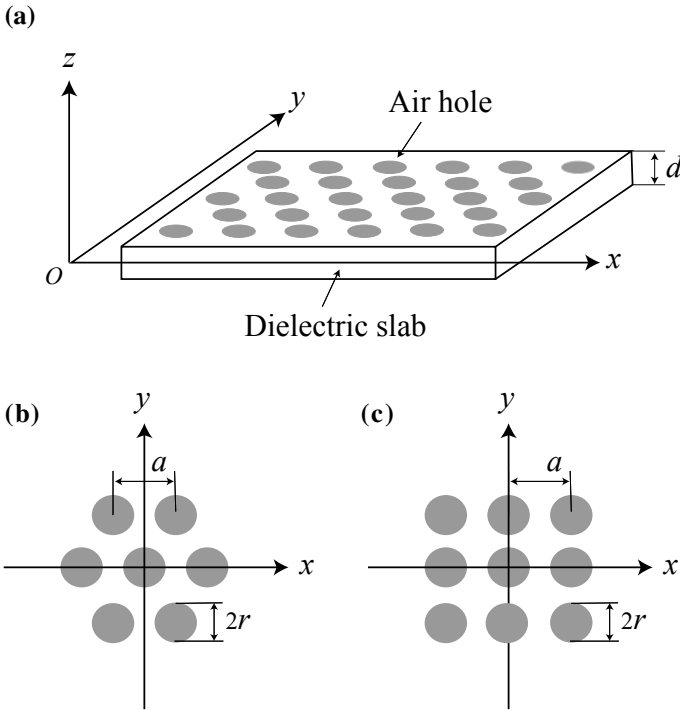


**Fig. 16.3** **a** Schematic illustration of a two-dimensional periodic metamaterials/photonic crystal slab. **b, c** Top view of the configuration of several air holes in the triangular-lattice photonic crystal slab of the  $C_{6v}$  symmetry and in the square-lattice photonic crystal slab of the  $C_{4v}$  symmetry, respectively

The wave equation with  $\mathbf{P}_m$  as a source term is

$$-\left(\frac{1}{c^2} \frac{\partial^2}{\partial t^2} + \mathcal{L}\right) \mathbf{H}(\mathbf{r}, t) = \varepsilon_0 \frac{\partial^2 \mathbf{P}_m}{\partial t^2}. \tag{16.57}$$

By using (16.52), we obtain

$$\mathbf{H}(\mathbf{r}, t) = -\frac{\mathbf{P}_m(\mathbf{r}, t)}{\mu_0} + \sum_{\mathbf{kn}} \frac{\omega_{\mathbf{kn}} \mathbf{H}_{\mathbf{kn}}^{(T)}(\mathbf{r})}{\mu_0 V} \int_V d\mathbf{r}' \int_{-\infty}^t dt' \mathbf{H}_{\mathbf{kn}}^{(T)*}(\mathbf{r}') \cdot \mathbf{P}_m(\mathbf{r}', t') \sin \omega_{\mathbf{kn}}(t - t'). \tag{16.58}$$

An important feature of this result is that the longitudinal eigenmodes were used to reconstruct the original oscillating magnetic polarization and the propagating part of the induced wave is solely described by the transverse eigenmodes. So, the unphysical longitudinal solutions do not explicitly appear in the result.

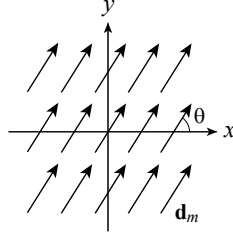


**Fig. 16.4** Distribution of the oscillating magnetic polarization with amplitude  $\mathbf{d}_m$  and tilt angle  $\theta$ . It has a phase factor  $e^{i(\kappa_x x + \kappa_y y)}$  to produce a plane wave propagating in the direction designated by  $\mathbf{k}_0 = (\kappa_x, \kappa_y, -\sqrt{\omega^2/c^2 - \kappa_x^2 - \kappa_y^2})$ . Reprinted with permission from [13]: Copyright ©2014 by the American Physical Society

Now, we go back to the problem of the excitation process of the Dirac-cone modes. The summation over  $n$  in (16.58) includes two types of eigenmodes. One is the waveguide modes localized on the slab, and the other is reflected, transmitted, and diffracted waves that propagate like plane waves when they are sufficiently away from the slab and do not have a large amplitude in the vicinity of the slab. The former have discrete eigenfrequencies for each  $(\kappa_x, \kappa_y)$  and compose the Dirac cone. On the other hand, the latter have quasi-continuous eigenfrequencies that may be designated by the  $z$  component of the wave vector. Because we are interested only in the former, we ignore the contribution from the latter.

Then, we replace the summation over  $n$  by a summation over waveguide modes in the relevant frequency range, which we distinguish by  $j$ . We denote the number of the slab modes that contribute to the Dirac cone by  $n_s$ , and introduce  $\langle \mathbf{u}_{\kappa j}^*(z_0) \cdot \mathbf{d}_m \rangle$  defined by

$$\langle \mathbf{u}_{\kappa j}^*(z_0) \cdot \mathbf{d}_m \rangle = \frac{1}{V} \int_V d\mathbf{r} \mathbf{u}_{\kappa j}^*(\mathbf{r}) \cdot \mathbf{d}_m \delta(z - z_0). \quad (16.59)$$

According to the conservation law of the frequency and the wave vector parallel to the slab surface, those of the incident wave have to be tuned exactly. But, this exact tuning is practically impossible. Rather, we have to assume a finite width for the eigenfrequency, which is caused by the finite lifetime of the eigenmode due to dielectric loss, diffraction loss, etc. Thus, the positive infinitesimal  $\delta$  should be replaced by a finite relaxation rate  $\gamma$  in (16.55). We ignore the counter resonant terms in the following.

To calculate the electromagnetic energy flux, we evaluate the divergence of time-averaged Poynting's vector,  $\bar{\mathbf{S}}$ . The result is given by [13]

$$\nabla \cdot \overline{\mathbf{S}(\mathbf{r}, t)} = \frac{i\omega\delta(z - z_0)}{4} \sum_{j=1}^{n_s} \left[ \frac{\alpha_{\kappa j} \mathbf{u}_{\kappa j}(\mathbf{r}) \cdot \mathbf{d}_m^*}{\omega - \omega_{\kappa j} + i\gamma_{\kappa j}} - \frac{\alpha_{\kappa j}^* \mathbf{u}_{\kappa j}^*(\mathbf{r}) \cdot \mathbf{d}_m}{\omega - \omega_{\kappa j} - i\gamma_{\kappa j}} \right], \quad (16.60)$$

where  $\alpha_{\kappa j}$  is defined as

$$\alpha_{\kappa j} = \frac{\omega_{\kappa j}}{2\mu_0} \langle \mathbf{u}_{\kappa j}^*(z_0) \cdot \mathbf{d}_m \rangle. \quad (16.61)$$

The electromagnetic energy radiated in a unit time is obtained by the spatial integral of  $\nabla \cdot \bar{\mathbf{S}}$ , whose propagation direction can be found by the following discussion.

We assume that the diffraction loss of the Dirac cone modes is relatively small, so their quality factor is sufficiently large. Then, their energy flux is nearly parallel to the slab surface. Then, its energy velocity, which is equal to the group velocity  $\mathbf{v}_{\kappa j}$  in the case of lossless media [14], is given by the slope of the Dirac cone. As a result, the energy flux in the slab plane,  $\mathbf{S}_{\parallel}$ , is given by

$$\mathbf{S}_{\parallel} = \mu_0 L_z \sum_{j=1}^{n_s} \frac{|\alpha_{\kappa j}|^2 \gamma_{\kappa j} \mathbf{v}_{\kappa j}}{\{(\omega - \omega_{\kappa j})^2 + \gamma_{\kappa j}^2\} |\mathbf{v}_{\kappa j}|}, \quad (16.62)$$

where  $L_z$  is the size of volume  $V$  in the  $z$  direction. In the following sections, we calculate  $\mathbf{S}_{\parallel}$  for the square-lattice and triangular-lattice slab structures.

### 16.3.3 Slabs of $C_{4v}$ and $C_{6v}$ Symmetries

Let us first examine the square lattice with  $C_{4v}$  symmetry. We examine the combination of an  $E$  mode and an  $A_1$  mode as an example. The eigenequation is

$$\begin{pmatrix} 0 & 0 & bk_x \\ 0 & 0 & bk_y \\ b^*k_x & b^*k_y & 0 \end{pmatrix} \begin{pmatrix} A \\ B \\ C \end{pmatrix} = \Delta\lambda \begin{pmatrix} A \\ B \\ C \end{pmatrix}, \quad (16.63)$$

where  $\Delta\lambda$  denotes the difference between the eigenvalues for  $\mathbf{k} \neq 0$  and for  $\mathbf{k} = 0$ . The eigenwave function is then given by

$$\mathbf{u}_{\mathbf{k}} = A\mathbf{u}_E^{(1)} + B\mathbf{u}_E^{(2)} + C\mathbf{u}_{A_1}, \quad (16.64)$$

where  $\mathbf{u}_E^{(1)}$  and  $\mathbf{u}_E^{(2)}$  are two wave functions of the doubly degenerate  $E$  mode.  $\mathbf{u}_{A_1}$  is the wave function of the  $A_1$  mode.

The three solutions are given as follows:

(i)  $\Delta\lambda = 0$

$$\begin{pmatrix} A^{(0)} \\ B^{(0)} \\ C^{(0)} \end{pmatrix} = \begin{pmatrix} \sin \phi \\ -\cos \phi \\ 0 \end{pmatrix}, \quad (16.65)$$

(ii)  $\Delta\lambda = |b|k$

$$\begin{pmatrix} A^{(+)} \\ B^{(+)} \\ C^{(+)} \end{pmatrix} = \frac{1}{\sqrt{2}} \begin{pmatrix} e^{i\beta} \cos \phi \\ e^{i\beta} \sin \phi \\ 1 \end{pmatrix}, \quad (16.66)$$

(iii)  $\Delta\lambda = -|b|k$ 

$$\begin{pmatrix} A^{(-)} \\ B^{(-)} \\ C^{(-)} \end{pmatrix} = \frac{1}{\sqrt{2}} \begin{pmatrix} -e^{i\beta} \cos \phi \\ -e^{i\beta} \sin \phi \\ 1 \end{pmatrix}, \quad (16.67)$$

where  $\beta = \arg b$  and  $\phi$  is the angle between vector  $\mathbf{k}$  and the  $x$ -axis.

When we denote the angle between  $\mathbf{d}_m$  and the  $x$ -axis by  $\theta$  (see Fig. 16.4), we can easily show from the transformation properties by symmetry operations that

$$\langle \mathbf{u}_E^{(1)}(z_0) \cdot \mathbf{d}_m \rangle = |\mathbf{d}_m| \langle u_{E,x}(z_0) \rangle \cos \theta, \quad (16.68)$$

$$\langle \mathbf{u}_E^{(2)}(z_0) \cdot \mathbf{d}_m \rangle = |\mathbf{d}_m| \langle u_{E,x}(z_0) \rangle \sin \theta, \quad (16.69)$$

$$\langle \mathbf{u}_{A_1}(z_0) \cdot \mathbf{d}_m \rangle = 0, \quad (16.70)$$

where

$$\langle u_{E,x}(z_0) \rangle = \frac{1}{V} \int_V d\mathbf{r} u_{E,x}^{(1)}(\mathbf{r}) \delta(z - z_0) = \frac{1}{V} \int_V d\mathbf{r} u_{E,y}^{(2)}(\mathbf{r}) \delta(z - z_0). \quad (16.71)$$

Finally, for three solutions of  $\Delta\lambda = 0$  and  $\pm|b|k$ , we obtain

$$\mathbf{S}_{\parallel}^{(0)} = \frac{\gamma_{\kappa 0} \omega_{\kappa 0}^2 |\mathbf{d}_m|^2 L_z |\langle \mathbf{u}_E(z_0) \rangle_0|^2 \mathbf{v}_{\kappa 0}}{4\mu_0 \{(\omega - \omega_{\kappa 0})^2 + \gamma_{\kappa 0}^2\} |\mathbf{v}_{\kappa 0}|} \sin^2(\phi - \theta), \quad (16.72)$$

$$\mathbf{S}_{\parallel}^{(\pm)} = \frac{\gamma_{\kappa \pm} \omega_{\kappa \pm}^2 |\mathbf{d}_m|^2 L_z |\langle \mathbf{u}_E(z_0) \rangle_0|^2 \mathbf{v}_{\kappa \pm}}{8\mu_0 \{(\omega - \omega_{\kappa \pm})^2 + \gamma_{\kappa \pm}^2\} |\mathbf{v}_{\kappa \pm}|} \cos^2(\phi - \theta). \quad (16.73)$$

In (16.72) and (16.73),

$$|\mathbf{v}_{\kappa 0}| \approx 0 \quad \text{and} \quad \mathbf{v}_{\kappa \pm} = \pm \frac{v\kappa}{|\kappa|} \quad (16.74)$$

for small  $|\kappa|$ , where  $v$  is the slope of the Dirac cone.

The velocity of the quadratic mode is vanishing at the Dirac point, so its energy flow along the slab surface is small. On the other hand, the velocity of the Dirac-cone modes is finite, so they propagate along the slab surface. Their propagation direction is parallel to the wave vector  $\kappa$ . We should note the presence of the  $\cos^2(\phi - \theta)$  term in  $\mathbf{S}_{\parallel}^{(\pm)}$ . This term is brought about by the anisotropic mixture of two dipolar wave functions as shown in (16.66) and (16.67). Due to this term, the induced energy flow along the slab surface is largest when the magnetic field of the incident plane wave is polarized in the same direction as  $\kappa$ .

We can analyze other cases of the mode combinations similarly. The results are summarized in Table 16.5. Each mode combination has its own angular dependence, so we can distinguish the mode symmetry by measuring the angular distribution of the energy flow.

**Table 16.5** Dependence of the energy flux  $S_{\parallel}$  on the polarization angle  $\theta$  of the incident magnetic field and the propagation angle  $\phi$ . “Silent” means that the coupling between the incident plane wave from the normal direction and the Dirac-cone mode is vanishing in the first-order approximation, so the Dirac-cone mode is not excited

Lattice symmetry	Mode1	Mode2	Angular dependence
$C_{4v}$	$E$	$A_1$	$\cos^2(\phi - \theta)$
	$E$	$A_2$	$\sin^2(\phi - \theta)$
	$E$	$B_1$	$\cos^2(\phi + \theta)$
	$E$	$B_2$	$\sin^2(\phi + \theta)$
$C_{6v}$	$E_1$	$E_2$	1
	$E_1$	$A_1$	$\cos^2(\phi - \theta)$
	$E_1$	$A_2$	$\sin^2(\phi - \theta)$
	$E_2$	$B_1$	silent
	$E_2$	$B_2$	silent

## 16.4 Superluminal Propagation

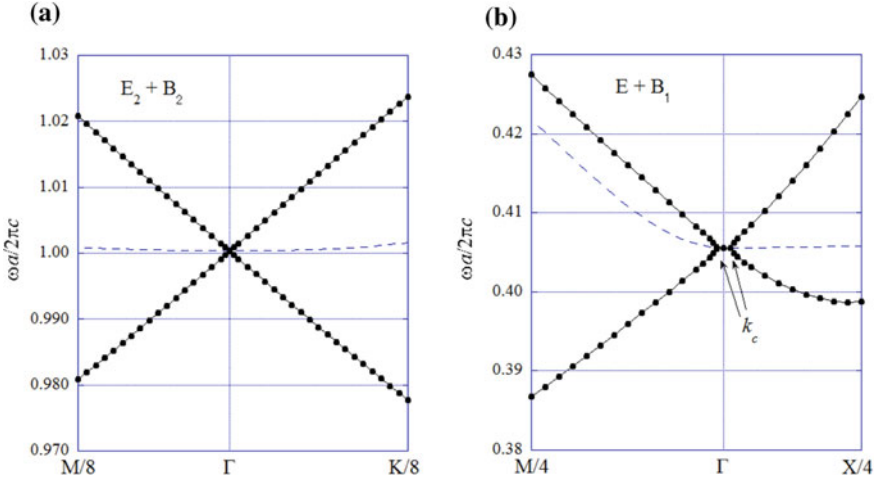
In this section, we follow the discussion in [16]. In non-Hermitian systems, we sometimes encounter superluminal propagation of photonic eigenmodes; that is, their group velocity exceeds the speed of light, which is an apparent violation of special relativity. Physicists have long been perplexed by this contradiction [17], and recently it was also found for photonic Dirac-cone dispersion [16].

Figure 16.5 shows two typical cases of normal and distorted photonic Dirac-cone dispersion curves found by numerical calculations. Figure 16.5a shows the Dirac cone materialized by an  $E_2$  mode and a  $B_2$  mode of a triangular-lattice photonic crystal slab, and Fig. 16.5b shows the Dirac cone materialized by an  $E$  mode and a  $B_1$  mode of a square-lattice photonic crystal slab. The critical difference between the two cases is the coupling to electromagnetic modes in free space. Here, we should recall that only  $E_1$  modes of the triangular lattice and  $E$  modes in the square lattice couple to electromagnetic modes in free space due to the symmetry matching [14, 18]. So, the  $E$  eigenmodes gradually escape (are diffracted) to free space while they propagate along the two-dimensional plane of the photonic crystal slab. This means that the Dirac-cone modes in Fig. 16.5b are lossy. So, the problem that we meet here is a new manifestation of superluminal propagation in non-Hermitian systems.

Now we extend our degenerate  $\mathbf{k} \cdot \mathbf{p}$  perturbation theory to the lossy case. It is convenient to deal with the angular frequency of the eigenmode rather than  $\lambda$  defined by (16.5), so we introduce a new matrix  $D^{(\mathbf{k})}$  according to (16.36).

$$D^{(\mathbf{k})} = \frac{c^2}{2\omega_{\Gamma}} C^{(\mathbf{k})}. \quad (16.75)$$





**Fig. 16.5** **a** Photonic Dirac cone materialized with a quadratic dispersion surface by the accidental degeneracy of an  $E_2$  mode and a  $B_2$  mode in a triangular-lattice photonic crystal slab of the  $C_{6v}$  symmetry. Specimen parameters: refractive index = 3.52 (silicon),  $d = 0.137a$ ,  $r = 0.474a$ . The vertical axis is the dimensionless frequency normalized with the lattice constant  $a$  and the speed of light  $c$ . The horizontal axis is the wave vector in the Brillouin zone, where M and K denote two highly symmetric points. M/8, for example, implies that the horizontal axis is magnified by eight times. **b** Deformed Dirac cone materialized by an  $E$  mode and a  $B_1$  mode in a square-lattice photonic crystal of the  $C_{4v}$  symmetry. Specimen parameters:  $d = 0.8a$ ,  $r = 0.318a$

Then, the eigenvalue of  $D^{(\mathbf{k})}$  gives the first-order correction of the angular frequency. For the accidental degeneracy of an  $E$  mode and a  $B_1$  mode,  $D^{(\mathbf{k})}$  is given by

$$D^{(\mathbf{k})} = \begin{pmatrix} -i\gamma & 0 & v_d k_x \\ 0 & -i\gamma & -v_d k_y \\ v_d k_x & -v_d k_y & 0 \end{pmatrix}, \quad (16.76)$$

where  $v_d$  is the slope of the Dirac cone without diffraction loss, which has a dimension of speed, and  $\gamma$  is the extinction rate that is given by the ratio of the Dirac point frequency  $\omega_\Gamma$  to the quality factor of the  $E$  mode. By diagonalizing (16.76), we obtain the following isotropic dispersion relation for the deformed Dirac cone.

$$\omega = \omega_\Gamma + \frac{-i\gamma \pm \sqrt{4v_d^2 k^2 - \gamma^2}}{2}. \quad (16.77)$$

So, the group velocity is

$$v_g \equiv \frac{\partial \omega}{\partial k} = \frac{2v_d^2 k}{\sqrt{4v_d^2 k^2 - \gamma^2}}, \quad (16.78)$$

which is divergent at a critical wave vector  $k_c = \gamma/2v_d$  and is even purely imaginary for  $k \leq k_c$ !

## 16.5 Periodically Modulated Quantum Well

Because the photonic Dirac cone is solely brought about by particular combinations of mode symmetries, a similar situation is expected to be materialized in other wave systems as well. The subbands of their energy spectra can be derived by introducing periodic structural modulation or applying periodic external potentials. When the symmetry of their wave functions satisfies the conditions described in the previous sections, Dirac cones should appear. In this section, we demonstrate it for a simple electronic system, that is, the periodically modulated quantum wells [19].

For the sake of simplicity, we assume that the electronic system is described by the one-component effective mass Schrödinger equation. When we denote the electron effective mass by  $m$ , the momentum operator by  $\hat{\mathbf{p}}$ , and the confinement potential of the periodically modulated quantum well by  $U$ , the Schrödinger equation is given by

$$\hat{\mathcal{H}}\psi_{\mathbf{k}n} \equiv \left( \frac{\hat{\mathbf{p}}^2}{2m} + U \right) \psi_{\mathbf{k}n} = E_{\mathbf{k}n} \psi_{\mathbf{k}n}, \quad (16.79)$$

where  $\mathbf{k}$  is the wave vector in the two-dimensional Brillouin zone and  $n$  is the band index. From the Bloch theorem,  $\psi_{\mathbf{k}n}$  is expressed as

$$\psi_{\mathbf{k}n}(\mathbf{r}) = e^{i\mathbf{k}\cdot\mathbf{r}} u_{\mathbf{k}n}(\mathbf{r}), \quad (16.80)$$

and  $u_{\mathbf{k}n}(\mathbf{r})$  is a periodic function:

$$u_{\mathbf{k}n}(\mathbf{r} + \mathbf{a}_i) = u_{\mathbf{k}n}(\mathbf{r}) \quad (i = 1, 2), \quad (16.81)$$

where  $\mathbf{a}_i$  is the two-dimensional elementary translation vector of the periodic modulation (see Fig. 16.6). Note that  $\mathbf{a}_i$  is *not* relevant to the atomic lattice translation vector. The wave function for the present problem is a complex scalar field, whereas that of the electromagnetic case was a complex vector field. So, the present problem is easier than the latter.

We assume that the modulation of the confinement potential possesses a certain spatial symmetry like the electromagnetic case. We denote its point group by  $\mathcal{G}$ . Then, the periodic modulation yields electronic subbands in the first Brillouin zone defined by the above  $\mathbf{a}_i$ . We assume that two subbands are degenerate on the  $\Gamma$  point and denote their eigenfunctions by  $\{u_{0l} | l = 1, 2, \dots, M\}$  allowing for the multiplicity of each subband. Then, we can discuss the conditions for materializing the Dirac cone in a similar manner as before.

Now, the first-order perturbation matrix,  $C^{(\mathbf{k})} = (C_{ij}^{(\mathbf{k})})$  ( $i, j = 1, 2, \dots, M$ ), for the present problem is much simpler than the electromagnetic case. By following

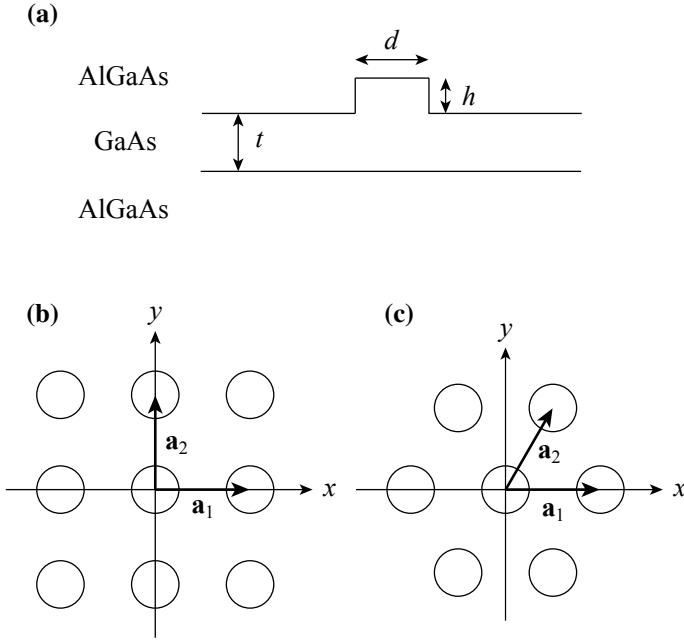


**Fig. 16.6** **a** Side view of a periodically modulated quantum well. We assume a cylindrical bump in each unit structure. Top view of the modulated quantum wells of **b** the square lattice of  $C_{4v}$  symmetry and **c** the triangular lattice of the  $C_{6v}$  symmetry. Reprinted with permission from [19]: Copyright ©2016 by the Physical Society of Japan

the same procedure described in Sect. 16.2.1, we can obtain its explicit form and the invariance under the symmetry transformations.

$$C_{ij}^{(\mathbf{k})} = \frac{\hbar}{m} (\mathbf{R}\mathbf{k}) \cdot \langle \mathcal{R}u_{0i} | \hat{\mathbf{p}} | \mathcal{R}u_{0j} \rangle_0 \quad (\forall \mathcal{R} \in \mathcal{G}), \quad (16.82)$$

where  $\mathbf{R}$  is the matrix representation of  $\mathcal{R}$  and  $\langle \cdots \rangle_0$  denotes integration over the unit cell. Because (16.82) has the same structure as (16.25), we can conclude that particular combinations of mode symmetries result in the formation of Dirac cones. For example, the first-order perturbation matrix is given as follows for the accidental degeneracy of the  $E$  and  $A_1$  subbands in the square lattice of the  $C_{4v}$  symmetry:

$$C^{(\mathbf{k})} = \begin{pmatrix} 0 & 0 & bk_x \\ 0 & 0 & bk_y \\ b^*k_x & b^*k_y & 0 \end{pmatrix}, \quad (16.83)$$

where

$$b = \frac{\hbar}{m} \langle u_E^{(1)} | \hat{p}_x | u_{A_1} \rangle. \quad (16.84)$$

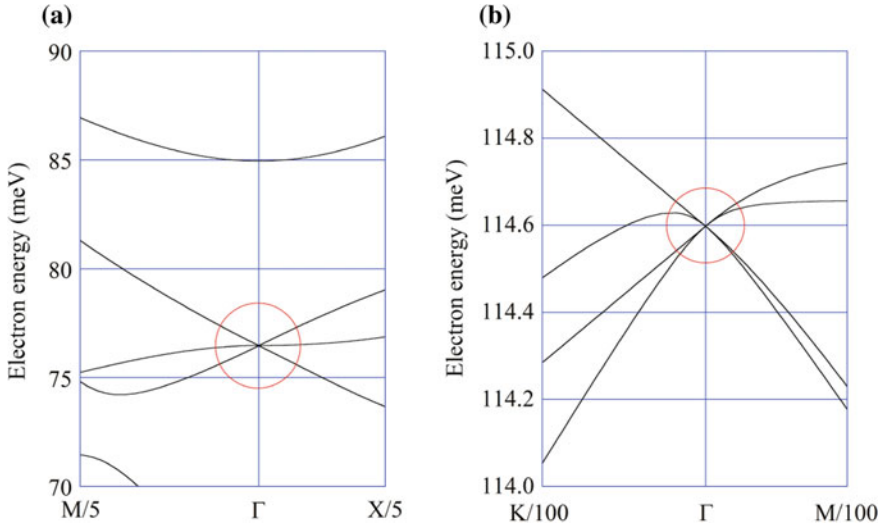


**Fig. 16.7** Subbands of the periodically modulated GaAs/AlGaAs quantum well. **a** Square lattice with  $|a_i| \equiv a = 30 \text{ nm}$ ,  $t = 15 \text{ nm}$ ,  $h = 6 \text{ nm}$ , and  $d = 22.8 \text{ nm}$ . **b** Triangular lattice with  $a = 30 \text{ nm}$ ,  $t = 15 \text{ nm}$ ,  $h = 6 \text{ nm}$ , and  $d = 20.55 \text{ nm}$ . The vertical axis is the electron energy measured from the bottom of the GaAs conduction band. The horizontal axis is the wave vector in the two-dimensional Brillouin zone, where  $X = (\pi/a, 0)$  and  $M = (\pi/a, \pi/a)$  for the square lattice and  $K = (4\pi/(3a), 0)$  and  $M = (\pi/a, -\pi/(\sqrt{3}a))$  for the triangular lattice. X/5, for example, means that the horizontal axis is magnified by five times. Reprinted with permission from [19]: Copyright ©2016 by the Physical Society of Japan

By solving the secular equation, we can obtain the first-order energy correction,  $\Delta E$ :

$$\Delta E = \pm |b|k, \quad 0. \tag{16.85}$$

Therefore, there are an isotropic Dirac cone and a quadratic dispersion surface. We can analyze the rest of the symmetry combinations and obtain completely the same conclusions as shown in Tables 16.2 and 16.3. We checked the analytical results by calculating the band structure using the finite element method [19]. As shown in Fig. 16.7, the numerical results agreed with the analytical calculation. The specimen parameters to materialize the accidental degeneracy are listed in the figure caption.

In the actual specimen fabrication, however, the probability of exact degeneracy by adjusting the specimen parameters is negligibly small, so there is always an energy mismatch between the two subbands even if it is small. Let us finally analyze this problem. We introduce an energy mismatch  $\alpha$  to the (3, 3) element of  $C^{(k)}$ .

$$C^{(k)} = \begin{pmatrix} 0 & 0 & bk_x \\ 0 & 0 & bk_y \\ b^*k_x & b^*k_y & \alpha \end{pmatrix}. \tag{16.86}$$

By solving the secular equation, we obtain the first-order correction to the electron energy.

$$\Delta E = \frac{\alpha \pm \sqrt{\alpha^2 + 4|b|^2 k^2}}{2} \quad (16.87)$$

Then, from the definition of the effective mass  $m^*$

$$\left. \frac{\partial^2 E}{\partial k^2} \right|_{k=0} = \frac{\hbar^2}{m^*}, \quad (16.88)$$

we obtain

$$m^* = \frac{|\alpha| \hbar^2}{2|b|^2} \quad (16.89)$$

So, the electron effective mass  $m^*$  in the periodically modulated quantum well is proportional to the energy mismatch. The effective mass vanishes when the energy mismatch becomes infinitesimally small. This phenomenon brings about a large electron mobility and may find a new application.

As we showed in this chapter, the accidental degeneracy of two eigenmodes with particular symmetry combinations materializes the Dirac cone. This phenomenon is common to all kinds of wave propagation in mesoscopic periodic systems including electromagnetic waves, electronic waves, phonons, magnons, excitons, and polaritons. In addition to common features like cloaking, there are such features that are peculiar to each wave system: small effective mass for electronic system and control of propagation direction by incident polarization for electromagnetic waves. We hope that these features may find peculiar applications in the future.

## References

1. A. Sanada, C. Caloz, T. Itoh, Characteristics of the composite right/left-handed transmission lines. *IEEE Microw. Wirel. Compon. Lett.* **14**, 68–70 (2004)
2. C. Caloz, A. Sanada, T. Itoh, A novel composite right-/left-handed coupled-line directional coupler with arbitrary coupling level and broad bandwidth. *IEEE Trans. Microw. Theory Tech.* **52**, 980 (2004)
3. A. Sanada, C. Caloz, T. Itoh, Planar distributed structures with negative refractive index. *IEEE Trans. Microw. Theory Tech.* **52**, 1252 (2004)
4. C. Caloz, T. Itoh, *Electromagnetic Metamaterials: Transmission Line Theory and Microwave Applications* (Wiley, 2005)
5. K. Sakoda, H.-F. Zhou, Role of structural electromagnetic resonances in a steerable left-handed antenna. *Opt. Express* **18**, 27371–27386 (2010)
6. K. Sakoda, Dirac cone in two- and three-dimensional metamaterials. *Opt. Express* **20**, 3898–3917 (2012)
7. K. Sakoda, Double Dirac cones in triangular-lattice metamaterials. *Opt. Express* **20**, 9925–9939 (2012)
8. J. Mei, Y. Wu, C.T. Chan, Z.-Q. Zhang, First-principles study of Dirac and Dirac-like cones in phononic and photonic crystals. *Phys. Rev. B* **86**, 035141 (2012)

9. K. Sakoda, Proof of the universality of mode symmetries in creating photonic Dirac cones. *Opt. Express* **20**, 25181–25194 (2012)
10. X. Huang, Y. Lai, Z.H. Hang, H. Zheng, C.T. Chan, Dirac cones induced by accidental degeneracy in photonic crystals and zero-refractive-index materials. *Nat. Mater.* **10**, 582–586 (2011)
11. M. Silveirinha, N. Engheta, Tunneling of electromagnetic energy through subwavelength channels and bends using  $\epsilon$ -near-zero materials. *Phys. Rev. Lett.* **97**, 157403 (2006)
12. A. Alu, M.G. Silveirinha, A. Salandrino, N. Engheta, Epsilon-near-zero metamaterials and electromagnetic sources: tailoring the radiation phase pattern. *Phys. Rev. B* **75**, 155410 (2007)
13. K. Sakoda, Polarization-dependent continuous change in the propagation direction of Dirac-cone modes in photonic crystal slabs. *Phys. Rev. A* **90**, 013835 (2014)
14. K. Sakoda, *Optical Properties of Photonic Crystals*, 2nd edn. (Springer, Berlin, 2004)
15. T. Inui, Y. Tanabe, Y. Onodera, *Group Theory and Its Applications in Physics* (Springer, Berlin, 1990)
16. K. Sakoda, H. Takeda, Dirac cones in photonic crystal slabs, in *Abstract Book of 10th International Symposium of Modern Optics and Its Applications*, Bandung (2015), pp. 68–69
17. See, for example, M. Tanaka, M. Fujiwara, H. Ikegami, Propagation of a Gaussian wave packet in an absorbing medium. *Phys. Rev. A* **34**, 4851–4858 (1986)
18. T. Ochiai, K. Sakoda, Dispersion relation and optical transmittance of a hexagonal photonic crystal slab. *Phys. Rev. B* **63**, 125107 (2001)
19. Y. Yao, K. Sakoda, Dirac cones in periodically modulated quantum wells. *J. Phys. Soc. Jpn.* **85**, 065002 (2016)